



COPYRIGHT AND USE OF THIS THESIS

This thesis must be used in accordance with the provisions of the Copyright Act 1968.

Reproduction of material protected by copyright may be an infringement of copyright and copyright owners may be entitled to take legal action against persons who infringe their copyright.

Section 51 (2) of the Copyright Act permits an authorized officer of a university library or archives to provide a copy (by communication or otherwise) of an unpublished thesis kept in the library or archives, to a person who satisfies the authorized officer that he or she requires the reproduction for the purposes of research or study.

The Copyright Act grants the creator of a work a number of moral rights, specifically the right of attribution, the right against false attribution and the right of integrity.

You may infringe the author's moral rights if you:

- fail to acknowledge the author of this thesis if you quote sections from the work
- attribute this thesis to another author
- subject this thesis to derogatory treatment which may prejudice the author's reputation

For further information contact the University's Director of Copyright Services

sydney.edu.au/copyright

Hyperspectral Benthic Mapping From Underwater Robotic Platforms

Daniel L. Bongiorno

A thesis submitted in fulfillment
of the requirements of the degree of
Doctor of Philosophy



THE UNIVERSITY OF
SYDNEY

Australian Centre for Field Robotics
School of Aerospace, Mechanical and Mechatronic Engineering
The University of Sydney

May 2015

Declaration

I hereby declare that this submission is my own work and that, to the best of my knowledge and belief, it contains no material previously published or written by another person nor material which to a substantial extent has been accepted for the award of any other degree or diploma of the University or other institute of higher learning, except where due acknowledgement has been made in the text.

Daniel L. Bongiorno

1 May 2015

Abstract

Daniel L. Bongiorno
The University of Sydney

Doctor of Philosophy
May 2015

Hyperspectral Benthic Mapping From Underwater Robotic Platforms

We live on a planet of vast oceans; 70% of the Earth's surface is covered in water. They are integral to supporting life, providing 99% of the inhabitable space on Earth. Our oceans and the habitats within them are under threat due to a variety of factors, including climate change, over-fishing, habitat destruction, pollution and bio-invasion. To understand the impacts and possible solutions, the monitoring of marine habitats is critically important.

Methods for monitoring can include physical sampling, sonar imaging and optical imaging with cameras. Optical imaging can provide a vast array of information. The types of information which can be obtained through optical imaging include the biological constituents living within a water body, the seafloor coverage types such as sand, coral, seagrass and various health indices of marine habitats such as the severity of coral bleaching. Imaging through water however is complex, with selective attenuation effects occurring as a result of the atomic nature of water as well as the constituents suspended and dissolved within it.

To compensate for the attenuation of light in water, this thesis presents a novel light propagation model and illustrates how it can improve optical imaging performance. Insights gained from this model are used to design an in-situ hyperspectral system. The optical system is comprised of two upward looking spectrometers at different positions in the water column. The downwelling light in the water column is continuously sampled by the system. This allows for the generation of a dynamic water model.

In addition to the two upward looking spectrometers the in-situ system contains an imaging module. This module can be used for imaging of the seafloor. It consists of a hyperspectral

sensor and a trichromatic stereo camera. New calibration methods are presented for the spatial and spectral co-registration of the two optical sensors. The dynamic water model is used in conjunction with the stereo camera to resolve water corrected RGB imagery and corrected hyperspectral reflectance data. The resultant image data is invariant to the changing optical properties of the water, weather conditions, scene structure and lighting changes. In this thesis the in-situ optical system is mounted onboard an Autonomous Underwater Vehicle (AUV). The utility of the corrected data from this system is demonstrated with data obtained during a coral reef survey over the Great Barrier Reef, Australia.

Data from the imaging module is also used to classify seafloor materials. The combined classification is shown to perform better than a single sensor modality. The classified seafloor patches are then integrated into a high resolution 3D benthic map of the surveyed site. This can provide informative details about underwater habitats for biological applications. Given the limited imaging resolution of the hyperspectral sensor used in this work, a new method is also presented that uses information from the co-registered colour images to inform a new spectral unmixing method to resolve subpixel materials.

Acknowledgements

This thesis would not have been possible without the support of my supervisors: Stefan Williams, Roy Hughes and Mitch Bryson, your guidance has been invaluable and thank you for believing and supporting this idea from the beginning. Thank you for your help in turning this piece of work into something readable. Many thanks to Oscar Pizarro and Richard Murphy for sitting on my review committee and providing valuable feedback throughout my PhD.

Thank you for the support from Defence Science & Technology Organisation and the Australian Centre for Field Robotics, both organisations have been extremely supportive with trials, travel, conferences, equipment and data collection. Thank you to Nautilus and Ocean Exploration trust, I had a fantastic experience onboard Nautilus, it gave me a real appreciation for large scale ROV operations. Thank you to all the crew aboard Nautilus you made my time aboard amazing.

Thank you to Andrew Durrant and Christian Lees for their enormous assistance in gathering the various datasets used in this work as well as many thanks to all the AUV team for providing excellent feedback along the way. Thank you Bryan Clarke assistance with collecting the colour correction dataset, I hope the sunshine and seaside workplace was not too much to endure. Thank you Adam Fairley, for your fantastic assistance with collecting the very early proof of concept examples, camera characterisation, lugging gear around the different areas of Sydney harbour and for helping develop some of the methodology. Thank you Donald Dansereau for allowing me to bounce thousands of crazy ideas off you and evaluate the plausible ones, also a big thanks for all that delicious beer, (grease for the gears of the mind - at least after a long week).

Sanity surely could not have been maintained without the enormous support of my wonderful wife Julia. You managed to keep me on track, motivated as well as have a load of adventures along the way. This entire endeavour would surely not have been possible without you.

My friends, my family in particular Den for allowing me to bounce ideas off you, Ruth for your jovial attitude and your great recitals of the Man from Snowy River and Mum & Dad for your constant support in this PhD. Thanks to great music (thank goodness for the advent of modern internet music streaming services).

To all the people I have gone/taken climbing, climbing has been a great outlet while undertaking this behemoth task. All those sore/scratched arms, legs, elbows, knees were definitely worth it.

Chapter illustrations in this dissertation are taken from Lewis Carroll's *Alice in Wonderland* (1865) & *Through the Looking Glass* (1871). They were beautifully drawn by Sir John Tenniel (1820 - 1914). I chose Alice in Wonderland and in particular the white rabbit to be the mascot for my research as I likened research to 'going down the rabbit hole', as you don't know where you will pop up. Each chapter illustration has been intentionally chosen to reflect the content of the chapter.



*For the adventurers which have been,
are here today and for those to come...*

Contents

Declaration	i
Abstract	ii
Acknowledgements	iv
1 Introduction	1
1.1 Thesis aims and objectives	4
1.2 Thesis Contributions	4
1.2.1 Spatial and spectral calibration techniques	5
1.2.2 Insitu water-corrected imaging	5
1.2.3 Spectral-based underwater classification & mapping	6
1.3 Thesis overview	7
1.4 System overview	8
2 Background & literature review	10
2.1 Introduction	10
2.2 Background	11
2.2.1 Understanding the water column and its effect on light	11
2.2.2 Water column modelling	13

2.3	Optical visibility improvements in water	17
2.4	Colour accuracy and correction underwater	19
2.4.1	Post processing techniques	19
2.4.2	In-water colour compensation	21
2.5	Benthic classification	22
2.6	Hyperspectral sensing underwater	23
2.6.1	Introduction to hyperspectral imaging	23
2.6.2	HSI imaging of coastal regions using remote sensing	24
2.6.3	Marine ecology applications	26
2.6.4	Defence applications	29
2.6.5	In-situ based spectral imaging	29
2.7	Spectral unmixing	30
2.7.1	Mixture models	31
2.7.2	Data reduction	35
2.7.3	Unmixing & inversion	35
2.8	Summary & outcomes	37
3	Spectral and spatial calibration	40
3.1	Introduction	40
3.2	FOV and spatial co-registration	41
3.2.1	Methodology	43
3.2.2	Results	46
3.2.3	Discussion	51
3.3	Relative radiometric calibration of spectrometers	52
3.4	Spectral sensitivities of RGB cameras	55

<i>CONTENTS</i>	ix
3.4.1 Previous work	56
3.4.2 Methodology	58
3.4.3 RGB camera characterisation results	65
3.5 Summary	68
4 In-situ water corrected imaging	74
4.1 Introduction	74
4.2 Environmentally based colour correction	75
4.2.1 Methodology	76
4.2.2 Test tank experimental setup	80
4.2.3 Test Tank Results	81
4.2.4 Real-world experimental setup	82
4.2.5 Real-world Results	84
4.2.6 Performance Evaluation	87
4.3 Colour correction of AUV imagery	92
4.3.1 AUV upward looking spectrometer	97
4.3.2 Ship-borne upward looking spectrometer	101
4.3.3 Limitations	101
4.3.4 Extended water model	102
4.3.5 AUV imagery colour correction results	105
4.4 Deriving spectral reflectance	109
4.4.1 Illumination at scene	110
4.4.2 Reflected irradiance at scene	110
4.4.3 Spectral imaging from an AUV	111
4.4.4 Spectral reflectance results	118
4.5 Summary	124

5	Spectral-based classification & mapping	126
5.1	Introduction	126
5.2	Spectral and spatial classification	127
5.2.1	Classification performance	130
5.3	Spectral mapping	131
5.3.1	Benthic habitat map	134
5.4	Spatially assisted spectral unmixing	136
5.4.1	Resolving number of materials	139
5.4.2	Informed and constrained unmixing	140
5.4.3	Reducing computational complexity	141
5.5	Unmixing results: synthetic dataset	143
5.5.1	Generating a synthetic dataset	144
5.5.2	Noise sensitivity	147
5.5.3	Results	148
5.6	Spectral unmixing results: coral reef dataset	157
5.7	Summary	162
6	Conclusions and future directions	164
6.1	Conclusions	165
6.2	Future directions	168
6.2.1	Water modelling onboard the AUV	168
6.2.2	Spatial distribution of optical properties	168
6.2.3	Upgrading to a HSI camera	169
6.2.4	Benthic health monitoring	169
6.2.5	Defence applications	170
6.2.6	Spectral unmixing	170

<i>CONTENTS</i>	xi
Bibliography	171
A Enhanced underwater visibility through polarisation	189
A.1 Introduction	189
A.2 Methodology	191
A.2.1 Modulation Transfer Function	193
A.2.2 Contrast Comparison	194
A.2.3 Visibility Enhancement	195
A.3 Results	195
A.3.1 Improvement to the Modulation Transfer Function	197
A.3.2 Contrast Improvements	197
A.3.3 Increased Visibility	198
A.4 Discussion	198
A.5 Conclusion	200
Appendices	188

List of Figures

1.1	AUV system design diagram	9
2.1	Demonstration of imaging underwater	12
2.2	Spectrum of downwelling irradiance in the sea	13
2.3	Parameters of water modelling	15
2.4	Back and forward scattering in water	17
2.5	Linear mixture model	32
2.6	Intimate non-linear mixture model	33
2.7	Bilinear non-linear mixture model	34
3.1	FOV calibration setup	44
3.2	Monitor angle variance	47
3.3	FOV mapping method comparisons	48
3.4	FOV sensitivity maps at difference distances	49
3.5	Images of FOV for co-registration	49
3.6	Depth map for stereo camera	52
3.7	Relative radiometric calibration curves	54
3.8	Examining spectrometer noise	55
3.9	Spectrometer noise variance	56

3.10	Histogram of the spectrometer noise variation	57
3.11	Experimental setup for camera characterisation	59
3.12	Linear variable edge filter	61
3.13	LVEF characterisation apparatus	62
3.14	LVEF characterisation apparatus - top view	63
3.15	Placement of spectrometer tip relative to LVEF	64
3.16	LVEF characterisation apparatus - bottom view	65
3.17	Transmission of the LVEF	66
3.18	Intensity response curves for cameras under test	67
3.19	The relative spectral responses of the Olympus μ Tough 8000	68
3.20	Spectral response curves for Nikon & Canon cameras	69
3.21	Curves using Pike Method	69
3.22	Chromatic reproduction using our method	70
3.23	RGB reconstruction swatches	70
3.24	Spectral response curves for cameras on AUV	73
4.1	Turbidity measurements	80
4.2	Test tank experimental setup	81
4.3	Bottom illumination modelling	82
4.4	Test tank colour correction result	83
4.5	Downwelling irradiance measurements	84
4.6	Colour correction - Outdoor Scene 1, 2 & 3	85
4.7	Colour correction - Outdoor Scene 4, 5 & 6	86
4.8	RGB error scatter plot for test tank data	91
4.9	Error in Lab colour space for test tank data	93

4.10	Colour correction ground truth	94
4.11	RGB error for colour correction of Clovelly data	95
4.12	Lab error for colour correction of Clovelly data	96
4.13	ACFR's AUV - Sirius	99
4.14	AUV system design diagram	100
4.15	Parameters of water modelling	103
4.16	Surface lensing FFT plot	106
4.17	Coral scene colour correction	107
4.18	2nd coral scene - colour correction	108
4.19	Colour correction of a seagrass patch	109
4.20	Inside AUV camera housing	112
4.21	AUV camera housing	113
4.22	Camera window transmission	114
4.23	AUV strobe profile	116
4.24	Lighting and imaging layout on AUV	117
4.25	Spectral reflectance of <i>Agropora Cytherea</i> coral	119
4.26	Spectral reflectance of <i>Montipora</i> coral	120
4.27	Spectral reflectance of sand	120
4.28	Spectral reflectance of <i>Acropora</i> coral	120
4.29	Spectral reflectance of seagrass	121
4.30	Spectra variance of classes - set 1	122
4.31	Spectra variance of classes - set 2	123
5.1	Histogram of chosen spectral features	128
5.2	Histogram of chosen LBP features	129

5.3	Proximity of subsequent spectral measurements	133
5.4	Spectral map - isometric view	134
5.5	Spectral map - horizontal view	135
5.6	Spectral map - zoomed in section	136
5.7	Mosaics showing classification results	137
5.8	Segmentation example	140
5.9	ISACS-GOGS graph explanation	145
5.10	MacBeth colour chart spectral reflectances	146
5.11	Mixing 4 materials together	147
5.12	Unmixing errors - synthetic dataset ISACS	149
5.13	Unmixing errors - synthetic dataset ISACS-GOGS	150
5.14	Misclassifications - synthetic dataset (ISACS - SAM metric)	152
5.15	Misclassification - synthetic dataset (ISACS - Euclidean metric)	153
5.16	Misclassification - synthetic dataset (ISACS-GOGS - SAM metric)	154
5.17	Misclassification - synthetic dataset (ISACS-GOGS - Euclidean metric)	155
5.18	ISACS-GOGS - change of T	156
5.19	Influence of T on ISACS-GOGS	157
5.20	Comparing unmixing methods	158
5.21	Comparing unmixing methods - Second and fourth EM	158
5.22	Coral unmixing - Seagrass	159
5.23	Coral unmixing - Acropora	159
5.24	Coral unmixing - Rocky	160
A.1	The principle behind polarisation underwater	190
A.2	Experimental setup	192

A.3	Turbidity = 3.2 NTU	196
A.4	Turbidity = 13.0 NTU	196
A.5	MTF for different polariser angles	197
A.6	Comparing constrast for different materials	198
A.7	Contrast improvements with use of filters	199

List of Tables

3.1	Spatial relations from FOV calibration	50
3.2	FOV calibration - Fit Error	51
3.3	LVEF transmission - table 1	71
3.4	LVEF transmission - table 2	72
4.1	Colour correction performance - Test tank - RGB	90
4.2	Summary of Colour correction performance Test tank - RGB	92
4.3	Colour correction performance for Figure 4.7d	94
4.4	Colour correction performance for Figure 4.7f	97
4.5	Colour correction performance for Figure 4.7b	97
4.6	Colour correction performance Clovelly - 1-6	98
4.7	Colour correction performance Clovelly - 7-12	98
4.8	Colour correction performance Clovelly - 13-18	98
5.1	Classification performance	131
5.2	Confusion matrix for coral reef dataset	132
5.3	Size of dataset for coral reef set	160
5.4	Performance of spectral unmixing on the coral dataset	161
5.5	Using all methods to find a solution	161

5.6 Computational time 161

Acronyms

ACFR	Australian Centre for Field Robotics.
AIMS	Australian Institute of Marine Science.
AOP	Apparent Optical Properties.
AOTF	Acousto-Optical Tunable Filter.
AUV	Autonomous Underwater Vehicle.
BRDF	Bi-Directional Reflectance Function.
CASI	Compact Airborne Spectrographic Imager.
CCD	Charge-Coupled Device.
CCFL	Cold-Cathode Fluorescent Lamps.
CDOM	Coloured Dissolved Organic Matter.
DVL	Doppler Velocity Log.
FFT	Fast Fourier Transform.
FOV	Field-of-View.
FWHM	Full Width at Half Maximum.
GBR	Great Barrier Reef.
HICO	Hyperspectral Imager for the Coastal Ocean.

HSI	Hyperspectral Imaging.
IMU	Inertial Measurement Unit.
IOP	Inherent Optical Properties.
IR	Infra-Red.
ISACS	Image Segmentation Assisted Constrained Spectral-unmixing.
ISACS-GOGS	Image Segmentation Assisted Constrained Spectral-unmixing Greedy Ordered Graph-based Search.
LBP	Local Binary Pattern.
LCD	Liquid Crystal Display.
LCM	Lightweight Communications and Marshalling.
LED	Light Emitting Diode.
LSF	Line Spread Function.
LVEF	Linear Variable Edge Filter.
MCM	Mine Counter-Measures.
MODIS	Moderate Resolution Imaging Spectroradiometer.
MTF	Modulation Transfer Function.
NTU	Nephelometric Turbidity Units.
PCA	Principle Components Analysis.
RGB	Red-Green-Blue.
ROV	Remote Operated Vehicle.
SAM	Spectral Angle Mapper.
SNR	Signal-to-Noise Ratio.
SVM	Support Vector Machine.

UCM Ultrametric Contour Map.

USBL Ultra-Short BaseLine.

UV Ultra-Violet.

WHOI Woods Hole Oceanographic Institution.

Chapter 1

Introduction



Alice came to a fork in the road. 'Which road do I take?' she asked.

'Where do you want to go?' responded the Cheshire Cat.

'I don't know,' Alice answered.

'Then,' said the Cat, 'it doesn't matter.'

- *Lewis Carroll, Alice in Wonderland*

We live on a planet of vast oceans with 70% of the Earth's surface covered by water. They are integral to supporting life on Earth, providing 99% of the inhabitable space on earth [144]. Our oceans and the habitats within them are under threat to due to a variety of factors, including climate change, over-fishing, habitat destruction, pollution and bio-invasion [169]. To understand the changes occurring and possible solutions, the monitoring of the marine habitats is critically important [203].

A variety of platforms are used for the monitoring of marine habitats. Above water remote sensing is generally used, to cover large areas at low resolution from aerial or satellite based platforms. Below water (in-situ) platforms such as towed video, towed diver [41, 136], scuba divers [81], Remote Operated Vehicles (ROVs) and Autonomous Underwater Vehicles (AUVs) [54, 157] are typically used when finer detail is required. Optical imaging is typically used on these platforms as it provides reliable fine detailed information necessary for marine habitat monitoring. Optical imaging is an attractive means to gather critical information about habitats within our oceans. This information can include the biological constituents living within a water body, the seafloor coverage types such as sand, coral, seagrass and various health indices of marine habitats such as the health of coral [7, 90]. Colour plays an important role in the inference of this health information.

Imaging through water presents many challenges. Ocean water and the particles dissolved and suspended within it have strong attenuating effects on light and thus on the data collected when imaging through it. This attenuating effect is wavelength dependant; the green portion of the visible spectrum passes most easily followed by blue, then red. Red light ($> 600nm$) can be attenuated quickly in a short depth of water. This thesis aims to develop methodologies for use on in-situ platforms that can remove the attenuation effects of the water. Once these effects are removed the data can be used to reliably classify different objects in underwater environments.

Colour is often thought of in the trichromatic domain which consists of combinations of Red-Green-Blue (RGB). This is due to how the human eye perceives colour. The colour of an object is a combination of the underlying illumination and the spectral reflectance of the object. A spectral reflectance profile defines how a material will reflect light at a given wavelength. Obtaining the spectral reflectance will give a spectral signature which can be used for identifying the material composition of the object as is commonly performed for example in terrestrial remote sensing [163]. Hyperspectral sensors are one of the many

sensors commonly found onboard remote sensing platforms. The term ‘hyperspectral’ refers to resolving the spectral reflectance signature at a fine spectral resolution.

When the colour of a scene is collected in the hyperspectral domain it can provide numerous features for discrimination of the various benthic types. Numerous studies are conducted above water in a remote sensing domain [29, 117] as well as sparse measurements at fine scales using contact sensors held by scuba divers [87]. These studies have been conducted to demonstrate the ability of hyperspectral reflectance to reliably classify material types, but there has been limited use of hyperspectral reflectance information from other in-situ platforms due to the difficulties of working with light underwater.

Hyperspectral Imaging (HSI) cameras, like colour cameras, capture an entire spatial image of a scene, however they may collect 100-1000s of spectral bands for each spatial ‘pixel’. Spectrometers are also hyperspectral sensors that capture a single cone of light (1 large pixel) but with similar or greater spectral resolution than a HSI camera. The trade-off with spatial resolution is countered by a lower cost, smaller form factor, lower energy requirements and better Signal-to-Noise Ratio (SNR). The better SNR is derived from collecting a large solid angle of light and larger pixel wells on the sensor’s collector.

In this work an in-situ imaging system is designed as well as methodologies for removing the attenuation effects of water. There are two parts to the in-situ imaging system. The first part is a system using upwards facing spectrometers at different depths in the water to continuously sample the water column to determine the optical properties of the water. This data allows for the creation of a dynamic water model which is constantly updated during imaging. This water model allows for the removal of the attenuation effects of the water the imaging system is working within. This removal method is commonly called colour correction in the trichromatic domain as it corrects the colours so it appears that the image was taken out of water. New methodologies for undertaking these corrections in both the trichromatic domain and the hyperspectral domain are discussed.

The second part of the in-situ imaging system is an imaging module which allows for the imaging of an underwater environment such as coral reef habitats. The imaging module allows for the hyperspectral and colour imaging of a scene. Techniques are developed to co-register the two sensors to maximise the benefits of each sensor. The corrected hyperspectral reflectance spectra and corrected colour imagery are used together to classify materials in an underwater environment.

1.1 Thesis aims and objectives

The two principal objectives of this thesis are:

1. To recover accurate and consistent colour and hyperspectral reflectance profiles using data from a trichromatic imaging camera and a spectrometer in underwater scenes.
2. To fuse this corrected data for accurately classifying materials on the seafloor.

1.2 Thesis Contributions

In this work methods are developed to parametrise a water model through the design and use of an insitu optical system. This model is used to correct traditional trichromatic and hyperspectral imaging for the changing optical properties and lighting within a water body.

The presented method was applied using sensors onboard an AUV. An adaptive water model was possible through the design and calibration of an apparatus to measure the optical properties of a body of water from an AUV. This model could then be used to recover RGB imagery and hyperspectral reflectance data corrected for water, lighting and structure influences by using an inverse attenuation model.

The utility of this corrected data is demonstrated with data obtained during a coral reef survey over the Great Barrier Reef (GBR). It is shown that the hyperspectral data can be fused with the RGB data to classify seafloor materials. In order to effectively fuse and exploit data coming from these two different sensor types, the spatial and spectral co-registration of the two sensors is required. Calibration in this context refers to (a) accurate knowledge of the spectral response function of the trichromatic imager in relation to the response of the hyperspectral sensor, and (b) the spatial response pattern of the hyperspectral sensor with respect to the Field-of-View (FOV) of the trichromatic camera. The fused information is classified using a supervised classifier. From the labelled patches, a 3D benthic map of the surveyed site is generated. Given the limited spatial resolution of the hyperspectral sensor used in this work, a new method is presented that takes information from the co-registered colour images to inform a new spectral unmixing method to resolve subpixel materials with the pixel of the hyperspectral sensor.

The following sections provide more detail on each of the contributions.

1.2.1 Spatial and spectral calibration techniques

In this work a new sensor combination is presented involving an RGB camera and a spectrometer for underwater high spectral and high spatial resolution imaging. New calibration techniques were developed to recover radiometrically accurate readings from this sensor combination:

Field-of-View (FOV) of spectrometers - The spectrometer provides a single spatial measurement of light radiance entering the FOV of the sensor. An automated method for characterising the field of view of spectrometers and providing a map of the sensitivity vs angle of incoming light was developed. The method is expanded to produce a three-dimensional sensitivity map of the spectrometer's FOV.

Co-registration - This new method provides a spatial calibration of a spectrometer spatial response pattern within the FOV of a RGB camera. This allows for the combined use of the two imaging technologies (RGB camera and spectrometer) for scene classification.

Camera spectral characterisation - Generally the spectral characteristics of a camera are not provided by the manufacture, these characteristics are essential for the task of colour correction. A new method is developed for determining the spectral sensitivities of a conventional RGB camera. The new method is faster and less complex than previous characterisation techniques.

Combining a spectral device with an imaging camera - In this work a novel sensor combination is presented. A stereo RGB camera system is combined with a high spectral resolution spectrometer. Techniques are explored for exploiting the benefits of the combined modalities. The engineering behind the software and hardware are discussed and results are presented for an AUV survey over the GBR.

1.2.2 Insitu water-corrected imaging

Current methods of colour correction and spectral correction are not capable of compensating for spatially and temporally varying optical properties of a water body. Correction refers to recovering the reflectance of an underwater object to make it appear as if the water was completely removed. The contribution in this area includes the following:

Estimation of optical properties of the water - A water model was parametrised through the measurement of a water body from two vertically-varying locations. This was achieved through the design of an optical system using two spectrometer facing upward to measure the downwelling irradiance of the water body. These measurements allowed for the estimation of the diffuse downwelling attenuation coefficient.

Colour correction - Colour correction was implemented using the parametrised water model as well as the spectral sensitivities of an RGB camera. This correction removes the selective attenuation effects as a result of imaging through a water body. The validity of this technique is demonstrated in several experiments, including a test tank setup where the target, water and lighting could be completely controlled and an outdoor ocean environment representing a real-world scenario. In this experiment, the target and depth could be controlled. A final experiment was conducted onboard an AUV. Lighting, depth and target were uncontrollable but measurable. This last scenario represented a real application with real varying environmental conditions.

Spectral correction - Spectral correction is necessary to resolve the reflectance spectra invariant to lighting and water attenuation effects. A new method is presented which models the lighting contributions and the optical properties of the water to obtain corrected spectral reflectance curves. These reflectance curves are similar to what a remote sensing platform would deliver. The presented method was able to recover spectral reflectance measurements at a much higher spatial resolution than what is possible from above water platforms.

1.2.3 Spectral-based underwater classification & mapping

The water-corrected colour imagery and corrected hyperspectral reflectance profiles allowed for the classification of materials in the data collected on an AUV survey mission. These corrections allowed the imagery and hyperspectral data to be spatially and spectrally consistent and accurate. This accuracy and consistency is necessary before the data can be used to classify or distinguish between coverage types. The classified data was then used to create maps of the different benthic material types on the seafloor. The contributions resulting from this include:

Abundance map generation - Utilising the spatial information from the RGB camera

(the texture features from the co-registered colour camera) and the spectral information from the spectrometer, a Support Vector Machine (SVM) based supervised classifier was trained and compared against other conventional supervised classifiers. Data from a survey mission was classified and overlaid on a 3D map of the seafloor. This is a new method for fusing in-situ RGB imagery with hyperspectral data to create a high resolution benthic map.

Informed Spectral unmixing - The co-registered RGB patches under each spectral patch were used to further determine the number and relative abundance of materials present in the scene. This segmentation process allowed for an informed spectral unmixing process that resulted in a constrained combinatorial problem for spectral unmixing. The computational complexity of this search was reduced using a greedy graph-based search algorithm developed for spectral unmixing. The contribution in this area is the development of two new algorithms for spectral unmixing.

1.3 Thesis overview

Chapter 2 provides a background on the properties of light underwater and the different modelling techniques available. Following the background section a review of the literature relevant to the contributions of this work is detailed. This includes methods for improving underwater visibility and the correction of underwater colour imagery. Extending to the hyperspectral domain, a review of HSI is provided with a emphasis on underwater and marine based HSI. This is followed by a literature review of spectral unmixing techniques and related background.

Chapter 3 details the spectral and spatial calibration methods necessary to resolve chromatically accurate colour and hyperspectral underwater imagery. This includes an automated method for determining the spatial sensitivities of a spectrometers FOV. In this work the spectrometer is combined with a RGB stereo camera. The spatial co-registration for this modality is described. Finally a calibration method for determining spectral sensitivities of an RGB camera is presented. This is necessary for the process of colour correction.

Chapter 4 presents the methods for recovering accurate and consistent colour from un-

derwater imagery. This is shown first for correcting the colour in RGB underwater imagery. The method was validated and demonstrated with three different imagery scenarios of varying realism and environmental control. These experiments included a test tank, an ocean swimming spot and lastly onboard an AUV. This method was then applied to the hyperspectral domain for correcting spectral reflectance data taken underwater. The correction techniques were performed on data from an AUV mapping mission. The mission was over a coral shoal of varying coral and benthic types. Several examples of the different benthic types are shown from the mission.

Chapter 5 demonstrates how the radiometrically corrected colour imagery and hyperspectral data can be used to create high resolution benthic maps. The AUV conducted a survey mission over an area of the GBR. From this mission over 14,000 stereo images and spectral reflectance data were collected. Several classifiers were trained on the survey data using the combined imagery and HSI data. The choice of spectral device imposes a spatial resolution limit. To resolve and classify materials smaller than the pixel size of the spectral device, spectral unmixing techniques are used. A new method is presented which improves the unmixing process by utilising the high spatial information from the co-registered RGB imaging camera.

Chapter 6 provides a conclusion of the presented work as well as future directions based on the contributions made in this thesis.

Appendix A presents a technique for improving underwater visibility with the use of polarising filters. This work is relevant to the background of visibility improvements but due to poor performance was not used in the final method. The work however should be presented as it could be used for future improvements to the proposed method.

1.4 System overview

In this thesis a spectral imaging system was developed for achieving the aims of this work. The imaging system was built onto an existing AUV. The AUV was a Woods Hole Oceanographic Institution (WHOI) designed seabed class AUV operated and customised by Australian Centre for Field Robotics (ACFR). Figure 1.1 shows the location of each of the

sensor used in this work. To characterise the water column, two upward looking spectrometers are used. One is onboard the AUV platform and the other onboard a surface vessel. Next the developed imaging module is mounted on the underside of the AUV for taking successive images of the seafloor as the vehicle transverses a planned route. The imaging module consists of a spectrometer spatially co-registered with a RGB stereo camera.

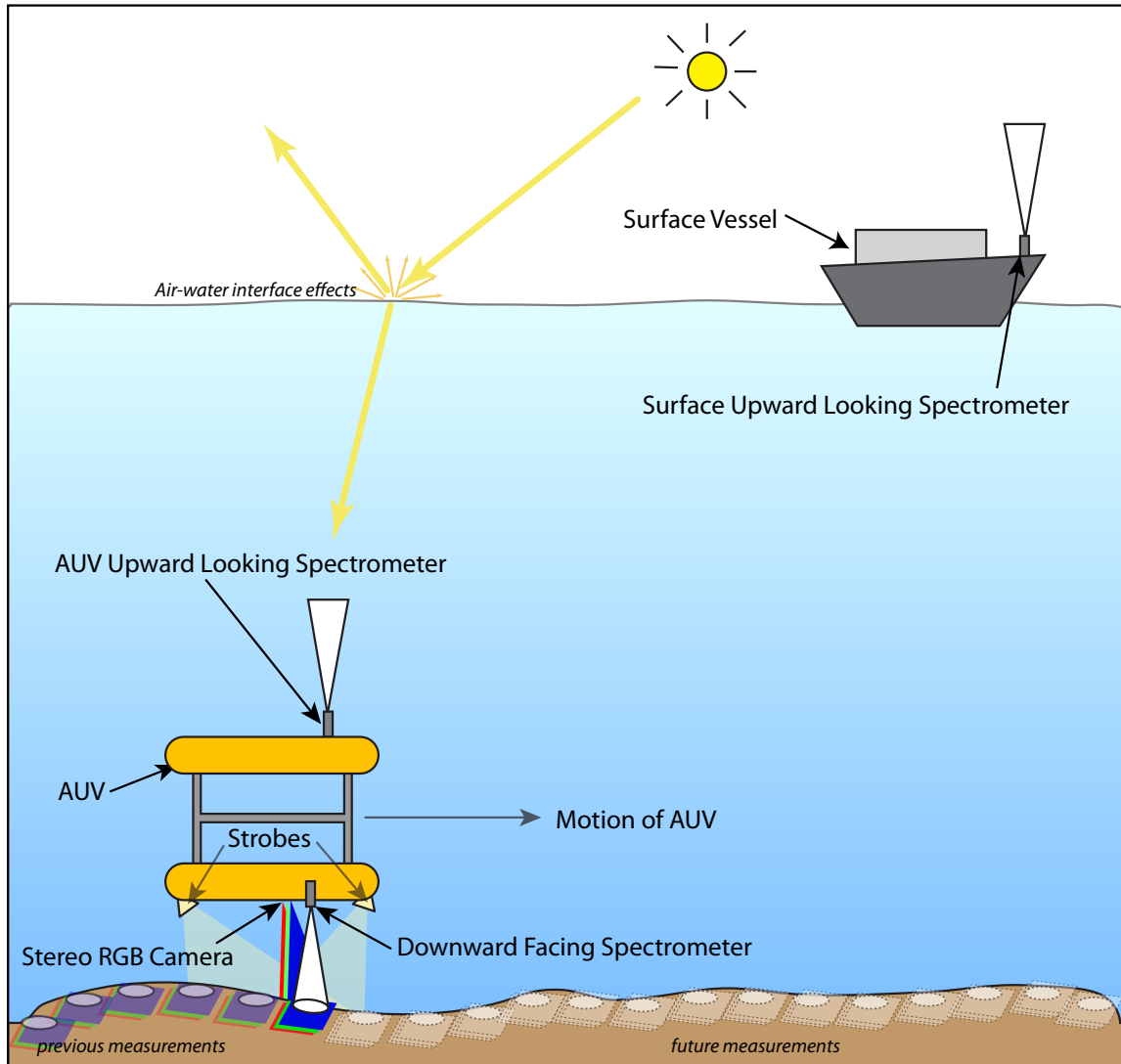
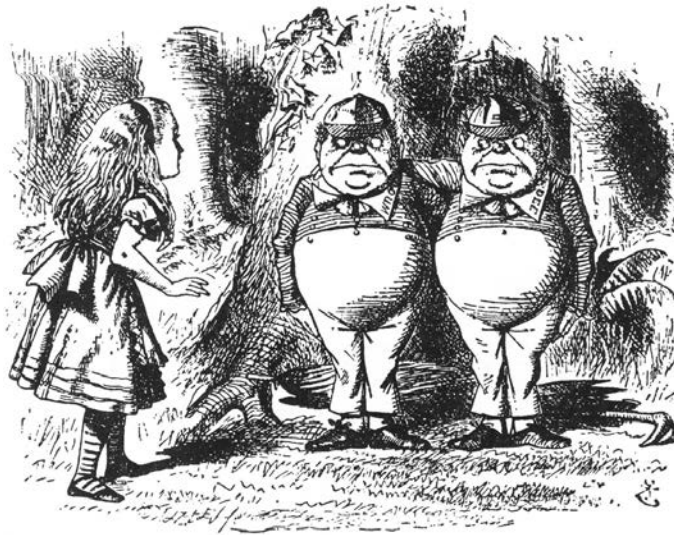


Figure 1.1 – Layout of the designed system showing the placement of the upwards looking spectrometers to characterise the water column and the co-location of the stereo camera and downwards looking spectrometer for benthic habitat mapping.

This system will be referred to in its separate sub-systems throughout this dissertation. Referring to this figure will assist the reader in understanding the context of each developed sub-system.

Chapter 2

Background & literature review



2.1 Introduction

The underwater environment presents formidable barriers towards its exploration, one of which is the limited passage of light. Typically underwater imaging has been undertaken through the use of sonar based systems. High spatial resolutions have been attainable with the advent of high resolution sonar systems such as side scan sonar. This modality however provides limited information on the types of materials under examination.

When performing close-range sensing underwater, optical underwater imaging is preferable to sonar based imaging due to its affordability, high resolution (both spatially and chroma-

ically) and ease of interpretation by an operator. However optical sensing in an underwater environment can be challenging due to the complex absorption and scattering properties of the water. These attenuation properties are dependant on factors such as the particles dissolved and suspended within the water, sunlight/weather variations and distance to the object of interest.

2.2 Background

2.2.1 Understanding the water column and its effect on light

Due to the atomic nature of water (H_2O), water molecules absorb almost all electromagnetic radiation except for photons within the visible band [137]. Typically bodies of water do not pass the visible spectrum evenly: green light (around 532nm) passes most easily through water followed by blue then red light. Figure 2.1 shows images taken of a colour chart in a typical underwater environment. In the left image the colour chart is close to the camera so that the colours appear similar to their values when observed out of water. In the right hand image the target is far away and it can be seen that the reds have been diminished to a greater degree than the blues or greens. Figure 2.2, illustrates sensing light from the surface from different depths within the ocean. It can be seen that Infra-Red (IR) ($> 700nm$) is most quickly attenuated, followed by reds ($> 600nm$). The transmission properties of the water also change with different particles dissolved and suspended within the body of water.

The interactions of light within a body of water will fall within one of two cases, either the light is absorbed or scattered. The degree to which these interactions occur depends on the water's constituents (particles dissolved or suspended within a body of water). A typical river for example is often more turbid than open ocean water. Here incident light flux may be attenuated more quickly due to the silt suspended within the water and algae growing near the surface of the river. In contrast a body of ocean water will have a smaller degree of particle suspension or biological growth. As a result the optical properties of these two examples will differ greatly.

In a medium where absorption is the only factor (no scattering), the visible range is a function of the light source illumination and the camera sensitivity [69]. In the blue region

(480nm) of the ocean, 60% of the water's attenuation is due to scattering and 40% due to absorption, whereas in other spectral regions absorption is the dominant attenuation factor [56]. Light energy in the red end of the spectrum is attenuated very heavily with complete extinction occurring around 10-15 metres for very clear tropical waters.

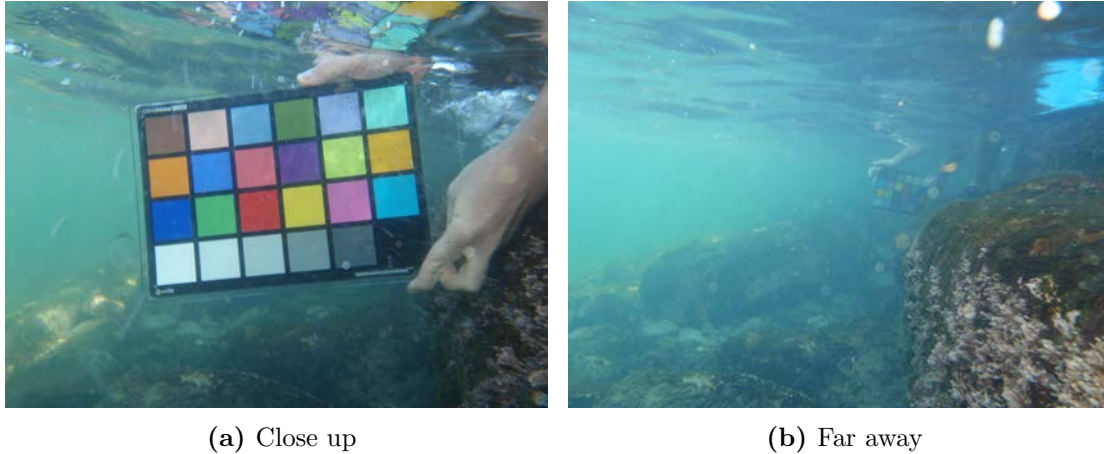


Figure 2.1 – This demonstrates the selective attenuation of a typical body of water, the far away image has a blue green colour-cast due to the reds being attenuated more quickly than blue or green.

The optical properties of a body of water are often given one of two labels: Inherent Optical Properties (IOP) or Apparent Optical Properties (AOP) [137]. The attributes of a body of water which only depend on the scattering and absorption characteristics and not on the geometric structure of the light field within the body of water are called the IOPs [159]. The amount of scattering is defined by the scattering coefficient, often denoted by the letter b . This quantity describes the fraction of incident flux scattered within the medium at a particular wavelength. The degree of absorption of a body of water is defined by the absorption coefficient. This is often assigned the letter a , which describes the fraction of incident flux absorbed within the medium at a particular wavelength. The total attenuation of a body of water is defined by the attenuation coefficient c and is simply $c = a + b$.

When the geometry of the light field is considered along with the attenuation properties of a body of water these are often classified as AOPs. To a large extent the attenuation of a body of water is defined by the IOPs [115], however they will change with the location and direction in which they were measured hence the need for defining the AOPs. A common quantity measured by oceanographers is the downwelling attenuation coefficient K_d . Similar to the attenuation coefficient c it characterises the light passing downwards through a water

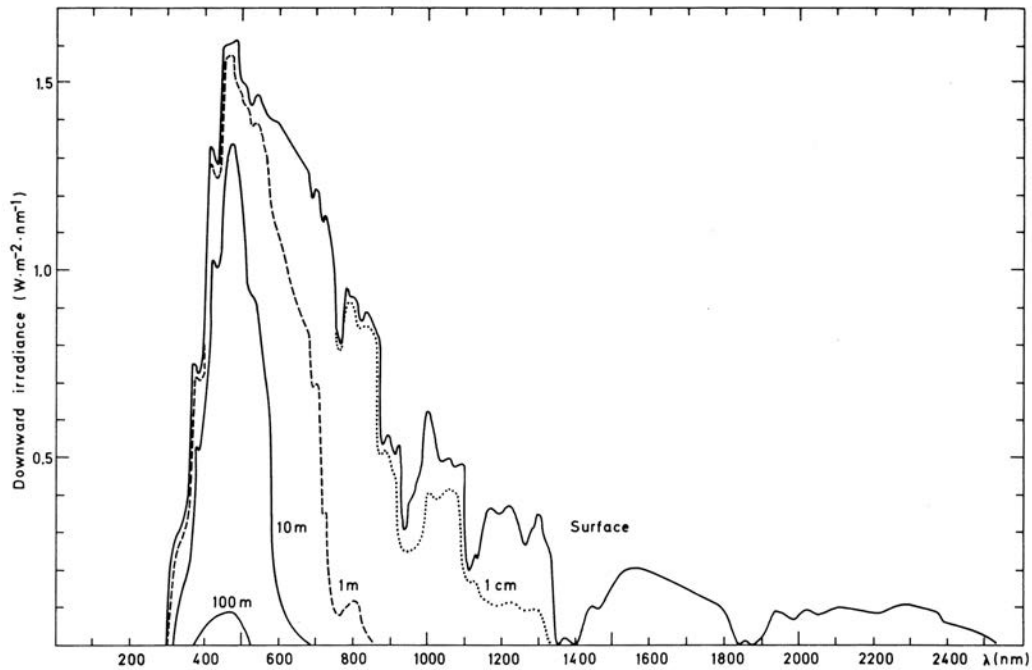


Figure 2.2 – The spectrum of downward irradiance in the sea for different depths below the surface, figure taken from Jerlov [101]

column. It measures the incident light loss due to absorption and scattering per unit distance at a particular wavelength of light. In a similar vein an upwelling attenuation coefficient K_u can be defined for the light passing upward through a body of water. In the next section it is shown how K_d maybe derived from optical measurements within the body of water.

2.2.2 Water column modelling

In the literature there have been several optical models for a given body of water. The majority of modern literature uses the Lee *et al.* method [122] or alternatively using the water modelling software *Hydrolight* [139]. These methods are able to model the attenuation effects due to the major constituents present in ocean waters, this can include Coloured Dissolved Organic Matter (CDOM) and photosynthesising chlorophyll. The methods are primarily aimed for use with correcting the water attenuation effects in remote sensing imagery and the retrieval of shallow water bathymetry [9, 116, 123]. These models rely on the in-situ measurement of CDOM, chlorophyll, scattering and absorption. These measurements are often only taken in one or very few locations at one moment in time. They do not actively measure the transmission of light through a body of water, with the exception of

several scattering and absorption sensors which often take measurements over a short passage of water. Several assumptions are made as to the homogeneity of a body of water both spatially and temporally. Other methods will use predefined models of ‘standard’ ocean waters. Jerlov [101] developed a set of standardised ocean water models. There are a set for coastal waters and a set for open ocean waters. The degree to which these standardised models generalise to all ocean water conditions is not clear [125].

The water’s attenuation properties may be modelled through the Lambert-Beers law:

$$E_{\delta}(\lambda) = E_s(\lambda)e^{-K_d(\lambda)\delta} \quad (2.1)$$

where: $E_{\delta}(\lambda)$ is the irradiance with respect to wavelength λ at depth δ , $E_s(\lambda)$ is the irradiance just below the surface, $K_d(\lambda)$ is the wavelength dependant diffuse downwelling attenuation coefficient for the water. We may re-write this as seen in Equation (2.2) to derive the diffuse downwelling attenuation coefficient $K_d(\lambda)$.

$$K_d(\lambda) = -\frac{1}{\delta} \log_e \left(\frac{E_{\delta}(\lambda)}{E_s(\lambda)} \right) \quad (2.2)$$

Due to the complex nature of the air-water interface, measurements taken above the water need further processing.

2.2.2.1 Air-water interface effects

Light passing through the air-water interface will be reduced through various factors such as reflection and refraction, arising from the angle of the sun, waves and wind elements. Figure 2.3 shows visually where these derived quantities come from. To determine the amount of reflection from the interface the refractive index is derived using the empirical equation for the index of refraction of seawater Equation (2.3) [162] which is a function of wavelength (λ in nanometres), salinity (S) and temperature (T).

$$n(S, T, \lambda) = n_0 + (n_1 + n_2T + n_3T^2)S + n_4T^2 + \frac{n_5 + n_6S + n_7T}{\lambda} + \frac{n_8}{\lambda^2} + \frac{n_9}{\lambda^3} \quad (2.3)$$

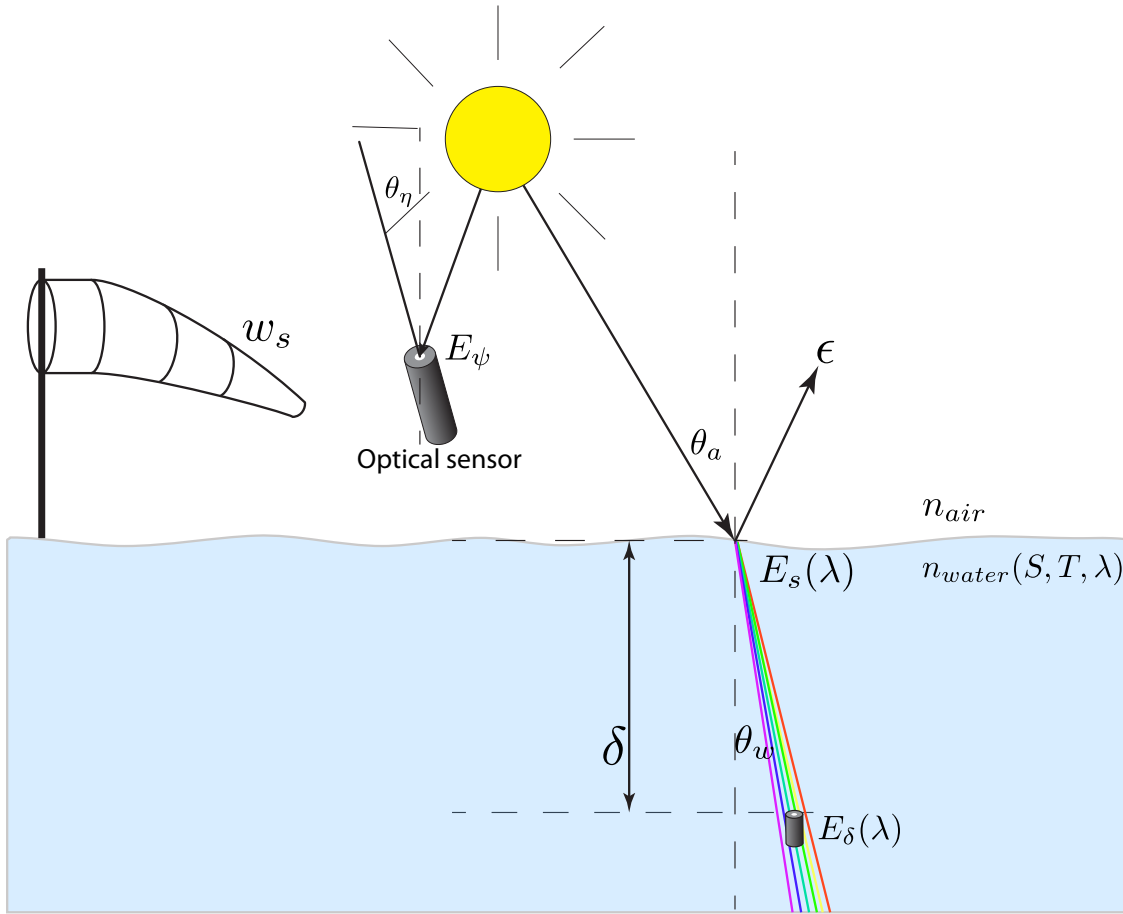


Figure 2.3 – This shows the complete parameters obtained for modelling for the air-water interface, see Section 2.2.2.1 for further details.

$$\begin{array}{cccc}
 n_0 = 1.31405 & n_1 = 1.779 \times 10^{-4} & n_2 = -1.05 \times 10^{-6} & n_3 = 1.6 \times 10^{-8} \\
 n_4 = -2.02 \times 10^{-6} & n_5 = 15.868 & n_6 = 0.01155 & n_7 = -0.00423 \\
 n_8 = -4382 & n_9 = 1.1455 \times 10^6 & &
 \end{array}$$

From the derived refractive index $n_{water}(S, T, \lambda)$, Snell's Law Equation (2.4) can be used to determine the exit angle of the light in the water. Note that this is for the angle of the incoming sunlight. The skylight contribution is diffused in the hemisphere around the area and so for these calculations it is not considered angle dependant for the purpose of modelling extinction.

$$\theta_w(\lambda) = \arcsin\left(\frac{n_{air}}{n_{water}(S, T, \lambda)} \sin(\theta_a(\lambda))\right) \quad (2.4)$$

Where the index of refraction of air $n_{air} \approx 1$ and the entry angle ($\theta_a(\lambda)$) is the zenith angle of the sun. The refracted angle at which the light now passes through the water after the air-water interface is defined by $\theta_w(\lambda)$. A proportion of light will be reflected at the interface surface and does not pass into the water. The reflectance r at the surface is a function of the zenith angle of the incident light in air (θ_a) and the exit angle (relative to vertical) in water θ_w . This relationship is given by Fresnel's Equation:

$$r = \frac{1 \sin^2(\theta_a - \theta_w)}{2 \sin^2(\theta_a + \theta_w)} + \frac{1 \tan^2(\theta_a - \theta_w)}{2 \tan^2(\theta_a + \theta_w)} \quad (2.5)$$

There will also be light reflection from wind derived white caps on the surface of the water which can be modelled using a white cap percentage [187], where windspeed w_s is in metres per second:

$$whitecap\% = 2.692 \times 10^{-5} w_s^{2.625} \quad (2.6)$$

The work of Koepke *et al.* [118] found the white caps had an effective reflectance of 22% over time due to their short life. The extinction percentage (ϵ) of the irradiance passing through the air-water interface is derived in Equation (2.7) with the resultant light irradiance just below the surface E_s being defined in Equation (2.8).

$$\epsilon = whitecap\% \times 22\% + r \quad (2.7)$$

Finally there needs to be a correction for the possible off-zenith angle of the measuring device above the water. Equation (2.8) shows the value for E_s which is the irradiance models just below the water's surface.

$$E_s = E_\psi \left(\frac{1 - \epsilon}{\cos(\theta_\eta)} \right) \quad (2.8)$$

where θ_η is the angle between the sensor's optical axis and the zenith angle at the time of acquisition. E_ψ is the irradiance measurement from the above water optical sensor.

The result of this process derives the irradiance just below the surface $E_s(\lambda)$. This encompasses the complex interactions of the air-water interface. This is used together with a measurement taken at some depth δ to derive the downwelling attenuation coefficient K_d .

2.3 Optical visibility improvements in water

With the complexities of imaging underwater due to the absorption and scattering of the body of water, there has been a lot of research into developing methods for improving visibility underwater. Visibility in this case refers to the ease of the transmission of light underwater. The techniques for improving visibility vary greatly from active illumination to optical filtering to various post-processing techniques.

When conducting imaging underwater with active illumination, scattering can stop or deflect light from entering the scene. The type of scattering is often categorised into two classes; if the reflected light from the scene is scattered by a particulate in the water column but the light continues forward (at a changed angle) this is called forward scattering. If the light is scattered back into the sensor without reaching the scene it is classified as backscattering [101, 126]. These concepts are visually explained in Figure 2.4. This distinction is often quite necessary as back scattering tends to inhibit visibility underwater by reducing the contrast of the image coming back from the scene, whereas forward scattering often results in blurring of the image.

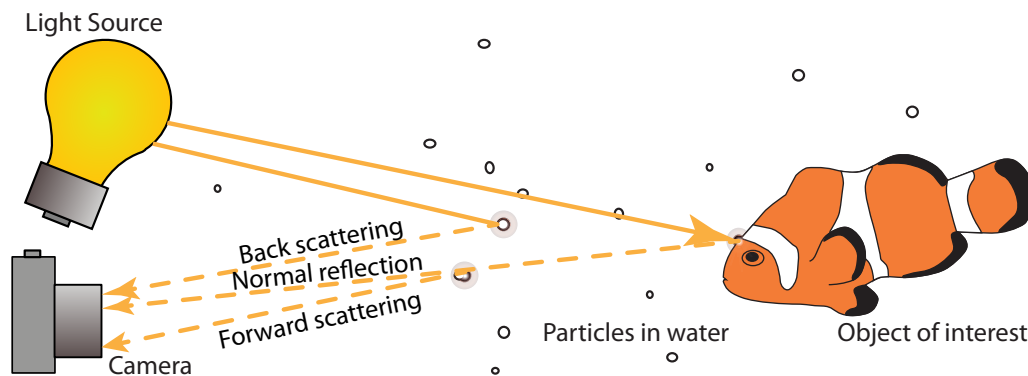


Figure 2.4 – This describes the process of back and forward scattering in the context of an underwater environment

A series of methods utilise the capacity for light to become polarised to improve underwater visibility. Polarisation naturally exists in the underwater environment up to depths of 200m

[101]. Light can become naturally polarised through several means. Firstly light from the sky can be partially polarised and pass through into the water. Secondly light can become scattered by the water molecules or by particles in the water column can polarise the light. Lastly the transmission of unpolarised sunlight through the surface of the water can result in elliptically polarised light, dependant on the incident angle [137].

One method for reducing the effect of the backscatter is through the use of polarisation filters [69]. The method is to place a filter in-front of the light source thus polarising the outbound light and another in-front of the sensor to filter the light entering the camera [176]. The probability of the polarisation orientation remaining intact is reduced as the number of incident reflections increases [69]. Therefore particles in the water column reflect the light back polarised whereas the object of interest reflects the light partially or fully depolarised dependent on the surface structure of the material [126, 177, 210].

Suspended particles in water tend to reflect the light only a limited number of times. This results in the reflected light from the particles remaining partially polarised. When using linear polarisation filters, this reflected light will be blocked if the filter in front of the light source is perpendicular to the filter in front of the sensor. This serves to reduce the amount of light reflected back into the sensor by the suspended particles thus reducing backscatter. Several papers have referred to using circular polarisers over linear due to the angle invariance of circular polariser, the slight performance advantage and the compatibility with digital SLR auto-focusing systems [69, 110, 177, 196, 197]. In this work the application of polarisation to improve visibility has been investigated and can be seen in Appendix A. The work has been inserted as an appendix due to its relevance to the topic but not directly to the design of the proposed system. It was found that this technique improved visibility but at the expense of luminous flux (the measure of the power of light). It reduced the quantity of flux by 91% which despite the visibility improvement was not seen as a good trade-off. This could however be a future upgrade to the system only if it were possible to mitigate the severe reduction in flux.

Another benefit of using polarising filters was the ability to generate a rough estimate of the 3D structure of a scene [196, 197]. This was however quite coarse and only had an effective distance reconstruction range of 1-2m.

The performance advantage of circular polarisers is considered to be better due to circular polarised light being more easily depolarised than linearly polarised light [100]. In [126] it

was also found that rougher surfaces such as rusty metal depolarises light whereas specular reflectors do not. An improvement in the performance of polarisation discrimination was found for an isotropically scattering medium as opposed to anisotropic media. Anisotropic particles are more representative of ocean particles [142]. Particles suspended within the water column are generally larger than the wavelength of light [100]. This results in scattering being independent of wavelength.

2.4 Colour accuracy and correction underwater

Colours in underwater photographs often appear with a strong blue green colour cast, due to the selective absorption of the water column. The colours will vary for different distances, change of lighting, weather conditions and changing water constituents. The properties of this colour shift will change depending on several factors such as the presence of particles such as viruses, colloids, bacteria, phytoplankton, organic detritus and large particles (eg. zooplankton & amorphous aggregates of smaller particles - marine snow) [137]. For a more accurate representation of the imaged scene, the underwater imagery needs to be colour corrected. Accurate and consistent colour aids in improving classification performance. There exists many post processing and in-situ techniques which aim to rectify the colour cast problem.

2.4.1 Post processing techniques

The first set of techniques implement some sort of processing of the underwater imagery after acquisition. Some are informed techniques, utilising extra information obtained during acquisition. Others are implementing image processing techniques to correct the colour.

Ahlen *et al.* [2–4] used spectrometer measurements of a colour plate at different depths. From these readings they obtained the attenuation coefficients of the body of water. Using the attenuation coefficients they were able to produce good colour correction for imagery from commercial off the shelf Red-Green-Blue (RGB) cameras. In addition to this they were able to create a pseudo hyperspectral image through the use of a Wiener filter.

Stigell *et al.* [192] developed a similar method, using Wiener estimation to make estimations from low-dimensional data into high dimensional data. They utilised peak-signal-to-noise

root-mean-square error metrics to validate their estimations. This was done by imaging a Macbeth colour chart (Pascale, 2006 [152]) using both a spectral camera and a digital SLR under standard D65 illumination[170]. The limitation of Ahlen *et al.* & Stigell *et al.* work is that it does not take into account scattering or a changing attenuation coefficient.

Yamashita *et al.* [206] had a similar method to Ahlen *et al.* [4] except they modelled for different artificial lighting and camera positions. Their method however was quite simplistic as they only performed lab based measurements of the water's attenuation. These were done in clean, clear water and captured with a standard RGB camera rather than a spectrometer. Many methods use image processing filtering techniques to perform the colour correction. The disadvantage of these methods is the filtering amount can be quite user subjective. They are not explicitly measuring the optical properties of the water column.

Torres-Mendez *et al.* [195] used a markov random field (MRF) and a belief propagation (BF) to solve for the colour correction. They used a supervised learning method using a model that is trained from a user-corrected patch of the image. Upon training the model the rest of the image is corrected based on the learnt correction to the training patch. This was a good method for colour correction by learning the mapping between uncorrected and corrected, however it required training the model which not only questions the accuracy of this method (as a user can be quite subjective), it also relies on the assumption that the user knows the perfect corrected image.

Garcia *et al.* [68] presents a frequency domain filtering method for correcting for lighting irregularities. This process is called homomorphic filtering and it involves performing a high pass filter on the image to remove the low frequency component caused by the light decaying towards the edges of an artificially lit scene, also known as vignetting. Colour correction was then performed as a process of contrast stretching [19]. The problem with this method is that it only suppresses prominent colour casts without taking into account the absorption phenomena [19].

Iqbal *et al.* [99] uses a slightly different method. Unsupervised Colour Correction Method (UCM) is designed to remove the colour cast in underwater imagery. In a three step process the image data for red, green and blue is equalised. The next step is that a contrast correction method is used to perform stretching of the upper side of the histogram for the red channel and stretching down the histogram for the lower side of the blue channel, then

the contrast is stretched for the histogram of the RGB image. The final step is performed in the Hue, Saturation and Value (HSV) colour space where a similar stretching is performed on the S & V channels. They compared the performance of UCM to Grey-World, White Patch and Adobe Photoshop Histogram Equalisation and found that UCM performed better using the metric of edge detection and width of histogram.

The method assumes the histogram of colour-cast-free underwater images are chromatically balanced. This assumption however would not hold for scenes containing a large object of just one colour. This method however works well for maximising the contrast of an image. The method works well for detection applications however it lacks the accuracy needed for chromatic reconstruction.

2.4.2 In-water colour compensation

Vasilescu [199] developed an adaptive underwater lighting system which produced notable results. The system involved six selectable flash elements of varying colours. The flash system determined the distance to the objects in the scene and lit the scene with increasing amounts of red for increasing distances. This was quite a novel approach, except the accuracy of the colour reconstruction is questionable as it assumes the same water spectral attenuation coefficients for all water types. This method would not be accurate for an organism-rich environment which may have a green tint and therefore will require different colour compensation compared to that of clear open ocean.

Chen *et al.* [46] notes the problem that there can be great post processing methods, but if the original scene is poorly illuminated, the post processing will perform poorly. The authors examined the metrics of image quality as well as the shortfalls of machine vision such as the limited dynamic range of the camera CCD. Chen *et al.* developed a Simulink[®] PID control model for controlling the light source to maximise dynamic range, maximise contrast and reduce glare. The approach however is very theoretical and is the applicability to a real work scenario appears to be limited.

In general the existing colour correction methods presented are too simplistic as they rely on the assumption of homogeneity of the water conditions. The methods mentioned performed well in controlled and predetermined environments, but would not work well in applications involving varying inherent optical properties such as a moving Autonomous Underwater

Vehicle (AUV) in the ocean.

2.5 Benthic classification

With large sections of the seabed being mapped by an AUV at a time, manual classification of the benthic substratum is challenging. Therefore automated methods are typically used to classify imagery of the seafloor. Several automated classification methods utilise the benthic image data using Gaussian Mixture Models [190], Support vector machines [141], K-Nearest Neighbours and various other supervised learning techniques [63, 121] are commonly used.

The scale of automated classification can change for different scientific objectives. Some work aims to classify broad scale benthic habitats, focusing on the dominant substrates of the area [131, 165, 189]. Others have focused on sub-image resolutions for finer scale benthic coverage estimation [104, 161, 183]. Many of these techniques have utilised texture features. A common method for determining illumination and rotation invariant texture features is through the use of Local Binary Patterns (LBPs) [149]. Colour features have been used for benthic classification along with texture features [186]. This method was rather naive to the attenuation properties of the water and utilised a histogram stretching technique to correct colour. Pizarro *et al.* notes that some benthic types are indistinguishable without the incorporation of the colour features in the classifier [156].

Another features commonly found in the literature is 3D structure information. The structure information comes from stereo cameras onboard AUV platforms [105]. Using the 3D data a large amount of information about the biological productivity of the scene can be inferred from the rugosity of the benthic structure [64]. Rugosity information has been combined with texture information for unsupervised classification of image-scale habitats [191].

When classifying sub-image scale materials, Clement *et al.* [48] used LBP as a classification feature. It was claimed that texture was the most suitable feature due to the difficulties associated with resolving accurate colour information. Other works have used colour for classification with good success [134]. Without good colour correction the method is unlikely to perform as well in different experimental situations or for different datasets.

2.6 Hyperspectral sensing underwater

In this section the literature related to hyperspectral imaging of ocean regions is reviewed. Two areas of applications in this domain are investigated: marine ecology and defence applications. Hyperspectral Imaging (HSI) from above water remote sensing platforms is reviewed as well as in-situ HSI.

2.6.1 Introduction to hyperspectral imaging

HSI is the process of the sensing of electromagnetic radiation in the spectrum range of Ultra-Violet (UV) through the visible spectrum up to IR wavelengths. Typically the spectrum is sensed in 10-100's of narrow spectral bands hence the name hyper-spectral. Multi-spectral imaging refers to imaging devices which sense 5-10 bands of broader spectrum light. A typical consumer camera will detect 3 bands of light in the visible spectrum. These standard cameras will detect light in similar spectral bands (RGB) to match the human visual system. These colour cameras can also be referred to as trichromatic cameras as they are measuring three colours. Combinations of these bands/colours will produce all the other colours which the human eye is sensitive to. The human visual system is highly complex and sophisticated, which is a result of the physical capabilities of our eyes and the visual processing abilities of our brains. Although the investigation of the human visual system is outside of the scope of this work, the capabilities should be noted when interpreting results pertaining to colour.

The ability to image at finer spectral resolutions than the human eye can see, allows for some unique abilities. HSI allows for improved characterisation and classification of the material imaged as different materials will absorb and reflect certain wavelengths of light in different ways [184]. Due to the high spectral resolution of HSI cameras it is often possible to distinguish materials from one another [39]. This is due to the chemical composition of the material which will show the presence of difference absorption features at certain wavelengths.

In order to acquire a hyperspectral image a HSI camera is needed. Typically hyperspectral images are taken using an instrument called an imaging spectrometer or a hyperspectral camera. These work by passing the light from a scene through a dispersing element which can be either a diffraction grating or a prism. This splits the light into many narrow and

adjacent wavelengths of light [184]. The divided light is projected onto an imaging sensor. By using a high resolution detector the spectral device can detect narrow bands of light. A hyperspectral camera has two main architectures: a pushbroom HSI camera and a tunable filter HSI camera.

Pushbroom cameras work like an array of 1D spectrometers. A dispersing element splits the light from a narrow slice of the spatial image onto a 2D imaging sensor. The pushbroom camera gets its name from the method of collection. In order to acquire the complete hyperspectral image the camera is pushed or scanned across the entire scene and subsequent slices are patched together. The disadvantage of this modality arises from the fact that co-registration of the slices can be challenging in dynamic environments. This is because each slice occurs at a different time, so this modality is only useful for static scenes.

The tunable filter hyperspectral camera utilises a filter element called an Acousto-Optical Tunable Filter (AOTF). The material of the filter changes its optical properties (namely its passband frequency) with changing acoustic excitation frequencies. The filter is able to change to a different frequency very quickly (typically $4 - 20\mu\text{sec}^{-1}$). The advantage of these filters is that they capture an entire scene at a single moment in time at a single frequency band. However, the frequencies must be stepped through in order to capture an entire HSI image. The disadvantage of this design is that it takes a finite amount of time to step through the frequencies.

2.6.2 HSI imaging of coastal regions using remote sensing

HSI in the marine domain has typically only been performed from air or space-borne platforms. It is an extremely challenging task due to the size and dynamic nature of the ocean environment [53]. When imaging from above the water, complicated light interactions come into play at the interface between the air and the water. Several additional processing steps are needed to occur for imaging through the air-water interface. These steps are necessary to mitigate surface artefacts such as glinting [76, 84]. Surface glinting occurs when light from the sun or sky is reflected directly back in the Field-of-View (FOV) of the camera imaging the scene [138]. Glinting will result in a localised increase in light intensity and reduced contrast at certain wavelengths of light. Glint removal is important in hyperspectral imaging of the ocean as it prevents unnecessary complications of seafloor classification.

¹<http://www.olympusmicro.com/primer/techniques/confocal/aotfintro.html>

This classification is based on the spectral reflectance which can be significantly distorted by surface glint. Typically, 50% of remote sensing images suffer from significant glinting issues [8]. Other effects on the air-water interface can come from the density change of the water layer and surface distortions due to the wind and ocean currents [137]. Modelling of these artefacts is discussed in Section 2.2.2.1.

Many applications for hyperspectral imaging of coastal regions have been focused on the retrieval of bathymetry [31, 123]. These have all been from satellite or aerial based platforms. However for these methods to work effectively their models must be parametrised by in-situ measurements of the IOPs [31]. These methods were also limited by cloud cover, and provide the horizontal spatial resolution may have been limited to 3.5m in this particular study [117], but that is not a general limitation for airborne systems. The spatial limitations of airborne platforms will be a function of imaging altitude and sensor resolution. Trade-offs are made between ground sampled distance (GSD) and ground coverage which are dependant on the application. Due to the physical properties of the water, sensing is limited to depths of 10m or less in tidal zones [31, 167] or up to 20m in very clear coral reef regions [117]. Other factors which vastly affect the ability to resolve the spectra of substratum, include the sensor Signal-to-Noise Ratio (SNR), wind speed and sun elevation [79]. When imaging above water (either space or aerial platforms) atmospheric effects should be compensated for [30].

There has been work looking into mapping coral reef regions using florescence however differentiation is limited between coral classes [209]. These fluorescence methods have however been shown to be useful in classifying coral bleaching [208]. Aerial HSI mapping of coral reef regions has been shown to have good fidelity when the number of classes was limited to three: coral, sand and algae [70]. Classification rates drop with the addition of more classes. It was found that there was a linear decrease in classification accuracy with increases in the number of classes [8]. For an 11-class dataset, cross validation accuracy is < 50% [8]. This was for a data set obtained in shallow and clear water which is ideal for these methods. Other remote sensing studies of coral reef benthos have returned similar rates of classification accuracy, with 65.13% for a 7-class problem[125]. The depth limit of accurate classification in this study was found to be 8m[125].

There are spatial resolution requirements for undertaking the assessment of coral bleaching [6], these are quite fine (0.4m - 0.8m [6]) and as such above water imaging platforms do not

satisfy these requirements [6, 179]. Over a variety of remote sensing applications the spatial resolution exerts a strong influence on the ability to extract environmental information from remotely sensed data [154]. There are methods to pull out subpixel information from remote sensing data [153, 164], these shall be discussed further in spectral unmixing (Section 2.7). Some examples of the spatial resolution limits (pixel sizes) from some current HSI sensor platforms include:

- Hyperspectral Imager for the Coastal Ocean (HICO) satellite in the International Space Station with 90m pixels
- Moderate Resolution Imaging Spectroradiometer (MODIS) satellite with 250m pixels but only in the visible spectrum
- HyMap aerial based sensor has 3.5m pixels [117] ²
- Compact Airborne Spectrographic Imager (CASI) aerial based sensor has 4m pixels [31] (altitude dependant).

Multispectral imagery has also been used for marine monitoring [72, 85, 96]. Multispectral imagery has a high spatial resolution but a lower spectral resolution (8 bands versus 100s in hyperspectral). Two multispectral sensor platforms commonly used in the literature are the WorldView 2 satellite³, with 8 multispectral bands and a spatial resolution of 1.84m at nadir. The other commonly used platform is Landsat 7⁴ with 7 spectral bands and 30m spatial resolution. Spatial resolution of imaging platforms is constantly improving, recently WorldView 3 satellite was brought online. It has a spatial resolution of 1.24m for the multispectral bands ⁵.

2.6.3 Marine ecology applications

Hochberg *et al.* [82, 83, 86, 87], Holden *et al.* [88–93] and Andréfouët *et al.* [6, 7] have lead the field in examining the spectral features of marine ecology and botany. They found that the health of some corals³ could be determined from spectral measurements. The research

²For this particular study, which is dependant on altitude and sensor resolution

³<http://www.satimagingcorp.com/satellite-sensors/worldview-2/>

⁴<http://geo.arc.nasa.gov/sge/landsat/17.html>

⁵<http://worldview3.digitalglobe.com>

conducted by Hochberg and Holden was also able to detect unhealthy coral covered in algae [88, 90]. The authors have taken many hundred in-situ spectral measurements with a spectrometer and have been able to distinguish coral taxa. Taxonomic variations were also found in the results of the spectra of coral[86]. In Hochberg *et al.*[86] the authors found corals generally fell into two spectral categories: blue corals and brown corals.

Barott *et al.* [17] also studied the spectral signatures of coral using much finer microscopic detail and examined coral/algae interactions, it was found that pigment changes could be detected with spectral imaging. The detection through spectral imaging could assist with determining which types of algae may cause stress to corals.

Andréfouët *et al.* [6] examined the ability to determine coral health from imagery collected from aerial vehicles. It was found a spatial resolution of 40-80cm (maximum pixel size) was needed for assessing the degree of bleaching on a coral reef, a common motivator for this area of work.

Some coral pigments exhibit fluorescent properties. One of the major pigments is chlorophyll which is within the symbiotic algae (zooxanthellae) found in the coral endodermal tissues [66]. Fuchs [66] developed a method to separate the fluorescent spectral signature from the rest of the coral's signature. This was done by taking two samples of the specimen, firstly with a broad spectrum white light source and secondly with a fluorescence-eliminating filter. Although separating the fluorescence signature could be useful it would be difficult to acquire from a continuously moving platform as two samples at the same location are needed. Joyce *et al* [107] looked at the photosynthetic capacity of coral by using a Pulsed Amplitude Modulated (PAM) Fluorometer to determine health. The process was very involved, which is one of the main limitations of the method. The coral had to be covered and in the dark for a period prior to the coral being pulsed with a light source. The response to the pulse was measured. This process would be slow and cumbersome from a moving platform or for wide spread mapping.

Hochberg *et al.* [87] found they were able to predict the amount of photosynthetic pigments present in coral from spectral reflectance measurements. This demonstrates a method for non-invasive monitoring of the coral. The measurements of the spectral reflectance of different corals was done from an in-situ close range spectrometer. The spectrometer was a similar model to the one used in this work.

A triple peak in the reflectance spectral signature at 570nm, 600nm and 650nm has been suggested as being ubiquitous for the pigments which exist in coral [82]. Many classification techniques employ the use of the first and second derivative and multivariate techniques such as Principal Component Analysis (PCA) to find the largest variance in the dataset [85],[89]. These techniques, which are thought to have limited general applicability [77], can discriminate without any priors concerning the chemical components of the materials in the scenes. Other techniques which do include these priors included hierarchical cluster analysis [93] and discrimination decision trees [124].

Due to the limited spatial resolution of HSI sensors often a single pixel will be composed of several materials. Hochberg *et al.* [83] examined the current remote sensing HSI platforms to determine if they could discern between coral, algae and sand as pure and mixed spectra. They presented a good method for unmixing spectra based *a priori* spectra for coral, sand and algae. It was found that current remote sensing platforms do not provide adequate spatial resolution. This was similar to the conclusions found in the work of Andréfouët *et al.* [6].

Most of the literature looking at the spectral reflectance of coral reef areas have used a spectrometer to obtain the spectral measurements [166],[130],[160]. However the techniques vary, particularly in the distance from sensor to sample. This is an issue as many do not measure and correct for the water inbetween the spectrometer and the sample. The water column is found to have a considerable effect on the ability to discriminate benthic types [92]. Also due to these being human measurements, often with a diver, the angle of measurement is not consistent and the water depths in which measurements are made is quite limited (often at most 5m) [166].

Internal shadowing has been said to have a noticeable effect on the magnitude of the reflectance [108] whereas other research has concluded that the morphology did not affect the spectra [89]. Other substrates around the measurement can greatly influence the resultant spectra. A bright substrate such as sand could strongly influence the shape of these mixed pixels [78],[7].

The Bi-Directional Reflectance Function (BRDF) of an object being imaged can complicate the spectral image processing. A BRDF defines how the spectral reflectance of an object changes with the angle of view. In general most benthic substrates have Lambertian like surfaces, however the coral genus *acropora* was found to have the largest angle variance

due to its morphology [108]. The proposed method in this thesis avoids the angle variance issue as a result of the platform chosen. AUVs have the ability to travel on a very stable trajectory. Also due to the AUV imaging system having a narrow field of view, the vehicle is always imaging the seabed from a near-nadir position (vertically facing downward).

2.6.4 Defence applications

HSI has been used extensively in terrestrial based remote sensing for defence/military application. These applications can include finding objects of interest and environmental analysis for operations planning. HSI is beginning to be used more in marine based applications.

Sulzberger *et al.* [193] has examined the task of sensor fusion for Mine Counter-Measures (MCM). Traditionally MCM has been achieved through the use of high frequency sonar [47]. In Sulzberger *et al.* [193] they used an AUV equipped with a magnetometer, sonar and camera. The camera had the ability to change its passband frequency based on the water conditions. The performance as a result of this design was not well established. The work aimed to fuse the sensor data from the variety of onboard sensors. Finding possible targets in the data was conducted manually, resulting in very slow detection.

A common defence application for HSI in a marine context is the retrieval of shallow water bathymetry[11, 13]. This process works by inverting the attenuation of downwelling light over an area of a similar substrate type. Then the HSI can be used to assess an area for traffic-ability [12–14, 36], which determines the load bearing strength of beach areas. The HSI information is used to determine the water quantity in the sands of a beach area. The trafficability is then derived through calibration and experimental testing. The testing investigates the amount of load per unit area which can be resolved for a particular soil type. These bathymetry and traffic-ability tasks are often done together to determine a location for landing military troops and heavy machinery.

2.6.5 In-situ based spectral imaging

HSI measurements taken in-situ generally have only been collected for the creation of spectral libraries. These are libraries of the underwater benthos such as coral [166], algae, sand and seagrasses [67], the purpose often being for the ground truthing of aerial measurements.

By imaging the seafloor benthos from under the water, a lot of the challenges of crossing the air-water interface can be circumvented. The possibility of utilising underwater HSI in applications has been discussed. Some of these applications include mapping of seafloor substrates, chemical composition, and marine mining. An underwater system which has shown promising results involves an underwater sliding HSI camera test rig with constant illumination[103]. In Johnsen *et al.* [103] they have discussed mounting this system to a moving platform such as an AUV. There has also been working implementing a hyperspectral camera onboard an Remote Operated Vehicle (ROV) and as a scuba diver based system [127].

In English & Carder [59] the authors present a method for determining the absorption coefficient, absorption and bottom reflectivity from a pair of upwelling and downward looking spectrometers on board an AUV. A similar concept onboard an AUV was seen in Hartmann *et al.* [75].

Davie *et al.* [50] used an RGB camera on board the Starbug AUV [55] for the application of benthic habitat mapping. They used an RGB key card in each image for colour correction process. The limit of the mapping is reliance on the ability for the RGB camera system to distinguish different materials of similar colours. Davie *et al.* [50] acknowledges this limitation and suggests the need for a multi-spectral imaging system.

Borrego-Acevedo *et al.* [28] used a spectrometer underwater aimed at reef platforms to extract the markers for chlorophyll-a. Their work aimed to find a relationship between the abundance of microphytobenthos and a spectral indicator. The goal was to determine the amount of microphytobenthos from space-borne platforms.

2.7 Spectral unmixing

Spectral unmixing is a relatively new hyperspectral imaging processing technique brought to the spotlight in 2002 in Keshava & Mustard's tutorial paper published in IEEE signal processing magazine [112]. Spectral unmixing is the procedure of resolving the endmembers within a single pixel and their corresponding fractional abundances. Endmembers generally are macroscopic objects in a scene, objects such as soil, vegetation, concrete etc. Spectral unmixing takes advantage of the vast spectral resolution available to pull out the sub-pixel constituents.

Unmixing is part of a chain of steps that lead to a final product. These steps are: 1. Atmospheric correction, 2. Data Reduction, 3. Unmixing, 4. Inversion [22]. Atmospheric correction is the process of compensating for attenuation and scattering due to the atmosphere affects on the radiance into the sensor. This process aims to recover the reflectance from the radiance data. Data Reduction is the process of identifying a lower-dimensional subspace in which the structure of the data is still retained. This serves to improve the performance of the unmixing algorithm and reduce computational complexity. Unmixing is the process of identifying the end-members in the mixture, this is done through various techniques which shall be discussed later. Inversion is the process of determining the fractional abundances of the materials present in the mixtures. Many hyperspectral unmixing approaches simultaneously determine the end-members present as well as perform the inversion step [22].

2.7.1 Mixture models

Mixture models refer to the assumptions of how materials in a scene are mixed together to give a resultant spectra. Mixtures models fall into one of two categories: linear and non-linear [112]. Linear mixture models are the most prevalent due to ease of computation and mathematics as well as for many applications a linear mixture model is a sufficient representation of the inter-material reflectance interactions. Non-linear mixtures become more relevant and accurate when there is either a situation of an intimate mixture and/or there is significant scattering from adjacent elements in close proximity. The choice of a mixture model is often determined by the application and scale required.

2.7.1.1 Linear mixture models

Linear mixture models are the most common mixture model in the literature and it is applicable if multiple scattering among materials in a scene is negligible. The premise of the linear mixture model is that within a scene there exists a small number of distinct materials (called end-members) and the mixture comprises of a linear combination of these materials which is relative to their proportion of composition (fractional abundances) in the scene/pixel [112]. A diagram of a linear mixture model is shown in figure 2.5.

In the linear mixture case the resultant spectral measurement y_i at spectral band $i \in$

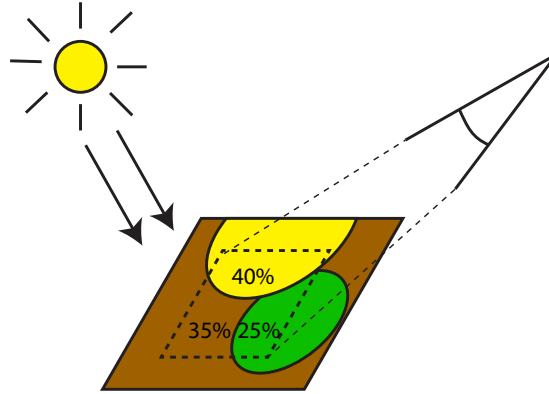


Figure 2.5 – This shows a typical linear mixture model, the resultant reflectance is proportional to the relative abundance of materials (indicated by the percentages) in the scene (as indicated by dotted line).

$\{1, \dots, B\}$, where B is the total number of spectral bands of the sensor; is given by the *linear mixing model (LMM)*:

$$y_i = \sum_{j=1}^p e_{ij} \alpha_j + w_i \quad (2.9)$$

where $e_{ij} \geq 0$ is the spectral measurement of endmember $j \in \{1, \dots, p\}$ at i^{th} spectral band, $\alpha_j \geq 0$ denotes the fractional abundance of endmember j , w_i denoted an additive perturbation which is made up of modelling errors and noise (predominately shot noise on the imaging sensor). The fractional abundances are subject to the following constraints:

$$\text{Non-negativity (ANC)} \quad \alpha_j \geq 0, j = 1, \dots, p \quad (2.10)$$

$$\text{Sum-to-one (ASC)} \quad \sum_{j=1}^p \alpha_j = 1 \quad (2.11)$$

In the literature [22] the non-negativity constraint is termed *abundance non-negativity constraint (ANC)* and the sum-to-one constraint is termed *abundance sum constraint (ASC)*. These two constraints are applied subjectively based on the application, the literature does not indicate any dominant rule or principle to assist with determining when to apply the constraints.

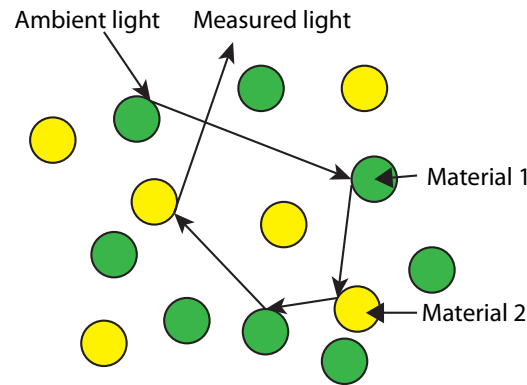


Figure 2.6 – Intimate mixture model is typically applicable when the materials in the scene are small and are in close proximity to each other, in this model the light interacts with multiple materials before reaching the sensor.

2.7.1.2 Nonlinear mixture models

A relatively new area in spectral unmixing is inferring that the mixture model is non-linear [80]. There are two predominate nonlinear mixture models, the Bilinear and the Intimate mixture model. The bilinear model was first introduced by Singer and McCord [182] to model the spectral reflectance of light and dark patches on the surface of Mars. The intimate mixture model describes scattering resulting in spectral mixing and was popularised by Hapke [73], [74].

2.7.1.3 Intimate non-linear model

Intimate mixtures occur where materials are in close contact with each other. The common example given is that of grains of pepper being mixed amongst grains of salt. The spectral reflectance characteristics depend on many factors such as the number of particles of each material, size, shape and location of the particles. In an intimate mixture light will often interact multiple times with the particles present before before being recorded by the sensor. For each interaction the light will be absorbed or scattered in some direction. A diagram of a typical intimate mixture model is shown in Figure 2.6.

2.7.1.4 Bilinear non-linear model

In certain spatial and structure configurations it is possible that light reflected from a surface has undergone multiple reflections, in this instance the secondary reflections are

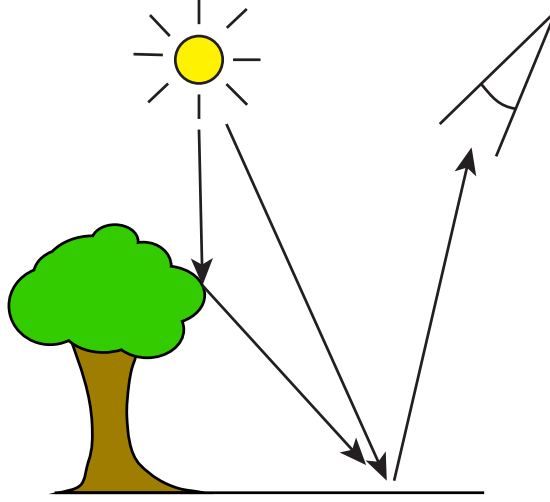


Figure 2.7 – This represents a common scenario for the use of a Bilinear mixture model. The tree canopy (due to reflected light) creates secondary illumination of the imaged area. As a result of the secondary illumination the calculation of the spectral reflectance contains a secondary term.

called bilinear interactions. An example is shown in Figure 2.7; here reflected light from a tree’s canopy is illuminating a patch in the scene which is also illuminated by direct sunlight.

Considering two end-members e_1 and e_2 , their bilinear interaction will take on the form of $e_1 \odot e_2$, where the \odot operator is a point-wise multiplication also called the Hadamard product.

$$\mathbf{x} = e_1 \odot e_2 \Leftrightarrow \forall n \in \{1, \dots, B\}, x_n = e_{1n}e_{2n} \quad (2.12)$$

Where B is the total number of spectral bands. Here a light ray is absorbed twice, once for each endmember, so the change in intensity as a function of wavelength is defined by the point-wise product of the spectral reflectance of the two endmembers. So the resultant two endmember bilinear model as proposed by Singer and McCord [182] is defined as:

$$\mathbf{x} = a_1 e_1 + a_2 e_2 + a_{12} e_1 \odot e_2 \quad (2.13)$$

with the constraints:

$$a_1 \geq 0, a_2 \geq 0, a_{12} \geq 0 \quad (2.14)$$

$$a_1 + a_2 + a_{12} = 1 \quad (2.15)$$

Where a_i is the fractional abundance for the i^{th} interaction/material. The Equation (2.14) is the same non-negativity constraint as in Equation (2.9) as is the sum-to-one constraint Equation (2.15). Here there are the standard linear mixtures a_1e_1 and a_2e_2 with the addition of the $a_{12}e_1 \odot e_2$ being treated like a third endmember in the unmixing process.

2.7.2 Data reduction

Generally the dimensionality of the spectral data is often much lower than the number of available spectral bands. Identifying a lower dimensionality subspace improves computational performance, complexity and storage of the spectral data. If a linear mixture model is an accurate assumption, the number of materials in the scene is equal to the dimensionality of the signal subspace minus one.

Band selection or extraction methods exploit the correlation between adjacent bands to select a few components to maximise the signal-to-noise ratio (SNR) [180], [44]. Some of these methods include a maximum likelihood approach such as Singular Value Decomposition (SVD) [175], or through the use of Principal Components Analysis [106].

2.7.3 Unmixing & inversion

Bioucas-dias [22] provides a very comprehensive overview of the state-of-the-art hyperspectral unmixing techniques. Methods using sparse-coding [150] show promise by avoiding the need of spectral libraries, instead learning the spectral separability from the data resulting in an advantage over traditional unmixing techniques which require a spectral library prior to the unmixing step. Often there are issues arising from calibration differences during the acquisition of the spectral libraries.

2.7.3.1 Geometric approaches

Geometrical techniques such as N-FINDR [205], are based on the premise that a linear mixture is a simplex which is constructed from pure end-members. A simplex is an n -dimensional volume. The outer vertices of the simplex are defined by the end-members

belonging to a predefined spectral library. The algorithm finds the set of pixels defining the largest volume by inflating a simplex inside the data. The unmixing is then based on the position of a data point in the simplex. The closer the point is to a vertex the more it contains that endmember represented by the vertex.

Pixel Purity Index (PPI) [24], [25] is similar to the N-FINDR algorithm except it assumes the presence of at least one pure pixel per endmember is present in the dataset. So the simplex has one pure pixel at each vertex. The unmixing is similar to N-FINDR in that the abundances are relative to the position of the data point in the simplex.

Vertex Component Analysis (VCA) [147] projects the data onto a subspace orthogonal to the endmembers already determined or found. The algorithm then iteratively attempts each combination until all endmembers are exhausted. This method is quite computationally intensive due to the combinatorial nature of the algorithm.

2.7.3.2 Statistical approaches

In hyperspectral unmixing often the number of materials and their abundances are unknown. Independent Components Analysis (ICA) has been proposed to unmix hyperspectral data [45], [18], [198]. ICA is based on the assumption that all the components are independent, which does not hold for hyperspectral data as the sum of the abundance proportions are constant and thus implies statistical dependence among the components [113, 148]. A dependence variant has been implemented which compensates for the dependence assumptions [145].

The work of Filippi & Archibald [61] uses support vector machines for extracting endmembers for use in spectral unmixing. Support Vector Machines (SVMs) were used in Sun *et al.*[194] for determining the ratio of Cyanobacterial Pigment C-phycoerythrin (C-PC) concentrations in turbid lakes in China.

2.7.3.3 Sparse regression

Sparse regression techniques unmix by assuming the measured (mixed) spectra can be expressed as a linear combination of known spectra. These spectra could be from a predefined spectral library. Unmixing is then performed by finding the optimal subset of these library

spectra that best model the observed spectra. Due to large libraries this can become a very computationally intensive task, since the number of endmembers present is usually very small compared to the library size. Linear sparse regression techniques are an efficient solution to this combinatorial problem [97, 98].

2.7.3.4 Spatial-spectral methods

Many HSI techniques neglect the spatial dimension in hyperspectral imagery [181]. Some methods aim to determine the pure endmembers (endmember extraction) in an image by iteratively examining the neighbours of each pixel at changing window sizes for spectral similarity. By using a defined threshold certain pixels are defined as more pure than others [135, 158]. To reduce the error during the unmixing process several methods aim to create a subset of possible endmembers for a particular pixel [51, 114]. A similar approach can be taken for clusters of multiple pixels. An image is partitioned into fields of pixels and then subsets of endmembers are determined [207].

Other methods look at the spatial correlation between abundance quantities as opposed to particular endmembers. The Jia *et al.* method utilises blind-source separation [102]. There will often be a similarity with abundances between neighbouring pixels. So a method was proposed which imposed regularisation on the search cost function. This allowed the abundance estimate to be generated from spectrally similar pixels in the neighbourhood [42]. Other methods use a Markov-random field for the regularisation of the cost function [57]. This is a promising area of HSI research as the spatial dimension is often neglected in HSI processing.

2.8 Summary & outcomes

In this chapter the background literature relating to light in the underwater environment has been reviewed. The selective attenuation properties of water were shown. Water will often inhibit the transmission of light in the red region of the visible spectrum first, followed by blue then green. The optical properties will change with different compositions of particles within the body of water. Light passing through water will either be absorbed or scattered by the water and its particulates.

Several water models were presented, many of the current methods rely on assumptions or in-water measurements to parametrise their water model. Often they rely on using standardised water models (Jerlov water models), however it is not clear how well this generalises to actual bodies of water. Some methods take measurements of the water however this often occurs just in one location and one depth. It is unclear how this single measurement extrapolates across large spatial areas. To improve the clarity of underwater images, several methods have been presented which utilise polarising filters. The filters act to reduce the backscatter within the water column which results in a loss of contrast. These methods did produce promising results however the light loss was very large.

As a result of the selective attenuation of light, underwater images possess a certain colour distortion. The degree of distortion will be dependant on several factors such as the distance of objects in the scene to the camera and the materials dissolved and suspended within the body of water. It is desirable to recover the true colour of underwater objects for the purpose of improving classification performance using colour features. Several post processing techniques exist which rely on histogram equalisation, or learning a mapping between the uncorrected and corrected colour. The consistency of these techniques is questionable as they do not sample the optical properties of the water the images are taken in.

Another colour correction technique utilises an active illumination system which can increase the amount of red in the illuminant to match the approximate distance to the scene. This technique makes an assumption about the optical properties of the water as well as assumptions about the structure of the scene. This method would have limited performance outside of the narrow parameters it was trained to operate within. A method which is able to correct the colour in underwater imagery using high resolution 3D structure information as well as utilising information about the optical properties of the water in front of the camera is yet to be undertaken.

Correcting the colour of underwater imagery would allow for the use of colour as features in underwater image classification. Current methods do not use colour due to difficulties in obtaining accurate and consistent colour information. Colour or spectral reflectance information at high spectral resolutions (such as hyperspectral) is able to provide high separability between benthic material types. In-situ hyperspectral measurements have been obtained in-situ using scuba divers, however these are often spatially sparse point measurements. A moving in-situ platform would be more ideal as it could cover much larger

regions. In-situ derived hyperspectral images have potential applications in defence such as the application of MCM for the detection of sea mines. At present this is being conducted using sonar or imaging from above the water's surface.

Optical imaging of the underwater environment from above the water's surface is complicated by the interface between the air and the water. Issues such as glinting, and distortion due to wind and refraction present serious challenges for obtaining clear imagery. Most above water imaging is being conducted by remote sensing platforms. These platforms are often aerial or satellite based. These platforms are able to cover large areas due to their altitude but this is often at the cost of horizontal spatial resolution. There are also depth limitations imposed by the attenuation properties of the body of water.

Much of the remote sensing imagery currently obtained is either in the form of a hyperspectral or multispectral sensor. A multispectral sensor has a higher spatial resolution than a hyperspectral camera, however this is at the expense of spectral resolution. Several works have examined the use of hyperspectral imaging of coral environments in applications of benthic health monitoring. It was concluded that there are fundamental spatial resolution requirements to undertake this task. Current remote sensing platforms do not satisfy these spatial requirements.

Classifying materials smaller than the spatial resolution limits of a hyperspectral imaging platform can be challenging. Spectral unmixing techniques however appear promising for resolving sub-pixel materials. Often these methods do not utilise the extra information contained in the spatial domain of the image. This in an evolving area of hyperspectral image processing, however methods which do utilise the spatial component are limited to the spatial resolution of the device. There has been a lack of research into fusing cameras of different spatial resolutions to improve the spectral unmixing performance.

Chapter 3

Spectral and spatial calibration for underwater imaging



3.1 Introduction

This chapter is focused on the methods for the calibration of the proposed imaging system. Spectrometers were used to determine the attenuation of the water column and the spectral profile of light into the scene. These spectrometers have an intrinsic FOV, this FOV . Also

unknown was the FOV of the spectrometer in the combined imaging system and how this FOV corresponded to the FOV of the stereo cameras used onboard the AUV. The FOV and spatial co-registration is covered in Section 3.2.

The sensitivities of each spectrometer to different wavelengths of light can vary greatly. In order to relate the response of one spectrometer to another a radiometric calibration must be undertaken. This is covered in Section 3.3.

Along similar lines to radiometric calibration is deriving a relationship between the spectrometer data to the spectral sensitivities of the cameras in the stereo camera. A good calibration allows for accurate correction of the colour from an RGB camera. The method presented to characterise the spectral sensitivities of RGB cameras relies on using a Linear Variable Edge Filter (LVEF) (a filter with the optical passband frequency varying spatially along one physical axis). The characterisation of the LVEF is presented in Section 3.4.2.1. Then to calibrate the spectral sensitivities of RGB cameras a new method is presented in Section 3.4.

3.2 FOV and spatial co-registration of spectrometers and RGB cameras

Spectrometers are a point measuring device. They have very high spectral resolution but very low spatial resolution. Despite only capturing data at a single point, spectrometers have an intrinsic spatial sensitivity to their FOV. The term FOV refers to the solid angle of light in front of the spectrometer which will be measured by the systems detector. A solid angle is the two-dimensional angle in three-dimensional space that an object subtends at a point. The SI unit of a solid angle is a steradian (abbreviated “sr”). In this instance the FOV can be thought of as a cone emanating from the aperture of the imaging device. This point-spread is not necessarily circular nor even. It has been shown that some spectrometers exhibit rectangular FOVs [40]. Knowledge of the FOV becomes important when the imaged target is spatially variable within the FOV. This may occur when measuring targets which are a mixture of materials.

In this work a new optical sensor combination is introduced. A spectrometer is combined with a conventional RGB camera (see Figure 3.1); the spectrometer provides high spectral

resolution with low spatial resolution and conversely the RGB camera provides high spatial resolution with low spectral resolution. The region of high spectral resolution within the high spatial resolution RGB image will allow for greater classification and characterisation abilities in remote sensing and mapping operations [204], [26]. This comes at a much reduced cost and size compared to a traditional hyperspectral imaging platform. Utilising the combined measurements from the sensors relies on an accurate spatial registration of the two sensor FOV.

In Hedley *et al.*[78] a series of coral, algae, sand and rock combinations were imaged with a spectrometer with the aim of recovering the abundances of each substrate type within the scene. The proportions of the substrate types within the scene changed their contribution to the resultant spectra and hence knowledge of the FOV response function was necessary.

Current methods for calibrating the FOV of a spectrometer are quite labour intensive, low resolution and slow. In Hedley [78] they present a method of moving a black target across the FOV at different angles to gain the FOV characteristics. The method from Caras *et al.*[40] involved mounting a spectrometer above a black surface imprinted with a light grid pattern. A white square was then placed on the black grid in front of the spectrometer. The process involved moving the white square one position on the grid and taking a spectrometer reading and repeating the process. This was then repeated for different distances to ensure the linearity of the FOV angle. From this the authors were able to generate a sensitivity map of the spectrometer's FOV. Experiments were also performed with different colour combination targets to estimate the spectral mixing sensitivity. MacArthur *et al.* [129] implemented a similar method but rather than translating a reflective object they translated a light source and measured the spectrometer's response to the position of the source.

These methods are laborious and there is an increased potential for human error through the involvement of an operator. The resolution is limited to how much time the operator wishes to expend and the size of the square used [40].

In the proposed calibration, the basic methodology from Caras *et al.*[40] has been used and an automated version developed which obtains much higher spatial resolution and does not require a constant human-in-the-loop. By allowing the system to be automated the number of measurements which can be taken can be dramatically increased because of the removal of the laborious task of moving the white square and taking spectral readings. The extension to this automated method is to allow the spatially co-registering of the spectrometer with

a conventional RGB camera.

3.2.1 Methodology

The method developed was implemented in two parts; the first part determines the FOV response function and the second spatially co-registers the RGB camera and the spectrometer together.

The spectrometer used was an Ocean Optics STS-VIS Micro-spectrometer with an optical resolution (Full Width at Half Maximum (FWHM)) of 6nm (100 μ m slit width), and a spectral range of 350-800nm. The camera used was the stereo camera rig from the AUV used in this work and was shooting in RAW format.

3.2.1.1 Determining the FOV

Determining the FOV response function involves replacing the black target board[40] with a computer LCD monitor (19inch Hewlett-Packard model: LP2065), which was imaged by the spectrometer and the two cameras within the stereo camera rig. See Figure 4.20 for the mounting of the spectrometer and the two cameras. The apertures are tethered together to ensure they do not shift from their relative positions to one another. A *MATLAB*[1] program was written to generate a user definable sized white square on a black background, which took a reading from the spectrometer then moved the square to the next adjacent position and repeats the process for the entire screen. One of the advantages of this method was the box size could easily be reduced which in turn generated a higher spatial resolution for the FOV map. However by reducing the box size less light is gathered so the spectrometer's integration time needs to be increased proportionally to the decrease in box area.

The monitor which is used for displaying the white square will have an angle variance. The measured intensity of the screens output will reduce as the angle increases from straight on. This factor needs to be compensated for in the calibration method. The angle response function of the monitor was determined by displaying a white screen, this was then imaged at various angles using the camera from a fixed distance. The initial reading was taken straight on to the monitor (0°) and the cameras exposure was adjusted to ensure the imaging system was not being saturated by the white screen.

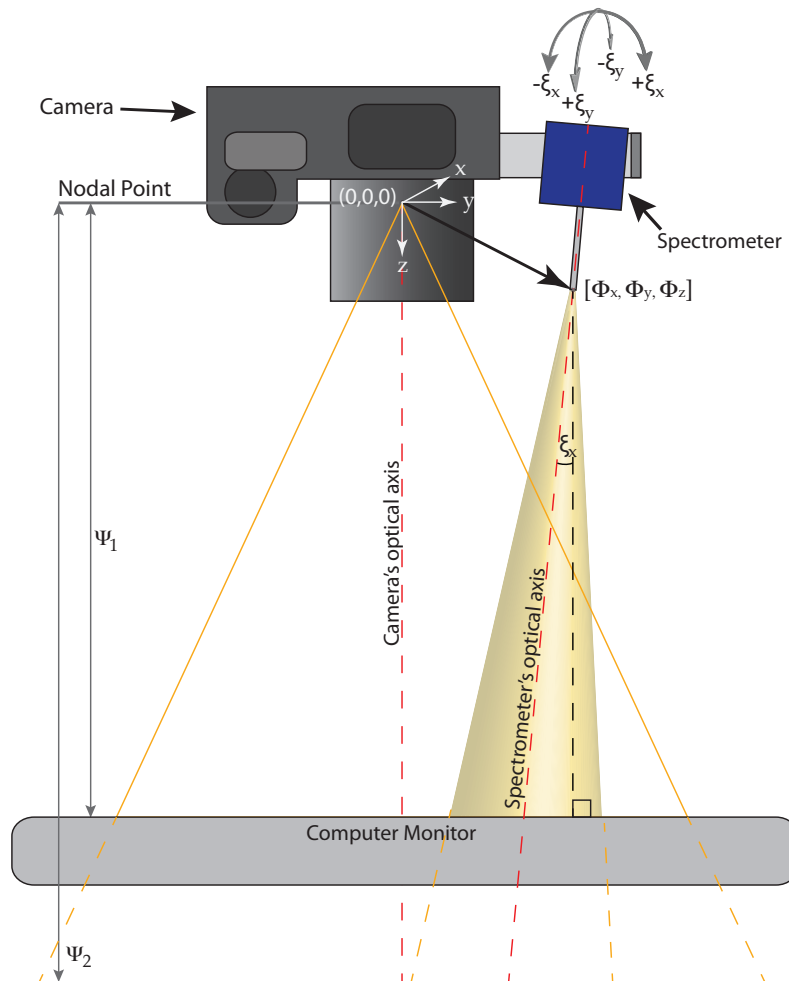


Figure 3.1 – Experiment Setup: a spectrometer tethered to an RGB camera was placed at height h above a computer LCD screen. The screen shows a white box on a black background. For each movement of the box a spectral measurement is taken. After spectral measurements have been taken for the whole screen, the sensitivity map is displayed and a picture is taken with the attached camera. The process is repeated at different distances.

After taking measurements for each box location the result was a three dimensional dataset consisting of 3 axes: a horizon, vertical and spectral axis. The spectrometer had 1024 spectral bins, however due to the narrow band output of the back-lighting in the screen only a few bands are usable, so an average over the usable wavelength bands were taken. Then the map is normalised so it is scaled from 0 to 1.

$$S_{x,y} = \frac{\bar{s}_{x,y}(\lambda_u) - s_{min}}{s_{max} - s_{min}} \quad (3.1)$$

where $S_{x,y}$ is the normalised sensitivity at position (x, y) , and $\bar{s}_{x,y}(\lambda_u)$ was the mean of the unnormalised sensitivity at position x, y for usable wavelengths λ_u . s_{min} was the minimum $\bar{s}_{x,y}(\lambda_u)$ for the whole map and s_{max} was the maximum $\bar{s}_{x,y}(\lambda_u)$ for the whole map. The readings were then rectified for the angle variance of the screen using:

$$A_{x,y} = v_{x,y}(\theta)S_{x,y} \quad (3.2)$$

where $A_{x,y}$ is the angle adjusted spectral reading for position x, y , $S_{x,y}$ is the sensitivity gathered in Equation (3.1) and $v_{x,y}(\theta)$ was the screen angle variance for position x, y where the angle variance has been normalised 0 to 1 for $\theta = 0^\circ$.

The collection of $S_{x,y}$ measurements are put together to form a sensitivity map. This map defines how sensitive the spectrometer is at a particular spatial location.

3.2.1.2 Spatial co-registration

The second stage of the calibration process is the spatial co-registration of the FOV of the spectrometer within the FOV of the imaging camera. This was achieved by displaying the completed spectrometer sensitivity map on the monitor and a picture of this map was taken with the camera. The first step of this method (Section 3.2.1.1) is repeated for different distances from the display, after each a photograph of the map is taken. From these photos of the FOV sensitivity map the center of the spectrometers FOV (spectrometer's center line/optical axis) was identified and the Euclidean pixel distance to the center of the photo was measured. This pixel distance was converted into real world units based on the camera's distance to the monitor and angle of view. The measurements of the optical axis's of the camera and the spectrometer for 4 different distances allowed for a line to be fitted in 3D

space for each device. This was performed by taking the four 3D points for the respective sensor and fitting a linear line in 3D space by minimising a sum of squares cost function.

From these generated optical axis lines a spatial transformation matrix was derived for the rotation and translation of a point on the camera axis to one in the spectrometer axis. To map the spectrometer's sensitivity, the FOV was modelled as a cone emanating from the fore optics of the spectrometer. It was determined from the angle of view of the spectrometer from the sensitivity maps gathered in Section 3.2.1.1.

The spatial transformation matrix β was derived from:

$$R_{YX} = \begin{bmatrix} \cos(\xi_y) & 0 & \sin(\xi_y) \\ 0 & 1 & 0 \\ -\sin(\xi_y) & 0 & \cos(\xi_y) \end{bmatrix} \begin{bmatrix} 1 & 0 & 0 \\ 0 & \cos(\xi_x) & -\sin(\xi_x) \\ 0 & \sin(\xi_x) & \cos(\xi_x) \end{bmatrix} \quad (3.3)$$

$$\beta = \begin{bmatrix} & & \phi_x \\ & R_{YX} & \phi_y \\ & & \phi_z \\ 0 & 0 & 0 & 1 \end{bmatrix} \quad (3.4)$$

Where R_{YX} is the rotation matrix derived from rotation about the x-axis ξ_x and about the y-axis ξ_y . The spatial transformation matrix β is then derived from R_{YX} and X, Y, Z translations ϕ_x , ϕ_y & ϕ_z . To obtain a point in the spectrometer frame P_{spec} from a point in the camera frame P_{cam} is calculated:

$$P_{spec} = \beta \begin{bmatrix} P_{cam} \\ 1 \end{bmatrix} \quad (3.5)$$

3.2.2 Results

3.2.2.1 Spectrometer FOV

The apparatus was set up as per the methodology described above. Prior to measuring the sensitivity maps the angle variance was measured. The response is shown in Figure 3.2. The spectrometer sensitivity maps for four different distances were measured, as shown in Figure

3.4. These results were derived by using a box size of 55×55 pixels which corresponds to a spatial size of $14 \times 14mm$.

For comparison the method from Caras *et al.*[40] was done, (see Figure 3.3), it had a much coarser spatial resolution than the proposed method ($2 \times 2cm$ vs $0.766 \times 0.766cm$). This result took approximately 2 hours to record all the data points and it was very labour intensive requiring the user to move the white square for every reading. The proposed method takes about 2.5 hours but does not require an operator, the duration is dependant on the number of boxes to measure (resolution) and the integration time for each measurement. From the result more detail can be seen in the sensitivity of the FOV whereas the Caras *et al.*[40] result did not detect the insensitive region right in the middle of the FOV.

The FOV of our spectrometer at the $-10dB$ point of the sensitivity map was found to be $12.935^\circ \pm 0.480^\circ$.

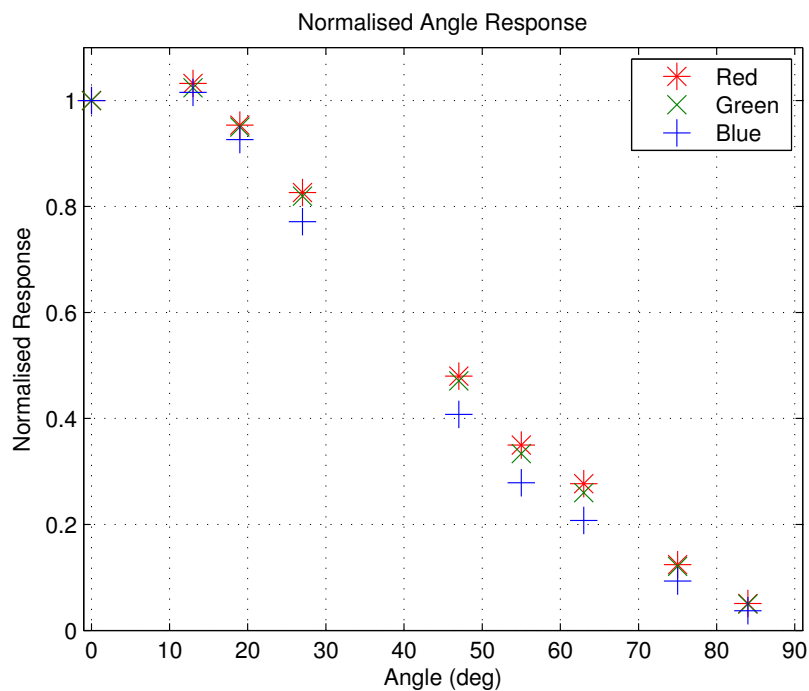


Figure 3.2 – Angle variance of the computer monitor, angle in degrees is from 0° perpendicular to the screen. There is a point missing around 35 degrees due to an error during acquisition of this measurement

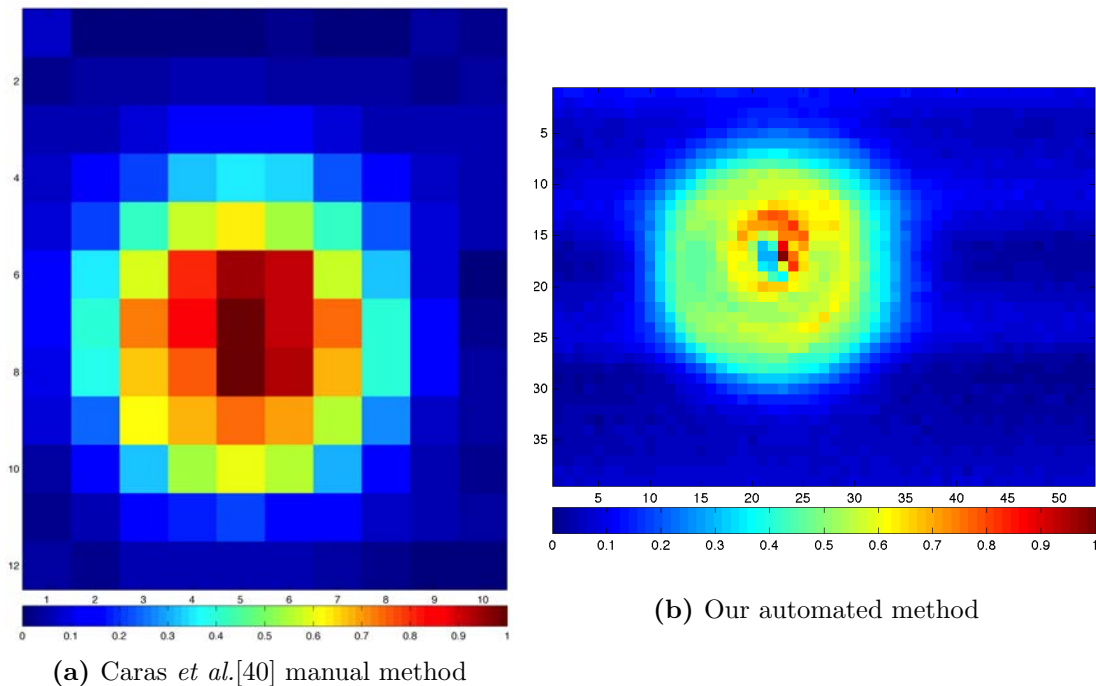


Figure 3.3 – (a) Spectrometer FOV map using the method of Caras *et al.*[40] with a 2cm white square (b) FOV map using the our method with a box size of 30 pixels ($7.6 \times 7.6mm$), spectrometer was 767mm from the screen. This shows a comparison between the proposed method and one from the literature. Our method is clearly higher resolution and autonomous. The spectrometer used was the upwards looking spectrometer. The axes refer to the square number. The magnitude scale is between the lowest value assigned blue and the highest sensitivity value is assigned dark red.

3.2.2.2 Spatial co-registration

After each FOV sensitivity mapping step the FOV map was displayed on screen and several photos of the map were taken with the stereo camera. Two examples from the 1655mm distance are shown in Figure 3.5.

To co-register the stereo camera with the spectrometer the pixel coordinates (x_{pix}, y_{pix}) for the middle of the FOV map in the images is determined. The middle of the camera image is defined to be the optical axis of the image. This means the calibration is only valid for this particular camera and spectrometer combination. Subsequent changes to the combination or relative positioning of either sensor would require re-calibration. The pixel coordinates are converted to real-world units for both cameras based on distance to target and camera FOV with the origin at the front of the lens in the optical axis of the cameras. This is repeated for each distance, and then a line is fit to these 3D points for each camera. The

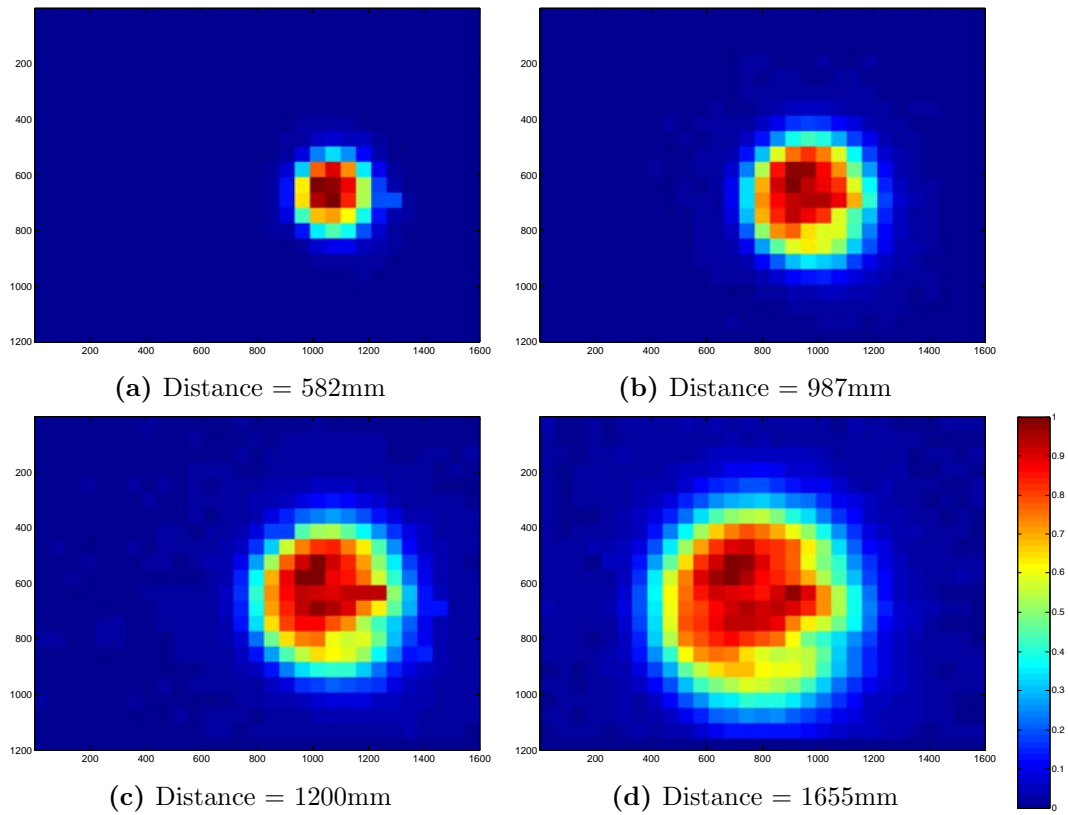


Figure 3.4 – FOV sensitivity maps for different distances between the spectrometer and the monitor.

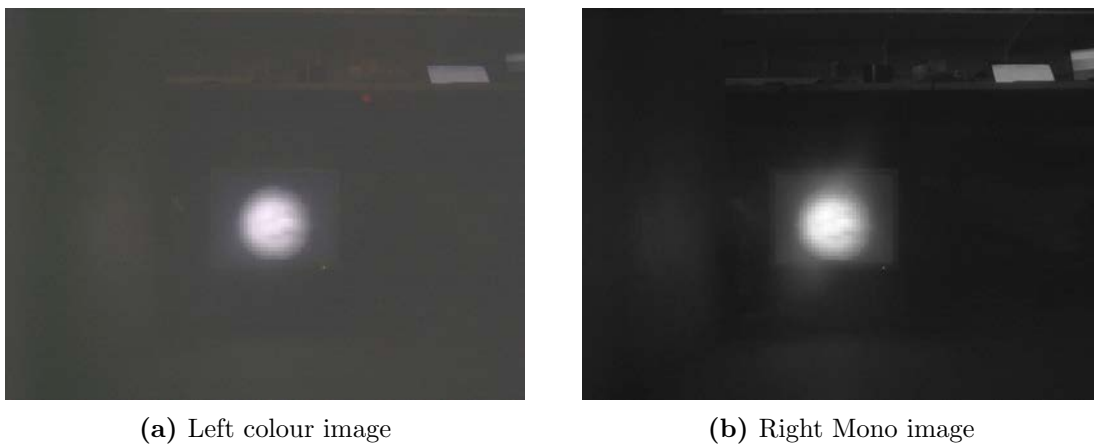


Figure 3.5 – FOV co-registration: Images of the FOV from the stereo camera at a distance of 1655mm from the monitor. These images are used to co-register the stereo camera with the FOV of the spectrometer.

error on the fit is shown in Table 3.2. It is the distance error between the 3D points for the spectrometer's optical axis and the fitted line for the spectrometer optical axis. The error is not large given the distance of the measurements from the screen. The errors are largest for the closer measurements at 582mm and 987mm. The spatial translations and rotations were found from this fit and the results are shown in Table 3.1. Then a translation and rotation matrix were defined for the optical axis of the spectrometer in each of the camera frames, which was then combined into a spatial transformation matrix [27] see Equation (3.6) - left colour camera, Equation (3.7) - right mono camera. There is not a z-axis rotation because the spectrometer does not have a definable orientation about its optical axis. So the orientation of the FOV is defined to be the same as the optical axis of the imaging camera.

<i>Quantity</i>	<i>Left Colour</i>	<i>Right Mono</i>
x-offset	45.3mm	-23.2mm
y-offset	33.3mm	34.4mm
z-offset	-0.6mm	-0.7mm
x-rotation	-1.27°	-1.26°
y-rotation	-0.46°	-0.23°
z-rotation	0°	0°

Table 3.1 – The spatial relations of the spectrometer's optical axis with respect to the optical axis of each of the stereo cameras

$$\beta_{LC} = \begin{bmatrix} 1 & 0.00018 & -0.0081 & 45.2605 \\ 0 & 0.9998 & 0.0221 & 33.2829 \\ 0.0081 & -0.0221 & 0.9997 & 0 \\ 0 & 0 & 0 & 1 \end{bmatrix} \quad (3.6)$$

$$\beta_{RM} = \begin{bmatrix} 1 & 0.00009 & -0.0040 & -23.1563 \\ 0 & 0.9998 & 0.0221 & 34.4314 \\ 0.0040 & -0.0221 & 0.9997 & 0 \\ 0 & 0 & 0 & 1 \end{bmatrix} \quad (3.7)$$

<i>Distance from screen</i>	<i>Left Colour Error</i>	<i>Right Mono Error</i>
582 mm	10.54 mm	7.53 mm
987 mm	21.80 mm	14.22 mm
1200 mm	7.09 mm	3.24 mm
1655 mm	4.14 mm	3.61 mm

Table 3.2 – This shows the distance error between the 3D points for the spectrometer optical axis and the fitted line for the spectrometer optical axis.

3.2.3 Discussion

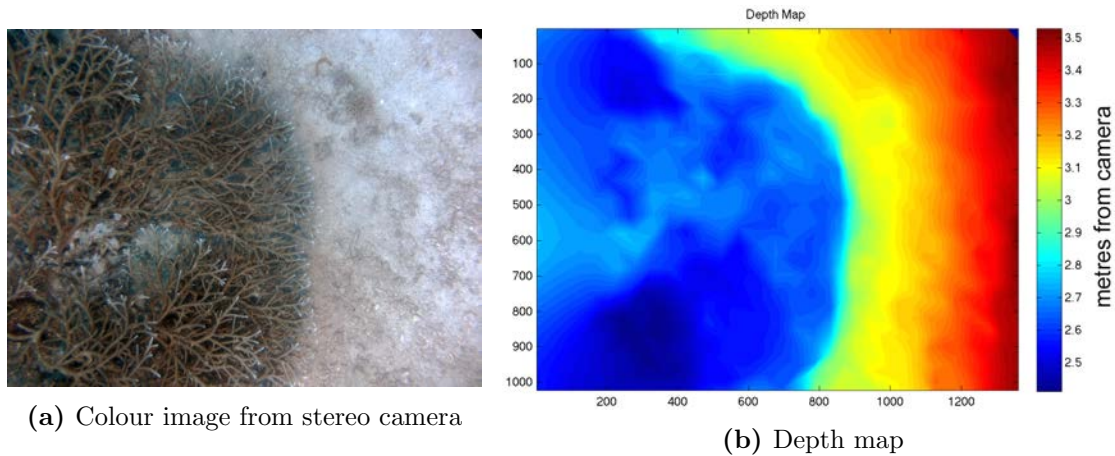
The computer monitor will have a limited spectral output due to the back-lighting source. In current Liquid Crystal Display (LCD) monitors the backlighting is usually a Light Emitting Diode (LED) whereas older LCD monitors are Cold-Cathode Fluorescent Lamps (CCFL). Either source is not broadband, however due to the spectral sensitivity of human eyes this light source appears white. So as a result one can not say much on the possible spectral variability of the FOV sensitivity map.

A higher spatial resolution of the sensitivity map may be obtained by decreasing the box size. As a result an increase in the spectrometer integration time would be needed to obtain the same signal strength. A smaller box size was not undertaken because the chosen box size provided adequate resolution for the requirements of the application.

Context of the FOV in the underwater environment

The FOV mapping was used for two reasons in this work. Firstly for assisting with classification, it was useful to know what was in the FOV of the spectrometer for improving classification performance. This will be discussed further in Section 5.2. Secondly the FOV mapping provided an improved estimate of vehicle altitude relative to the imaging pod. Vehicle altitude was traditionally provided by a reading from the Doppler Velocity Log (DVL), however the DVL was located at the rear of the vehicle and the imaging pod towards the front. As a result as the vehicle passes over changing elevations in terrain, an estimate for altitude from the DVL is not correct for the imagery.

To solve this problem the stereo imagery was used. From the stereo imagery a 3D mesh was obtained and a depth map could be derived. In the depth map each pixel was the distance in metres from the centre of the camera to the respective point in the scene. An example of a depth map for a stereo camera image is shown in Figure 3.6.



(a) Colour image from stereo camera

(b) Depth map

Figure 3.6 – An example of a depth map derived from the 3D mesh generated from the stereo camera data. These depth maps allow for an accurate measurement of altitude for the spectrometer reading. An accurate altitude reading is critical for correcting the spectra for water attenuation.

To obtain an accurate altitude for camera system, firstly the altitude was initialised from the DVL measurement and then the size of the FOV in the scene was determined from the calibration model of the spectrometers FOV. Then mapping the FOV into the 3D depth map a better altitude measurement was obtained, the process was then repeated: define the FOV, map into the 3D scene, and obtain an altitude measure. This process was repeated until it converges to within 1mm. This new altitude reading was used for subsequent radiometric corrections needed in this work.

3.3 Relative radiometric calibration of spectrometers

In this work multiple spectrometers were used. The sensitivity of each spectrometer at a particular wavelength of light differed slightly. This difference also applied to the two spectrometers of identical model and acquisition date. This was most likely due to slight variations in the diffraction grating and the mechanical mounting of the grating with respect to the imaging sensor. Also each spectrometer sat behind different underwater windows of varying thickness and material composition. In order to compare and utilise the data from each spectrometer the sensors were calibrated to create a relative radiometric calibration. The output of the spectrometers were not calibrated to absolute units but rather defined scaling factors as a function of wavelength which allowed for inter-sensor output comparison.

The system was not calibrated to absolute radiometric units due to the difficulty in undertaking this task. Facilities for this task were not easily available during the undertaking of this research. For this system however a relative radiometric calibration was adequate.

To calibrate the spectrometers a large panel of Quartz-doped Teflon which was chosen as it was spectrally similar to Spectralon (a common spectral reflectance target). The choice of reflectance target is particularly important as it needs to provide a near lambertian surface which is both spectrally and spatially even. The target panel was evenly illuminated by diffused halogen lamps, an even illumination was achieved through indirect illumination off the flat even ceiling above the target panel. Care was taken to ensure the lamps had warmed up prior to acquisition (the lamps were left on for over an hour). The three spectrometers used in the system were aimed from identical distances at the panel. The spectrometers were mounted in their housings so as to incorporate the influence of the housing windows on light transmission into the sensors.

To remove the variance which would occur from different exposure times (integration times) the sensor's digital count (DC) output was divided by the respective integration time in milliseconds resulting in the units (DC/ms). Figure 3.7 shows the spectral measurements obtained by the three spectrometers over the wavelength range 400-820nm. Conversion of one spectrometer's output to the relative units in another is done through the multiplication of the output by the ratio from this calibration of the source and destination spectrometer. Note each spectrometer plot has a different amplitude, this is due to each spectrometer having a different response to the lit panel.

To obtain an estimate on the noise of a spectrometer reading, the test was repeated for each spectrometer. In this experiment the integration time was varied from very short to very long (5ms - 1600ms). The spectrometer was faced towards a spectralon reflectance panel and was illuminated by a halogen lamp. For each reading at a different integration time the dark spectrum was measured and subtracted from the reading. To test the ability to read the radiance invariant of the integration time the intensity output was divided by the integration time. This in effect gathered the power of the reading. Figure 3.8 shows the spectrometer readings divided by their respective integration time. Intuitively it shows more noise relative to the signal is present on the short integration times.

To examine the variance of the noise, Figure 3.9 shows a plot of the noise variance with respect to wavelength. This shows it is reasonably even across the different wavelengths

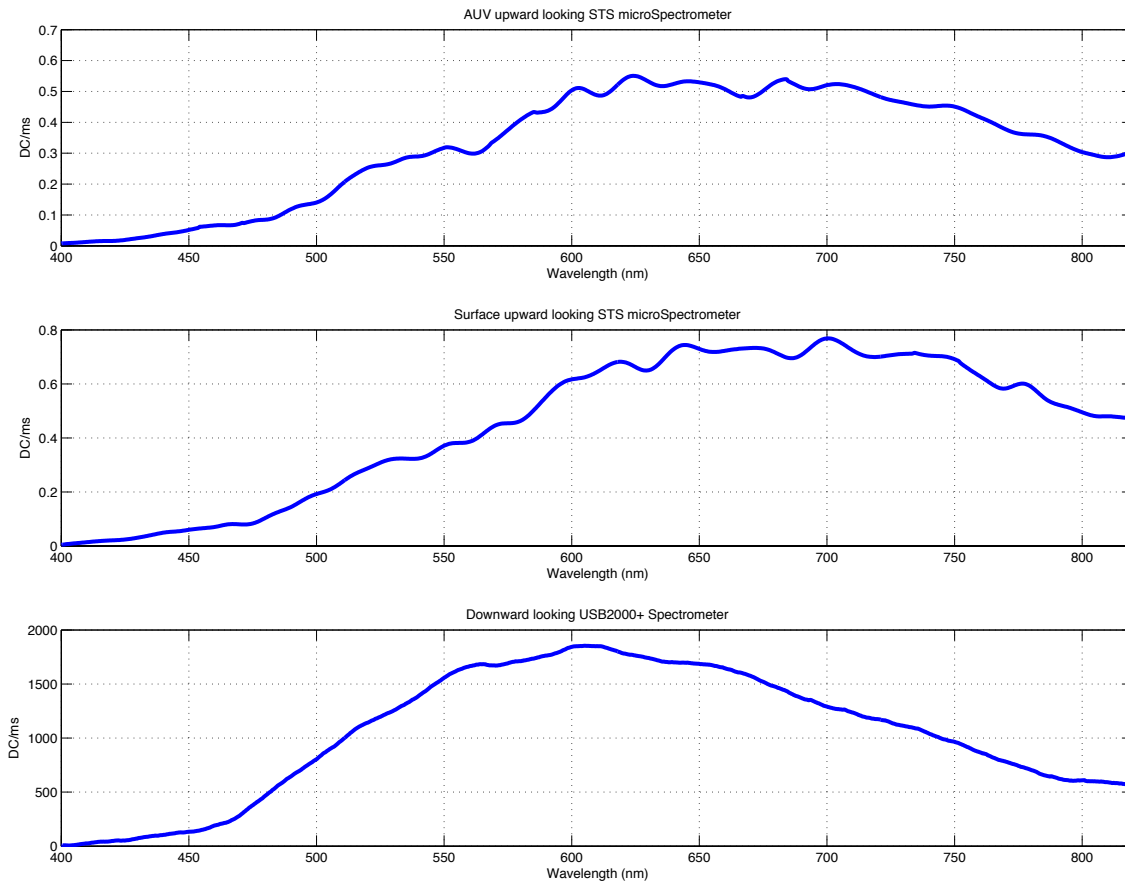


Figure 3.7 – This figure shows the response of the three spectrometers to a reference reflectance panel. This demonstrates the need for a good radiometric calibration. Ideally they should all resolve a similar reading, however even the two upward looking spectrometers which contain the same imaging Charge-Coupled Device (CCD) and are the same model of spectrometer are not the same. The calibration is also beneficial as it compensates for the transmission properties of the windows of the underwater housings for the instruments. The units are in digital counts per millisecond, this is to make the measurements invariant of exposure time.

of the spectrum. The mean of the power curves was taken and then a histogram of the distance from the mean was obtained for several different integration times. This is shown in Figure 3.10, it shows that noise on the spectrometer readings are normally distributed about the mean. This also shows the SNR increases as integration time increases which would be expected with a larger integration time.

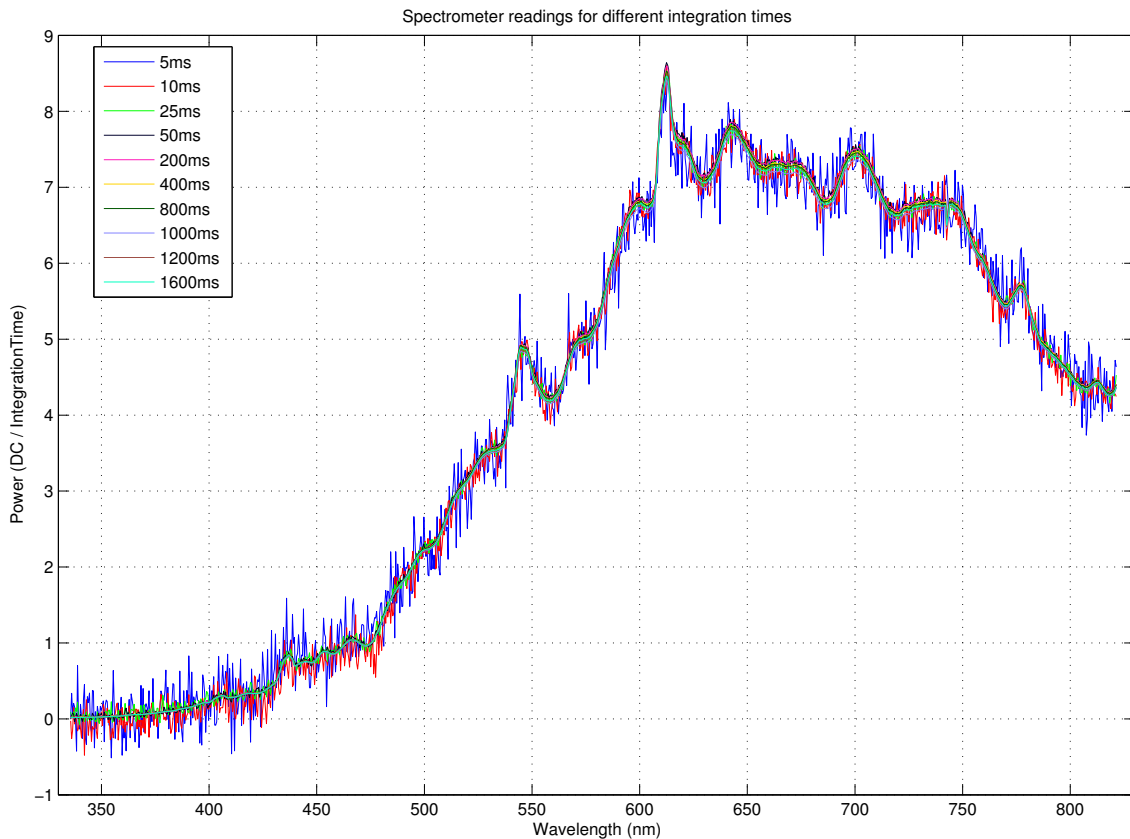


Figure 3.8 – This figure shows the noise for different integration times. These curves are taken from the spectrometer reading divided by the respective integration time.

3.4 Spectral sensitivities of RGB cameras

Knowing the spectral sensitivities of the RGB cameras used in the proposed system is important. It allows for the translation of the water model obtained using the spectrometers in the hyperspectral domain into the trichromatic domain of the colour cameras used. The application which it shall be utilised for is in underwater colour correction where the aim is to mitigate the water's optical attenuation effects. This will also help in allowing data of the same underwater area taken on different cameras to be chromatically comparable.

The advantage of the method is the simplicity of the experimental setup, the small number of measurements needed and the simplicity of the characterisation.

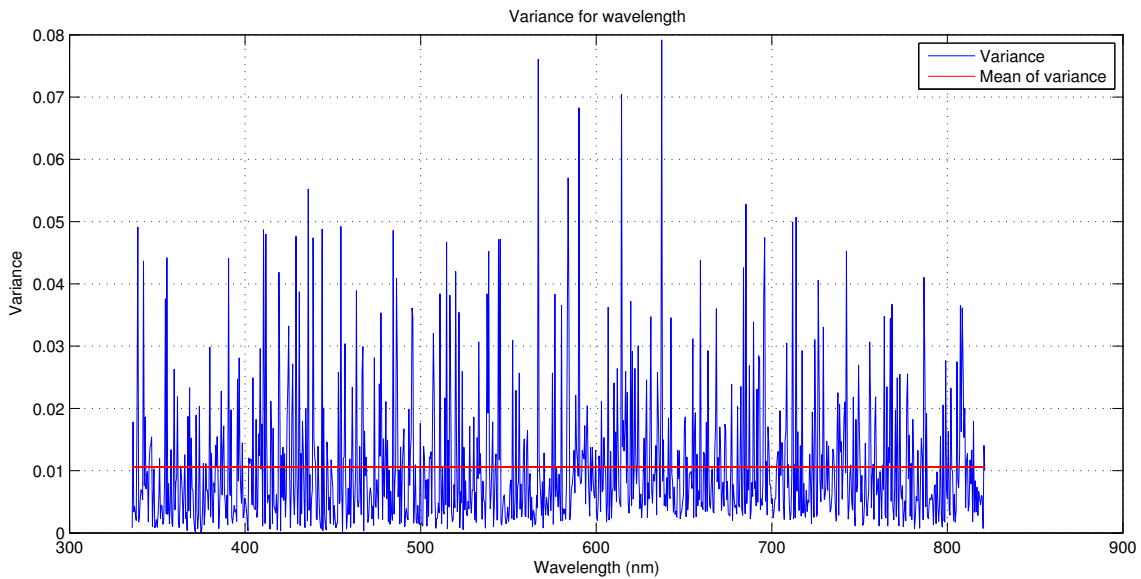


Figure 3.9 – Plot of the variance of the noise per wavelength from the readings in Figure 3.8

3.4.1 Previous work

One of the issues with spectrally characterising trichromatic cameras is knowledge of the light intensity response characteristics. Vora *et al.* [202] used a method of photographing a target with different exposures for defining the linearity of photometric response. Grossberg and Nayar [71] developed a method using Principal Components Analysis (PCA) to derive constraints from the intensity response of a large number of cameras, which was then used to determine the response function for a new camera.

An accurate method of chromatic characterisation is to use a monochromator to generate a narrowband light source which is imaged off a reflectance standard into a camera under test and a spectrophotometer [201]. Vora *et al.* [201] presented a processing technique using Wiener estimation methods to correct for errors due to the non-zero width of the spectral power distribution of the narrowband light source. The monochromator method is defined as the standard for the European Machine Vision Association (EMVA) [60]. The disadvantage of the monochromator approach, despite the high resolution achieved, is that it requires costly hardware or needs strictly controlled acquisition conditions [173].

A variation of the monochromator technique is seen in Mauer *et al.* [133] where 39 interference filters were used to characterise the spectral response of the RGB camera. The technique does not provide as high a resolution of characterisation as the monochromator

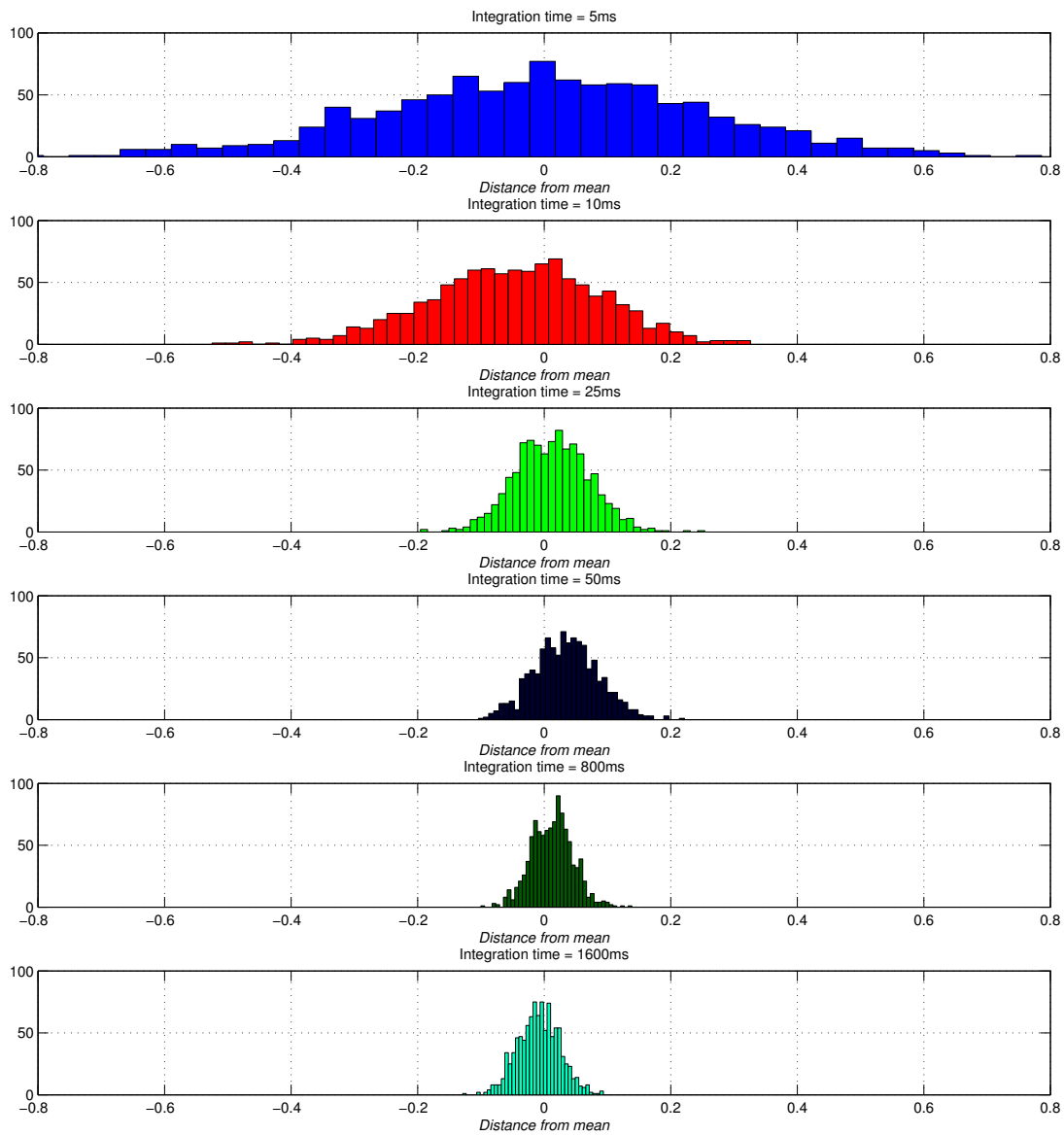


Figure 3.10 – This shows noise distribution, the distance from the mean for the readings shown in Figure 3.8 for different integration times. The units for Distance from the mean is in Power units (digital count/integration time) as seen in Figure 3.8

technique, but did produce good results. This would be a slow process as at least 39 measurements need to be taken. An alternative method for generating monochromatic light is through the use of a liquid crystal tunable filter in front of the camera which can tune into a specified narrow frequency (bandwidth = 10nm) [173].

A quick method is seen in Finlayson *et al.* [62] who devised a quadratic programming technique to gather the sensitivity response by imaging a Macbeth colour chart¹ and gathered the spectral reflectance profiles of the lighting and Macbeth colour chart swatches. These measurements of the swatches from the camera and the spectral measurements impose a set of constraints that naturally form a series of linear inequalities which lends itself to a quadratic programming routine. The process could also be further simplified by using a pre-existing Macbeth colour chart reflectance library [120].

The quadratic programming technique [16, 120, 155] works well, requiring only one picture of the colour chart for each illuminant type. There are however two issues with this technique: the first issue is that they assume that the lighting is identical between the photograph of the chart and the spectral measurements of the chart. This may not be the case if using a spectral library [120]. The second issue is that the color chart is made for photography applications, and so the colour panels are not evenly distributed in the spectral domain [173].

3.4.2 Methodology

The standard approach would use a monochromator, however one was not used in this work because one was not available. Monochromators are also quite expensive hence a new lower cost method needed to be developed. The proposed approach involves imaging a light source of known frequency and intensity. This is done through the use of a filter which produces narrow-band light. This could be analogous to a monochromator. Then the sensitivity of the camera at a particular band can be obtained by reading its response to the narrow wavelength light. The major difference in the proposed method to the literature is the speed of acquisition. The filter used produces all the required narrow bands of light at once in one filter. This method is also advantageous for ease of implementation, a monochromator is an expensive and thus hard to obtain piece of equipment. The filter is called a LVEF and further details on the filter are provided ahead.

¹Xrite Photo ColorChecker Classic http://xritephoto.com/ph_product_overview.aspx?ID=1192

The equipment used was a broad spectrum light source such as the sun or an incandescent light bulb, a LVEF[58], a dark box, a Spectralon reflection target, a spectrometer and the RGB camera under test. Choosing a broadband light source is important. Lighting sources such as fluorescent and LED lights should be avoided due to their sharp spectral peaks and large troughs [155, 171, 185]

The LVEF is mounted on one side of the dark box and the camera under test on the other looking through the LVEF. On the outside of the box next to the LVEF, a Spectralon target is placed so as to reflect light from the light source through the LVEF into the camera. The dark box is important as it cuts out stray light which may reflect off the back side of the LVEF into the camera. The LVEF is very reflective on both sides, so stray light will greatly influence the results.

The spectrometer is mounted so as to measure the reflectance of the light source upon the Spectralon target. This gives us the spectral profile of the light before it passes through the LVEF. The spectrometer should acquire a spectrum of the light at the same time as the RGB image is acquired. The spectrometer used was an Ocean Optics STS-VIS Microspectrometer with $100\mu\text{m}$ slit width, 6nm resolution (FWHM) and a spectral range of: 350-800nm. The setup can be seen in Figure 3.11.

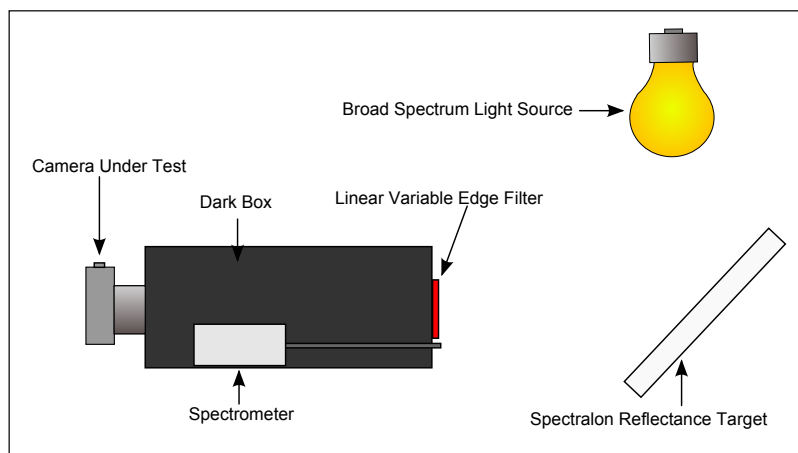


Figure 3.11 – Experimental setup for camera characterisation

To obtain the unnormalised spectral response of the RGB camera, an image of the target is taken through the LVEF. Most point-and-shoot cameras are unable to save raw photographs. In this instance *Day light* white balance was found to be the best to select because it was closest to a halogen light source. This was important for minimising the colour distortion

the camera's software was imposing. Ideally only cameras which can shoot in RAW should be used, however this methodology shows it can be applied to any point-and-shoot camera. An exposure was chosen such that the image was not over exposed. Due to geometric lens effects, the signal around the outer edges of the image plane is attenuated (vignetting) where the fall off is proportional to the fourth power of the cosine of the off axis angle [16]. To minimise these effects we use only the central portion of the image.

To accompany the spectral sensitivity response of the camera system, the intensity response was also gathered. It was found that the consumer grade *point-and-shoot* cameras applied a gamma curve (non-linear response) to the received image. Cameras shooting in RAW exhibited a linear intensity response. To determine the intensity response a calibrated Spectralon 50% reflectance target was imaged over different shutter speeds.

For validating the camera model a variety of colour objects needed to be imaged with the RGB cameras and their reflectance measured with the spectrometer. We used 55 different paint sample swatches which varied chromatically across the visible spectrum. The paint sample swatches had the advantage over artificially created printed swatches in that they were made of well mixed paint pigments as opposed to four discrete inks (Cyan, Magenta, Yellow & Black - CMYK) in the case of digital printing.

3.4.2.1 LVEF characterisation

To characterise the spectral sensitivities of an RGB camera a method was developed which is discussed in Section 3.4, this method relies on the use of a LVEF. This is an optical bandpass filter (dimensions: 59mm wide x 24mm high) whose passband frequency changes linearly with translation along the longest axis of the filter. At one end it only passes light at 369nm while at the other end only 737nm. Figure 3.12 shows what would be seen if one were to look through the filter onto broadband illumination. The information provided on this filter however was inadequate and required knowing the transmissions of the device at finer resolutions, hence further investigation was needed.

To examine the transmission properties a rig was built from LEGO to hold both the spectrometer and LVEF in place. Using a corkscrew gearing system a translational stage for the LVEF was designed, by rotating a crank as can be seen in Figure 3.13 the LVEF is translated horizontally in front of the spectrometer's tip. The spectrometer was held in

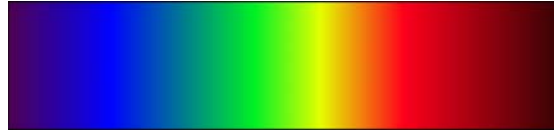


Figure 3.12 – Linear Variable Edge Filter - pass band frequency changes along the horizontal spatial dimension

place by cable ties and the LVEF was held in place by the Lego frame and Blu Tac. The LVEF was illuminated behind by a spectralon 50% target and the light source was a halogen desk lamp.

The spectrometer used was an Ocean Optics STS-VIS Micro-spectrometer with $100\mu\text{m}$ slit width, and a spectral range of: 350-800nm. It's tip was mounted 1mm away from the surface of the LVEF (see Figure 3.15). This was the same spectrometer as used for the upwards looking sensor in this work. The FOV of the spectrometer is approx 12° as determined during the FOV calibration in Section 3.2.

The experiment was conducted at two spatial resolutions, coarse and fine. The fine resolution was conducted at $\frac{1}{2}$ rotations of the crank per reading and the coarse at single rotations per reading. The relationship between rotations and translation is described by the following:

$$\textit{translation}(mm) = 2.1298\textit{rotations} \quad (3.8)$$

The zero starting point was defined as the edge of the filter in the near UV end covering half of the aperture of the spectrometer. A similar position but at the other end defined the end of the measurements. There will be some fringing effects at these end points so the data is not to be trusted.

At each new location a transmission reading was taken and subsequently plotted as is show in the results section.

3.4.2.2 LVEF transmission curves

The results for the fine resolution are shown in Figure 3.17. The results show transmission bands for a certain spatial location to be extremely even and consistent. The FWHM for

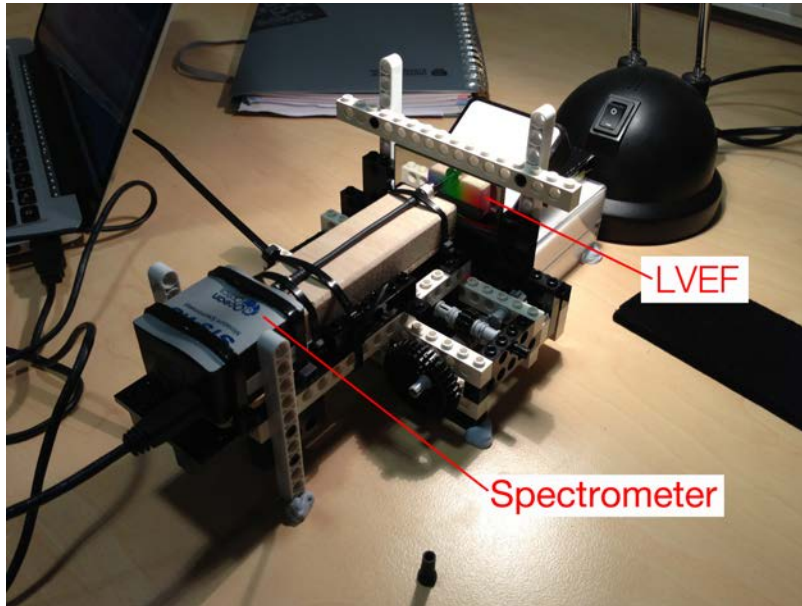


Figure 3.13 – The LEGO rig with the spectrometer and LVEF mounted in place

the transmissions is found to be 13.8nm (taken from the transmission band at 566.53nm from the fine resolution).

Tabulated results for the translation and transmission are show in Tables 3.3 & 3.4.

3.4.2.3 Processing

To acquire the unnormalised spectral response of the RGB camera a row vector was obtained from each of the chromatic channels of the acquired image. To reduce noise, the mean of the imaging sensor values perpendicular to the frequency axis was measured. For each channel the response of the imaging sensor colour filter was obtained with the limits of 380nm to 745nm due to the limits of the LVEF.

The LVEF inherently has some leakage or blurring at any point, whereby it will pass a peak frequency but with a Hann window [23] like shape passing neighbouring frequencies. The width of this window was found through the use of a red laser; the frequency width of the laser was measured without the LVEF and then measured through the LVEF. The window was found to have a width of approximately 17nm. To reconstruct the effect of frequency blurring we constructed a Hann window. The window is normalised such that the sum of the window is equal to 1 in order to maintain the power density of the spectra.

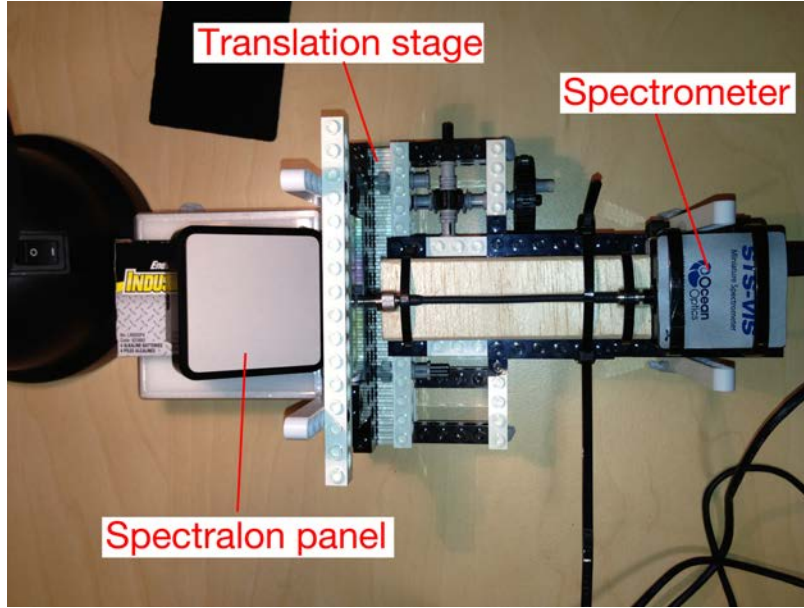


Figure 3.14 – Top view of the LVEF LEGO Rig

$$F_w = \frac{h_w}{\sum h_w} \quad \sum F_w = 1 \quad (3.9)$$

where: F_w is the LVEF normalised Hann window, h_w is a Hann window of width 17.6nm. This was chosen to be close to the inherent window width of the LVEF.

The light received through the camera system is a combination of the light source, the LVEF transmission properties, the cameras' Bayer filter and the camera sensors' spectral sensitivities. We define the spectral sensitivity of the camera in the wavelength, λ , as $C(\lambda) = \beta(\lambda)\sigma(\lambda)$, where $\beta(\lambda)$ is the three channel Bayer filter spectral transmission properties and $\sigma(\lambda)$ is the transmission properties of the imaging sensor at wavelength λ . The spectrum of light received at each band b can be written as $S_b(\lambda)$:

$$S_b(\lambda) = C(\lambda)(F_w \cdot (F_t(\lambda)L(\lambda))) \quad (3.10)$$

where $F_w(\lambda)$ is the smoothing window of the LVEF, $F_t(\lambda)$ is the transmission of the LVEF, $L(\lambda)$ is the spectra of the light being reflected off the spectralon target into the LVEF and λ is the wavelength range of the LVEF.

The spectral response function can be used to convert spectra into the camera's RGB colour space. The RGB response R_b to a certain spectra of light is the integral over all the K

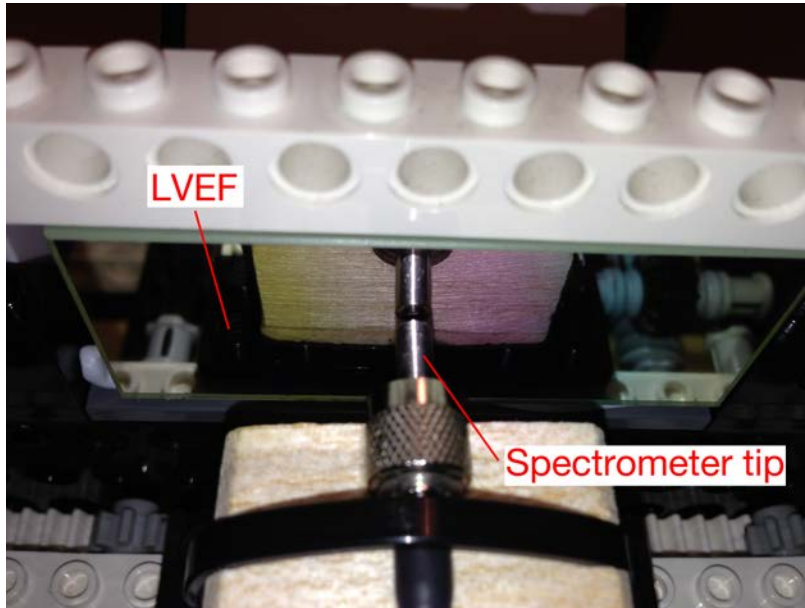


Figure 3.15 – Spectrometer tip mounting against the LVEF, approx 1mm off filter surface

measured wavelengths of light of S_b for each band b (red, green & blue):

$$R_b = \sum^K S_b(\lambda) \quad (3.11)$$

3.4.2.4 Validation of model

To validate the camera response model the quadratic programming method as seen in Pike [155] was utilised. This solves for $C(\lambda)$ in the camera model:

$$R_b = \sum^K \rho(\lambda)C(\lambda) \quad (3.12)$$

where $\rho(\lambda)$ is the radiance of each of the colour swatches of the macbeth colour chart, which was measured with a spectrometer. $C(\lambda)$ was the camera model Equation (3.10) which refers to the spectral sensitivity for the b th RGB colour band, taking into account the transmission properties of the lens, colour filters and onboard processing. R_b was a RGB value gathered from each swatch from an image of the Macbeth colour chart taken by the camera under test.

To compare the LVEF method to the *Pike*[155] method, a validation data set was made

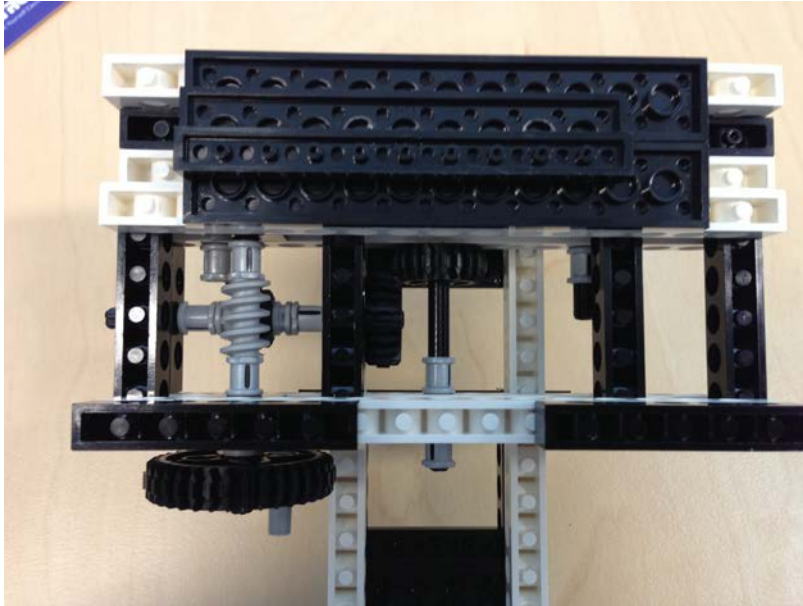


Figure 3.16 – Bottom view of the LVEF LEGO Rig showing the cog gearing system

consisting of 55 different colour swatches. The aim was to accurately reproduce the RGB value of these swatches from the measured spectral reflectance. The reconstructed RGB value from the LVEF model is derived from R_b using the Equation (3.12).

The chromatic accuracy was an important aim of this research, so to compare the performance of the LVEF method to the Pike method, a Euclidean distance metric was used in a chrominance only colour-space. The colour-space chosen was the $YCbCr$ colour-space. To have a chrominance only measure the Y (luminance component) was negated.

3.4.3 RGB camera characterisation results

In this section the results for the intensity response (section 3.4.3.1) and the spectral response (section 3.4.3.2) for the three cameras under test are presented. In section 3.4.3.3 the model is validated by comparing to the Pike method[155]. In Section 3.4.3.4 the results of the spectral sensitivities of the stereo cameras on-board the AUV used in this work are shown.

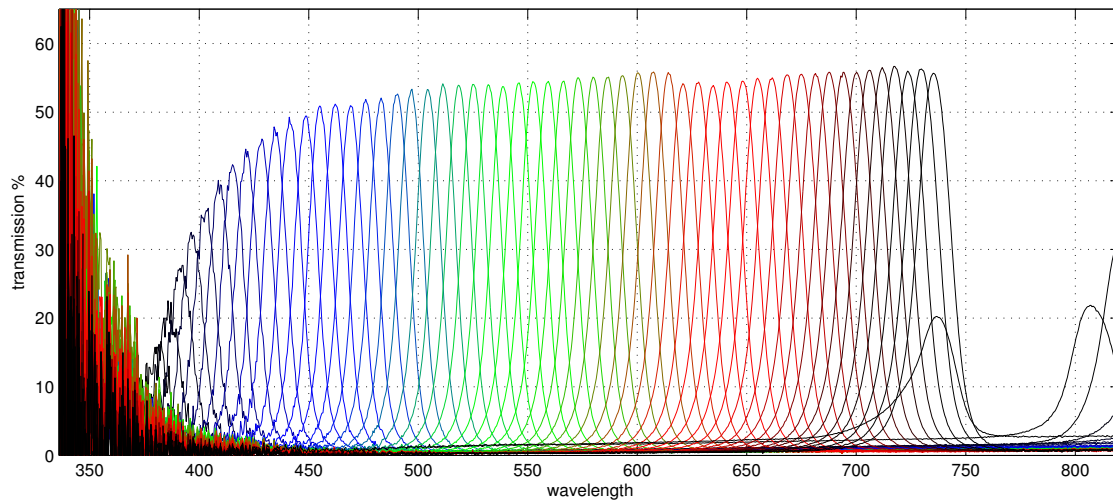


Figure 3.17 – Transmission of the LVEF, each peak represents a measurement, it shows the even and consistent transmission for a point along the filter. The FWHM was found to be 13.8nm. There is noise below 375nm due to insufficient light flux.

3.4.3.1 Intensity response

Figure 3.18a illustrates the intensity response for the *Nikon D5000* with the images taken in RAW mode; this shows the camera exhibited a linear intensity response. In comparison the intensity response of the *Canon Powershot A2000* and the *Olympus μ Tough 8000* are clearly nonlinear (Figure 3.18b & 3.18c). The scale of the intensity response for the *Nikon* is greater than the other two cameras due to the *Nikon* capturing the photo in 12-bit resolution as opposed to the 8-bit resolution of the *Canon* and *Olympus*. The Red, Green and Blue channels are offset due to the colour of the lighting, as it had quite a yellow/red bias. The intensity response curves (Figures 3.18a-3.18c) are shown with the error bars showing the standard deviation of the measurements.

3.4.3.2 Spectral responses

The spectral response graph for the *Nikon D5000* is shown in Figure 3.20a. The *Canon Powershot A2000* response is shown in Figure 3.20b showing the *Sunny* white balance response. The spectral response of the *Olympus μ Tough 8000* over four different white balances is shown in Figure 3.19. The vertical axis of the spectral responses are scaled such that the cross product of an imaged surface with the spectral response will result in an accurate reproduction in the camera's RGB space for a particular shutter speed. This

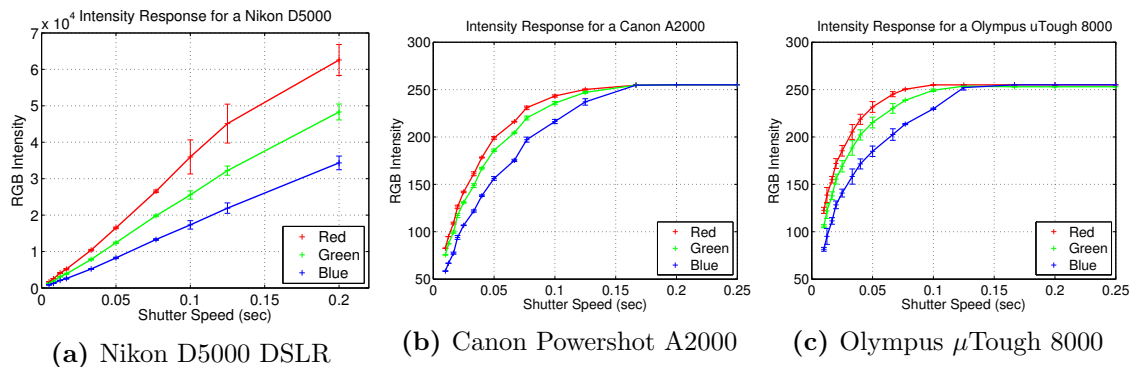


Figure 3.18 – Intensity response curves for cameras under test

shutter speed is what was used when generating the spectral response. Provided the non-linearity of the camera is known, the spectral response may be scaled to accommodate different exposure levels.

3.4.3.3 Validating the model

Using the quadratic fitting method from *Pike*[155] we were able to generate spectral responses for all the cameras under test. The spectral response for the *Nikon D5000* derived from the *Pike* method is shown in Figure 3.21. To compare the performance of our method we determine the Euclidean distance of the chrominance components in the YCbCr colour-space. The LVEF method performance is shown in Figure 3.22a and the Pike method performance is shown in Figure 3.22b, with a table of the mean and standard deviation of the errors shown in Table 1. These results show the presented method to be more consistent in the response modelling and result in less modelling error overall. The RGB reconstruction is shown in Figure 3.23 this shows a visual example of the RGB reconstruction performance of the two methods.

3.4.3.4 AUV stereo camera response

On the AUV, the stereo camera consisted of two different cameras, both were Prosilica GC1380 cameras from Allied Vision Technologies, but one was a colour camera (trichromatic) while the other was a mono camera. They were connected to the data acquisition system in the vehicle over ethernet. They have 12 bit Sony ICX285AQ (colour) and

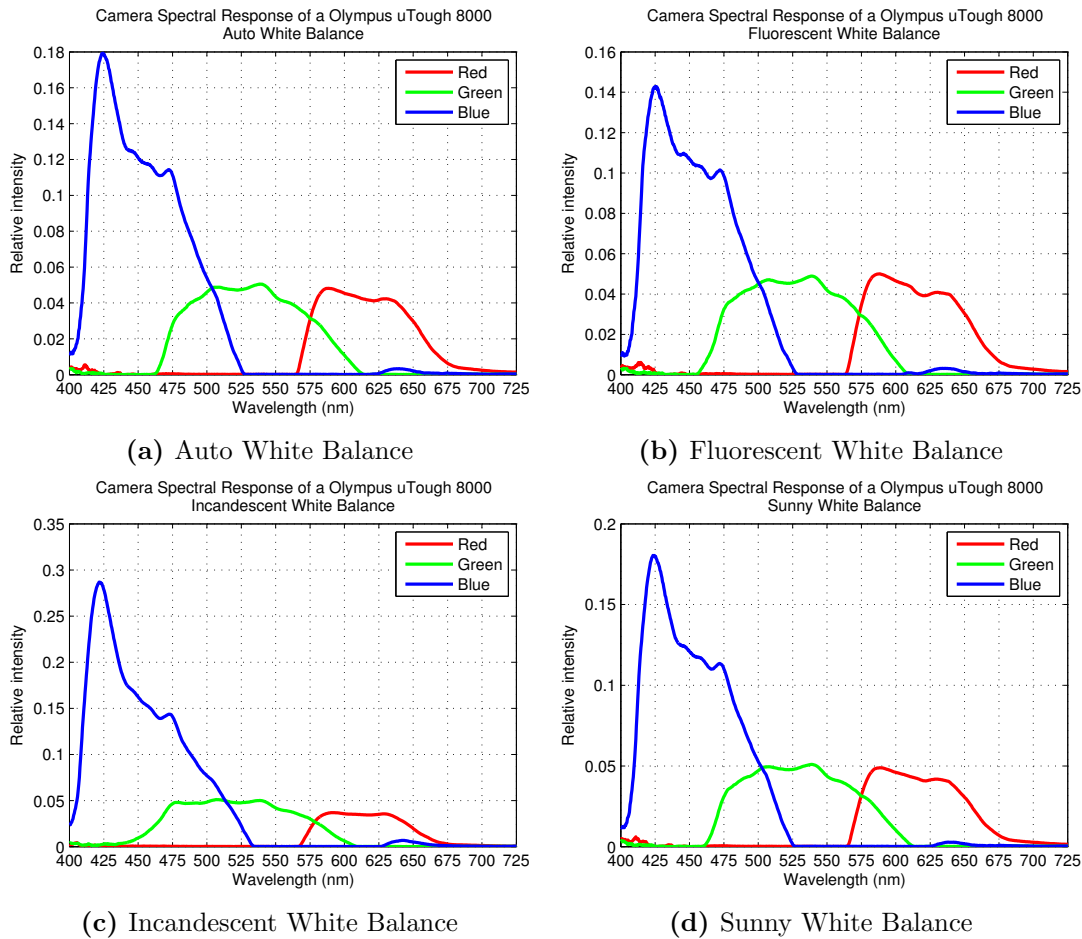


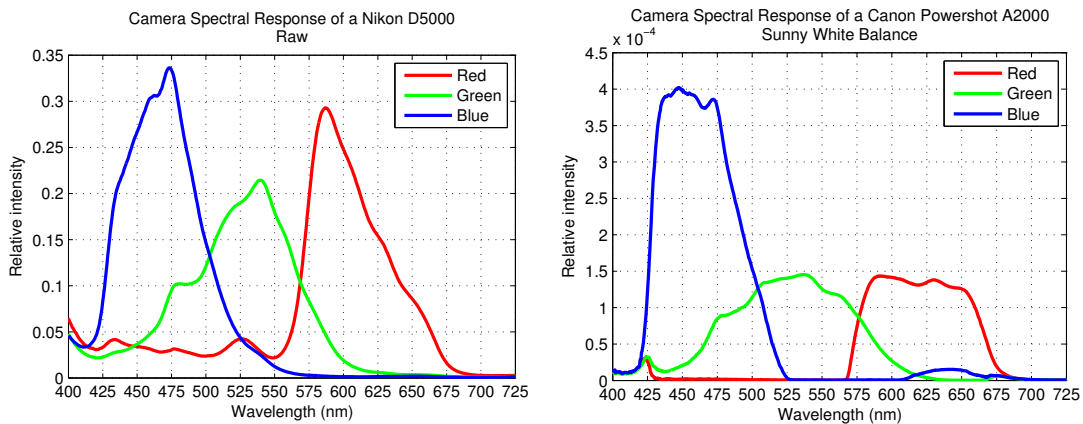
Figure 3.19 – The relative spectral responses of the Olympus μ Tough 8000

ICX295AL (mono) CCD progressive type imaging sensor, and pixel size was $6.45\mu m$. The images were acquire as RAW, so no compression or down-sampling was applied.

The spectral response curves for the colour camera in the stereo camera pair onboard the AUV is shown in Figure 3.24.

3.5 Summary

In this chapter several new calibration methods were presented for the spatial and spectral characterisation of the imaging sensors used in this thesis. The spatial sensitivities of the spectrometers FOV was shown in Section 3.2. Then the spatial relationship between the spectrometer and a conventional imaging camera was presented.



(a) Spectra response Curves for a Nikon D5000 DSLR (b) Spectral response Curves for a Canon PowerShot A2000

Figure 3.20 – Spectral response functions for the Nikon and Canon cameras

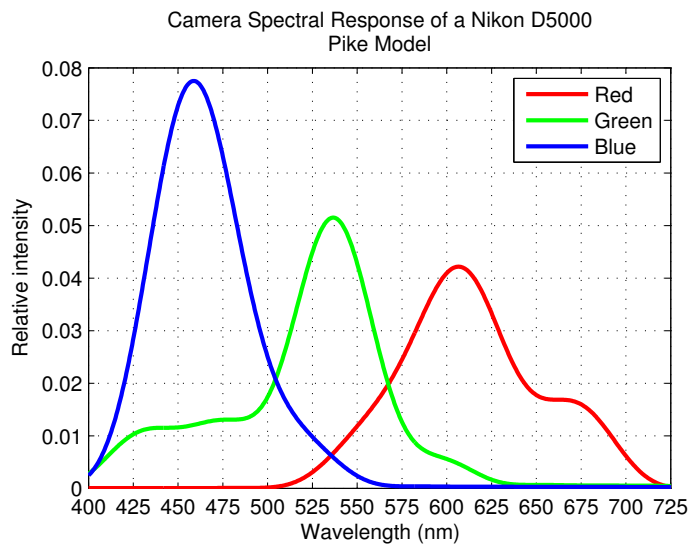


Figure 3.21 – Spectral response curves generated using the *Pike* method[155]

The spectral relationships between the spectrometers was calibrated for in Section 3.3. Then finally the spectral sensitivities of an RGB camera was established using a LVEF in Section 3.4 with the characterisation of a LVEF covered in Section 3.4.2.1.

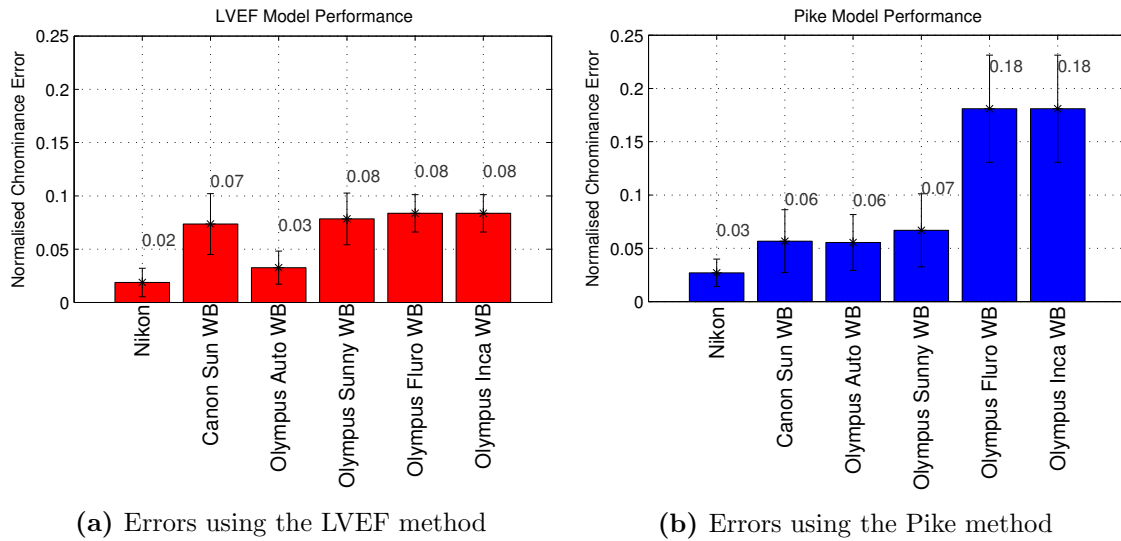


Figure 3.22 – Chrominance RGB reproduction error for the LVEF and Pike methods for the different cameras and white balances. The error bars define the magnitude of the standard deviation. Note: Nikon error has been scaled from 16bit to 8bit for comparative purposes.

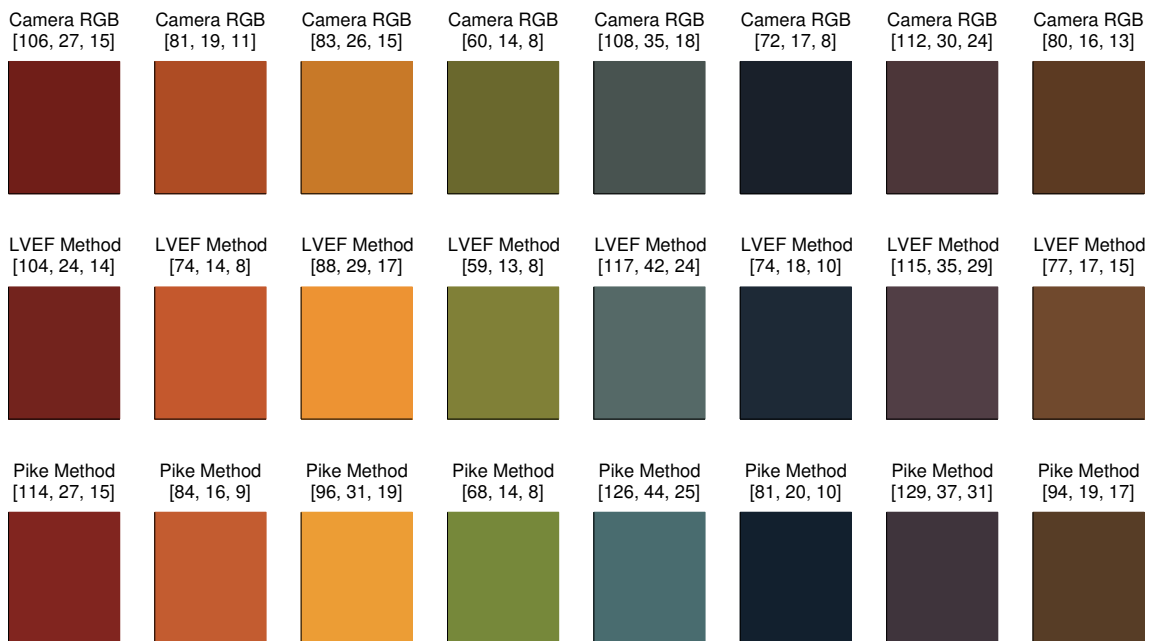


Figure 3.23 – RGB reconstruction from spectral measurements of Colour Swatches. The top row is the swatch as seen by the camera, these are the truth measurements; the reconstruction process is attempting to create a RGB coordinate as close to what the camera would image. The second row is the RGB reconstruction using the model generated by the LVEF method and the 3rd is the RGB reconstruction using the model generated by the Pike method. Above each swatch is the RGB coordinate of the swatch.

Rotation (# turns)	Translation (mm)	Wavelength Peak (nm)	Transmission (%)
0.0	0.00	369.09	-
0.5	0.89	375.78	-
1.0	1.96	382.47	-
1.5	3.02	389.16	-
2.0	4.09	395.84	32.51
2.5	5.15	402.53	36.01
3.0	6.22	409.22	40.08
3.5	7.28	415.68	42.34
4.0	8.34	421.69	44.63
4.5	9.41	429.09	46.09
5.0	10.47	434.65	47.86
5.5	11.54	441.61	49.26
6.0	12.60	449.04	49.43
6.5	13.67	455.56	50.91
7.0	14.73	462.54	51.18
7.5	15.80	469.54	50.95
8.0	16.86	476.55	51.86
8.5	17.93	483.56	52.06
9.0	18.99	491.05	52.65
9.5	20.06	497.62	53.35
10.0	21.12	504.66	53.30
10.5	22.19	511.71	54.14
11.0	23.25	518.77	53.93
11.5	24.32	525.37	54.06
12.0	25.38	532.44	54.02
12.5	26.45	539.06	53.75
13.0	27.51	546.62	54.27
13.5	28.58	552.78	54.45
14.0	29.64	559.88	54.49

Table 3.3 – The results for the fine resolution characterisation of the LVEF. It shows the wavelength of the passband peak as well as the transmission of the filter for that translation along the LVEF.

Rotation (# turns)	Translation (mm)	Wavelength Peak (nm)	Transmission (%)
14.5	30.71	567.00	54.53
15.0	31.77	573.65	55.00
15.5	32.84	580.30	55.11
16.0	33.90	587.44	55.11
16.5	34.97	593.64	55.31
17.0	36.03	600.79	55.75
17.5	37.10	607.95	55.85
18.0	38.16	614.64	55.77
18.5	39.23	621.33	54.17
19.0	40.29	628.51	54.38
19.5	41.36	635.22	53.89
20.0	42.42	641.46	54.38
20.5	43.49	648.66	54.53
21.0	44.55	655.39	54.95
21.5	45.62	662.12	55.01
22.0	46.68	668.86	55.44
22.5	47.75	675.60	55.52
23.0	48.81	681.87	55.63
23.5	49.88	688.14	55.83
24.0	50.94	694.90	55.81
24.5	52.01	700.70	55.80
25.0	53.07	706.50	56.11
25.5	54.14	712.30	56.50
26.0	55.20	717.63	56.67
26.5	56.27	723.93	55.97
27.0	58.40	730.23	56.29
27.5	60.52	735.56	55.66
28.0	62.65	737.02	20.24

Table 3.4 – The results for the fine resolution characterisation of the LVEF continued from Table 3.3. It shows the wavelength of the passband peak as well as the transmission of the filter for that translation along the LVEF.

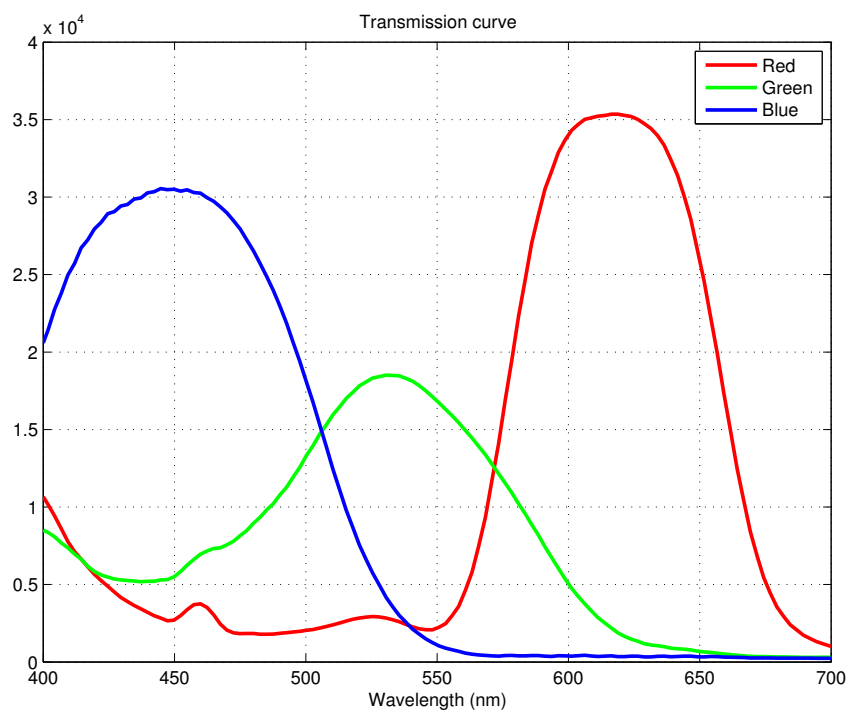


Figure 3.24 – Spectral response curve for the Colour camera onboard Sirius AUV

Chapter 4

In-situ water corrected imaging



4.1 Introduction

In the previous chapter the spatial calibration was presented for a spectrometer. Knowing the spatial sensitivity allowed the spectrometer to be used as a very poor spatial resolution imaging camera. The spatial co-registration of the spectrometer with a Red-Green-Blue (RGB) camera was shown as well as a method for determining the spectral sensitivities of a RGB camera.

The main aspect of this chapter is the correction of underwater imagery from a traditional imaging camera and a hyperspectral sensor. A method for correction is developed which uses an empirically derived model of the optical properties of the water. Correction occurs through an inversion step which shall be detailed. The method is first presented for the

correction of RGB imagery. It is demonstrated in a controlled test tank first where the correction process is validated with chromatic comparison to ground truth. It is then applied to imagery taken in an outdoor underwater scene where the depth, target scene and environmental factors are controllable.

Finally the method is implemented on data from an Autonomous Underwater Vehicle (AUV) mapping mission. The AUV mission was over real world coral reef scenes. In this setting it was possible to generate a dynamic water model through the continuous use of the upwards looking spectrometers. The correction of imagery from an AUV differs from the previous scenarios because the AUV uses a stereo camera which provides scene structure information as well as the vehicle also carries strobe lights for additional illumination.

The reason for performing the proposed methodology in three different locations was for ease of validation. Obtaining ground truth for the AUV imagery is very hard due to the depths and rough open ocean environments the vehicle is operating in. Conversely this was easy with the test tank and the outdoor swimming spot environment.

The last aspect of this chapter covers the correction of spectral reflectance data. Hyper-spectral data comes from the spectrometer within the imaging module. Spectral reflectance is recovered after water correction and scene illumination modelling. Results are presented for a coral reef mapping mission. The correction of the RGB imagery and the spectral data allows for the training of a classifier and the generation of a benthic map. This will be discussed further in the next chapter.

4.2 Environmentally based colour correction

In this section a new method is presented which uses a model of the water to correct the colour in RGB imagery. The current colour correction techniques were reviewed in Section 2.4. Most techniques rely on various assumptions about the environment, such as assuming that the mean colour of an image is grey, as in the Greyworld colour correction technique, that the lighting is homogeneous over time [68] or that scene structure is flat [19]. These are poor assumptions as the colour channels will not always be balanced (as when imaging colourful coral [132]) and the environmental lighting will not remain constant as weather and time of day influence the intensity and spectral profile of the solar radiance [115]. In addition, the underwater scene will have some form of structure. Even in the case of a flat

scene the path length from scene to camera frame will be longer for the edges of the image compared to the center [38].

Other methods are too simplistic due to their assumption of homogeneity of the water conditions [200]. These methods performed well in controlled and predetermined conditions, but would not work well in applications of varying optical properties such as in the case of a moving AUV.

New techniques have been presented which gather the optical properties of the scene by utilising 3D structure information from multiple viewpoints of a scene point, from which the imagery is corrected on a very fine spatial scale and allows for changing lighting conditions [38]. This technique however only gathers the optical properties of the water in the trichromatic domain. By sensing in the hyperspectral domain this could allow the data to be used in applications such as ground-truthing above water hyperspectral imaging, and deriving various levels of biological constituents from within the water column [15].

In this section the methodology will be presented first. This will show the technique for measuring and removing the attenuation effects of the body of water. After the methodology some details on the assumptions made in the methodology are presented. The experimental setup for the first colour correction experiment is detailed, this is proceeded by the results for this experiment. The proposed method is repeated for a real world experiment conducted outside in a local ocean swimming area. After the results for the test tank and the real world experiments are presented a method for evaluating the performance and validation of the proposed technique is shown. Lastly an extension of the colour correction technique is presented using imagery taken onboard an AUV with results presented from a coral reef survey mission.

4.2.1 Methodology

The water model presented in Section 2.2.2 is used and is translated for use in the RGB domain. This is not a trivial task as the RGB cameras have varying sensitivities to the different wavelengths of light, and their response is unknown. In Section 3.4 a new calibration technique was shown for obtaining the spectral sensitivities of RGB cameras. This calibration provided the translation from the hyperspectral domain into the trichromatic domain.

To parametrise the water model, irradiance measurements were obtained with a spectrometer looking upwards just below the surface and also facing upwards at a known depth; from these measurement the downwelling attenuation coefficient K_d of the water column can be derived using the rearranged Beers law Equation (4.1) and reproduced here:

$$K_d(\lambda) = -\frac{1}{d} \log_e \left(\frac{E_\delta(\lambda)}{E_s(\lambda)} \right) \quad (4.1)$$

where: $E_\delta(\lambda)$ is the irradiance with respect to wavelength λ at depth δ , $E_s(\lambda)$ is the irradiance just below the surface, $K_d(\lambda)$ is the wavelength dependant diffuse downwelling attenuation coefficient for the water.

After determining the attenuation coefficient the incident irradiance at a different depth d can be modelled using the Lambert-Beers equation for attenuation through water Equation (2.1).

A chromatic transfer function τ describing the light from the surface changes for a given depth of water at a fixed point in time:

$$\tau(\lambda) = \frac{E_s(\lambda)}{E_d(\lambda)} \quad (4.2)$$

where the transfer function $\tau(\lambda)$ at wavelength λ is defined as the ratio of the irradiance at the surface E_s to the irradiance at the bottom of the tank E_d (this is also defined as the irradiance at the scene, where the scene is at the bottom of the tank). The irradiance at E_d may be unknown if measuring E_δ above the scene. So E_d may be modelled from:

$$E_d = E_\delta e^{K_d(\delta-d)} \quad (4.3)$$

This transfer function exists in the discrete frequency domain. In order to convert the hyperspectral transfer function to the RGB domain the following is used:

$$\tau_b = \sum^k \tau(\lambda_k) C_b(\lambda_k) \quad (4.4)$$

where the weighted RGB transfer function is τ_b for colour band b where the colour bands are

Red, Green & Blue, $C_b(\lambda)$ is the camera spectral characteristic function for colour band b , k is the number of discrete wavelength bands of the camera spectral characteristic function.

To correct the colour in the underwater image the image bands are multiplied by their respective weights as gathered from the transfer function in Equation (4.4).

$$I_{CC}(b) = I_{UC}(b)\tau_b \quad (4.5)$$

Where $I_{CC}(b)$ and $I_{UC}(b)$ are the colour corrected and uncorrected colour images for colour band b (RGB) respectively.

Given this transfer function describing the selective attenuation of light through water, our objective is to estimate the parameters of the model from a set of observations. The next section outlines some of the assumptions which were made in developing the water modelling methodology. The remainder of this section outlines the method used to validate this model.

Methodology assumptions

The water model is parametrised by measuring the downwelling light at E_s and E_δ . The light at the scene E_d (bottom of the tank) is interpolated from the water model. An accurate estimate of E_d is based on the assumption that the optical properties of the last section of water between E_δ and E_d (interpolated section) is the same as the measured section between E_s and E_δ . The validity of this assumption will vary with several factors.

As the ratio between the distance of the interpolated section to the distance of the measured section decreases the errors are assumed to reduce. This intuitively makes sense as the region which is being interpolated is getting smaller in proportion to the measured section. Depending on the clarity of the water and the location of sampling, there can be stratification of the particles within the water column [15]. These considerations need to be taken into account when using the water model. A possible method for assessing the degree of stratification would involve examining the upward looking spectrometer data as the system descends through the water column to the working depth. One might see if any layers are present, however the stratification measurements would only hold for that

location at that one point in time. If the imaging platform were to move large distances assumptions would need to be made as to the horizontal extent of the stratification layer.

In the latter section of this chapter, the water model is generated from the in-situ system mounted on an AUV. The water column was found to be quite uniform when mapping in the tropical reef area. To measure the amount of scattering in the water column a turbidity meter (nephelometric turbidimeter) was used. A turbidity meter measures scattered light using a light source at 850nm and a photomultiplier at 90° to the beam angle. The units of a turbidity meter are nephelometric turbidity units (NTU) which are measured relative to an artificial standard with reproducible light scattering properties [115]. Several turbidity profiles of the water column were made at the survey sites during AUV missions over the Great Barrier Reef (GBR). The turbidity meter was calibrated prior to use. The calibration was done with turbidity standards of 100NTU and 20NTU¹. The instrument used was a Turner Designs C6 system².

Figure 4.1 shows the turbidity profile measurements for 6 different sites. It shows depth vs turbidity reading in NTUs. For most of the sites turbidity was approximately 6 NTU. This is quite clear water, an example of the water clarity for 3.2 & 13.0 NTU is shown in Figure A.3 & A.4.

A limitation of the proposed method is only the downwelling attenuation coefficient K_d is derived. K_d encapsulates both the scattering and absorption of the water column. This carries two limitations, as it is an apparent optical property, the measurement is generally only valid for the location and light field at the time of acquisition. This is not a problem for the purpose of colour correcting imagery taken at that location and time. Using K_d for future or past corrections at different locations would require some assumptions to be made about homogeneity of the water column's optical properties and light field structure. This leads to the second limitation: other water models may require scattering and absorption to be separate. As the scattering and absorption coefficient are encapsulated in K_d , feeding the optical measurements into an external model could be challenging. So this can restrict the external use of these water measurements. There have been methods for inverting K_d to recover the inherent optical properties of scattering and absorption (a & b), however these require further measurements of the materials within the water column [140].

¹Hach StablCal Turbidity standards

²Turner Designed C6 multi-sensor platform

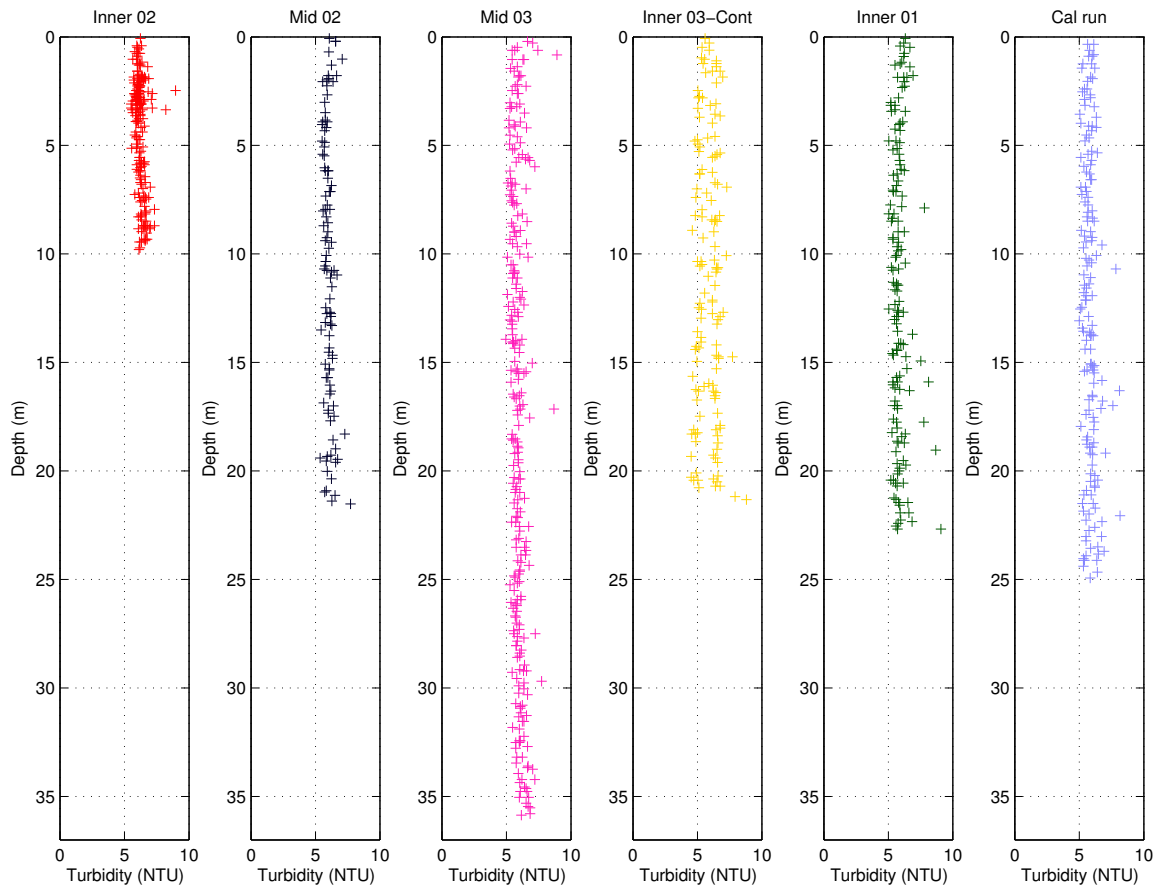


Figure 4.1 – Turbidity measurements for 6 different sites over the glsgbr. It shows a uniformity for most of the water column. NTU - Nephelometric Turbidity Units

4.2.2 Test tank experimental setup

The first validation was performed under controlled conditions in a test tank. This allowed aspects of the model, such as illumination, distance between the scene and the camera and the depth of the spectrometer to be precisely controlled. The setup involved a spectrometer, an underwater camera (Olympus μ Tough 8000), a 1.77m test tank filled with chlorinated/salt water, a MacBeth Colour target and a photographic broad spectrum lighting rig. The test tank was non-transparent and was painted with a matte / non-reflective paint. The room which housed the tank was dark with the only light coming from the experiments light source. The spectrometer used was an Ocean Optics STS-VIS Microspectrometer with $100\mu\text{m}$ slit width, and a spectral range of 350-800nm. The spectrometer was mounted in an underwater housing. The spectral response function of the RGB camera was gathered using the Linear Variable Edge Filter (LVEF) method presented in Section

3.4. The experimental setup is shown in Figure 4.2.

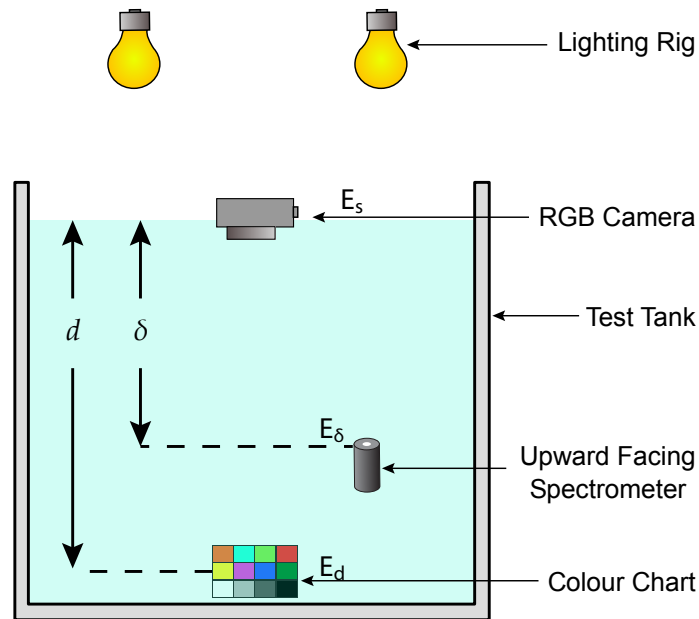


Figure 4.2 – The equipment setup for the test tank experiment

4.2.3 Test Tank Results

The uncorrected image of the MacBeth Colour Chart is shown in Figure 4.4a. The irradiance was measured just below the surface and again at 1.51m with the upwards looking spectrometer. From these measurements the attenuation coefficient of the water in the tank was obtained using Equation (4.1). Then the irradiance was modelled at the bottom of the tank at 1.77m using the Equation (2.1). Figure 4.3 shows the surface and 1.51m lighting spectrum, and the predicted bottom irradiance. From this figure it can be seen quite clearly that the light in the red end of the spectrum ($> 600nm$) has been heavily attenuated. The light energy in the other regions such as green ($500nm - 600nm$) and blue ($400nm - 500nm$) has been reduced but not nearly to the same degree. A transfer function was generated for the light over all the wavelengths using Equation (4.2). The transfer function is then converted into the RGB colour space of the camera Equation (4.4). This process then allowed for the image of the target to be corrected using Equation (4.5).

Using the presented technique the results for colour correction of the test tank imagery are shown in Figure 4.4.

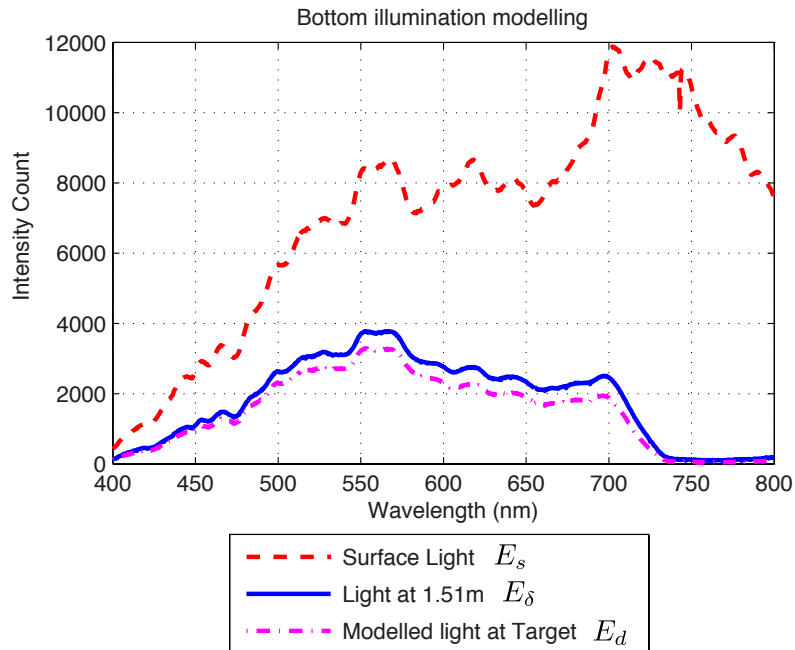


Figure 4.3 – The prediction of the illumination on the bottom of the tank based on the surface and 1.51m measurements. The integration time of the spectrometer was kept constant for both the surface and the 1.51m measurement.

4.2.4 Real-world experimental setup

A local ocean swimming area was used for testing the proposed method in a real world situation. In this situation depth and target could be controlled. In Clovelly, Sydney, Australia (-33.915° , 151.268°) there is a sheltered tidal bay which contained a few typical benthic substrates including rock, sand, algae and seagrasses. Measurements were taken at approx. 13:00 on 28 March 2013 the sun was approximately at a angle of: zenith = 36.9° , azimuth = 0.0° [172].

A methodology similar to that used in the test tank was used, except that a cosine corrector³ was used on the end of the spectrometer to reduce the sensitivity to angle variance of the measurements. It allowed for collection of the hemisphere of sky/sun light. The colour target used was an *Amphibico - Underwater Colour Bar*⁴. This was used instead of the Macbeth colour chart as it was water damaged in a previous experiment.

³Ocean Optics CC-3 Cosine Corrector: <http://www.oceanoptics.com/Products/cc3cosinecorrectors.asp>

⁴<http://www.amphibico.com>

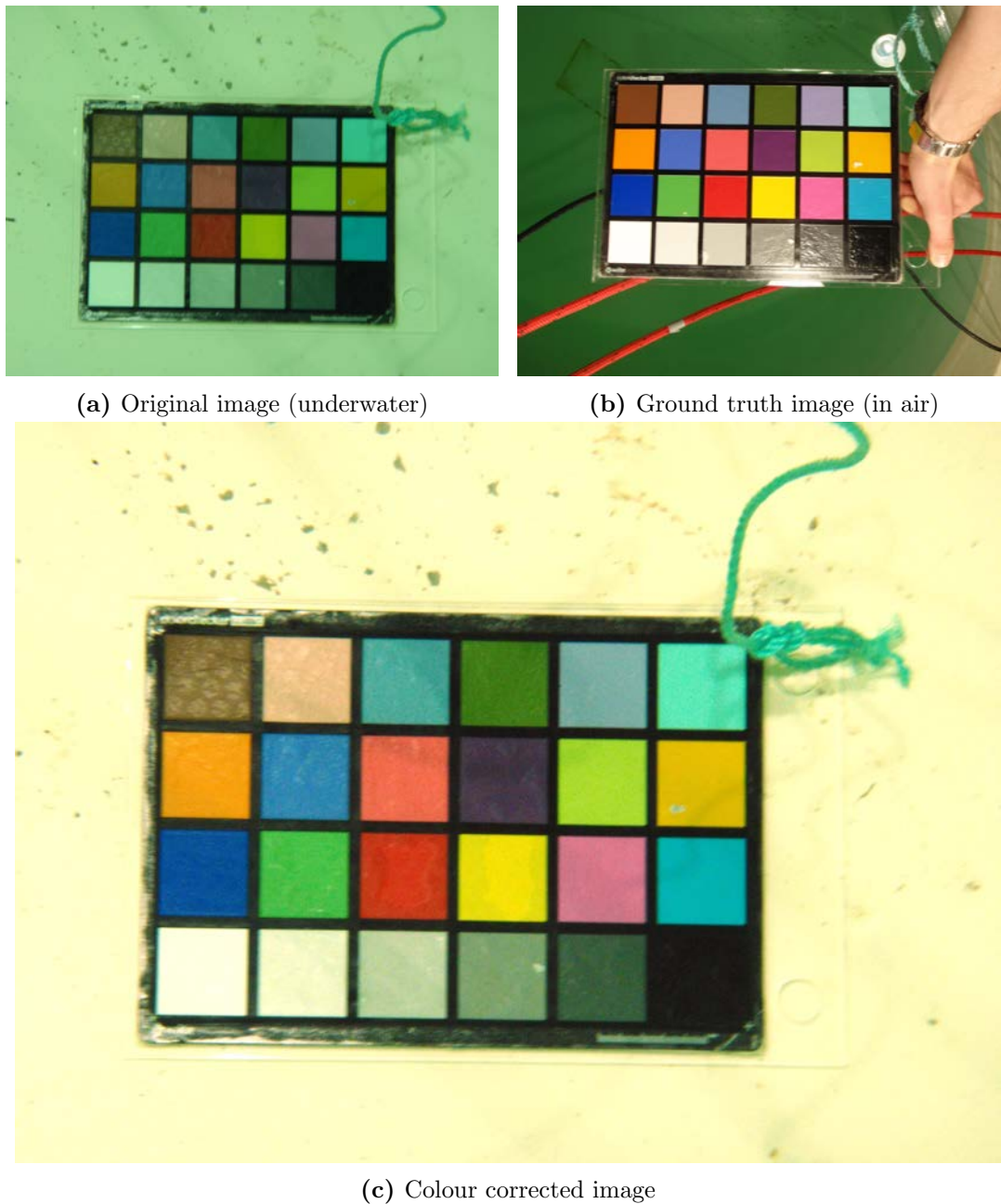


Figure 4.4 – Results of colour correction method (a) This image was taken at the surface of the test tank looking down at the MacBeth colour chart on the bottom of the tank at a depth of 1.77m, (b) the MacBeth colour chart - ground truth image: photo taken out of water under the same illumination, (c) The colour corrected image of the MacBeth colour chart in the test tank after using the proposed technique.

4.2.5 Real-world Results

The results from the data collected at Clovelly are shown in figures 4.6 and 4.7. The downwelling irradiance measurements (Figure 4.5) show the irradiance for the spectrometer at the surface, 67cm, 1.55m and the modelled irradiance at 1.77m. It can be seen from this graph that the light energy in the reds ($> 600nm$) drops off quite quickly underwater similar to what was seen in the test tank.

The camera was set to a fixed ISO and white balance was set to *Sunny*. This was consistent with the spectral sensitivity calibration shown in Section 3.4.3.2. The result from the colour correction will still look like it was taken using the same white balance just without the water. Using the Sunny white balance results in a slight chromatically warmer than expected result in the corrected imagery.

The colour correction performs quite well despite the green water. The cloudiness of the water does result in some blurring within the images. There are also some large water particulates which can be seen in the pictures. The performance of the colour correction is shown in the next section.

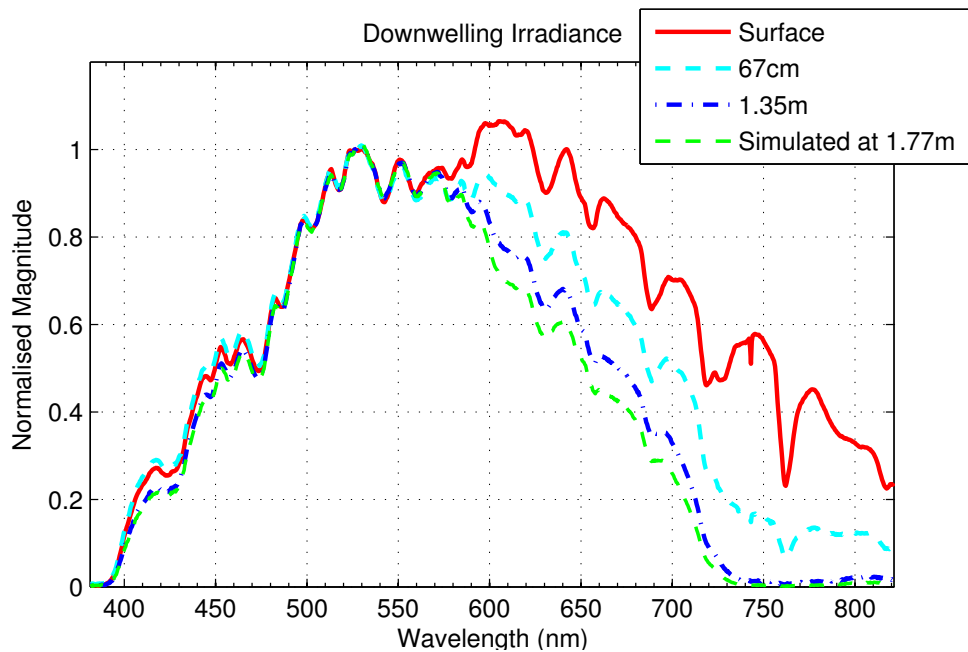


Figure 4.5 – Downwelling irradiance measurements from real-world results. The curves have been normalised about the peak in the green at 526nm.

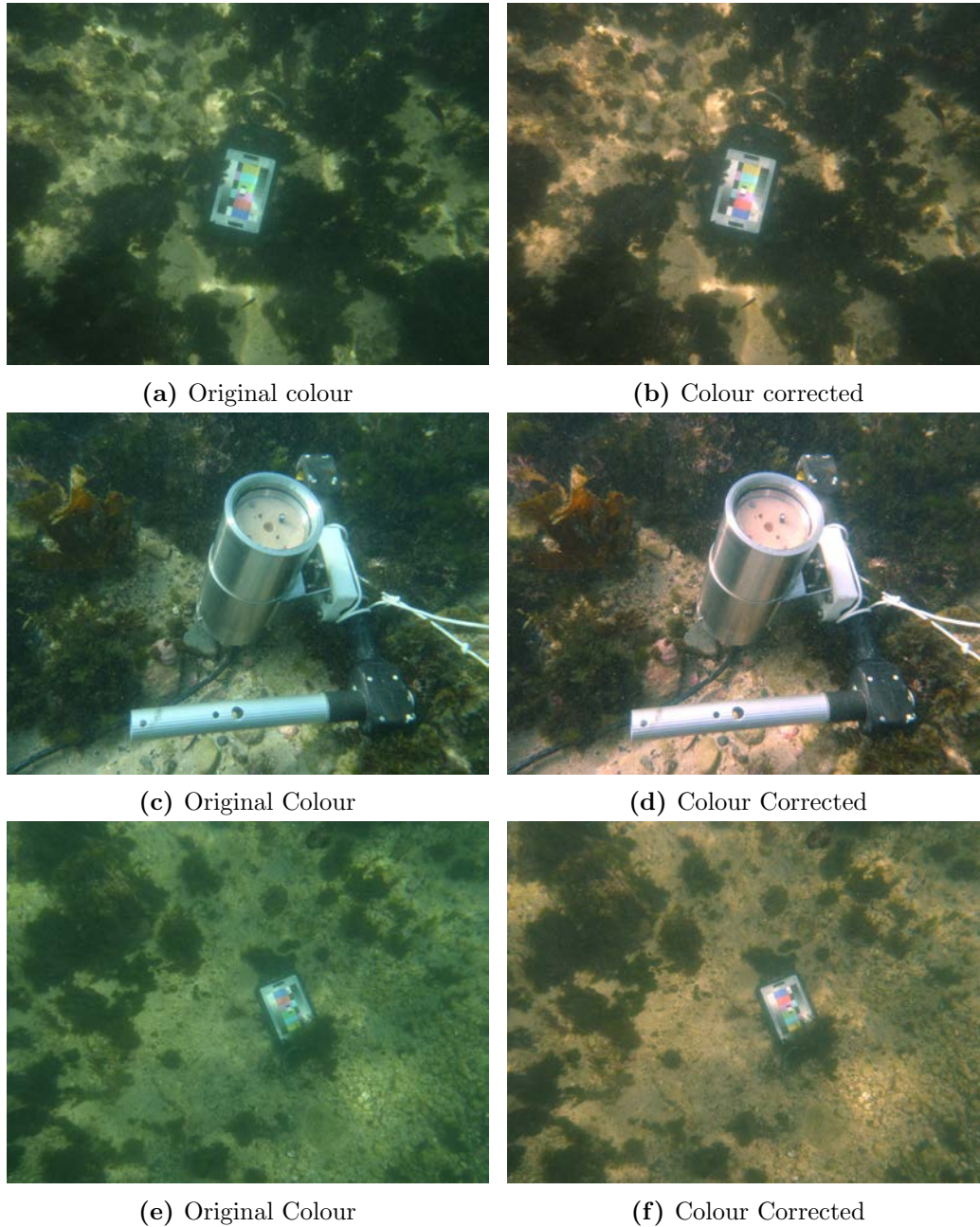


Figure 4.6 – (a) & (b) This image was taken at the surface of the water looking at a colour target at a depth of 1.4m. (c) & (d) were at a depth of 1.55m. (e) & (f) were at a depth of 1.77m

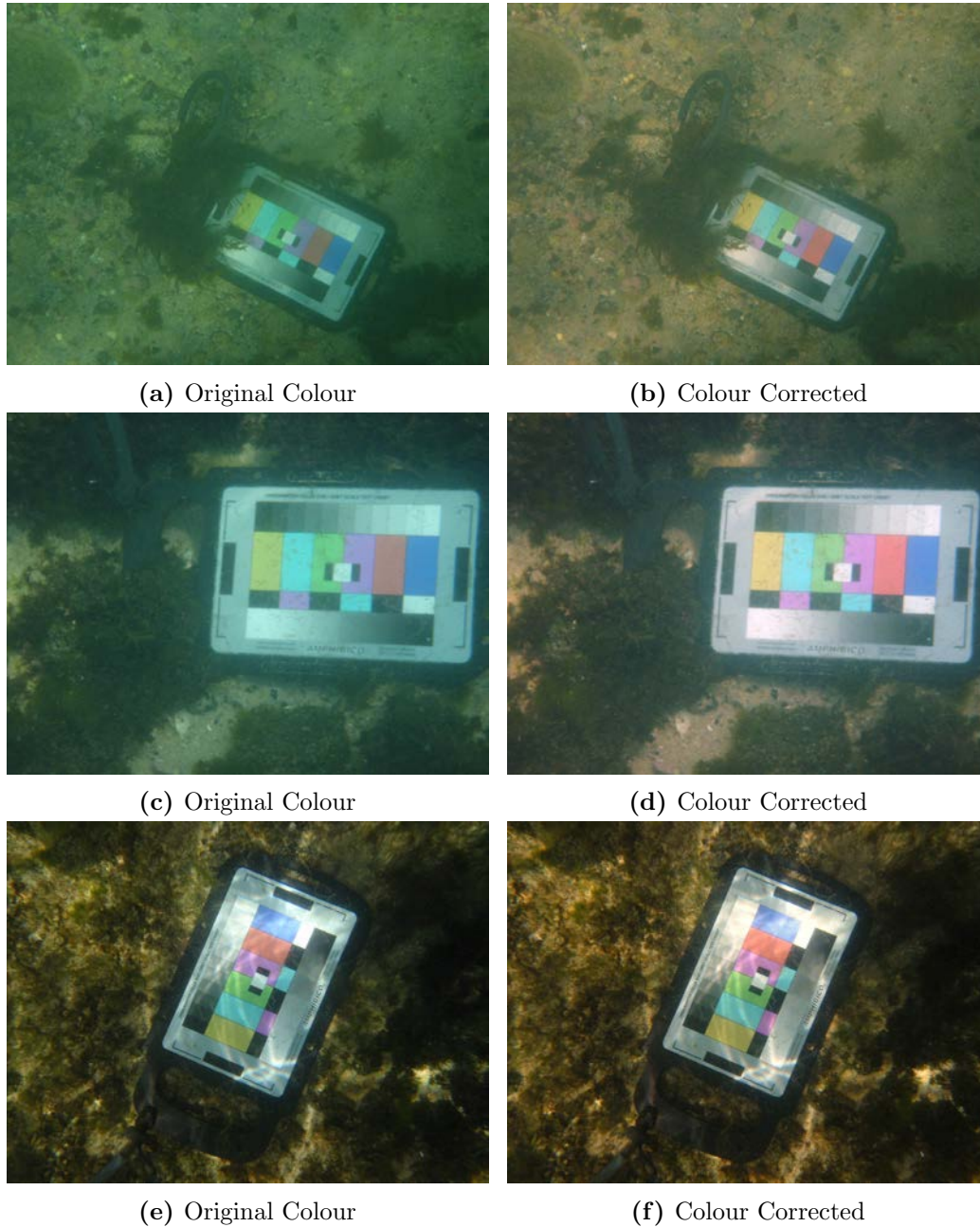


Figure 4.7 – (a) & (b) This image was taken at the surface of the water zoomed in looking at a colour target at a depth of 1.77m. (c) & (d) were at a depth of 1.55m. (e) & (f) were at a depth of 67cm.

4.2.6 Performance Evaluation

To establish the performance of the colour correction method several swatches of the colour target were compared in the corrected underwater image with the same swatches from a picture of the colour target taken out of water (ground truth) but shot with the same ISO, white balance and under the same illumination.

Most cameras will implement some form of auto-exposure (AE). AE will meter the light level in the scene and adjust the exposure time to maximise the Signal-to-Noise Ratio (SNR) and will aim to minimise over exposing the image. Light from a scene can be broken down into two components, the intensity of the reflected light from the scene and the chrominance. For the evaluation of the correction of colour in the RGB domain, changes or errors in intensity are less of interest but rather just the chromatic component of objects. In latter sections, correction of the spectral reflectance is performed where the absolute radiometric quantities are necessary and are evaluated.

The performance of the colour correction technique is first demonstrated visually by showing a crop of the patches of the colour charts. These show the original uncorrected colour, the colour corrected result using the proposed technique and the ground truth.

To minimise the differences in intensity due to AE, each of the images were normalised based on the black and white squares on the colour chart. Consideration was taken to ensure the normalisation process did not over expose the colours. The first metric to evaluate performance was looking at the colour error between corrected and ground truth for the same colour patch. The colour error was defined as the absolute difference between the RGB values of the respective patches and channels. The mean error for each colour channel is plotted against the standard deviation for each pixel in the corresponding patch (colour corrected to ground truth). This allows us to see which colours are being corrected the best as well as the variance of the measurements.

The next analysis is conducted using a chrominance only metric. To do this the RGB values are converted to the CIE $L^*a^*b^*$ colour space. In this colour space L^* defines the lightness of the colour, where $L^* = 0$ is black and $L^* = 100$ is diffuse white. Then the two chrominance channels define the following: a^* - defines the colours green to magenta and b^* - defines the colours blue to yellow. In this colour space the error for a^* and b^* between the corrected result and the ground truth is evaluated. These errors are plotted a^* versus

b^* to show which patches and colours perform best.

4.2.6.1 Test tank performance

A qualitative validation of the colour correction method for the test tank experiment is done first. The results are compiled into Table 4.1. The first observation of the uncorrected patches is they are particularly green. The red and yellow patches are almost indistinguishable from the green patches. Blue patches are quite similar between the original colour and the ground truth. Visually the colour correction has performed very well, the corrected patches appear to be quite similar to the ground truth. Some patches such as Brown (no. 1), Skin (no.2), Foliage (no. 4), blue flower (no. 5), Purple (no. 10) and Magenta (no. 17) appear to be chromatically similar but appear slightly too light or too dark.

The next analysis technique is using plots of the error versus standard deviation for each colour channel. This is shown in Figure 4.8. First the Red channel is examined. We would expect this channel to have the largest errors as the water distorts the red channel the most. The largest errors are seen with patches 10, 6, 5, 17. This confirms some of the distortions observed visually from Table 4.1. The standard deviations of the patches is not very high despite some obvious texture in the images.

In the other channels (green and blue) there are some stand out errors. Patch 1 in both the green and blue has a large error and variance. This is due to the texture features on the patch. A texture variance is also seen in Patch 8 with white areas causing errors in all channels. As validation that the colour correction is performing equally across the colour channels the mean and standard deviation of the errors is taken for each colour channel. The error is shown for before and after colour correction. This is shown in Table 4.2. It can be seen that the mean error for the corrected patches are essentially the same, with very similar standard deviations, unlike the uncorrected error. So this implies the correction process is not favouring one colour channel over another. A correction process which was not performing correctly would have a bias on one of the colour channels in this analysis. The colour bias can be seen in the same table under uncorrected mean error. There is a large red error with a moderate blue error. This is implying that the image should have a green bias due to the large errors in red and blue. This is visually confirmed by examining the uncorrected image or patches. The image has quite a green colour cast. This is due to

how this particular (rather green) water body is attenuating the light. This highlights that different water bodies require different attenuation models. Being able to measure these models in-situ allows for this adaptability.

To examine the errors in a chrominance only colour space, the patches are converted to the $L^*a^*b^*$ colour space. The errors in a^* versus b^* (just denoted a & b) are plotted in Figure 4.9. The same patches (no. 6, no. 1, no. 5, no. 10 and no. 17) show up as performing the worst, confirming the analysis in the RGB colour space.

4.2.6.2 Real-world performance

In this section the performance of the real world (Clovelly) colour correction dataset is discussed. The full colour corrected images are shown in Figures 4.6 & 4.7. Tables 4.3 - 4.5, show the uncorrected patch, the corrected patch using the proposed correction method and the ground truth patch. Qualitatively it can be seen from the patch tables that the correction process has performed quite well. In particular the correction shown in Figure 4.7f and Table 4.4 was for imaging the target at a distance of 1.77m. The original has a very distinct green colour bias. The correction fixes this quite well. The correction shown in Figure 4.7b and Table 4.5, appears to have the correct colour but the patches are distorted by caustics. This should be taken into account when viewing the numeric results. One advantage of the proposed colour correction method is it does not use a colour chart for the correction process and thus is not distorted by optical effects such as caustics.

To evaluate the performance quantitatively, the error in RGB colour space is first examined. The mean error versus standard deviation for the Clovelly results is shown in Figure 4.11. First thing to note is the standard deviation is much larger on all channels than was seen in the test tank results. This is due to the texture of the colour board creating small variations in the reflected colour. The other reason, as just mentioned, is the presence of caustics and particles in the water creating local image texture variations on the sampled patches.

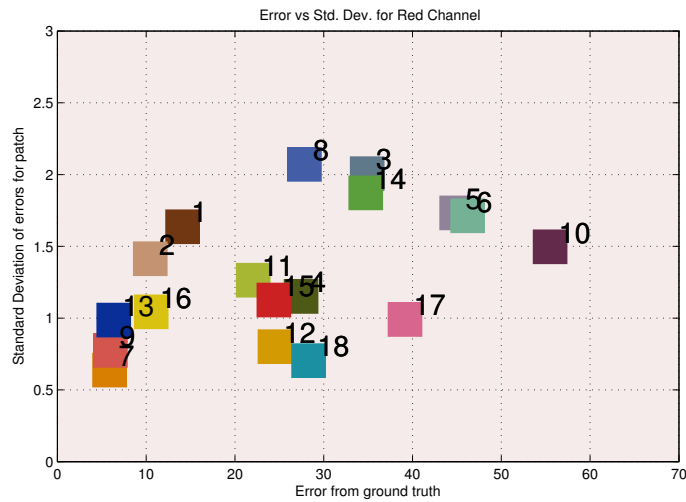
Examining the RGB error charts (Figure 4.11), it can be seen that patches 1, 9, 11, 12, 13, 14 have relatively large errors after the corrections. These same errors are reflected in the $L^*a^*b^*$ colour space plot shown in Figure 4.12. These errors can be largely attributed to the mentioned environmental effects of imaging in an outdoor underwater environment. Establishing clean performance metrics in this dynamic environment is challenging.

<i>Patch Index</i>	1	2	3	4	5	6
<i>Original Colour</i>						
<i>Colour Corrected</i>						
<i>Ground Truth</i>						

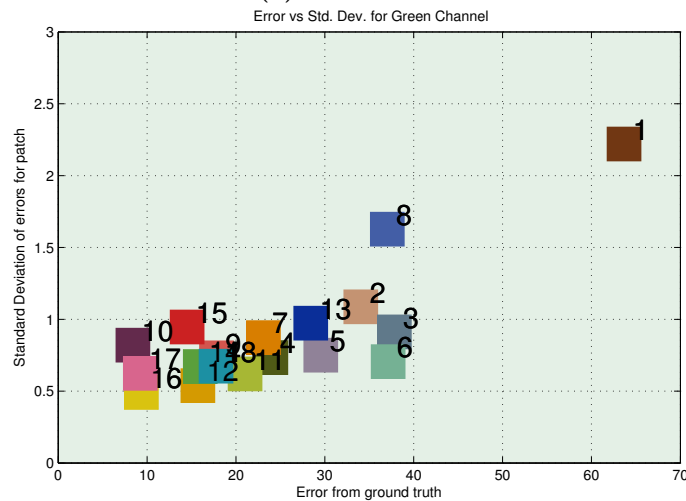
<i>Patch Index</i>	7	8	9	10	11	12
<i>Original Colour</i>						
<i>Colour Corrected</i>						
<i>Ground Truth</i>						

<i>Patch Index</i>	13	14	15	16	17	18
<i>Original Colour</i>						
<i>Colour Corrected</i>						
<i>Ground Truth</i>						

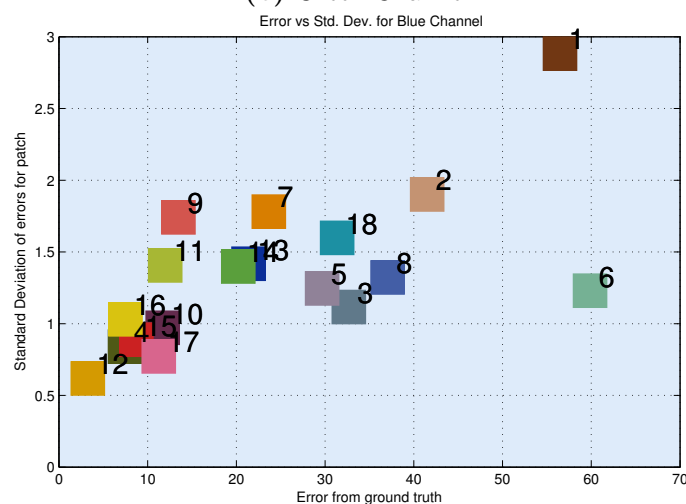
Table 4.1 – The performance of the colour correction for the test tank result (Figure 4.4) in the RGB colour space. The top row shows the uncorrected patch (underwater image), second row the corrected patch using the proposed correction method, and the third row are the patches from the ground truth image taken in air. The ground truth was taken from a picture of the target panel out of water but under the same illumination. The colour chart was laminated and this can be seen in patch 1 as small circle on the swatch. This would have resulted in high patch error variance, the influence on the other patches appears minimal.



(a) Red Channel



(b) Green Channel



(c) Blue Channel

Figure 4.8 – Each scatter plot is for analysis of a different colour channel. Each scatter plot shows error versus standard deviation. Error refers to the distance in 8-bit RGB colour coordinates between the ground truth and the colour corrected panel for the respective colour channel. The standard deviation refers to the deviation of the errors for a patch, with units again in 8-bit colour coordinates. An ideal correction would be placed close to the bottom left corner (0,0). The numbers on the plots correspond to the respective patch in Table 4.1.

	Corrected Mean Error	Corrected Std.Dev. of error	Uncorrected Mean Error	Uncorrected Std.Dev. of error
Red	25.7	15.0	87.6	37.2
Green	24.7	13.8	19.4	12.7
Blue	23.8	16.8	37.2	23.6

Table 4.2 – This is a summary of the test tank colour correction performance in the RGB domain. It shows the mean RGB error for all colour swatches as shown in Table 4.1 and the standard deviation (std.) of the errors for each swatch. This validates the colour correction method. A good correction should have even colour errors across the colour bands (Red/Green/Blue).

Validation of the correction process for the 3 sets of 6 patches is shown in the Tables 4.6 - 4.8 respectively. In Table 4.6 it can be seen that there was a large red channel error and a very small green and blue colour error. The correction process equalised these colour errors, and as a result actually made blue and green worse on average (within the bounds of the standard deviation). Table 4.8 shows good performance in correcting the red channel errors and equalising the errors across the colour channels. The uncorrected errors as shown in Table 4.7 are the largest errors seen in the Clovelly dataset. Red is particularly distorted to a lesser extent so is blue. Green in contrast does not have distorted colour, this is confirmed in the imagery. The imagery has a green colour cast. The correction process does a good job of reducing these colour errors with the exception of green error which increases.

Overall the colour correction in the Clovelly dataset performs quite well given the variability of the environmental conditions. In the next section the same colour correction method is applied to data obtained onboard an AUV while conducting a survey mission of a coral reef shoal on the GBR.

4.3 Colour correction of AUV imagery

Two AUVs are operated at the *Australian Centre for Field Robotics (ACFR)*⁵; an IVER II AUV and a Woods Hole Oceanographic Institution (WHOI) Seabed class AUV (SIRIUS). The vehicle chosen for this work was the seabed class AUV (Sirius). A photo of the AUV is shown in Figure 4.13. A suite of sensors are installed aboard SIRIUS, such as a Doppler Velocity Log (DVL), Multi-beam Sonar, Wetlabs EcoPuck, GPS, Ultra-Short BaseLine

⁵<http://www.acfr.usyd.edu.au>

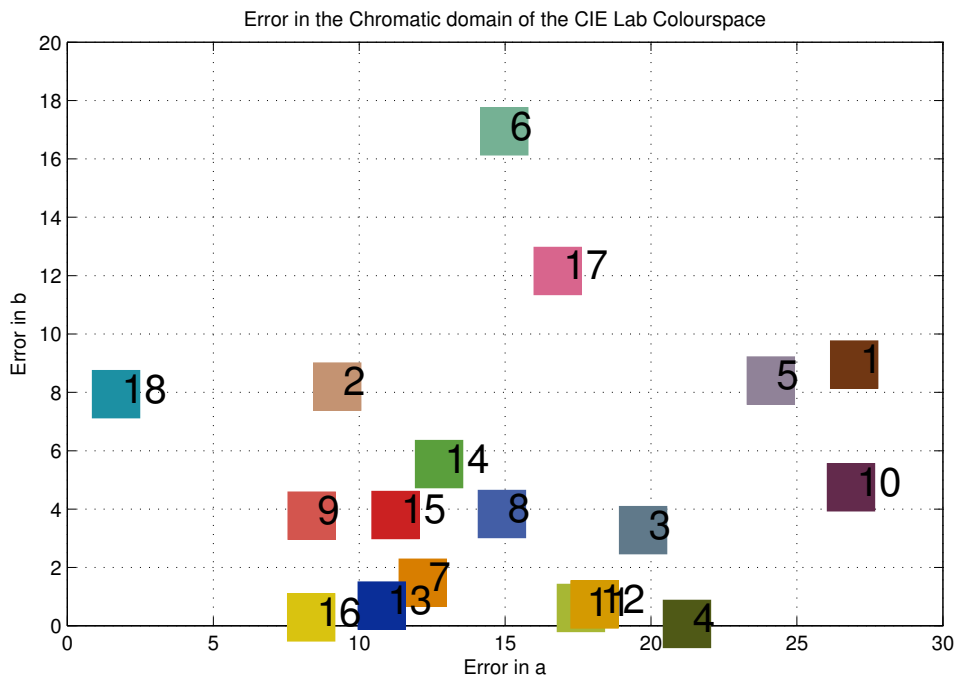


Figure 4.9 – This shows the chromatic error in CIE Lab colour space. The further from the origin the greater the chromatic error. The luminance channel (L) has not been shown as we wish to isolate just chromatic error.

(USBL), Conductivity/Temperature probe and a Stereo camera with Light Emitting Diode (LED) strobes for artificial lighting [204]. The AUV typically travels at 0.5m/s and aims to maintain an altitude of 2m from the seabed.

To further improve the colour correction, knowledge of scene structure is important. Three-dimensional depth maps were obtained from the stereo imagery. These depth maps give the distance of every pixel from the camera frame to the scene (see Figure 3.6). The water model can be used to correct the AUV images to be invariant of scene structure. Instead of correcting for a single distance as in the test tank (Section 4.2.2) and the real-world scenario (Section 4.2.4), each pixel can be corrected individually for its respective distance to the camera. This was only possible through the use of the stereo camera which provided structure information. This was unnecessary for evaluating the performance in the test tank and real world results as the colour target was in the middle of the camera’s Field-



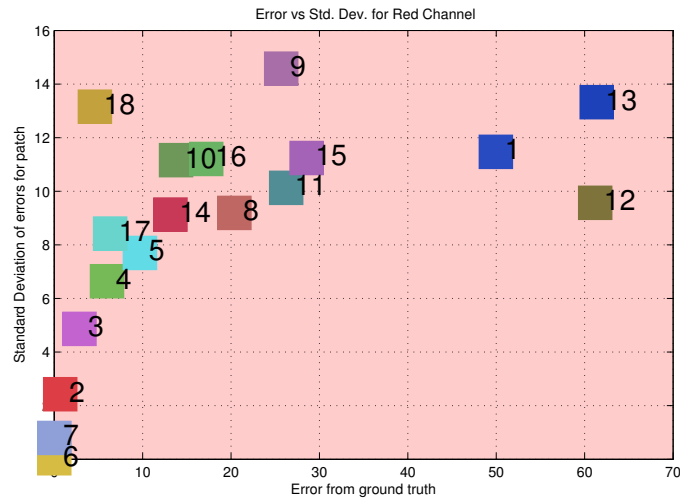
Figure 4.10 – This is the ground truth image for the real-world results, the image is taken under the same lighting, ISO and white balance as the underwater images.

<i>Patch Index</i>	1	2	3	4	5	6
<i>Original Colour</i>						
<i>Colour Corrected</i>						
<i>Ground Truth</i>						

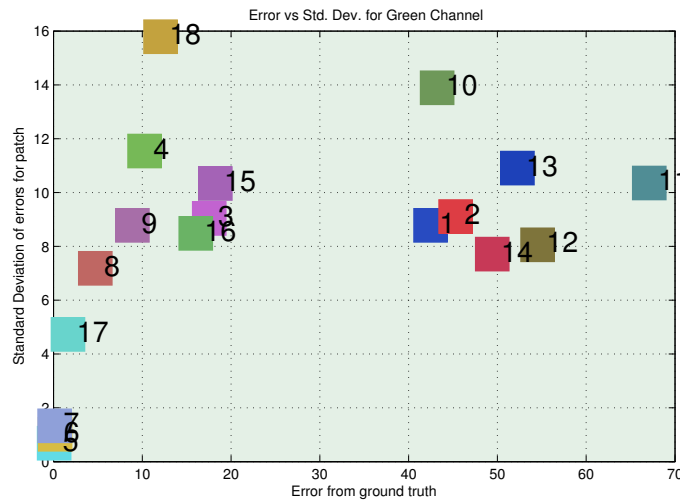
Table 4.3 – The performance of the colour correction for Figure 4.7d compared to the ground truth image (Figure 4.10) taken out of water under the same lighting, ISO and white balance.

of-View (FOV) and the distance was measured from the camera to the colour target. In addition to compensating for scene structure, vignetting is also taken into account using the cosine-fourth rule [111]. A comparison is done qualitatively against the greyworld method for colour correction.

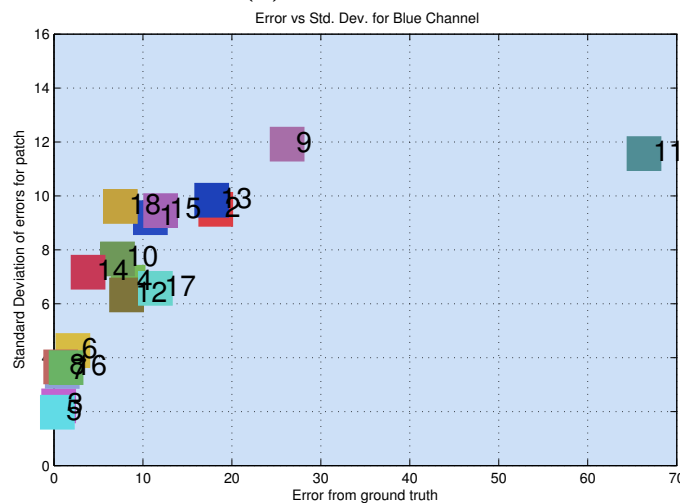
For the proposed system a series of spectrometers were installed aboard the AUV and on the support surface vessel. Figure 4.14 shows the positioning of these spectrometers. The two upward looking spectrometers collect the downwelling irradiance at two different locations; on the surface before the light enters the water (support vessel mounted) and as the surface



(a) Red Channel



(b) Green Channel



(c) Blue Channel

Figure 4.11 – Each scatter plot is for analysis on a different colour channel. Each scatter plot shows error versus standard deviation. Error refers to the distance in 8-bit RGB colour coordinates between the ground truth and the colour corrected panel for the respective colour channel. The standard deviation refers to the deviation of the errors for a patch, with units again in 8-bit colour coordinates. An ideal correction would be placed close to the bottom left corner (0,0). The numbers on the plots correspond to the respective patch in Tables 4.3 - 4.5.

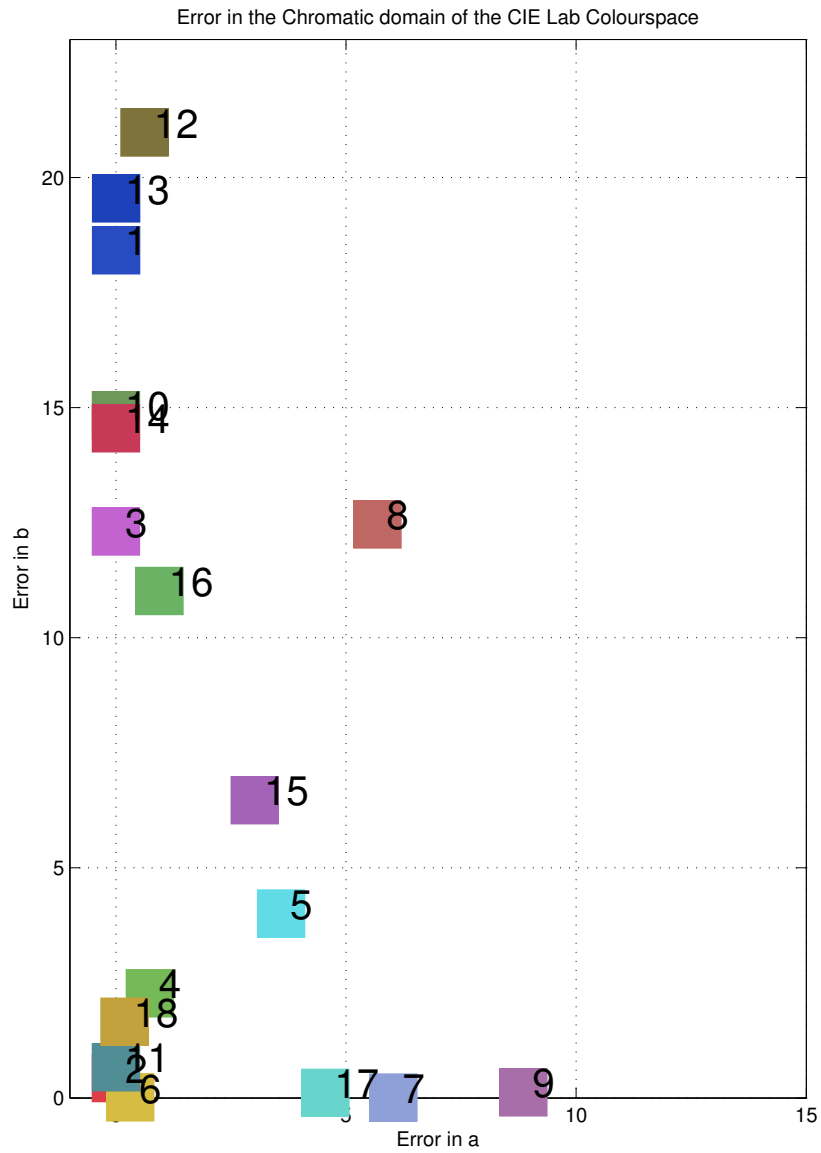


Figure 4.12 – This shows the error in CIE Lab colour space, the further from the origin the greater the chromatic error. The units are in the 8-bit Lab colour coordinate space.

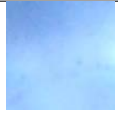
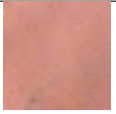

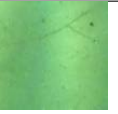

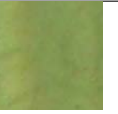

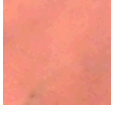
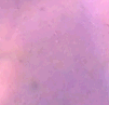






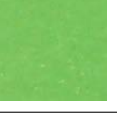
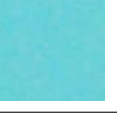
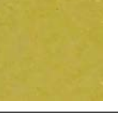
<i>Patch Index</i>	7	8	9	10	11	12
<i>Original Colour</i>						
<i>Colour Corrected</i>						
<i>Ground Truth</i>						

Table 4.4 – The performance of the colour correction for Figure 4.7f compared to the ground truth image (Figure 4.10) taken out of water under the same lighting, ISO and white balance.

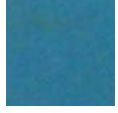
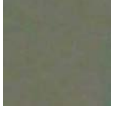
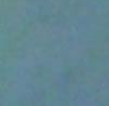
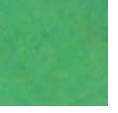
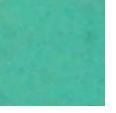













<i>Patch Index</i>	13	14	15	16	17	18
<i>Original Colour</i>						
<i>Colour Corrected</i>						
<i>Ground Truth</i>						

Table 4.5 – The performance of the colour correction for Figure 4.7b compared to the ground truth image (Figure 4.10) taken out of water under the same lighting, ISO and white balance.

light (sunlight and skylight) passes the vehicle (AUV mounted). Further details of these spectrometers are provided in Sections 4.3.1 & 4.3.2.

4.3.1 AUV upward looking spectrometer

An upwards looking spectrometer was installed on the top of the AUV for collecting the downwelling irradiance. This data along with the data from the surface based spectrometer was used to create the water model. This spectrometer sampled the sun and sky light penetrating down through the water column from the surface above. The signal received by this sensor is limited by depth and consequently sensor SNR, beyond a certain depth at

Colour channel	Corrected mean error	Corrected std. dev. of error	Uncorrected mean error	Uncorrected std. dev. of error
Red	11.5	19.2	28.8	17.1
Green	19.3	20.2	0.1	0.2
Blue	6.7	7.1	1.1	2.1

Table 4.6 – This summaries the errors and standard deviations of the colour correction process for patches 1-6. The patches are shown in Figure 4.3. A good correction should have even colour errors across the colour bands (Red/Green/Blue).

Colour channel	Corrected mean error	Corrected std. dev. of error	Uncorrected mean error	Uncorrected std. dev. of error
Red	6.1	10.9	16.3	17.9
Green	7.9	10.5	8.6	11.3
Blue	7.8	16.6	6.7	14.8

Table 4.7 – This summaries the errors and standard deviations of the colour correction process for patches 7-12. The patches are shown in Figure 4.4. A good correction should have even colour errors across the colour bands (Red/Green/Blue).

a given water clarity the sensor will not receive enough light for a reasonable signal.

The spectrometer used was an *Ocean Optics STS microspectrometer*⁶ which was chosen due to its high resolution and small form factor (40mm x 42mm x 24mm). The spectral sensitivity range of the STS spectrometer was 335nm to 820nm. This encompassed all of the visible spectrum with a small amount of near Infra-Red (IR) and near Ultra-Violet (UV). The optical resolution (Full Width at Half Maximum (FWHM)) was 6nm, this was dependant on the dispersion slit width size which was 100 μ m.

A 400 μ m fibre optic is permanently attached to the front of the STS spectrometer. A cosine

⁶<http://www.oceanoptics.com/products/sts.asp>

Colour channel	Corrected mean error	Corrected std. dev. of error	Uncorrected mean error	Uncorrected std. dev. of error
Red	21.9	21.2	65.0	29.4
Green	24.9	20.9	10.3	11.9
Blue	9.0	6.0	26.6	29.1

Table 4.8 – This summaries the errors and standard deviations of the colour correction process for patches 13-18. The patches are shown in Figure 4.5. A good correction should have even colour errors across the colour bands (Red/Green/Blue).

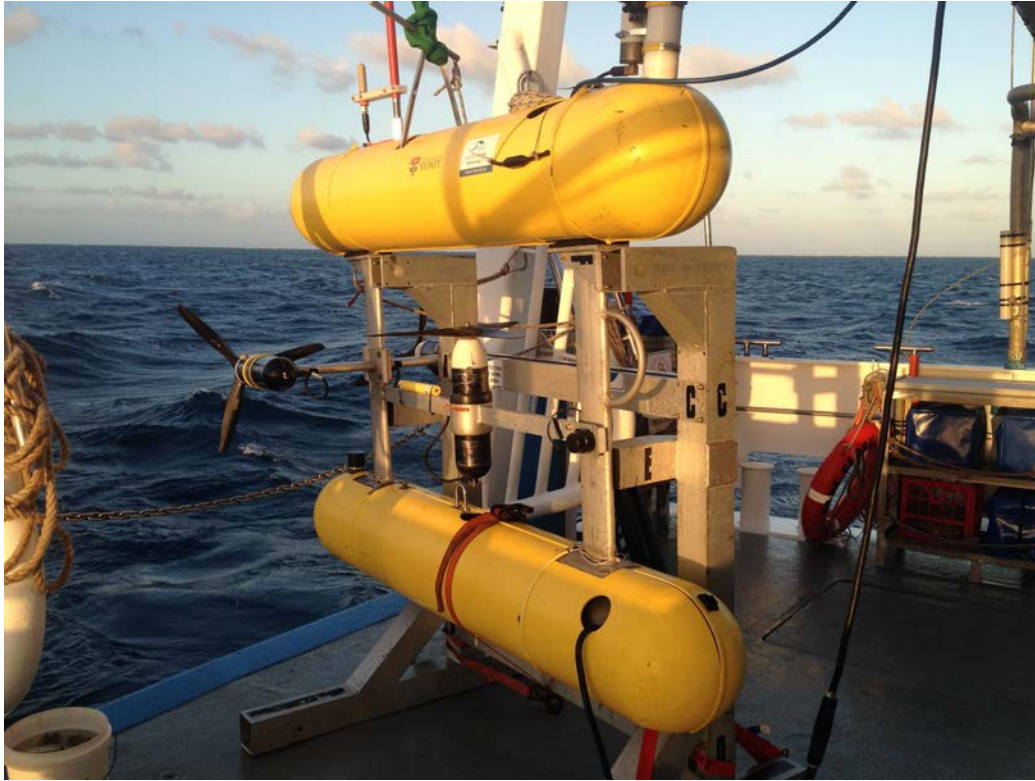


Figure 4.13 – A photograph of Sirius the main AUV operated at ACFR

corrector⁷ was installed on the fore-optics, for integrating the incoming radiance. The cosine corrector's sensitivity is a function of the cosine to the nadir angle of the corrector.

In front of the cosine corrector is the window of the underwater housing. A 4mm thick window was chosen due to the possible depths which the vehicle may descend to. The material of the window was chosen to be UV fused silica which has excellent flat transmission properties ($> 95\%$) over the wavelength range of interest.

To receive data from the AUV based upward looking spectrometer a custom driver was written in C to interface with the Lightweight Communications and Marshalling (LCM) logging system [95] of the vehicle. Communication between the sensor and the data acquisition computer was over RS-232. As the spectrometer was in a different housing to the downward facing spectrometer it was impracticable to link up a trigger line for this spectrometer. As a result triggering was done in software at a sample rate of approximately 1Hz, (similar to the camera system). Synchronisation was implemented in post mission processing.

⁷Ocean Optics CC-3: Opaline glass, 180° FOV, 350-1000nm wavelength range

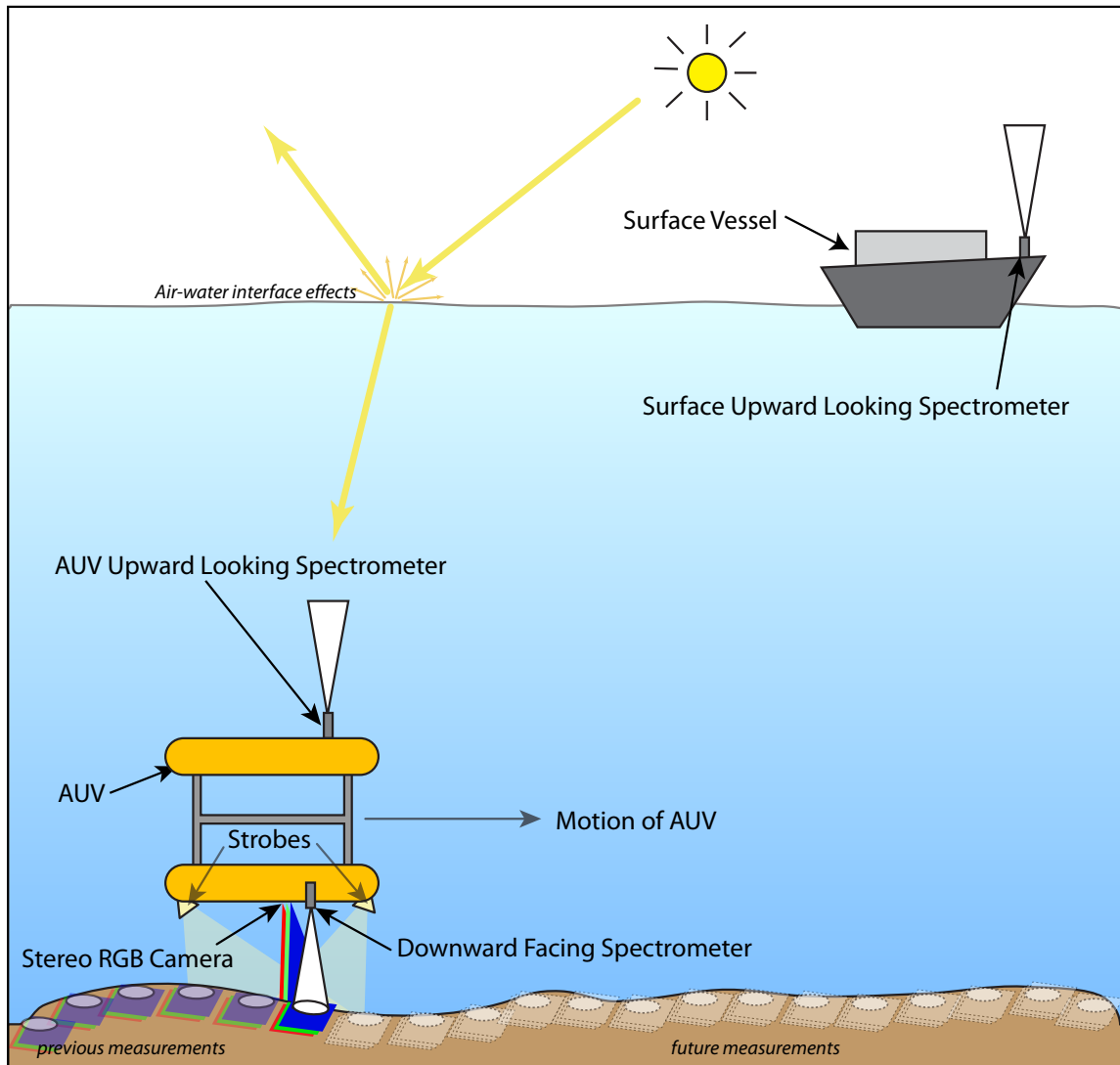


Figure 4.14 – Layout of the designed system showing the placement of the upwards looking spectrometers to characterise the water column and the co-location of the stereo camera and downwards looking spectrometer for benthic habitat mapping.

An auto-gain functionality was implemented in the interface driver to adjust integration time to a suitable signal level. This was done every 30secs (or user definable time period) taking the mean of the signal across the visible spectrum, and scaling the integration time by the ratio of measured mean to a user definable mean (essentially ensuring a certain power level). There were also checks to ensure the signal did not saturate and to ensure the integration time did not change too quickly. This system worked well and produced balanced signals which were neither saturated nor at noise level. This auto-gain system was implemented in the code for all of the spectrometers.

4.3.2 Ship-borne upward looking spectrometer

To measure the irradiance before it entered the water an upwards looking spectrometer on the support vessel on the surface was installed. This spectrometer was mounted in the zenith position in an unobstructed high vantage point on the ship. The sensor was identical to the upward facing spectrometer on the AUV: an *Ocean Optics STS micro-spectrometer*, with the same fore-optics (cosine corrector) and was mounted inside a waterproof housing with an acrylic window. An acrylic window is quite comparable to a Quartz glass window within the visible spectrum. The acrylic window starts to heavily attenuate light in the near-UV spectrum. As this is outside of the wavelengths easily passed by water it is considered a negligible trade-off. Further detailed analysis of the transmission of an Acrylic window is provided in Section 4.4.3.

The spectral data is logged to a ship based computer over RS-232 serial using a custom Python-based driver. An auto-gain system was implemented in the device driver similar to the one on the AUV spectrometer (see Section 4.3.1). The time on the surface data logging computer was synchronised with the AUV's onboard computer preceding each dive. The data acquisition system was also logging spectra at approximately 1Hz. Position, roll, pitch and heading were recorded from an Inertial Measurement Unit (IMU) mounted on the support vessel, these were sampled at 10Hz.

4.3.3 Limitations

Imaging underwater whether it be in the hyperspectral or traditional trichromatic domain presents similar challenges, particularly in gathering sufficient light. The selective absorption of the water means a lot of the light energy was lost. One method to increase the SNR would be to increase the integration time of a Hyperspectral Imaging (HSI) camera; (this would be analogous to a longer shutter speed on a camera) which would result in spatial blurring of the image due to the movement of the AUV. So having a higher spatial resolution would not achieve much except long blurred streaks of the substrate.

The illumination of the scene had limited spectral bandwidth; the strobes on the AUV were LEDs, although chosen to have a broader spectral profile than standard LEDs, the illumination profile was heavily diminished by 700nm (near IR) (see Figure 4.23). The solar illumination below 2-3m has lost almost all of the flux in this region too. However there is not

much information that can be inferred if information was known anyway. Photosynthesising organisms will have a distinct absorption at 675nm followed by a sharp IR reflectance after 675nm. This absorption band is enough to characterise this type of pigment [115].

4.3.4 Extended water model

The upward looking spectrometers onboard the AUV and above the surface on the support vessel were used to gather information about the optical attenuation properties of the water. This method was the same as was introduced in the test tank and Clovelly experiments. These attenuation properties encapsulated both the scattering and absorption of the water as well as the constituents within it. All the parameters estimated in the extended water model are visually presented in Figure 4.15.

Due to the complex nature of the air-water interface the surface spectrometer measurements cannot be used without first compensating for the surface effects. These effects will vary vastly with time of day, wind speed and tilt of the vessel. Onboard the support vessel a *Novatel ProPak G2* IMU and GPS receiver was mounted. They were sampling at 10Hz, collecting the latitude, longitude, altitude, roll, pitch and heading of the support vessel.

The position of the sun (azimuth and zenith) can be obtained from time, date, position and altitude [172]. Measurement of the ship's orientation is important due to it's continuous movement and the spectrometer's cosine corrector was sensitive to light as a function of the cosine of the angle of the incoming light flux to the nadir of the optical axis of the sensor.

Using the theory of air-water interface modelling presented in Section 2.2.2.1. The model took into account several factors which influence the passage of light through the water column. These factors included: refractive index, entry angle (angle of the sun), reflections off the surface of the water, roughness of the water's surface due to wind.

The refractive index of the water is a function of wavelength, salinity and temperature. The salinity and temperature of the water were continuously collected from a conductivity and temperature sensor (*Seabird SBE 37-SI MicroCAT*) on-board the AUV. Using Snells law Equation (2.4) the exit angle into the water can be modelled. Then the reflected component at the surface can be computed using the Fresnel equation Equation (2.5).

Wind induced surface disturbances can also influence the amount of surface reflection. Wind measurements for the experiment were collected from an *Australian Institute of Marine*

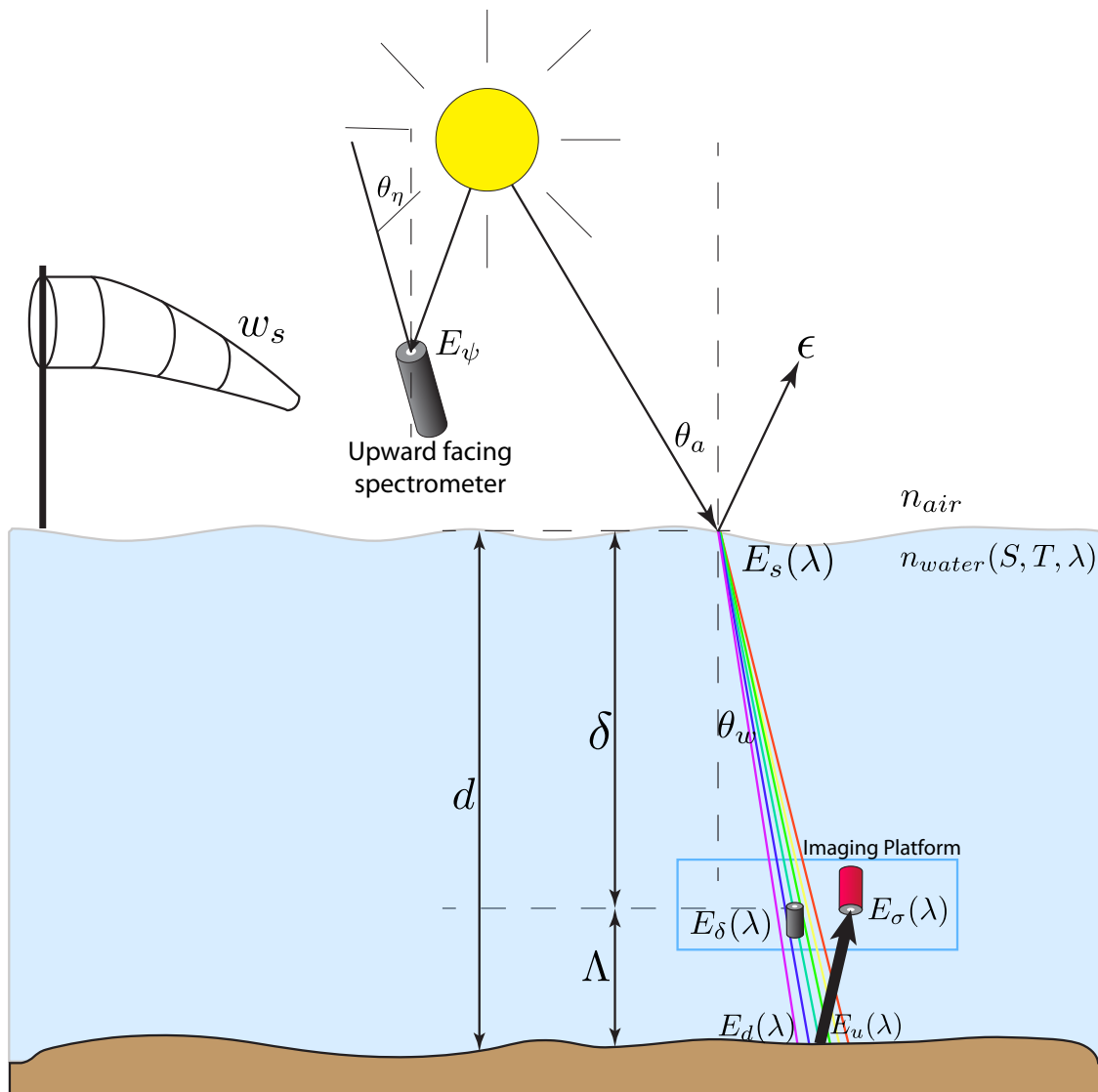


Figure 4.15 – This shows the complete parameters obtained for modelling for the air-water interface, as well as the parameters for resolving the seafloor spectral reflectance.

Science (AIMS) offshore weather station at Davies Reef (18.83S, 147.63E)⁸ which was close to the mapping sites. To convert the spectrometer readings into the same units as each other, firstly the radiometric calibration is done (Section 3.3) then the readings are transformed accordingly.

Through this process a measurement for the diffuse downwelling attenuation coefficient K_d was obtained Equation (4.1). A new K_d was gathered for each spectral reading measurement

⁸<http://data.aims.gov.au/aimsrtds/station.xhtml?station=4>

(approximately once a second). This allowed the water model to adapt to changes in the environmental conditions both in the water column above the imaging platform and above the water. These changes include the position of the sun and weather/cloud conditions. This does become a consideration when used for AUV surveying missions. The length of an AUV survey mission can last for 8-10 hours, over which time the conditions above the water will change dramatically.

The weather or water conditions were not expected to change rapidly within a second or even within 30 seconds, but due to noise in subsequent measurements of the attenuation coefficient K_d temporal smoothing was needed. So the attenuation coefficient needs smoothing not only in the time domain but also in the frequency domain. The AUV upwards looking spectrometer was susceptible to low signal noise in the fringe regions of the visual spectrum where the passage of light is considerably attenuated. For the data smoothing a Savitzky-Golay filter [174] was used. This is commonly used in HSI processing and is achieved by fitting successive subsets of the spectra with a low-degree polynomial. The major advantage of Savitzky-Golay filtering over other smoothing techniques is that it removes noise while preserving the amplitude and shape of features within the data (within the limits of the width of the fitted polynomial).

4.3.4.1 Surface lensing effects

In the air-water interface model surface disturbances such as waves and the resultant lensing effects which ensue are not compensated for. These optical effects are often observed on the seafloor in shallow regions and are characterised by moving lines and regions of light and dark. These are commonly referred to as caustics [128].

As part of the calibration routine for the USBL (sensor used for the localisation of the AUV); the AUV remains in the same position at a depth of approximately 25 metres, for 20 minutes. To see if there were visible caustics in the spectral data, the AUV based upward looking spectrometer data was examined over the 20 minutes period. A Fast Fourier Transform (FFT) was performed on one of the spectral bands in the ‘green’ section of the visible spectrum, this is shown in Figure 4.16. The same band was examined in the downward looking spectrometer data, as well as readings from the depth sensor, altitude recorded by the DVL and the motion of the ship. The FFT on the ship’s tilt and roll gave the wave

period, which was found to be 5.9 seconds. This feature was further confirmed to be wave motions from the wind data. The wave period was modelled based on the wind data (wind speed = 8.5 metres/second) at the time and location of the measurements [151].

In the depth, altitude and downward spectrometer data an oscillation was found with a period of 13 - 14 seconds, this was traced to be the period of the control system of the AUV maintaining the constant altitude for the 20 minutes. No oscillations in the upwards looking spectrometer data were seen at either wave nor vehicle motion frequencies. The reason caustics were not seen at this depth is because the scattering properties of the water have heavily diffused the downwelling light. It should be noted that this only applies in this situation and dataset. In a shallower area the downwelling light may not have fully diffused and so some temporal smoothing or equivalent may need to be applied. In other studies at shallower depths surface effects were found to influence the ability to make reliable measurements[140].

4.3.5 AUV imagery colour correction results

An AUV survey was conducted over a coral shoal at Pakhoi Bank ($+147.883^{\circ}N$, $-19.441^{\circ}E$), on the GBR, Queensland, Australia (17th December 2013, 14:02 - 16:40). This was a coarse grid transect with approximately 100m in-between parallel grid lines. A map showing the path and bathymetry of the survey is shown later in Chapter 5 - Figure 5.4. This was a long mission where 14,168 stereo pairs of images and corresponding spectrometer readings were taken. The mean depth was 27.1m and mean altitude of the vehicle was 2.2m. Typically the AUV runs at an altitude of 2m, but this will vary as it passes over undulating terrain. This was one of many surveys conducted over small shoals on the GBR approximately 60kms off the coast of Townsville. This particular survey was chosen due to its wide variety of substrate types present.

Figures 4.17 - 4.19, show the results for using the proposed method on AUV imagery. (a) is the original image, (b) is the depth map outputted from the stereo camera generated mesh, (c) is colour correction using the traditional greyworld correction technique and (d) is the result from our proposed method. The images are of typical coral reef structures as well as a flat seagrass environment.

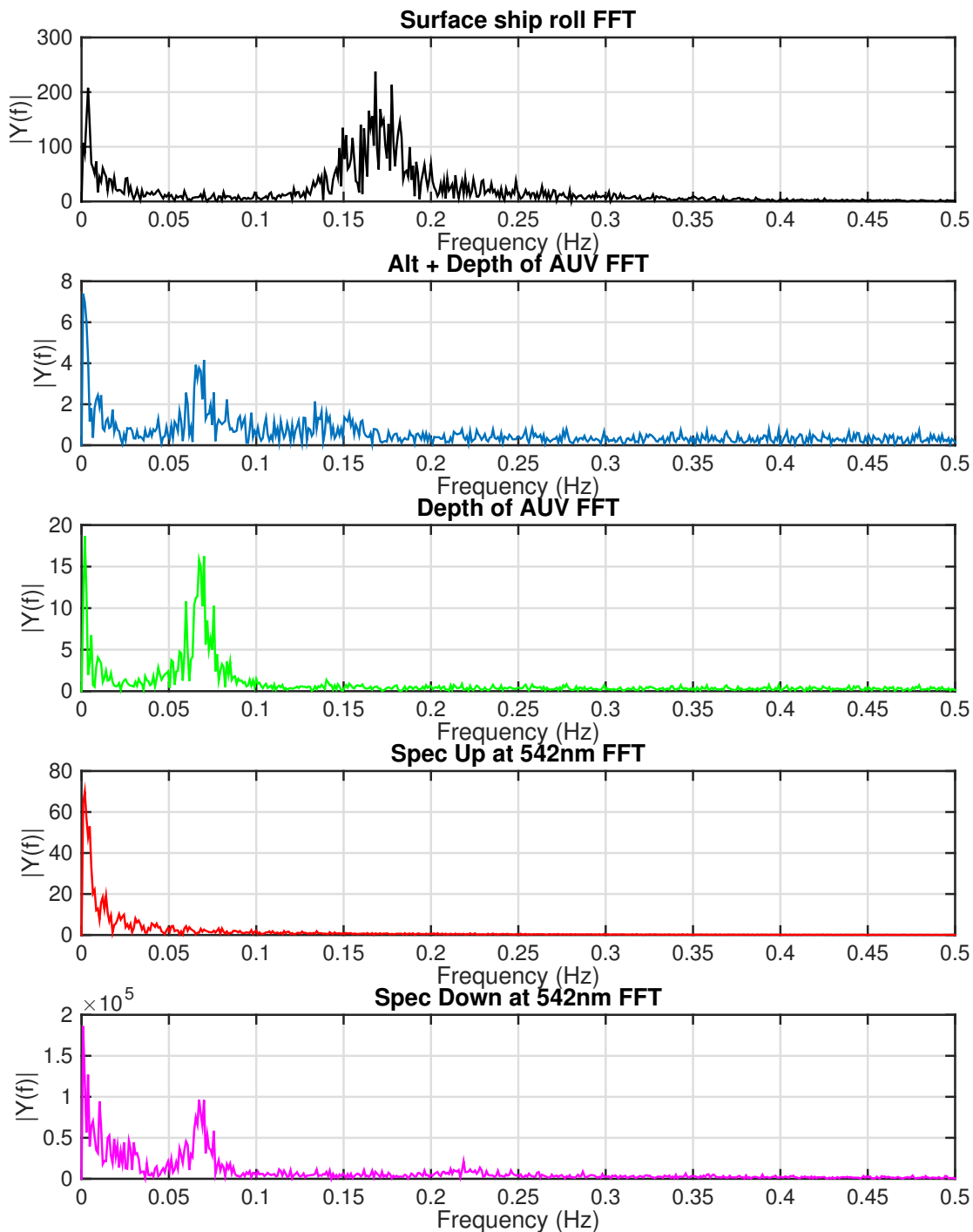


Figure 4.16 – The top plot shows an FFT of the roll of the surface ships movements, the 2nd and 3rd are of the depth and altitude + depth of the AUV at depth. The 4th plot is of data at 542nm for the upwards looking spectrometer on the AUV and the last plot is a FFT plot of the downwards looking spectrometer at 542nm on board the AUV. This figure shows that the motion of the water (shown by the ships motion) does not influence the optical readings of the AUV below. The optical readings are more influenced by variations in the movement of the vessel in the water column.

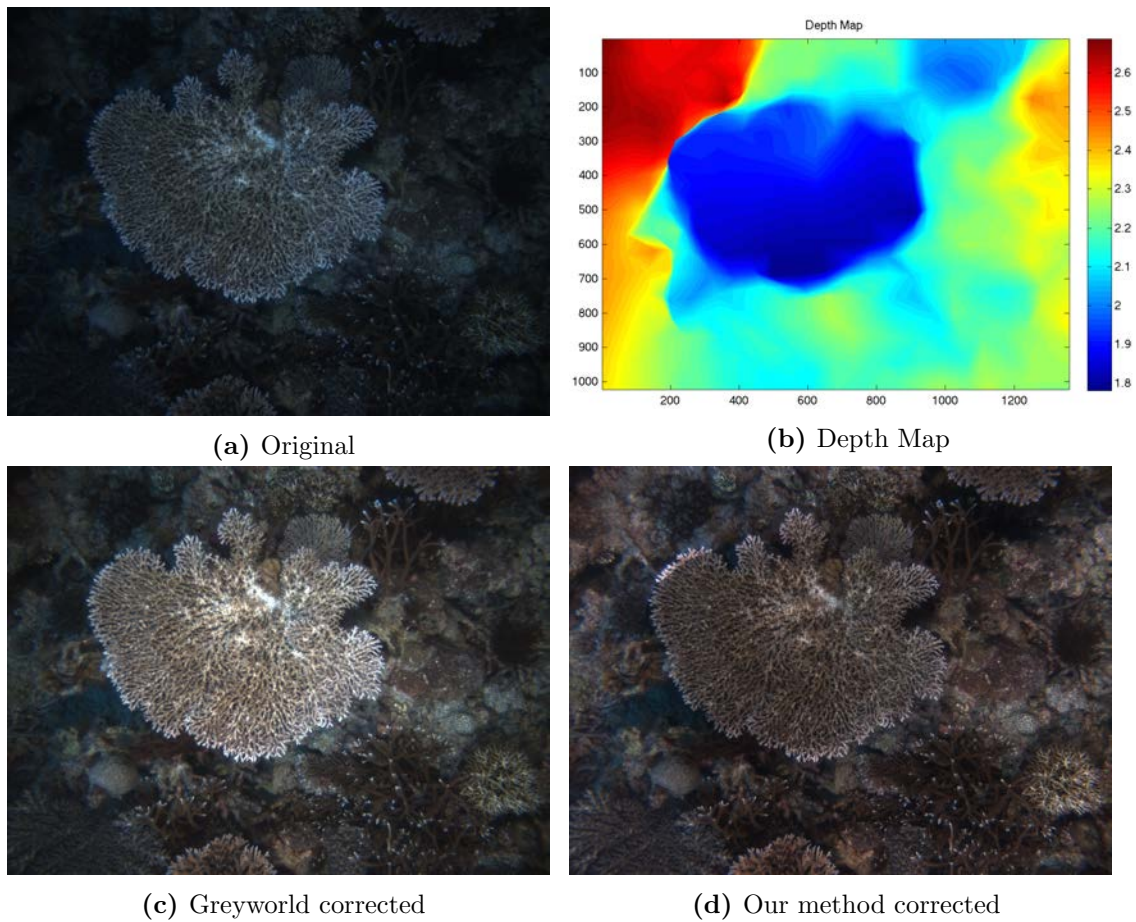


Figure 4.17 – This coral scene demonstrates the colour correction for large change of depth from the camera due to large variations in the structure of the scene.

AUV colour correction performance

Earlier colour correction results from a test tank and real-world scenario show the validity of the proposed correction method. Instead of manually measuring the distance to the scene the stereo camera is used to resolve the distance from each point in the scene to the camera. Given the lack of ground truth, it is hard to give a proper quantitative evaluation of the colour correction performance. However qualitatively it can be seen that scene colour is more ‘natural’ looking and does not have the colour cast which was obvious on the original. The greyworld correction does quite a good job of removing the colour cast however is ignorant to scene structure. This results in elements further away still maintaining a blue colour casting. The inverse also applies to objects close by which appear much brighter than the surrounding substrate which can be seen in Figure 4.17. There is a broad range

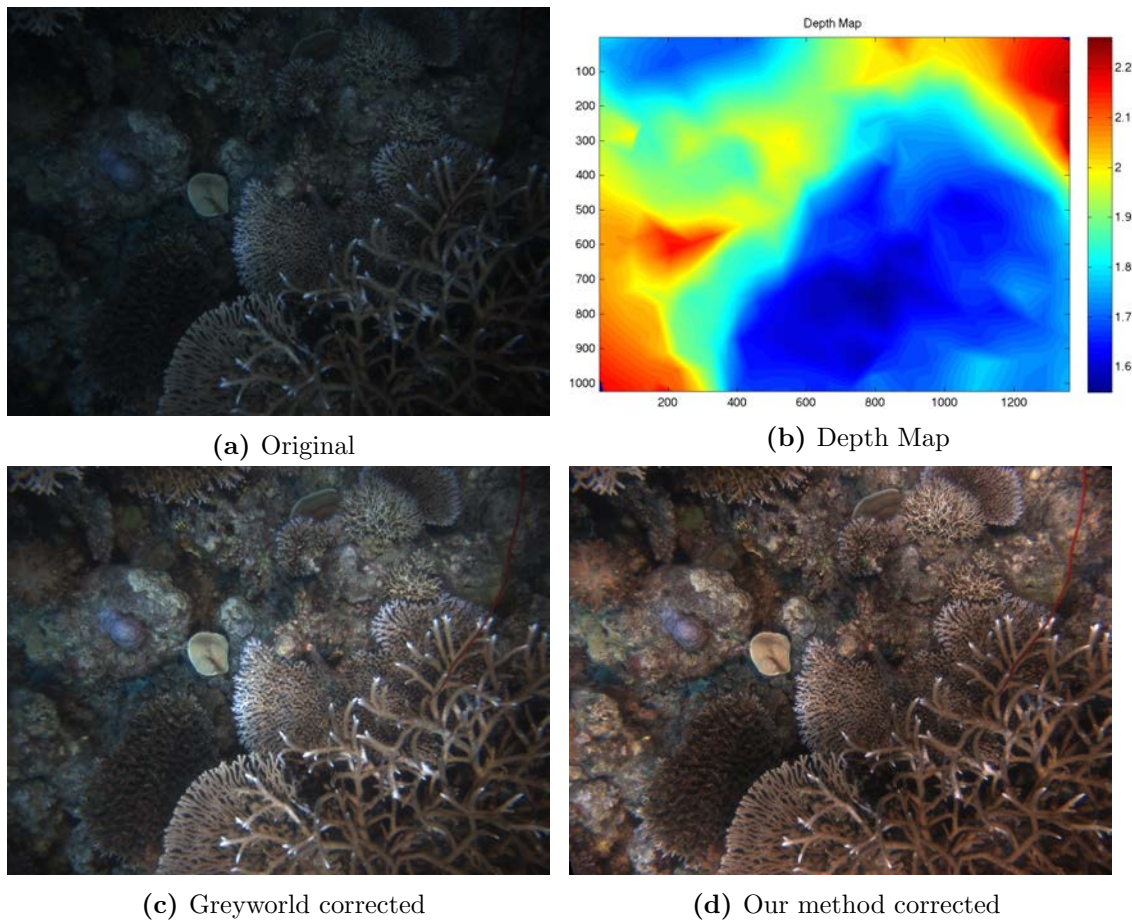


Figure 4.18 – This demonstrates clearly the use of the 3D mesh for correcting the colour and intensity balance in the image, the coral in the foreground on the greyworld corrected image is much brighter than the background, whereas our method produces a more even balance.

of depths in the scene, it covers 1.8m - 2.7m. From these distance variations it can be seen that the correction method can compensate for a variety of distances.

The naive greyworld method also does not take into account the vignetting effect which the proposed method also compensates for using the cosine fourth correction. The vignetting effect can be seen in a flat scene as in Figure 4.19. In this image the edges appear much darker than the foreground, however this is compounded by the greyworld method not compensating for the scene structure. The proposed method will allow for more consistent and accurate colour in underwater colour distorted imagery. The colour correction method also has the advantage over conventional methods because it utilises a water attenuation model which is updated at the time of every image.

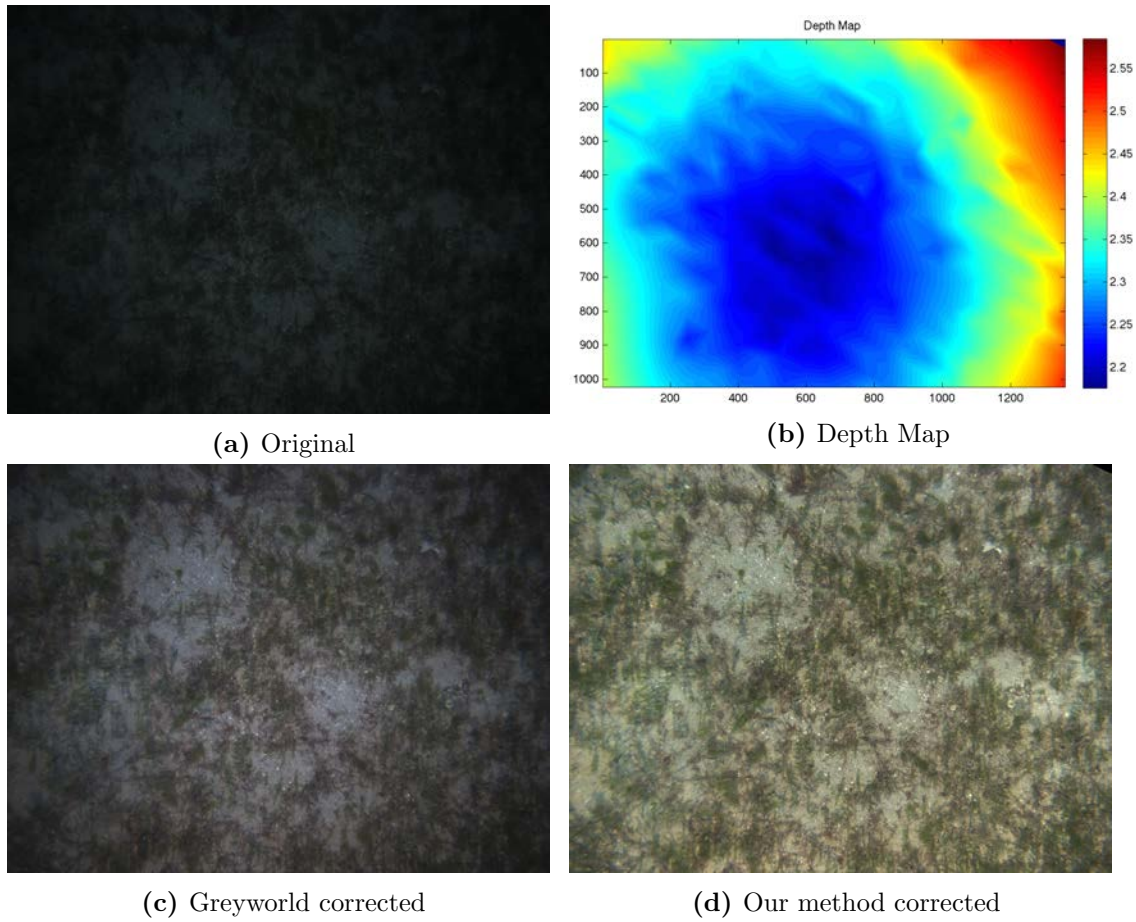


Figure 4.19 – Vignetting Correction for a flat scene containing seagrass

4.4 Deriving spectral reflectance

In hyperspectral imaging, deriving the material reflectance of objects in a scene allows for their classification. The spectral reflectance was obtained from Equation (4.6) where $E_u(\lambda)$ is the reflected upward irradiance from the scene which was illuminated by the downwelling irradiance at the scene $E_d(\lambda)$.

$$R(\lambda) = \frac{E_u(\lambda)}{E_d(\lambda)} \quad (4.6)$$

$E_u(\lambda)$ can be measured by an in-situ spectral device facing downwards. If the downwards facing device is at a distance above the scene spectral correction needs to be undertaken to invert the water attenuation effects. This correction methodology will be covered further in Section 4.4.2. $E_d(\lambda)$ can come from a variety of sources, this could be the ambient illumi-

nation from above the water. In the case of imaging from an AUV, additional illumination might come from an artificial source on the platform.

4.4.1 Illumination at scene

A model of the scene illumination needs to be obtained to be able to recover spectral reflectance. As previously mentioned the upwards looking spectrometers were used for generating a model of the water. The upwards spectrometer on the in-situ platform may also be used to measure the contribution of ambient illumination coming from above the imaging platform.

In order to derive the ambient illumination at the scene level Equation (2.1) was used (Beers Law),

$$E_d(\lambda) = E_\delta(\lambda)e^{(-K_d(\lambda)\Lambda)} \quad (4.7)$$

where E_δ is the downwelling irradiance measured by the upward looking spectrometer on the imaging platform, K_d is the attenuation coefficient curve at wavelength λ and Λ is the altitude of this spectrometer from the scene. This results in the ambient illumination at scene level.

4.4.2 Reflected irradiance at scene

To determine the spectral reflectance of the materials in the scene, the reflected light from the scene was obtained with a downward facing spectrometer. To convert the measured spectra to what was reflected at scene level, the inverse of Beers law Equation (2.1) as shown in Equation (4.8) was used.

$$E_u(\lambda) = \frac{1}{e^{-K_d(\lambda)\Lambda}} E_\sigma(\lambda) \quad (4.8)$$

where $E_u(\lambda)$ is the upwelling irradiance at scene, K_d is the attenuation coefficient curve and Λ is the altitude of the vehicle, E_σ is the irradiance measured by the downward looking spectrometer onboard the imaging platform.

4.4.3 Spectral imaging from an AUV

Using the AUV setup introduced in Section 4.3, a spectrometer was co-located with the downwards facing stereo camera. The FOV calibration was undertaken on this spectrometer (Section 3.2) as well as a radiometric calibration (Section 3.3). Figure 4.21 shows a photo of the window of the camera housing showing the positioning of the downwards facing spectrometer co-located with the stereo camera.

A spectrometer was chosen for the downward looking spectral measurements over a HSI camera for a few reasons: a spectrometer can achieve higher SNR due to larger pixel wells on the receiving imaging sensor and will also gather more light due to a larger swath. Spectrometers are also much smaller, use less power, less data storage requirements and are cheaper, but at the cost of spatial resolution. In the current configuration, pairing a stereo camera with a HSI camera would not be possible. At the moment, the strobes fire and the cameras trigger at the same time, acquiring the whole image. With a push-broom HSI camera this would result in only acquiring a single line of spectral measurements not an image. To acquire an image over the same area constant illumination would be needed. This would be very power intensive and unfortunately an AUV can only carry so much power. This may suit a Remote Operated Vehicle (ROV) which are often tethered to a support vessel. The other form of HSI camera is an Acousto-Optical Tunable Filter (AOTF) camera. Under the same strobe illumination this HSI camera would capture the whole scene at once but only at one narrow wavelength. Hundreds of flashes or constant illumination would be needed to capture an entire spectral image. The AOTF modality also has an issue of imaging from a moving platform. Each frame would be displaced from the previous. These frames could be stitched together later, however parallax effects could cause issues if moving over a complex 3D scene.

To implement the proposed system the stereo camera housing on the AUV was re-engineered to fit an *Ocean Optics USB 2000+*⁹ spectrometer (dimensions: 89.1mm x 63.3mm x 34.4mm). The USB 2000+ collects 2048 spectral bins with a FWHM of 7.7nm. It is sensitive in the spectral region of: 340nm - 1032nm, and it achieves this through a 200 μ m entrance slit. A high sensitivity CCD (Sony ILX-511B¹⁰) was installed in the spectrometer to account for low light levels when imaging underwater. The design of the Ocean Optics USB 2000+ is

⁹<http://www.oceanoptics.com/products/usb2000+.asp>

¹⁰[http://www.oceanoptics.com/technical/ILX511B\(E\).pdf](http://www.oceanoptics.com/technical/ILX511B(E).pdf)

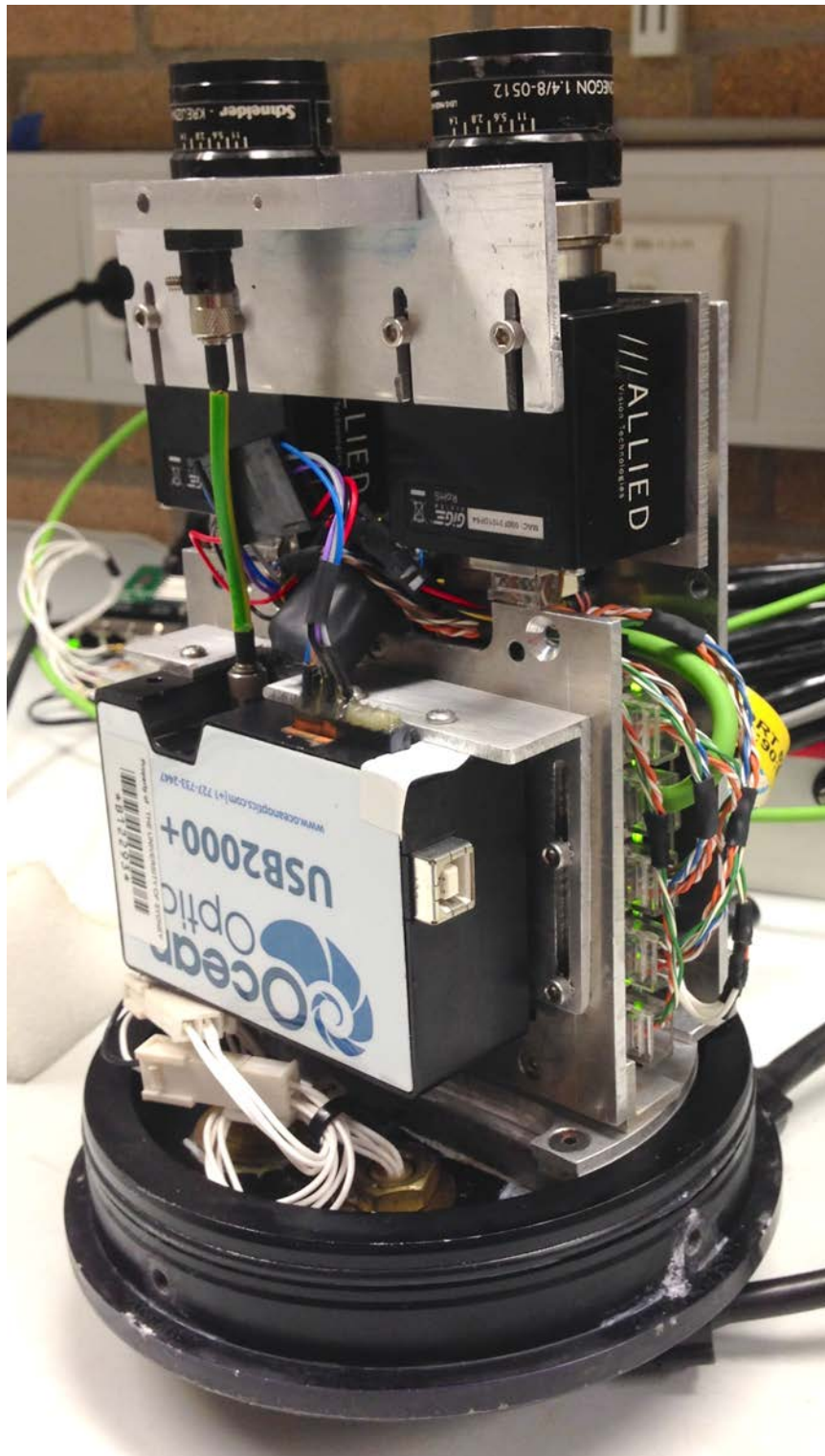


Figure 4.20 – The internals of the camera pod, at the top is the two camera system, which make up the stereo pair, and below is the spectrometer (Ocean Optics USB2000+). The spectrometer is connected by a fibre optic to a collimating lens in the aluminium bracket shown in the picture.

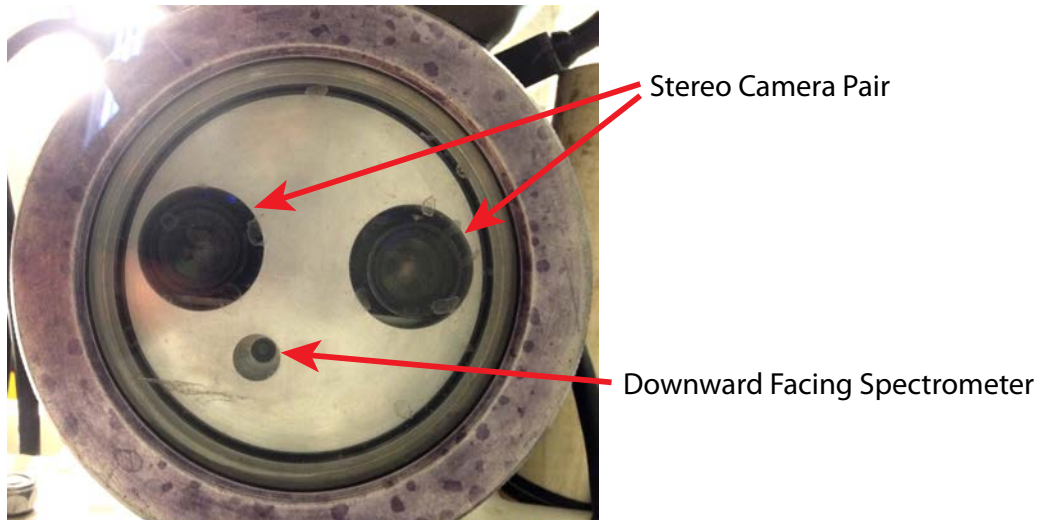


Figure 4.21 – This is a view of the camera housing window and shows the positioning of the spectrometer’s aperture (small hole) with respect to the lenses of the stereo cameras (two larger holes). The downward facing spectrometer used was an Ocean Optics USB 2000+ with a wavelength range of 340nm - 1032nm, and a FWHM of 7.7nm.

a Symmetrical crossed Czerny-Turner type architecture. The USB 2000+ optical entrance is connected via a 10cm fibre optic cable to a collimating lens¹¹ co-located with the stereo camera lenses at the window of the camera system (Figure 4.21). The fibre optic diameter was chosen to be $400\mu\text{m}$. Should a different quantity of light be needed in future revisions a fibre of a different diameter can be installed. Figure 4.20 shows the internal components of the camera pod. Here the cameras and spectrometer can be seen.

The collimating lens on the fore-optics of the system allows for the focusing of the FOV of the spectrometer to a sharp edged spot. The lens was focused through sliding a lens away or towards the tip of the fibre, with a grub screw locking the position of the lens in place. Knowledge of the FOV of the spectrometer is important for co-registration and subsequent use with the stereo camera system. The details of determining the FOV and the spatial co-registration were detailed in the previous chapter (Section 3.2).

The cameras used for the stereo pair were *Allied Technologies Prosilica GC1380* ethernet cameras. One camera was mono and the other colour in a Bayer configuration. More technical details are provided in Section 3.4.3.4.

Another consideration in combining the two sensors was synchronisation of acquisition. The cameras in the stereo imaging system, the spectrometers and the strobes were all triggered

¹¹Ocean Optics 74-VIS: 350-2000nm wavelength range, f/2 BK-7 glass

together on the same trigger line. This method ensured they both saw the same scene. The strobes are on for approximately 7-11ms, providing enough light for a well balanced exposure of the cameras and spectrometers, while minimising motion blur. Communication to the spectrometer is via RS232 serial. Custom software was written in C to interface the sensor data into the LCM [95] vehicle logging system.

The spectrometer has the ability to integrate the light falling on the CCD over a user definable period. This acts similarly to controlling the shutter period on a conventional camera.

Despite the wide bandwidth of the spectrometer there are limitations on the wavelengths of light which may enter the optical system. These restrictions come from the windows of the underwater enclosures and secondly from the optical transmission of the water. The window used on the camera housing was made of acrylic. The transmission was near flat at 91-94% between 400-800nm, but it did not pass light below approximately 400nm. The measured transmission curve is shown in Figure 4.22.

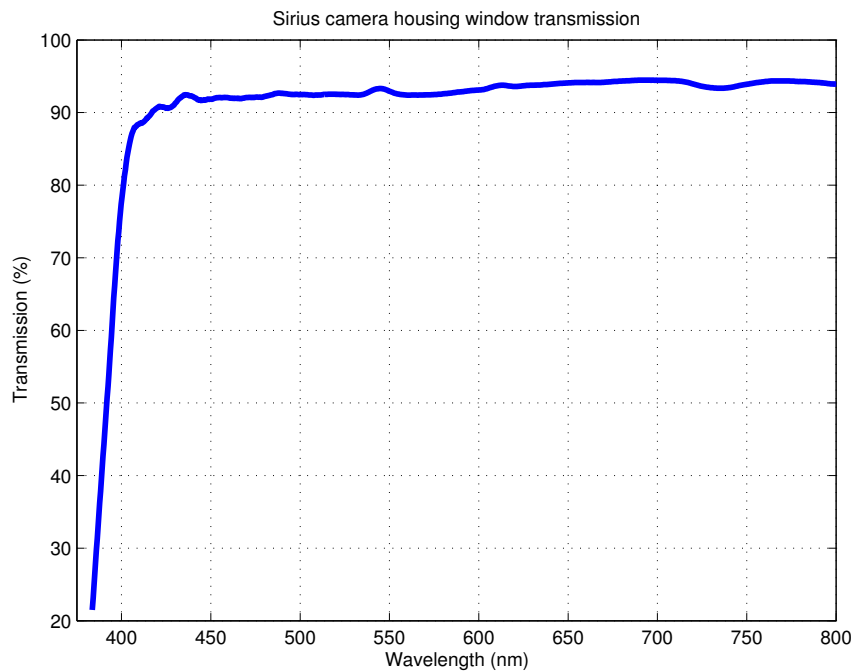


Figure 4.22 – The optical transmission curve of the acrylic window of the camera housing onboard Sirius

4.4.3.1 Illumination modelling on an AUV

Illumination modelling on the AUV is an extension of the illumination modelling introduced in Section 4.4.1. In addition to ambient illumination to the scene, the AUV carries LED strobes for additional light. However the strobes (which was the major source of illumination to the scene) can not be directly isolated and measured for each frame. So an illumination model was created for each frame based on the ambient light measurement and a strobe model based on the altitude from the scene.

To generate a strobe model, measurements of a sandy substrate were taken at an altitude of 1.9 metres and depth of 32.3 metres. A series of measurements of the downwards spectrometer with the strobes on were acquired. This gathered the ambient and the strobes contribution, and then a series of measurements with strobes off were measured (just the ambient contribution). Both surface and AUV upward looking spectrometer readings were simultaneously collected so a model for the attenuation of the water was obtained. The assumption was made that the spectral reflectance of the sand in the first set of measurements (strobes on) is the same as the sand in the second set of measurements (strobes off). This is so the strobe contribution can be isolated and spectral profile obtained. This assumption was fair as both measurements occurred in the same location. The spectral profile of the LED strobes used on board the AUV used is shown in Figure 4.23.

As the AUV passed over different benthic substrates there was variance in the altitude. The vehicle aims to maintain an altitude of 2m but has limits on how quickly it can descend and ascend over terrain while still maintaining a certain forward trajectory. As a result the illumination model and subsequently the strobe model needed to accommodate these variances. Figure 4.24 shows the physical positioning of the strobes with respect to the seafloor and imaging package. This figure is from the side perspective of the vehicle, looking length ways along the side of the AUV.

The first step was calculating the strobe angles (θ_f & θ_r) from strobes to the scene then calculating the path lengths for both strobes (p_f & p_r). The angle variance Equation (4.9) of the strobes was modelled using a cosine model. The light disperses spherically, but the scaled variance from the strobe illumination model taken in the strobe calibration was required. So spherical spreading Equation (4.10) can be rewritten to give the ratio S_{ratio} of light power of the new distance to the power at the calibration distance Equation (4.11).

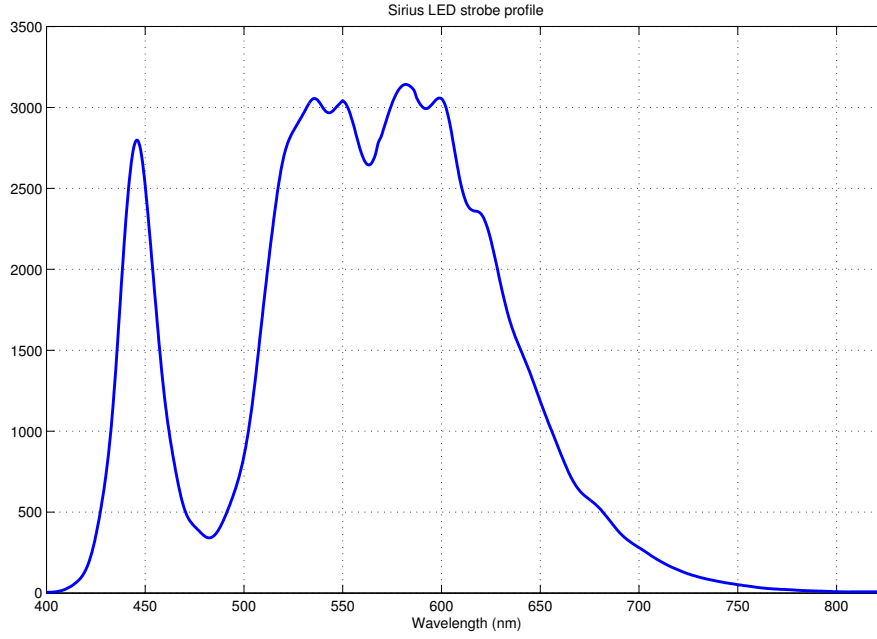


Figure 4.23 – The spectral profile of the LED strobes onboard the AUV used in this work. This measurement was taken in air. Unit on the vertical axis is in raw digital count from the spectrometer.

Where: L_0 is the light intensity at the strobes, L_Λ is the light intensity at distance Λ , $pcal_f$ & $pcal_r$ is the path length for the calibration for both front and rear strobes, and p_f & p_r is the path length to the scene from the strobes for front and rear for the current altitude measurement.

$$V = \cos(|\theta - \psi|) \quad (4.9)$$

$$L_\Lambda = \frac{L_0}{\Lambda^2} \quad (4.10)$$

$$S_f = \frac{pcal_f^2}{p_f^2} \quad S_r = \frac{pcal_r^2}{p_r^2} \quad (4.11)$$

Attenuation due to the water is also taken into account using Equation (2.1), where the variation from the calibration altitude was considered. If the altitude was less than the

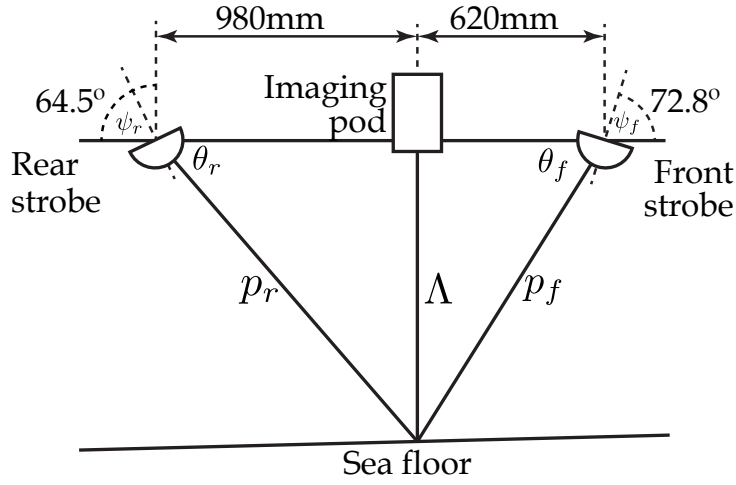


Figure 4.24 – This shows the layout of the imaging pod and the strobes on our AUV. This is important for modelling the strobe illumination: a - altitude of vehicle & imaging pod, p_f & p_r - strobe path length from strobe to scene for front and rear strobes respectively, θ_f & θ_r - illumination angle as a function of altitude and linear offset on the AUV, ψ_f & ψ_r - fixed tilt of the strobes on the vehicle.

calibration altitude the reciprocal of Equation (2.1) was taken, otherwise Equation (2.1) was used to attenuate the strobe contribution to scene level. This variation due to water attenuation was defined as $K_f(\lambda)$ & $K_r(\lambda)$ at wavelength λ . Then combining these variations Equation (4.14) from the strobe calibration model (B_{cal}) it was assumed the spectral profile of the front Equation (4.12) and rear strobes Equation (4.13) were nearly identical. The final strobe contribution to the scene illumination $E_B(\lambda)$ is defined in Equation 4.15.

$$scaling_f(\lambda) = V_f \times S_f \times K_f(\lambda) \quad (4.12)$$

$$scaling_r(\lambda) = V_r \times S_r \times K_r(\lambda) \quad (4.13)$$

$$scaling(\lambda) = \frac{scaling_f(\lambda) + scaling_r(\lambda)}{2} \quad (4.14)$$

$$E_B(\lambda) = scaling(\lambda) \times B_{cal} \quad (4.15)$$

The strobe contribution at scene level is done in a similar way, $E_b(\lambda)$ Equation (4.15) was attenuated using Equation (2.1). This derived the strobe contribution at scene level.

To then obtain the total downwelling irradiance at scene $E_d(\lambda)$ the strobe and ambient illumination at scene were added together.

$$E_d(\lambda) = (E_B(\lambda) + E_\delta(\lambda))e^{(-K_d(\lambda)a)} \quad (4.16)$$

In the modelling of the strobe illumination some assumptions were made. Shadowing by the AUV over the scene was not investigated in great detail and was assumed to be the same as what was seen in the in-water calibration process. In the future it might be worthwhile investigating further shadowing effects.

4.4.4 Spectral reflectance results

In section 4.3.5 results were presented for correcting the colour of AUV imagery from a surveying mission of a reef on the GBR. In this section hyperspectral reflectance results are presented from the same surveying mission.

In the presented results (Figures 4.25 - 4.29) the colour image on the left (a) showing a red circle indicates the FOV of the spectrometer, to the right (b) is the derived spectral reflectance for that sample. (c) this shows the upwards looking spectrometer readings, on-board the AUV and above the water. (d) shows the resultant attenuation curve derived from the upwards looking spectrometer readings, note the decrease beyond 625nm is due to low signal/noise. By examining the spectral reflectance more information can be extracted about the pigments present within the sample. It can be seen in Figure 4.26 that there is more green pigment (475-575nm) in the Montipora than the more distinctly brown colouration of the Acropora in Figure 4.25. The distinctive blue tips of the Pocilloporidae Seriatopora (Figure 4.28) are seen as a small peak in the spectral reflectance around 480nm. Samples other than coral were also imaged; the distinct chlorophyll b absorption in the near IR at 675nm can be seen in a measurement of seagrass (Figure 4.29).

Figures 4.30 - 4.31 show the variance of the spectra for a particular class. These class labels have been hand labelled by a coral expert. The white line indicates the median of the spectra for that class. Then the different shaded regions show the percentage of spectra which fell in that region. The black indicates the middle 25% about the mean, dark grey is the middle 50%, medium grey - 75% and light grey - 95%. Tighter regions indicate less

variance between the measurements. For example the Sand shown in Figure 4.30 has quite close regions. Sand is particular even as there is not a lot of variance between different readings for sand. Unlike Soft Coral shown in Figure 4.31.

To demonstrate the effectiveness of the proposed method for recovering the reflectance spectra of the spot on the seabed, a spectral library was created from select data points in the survey, labelled by an expert, and classification was performed on the dataset. This will be shown in Section 5.2. The materials with larger variances often resulted in poorer classification performance. As will be shown in the classification section, Sand and Seagrass have very good classification accuracies as a result of low spectral variance and good interclass separability.

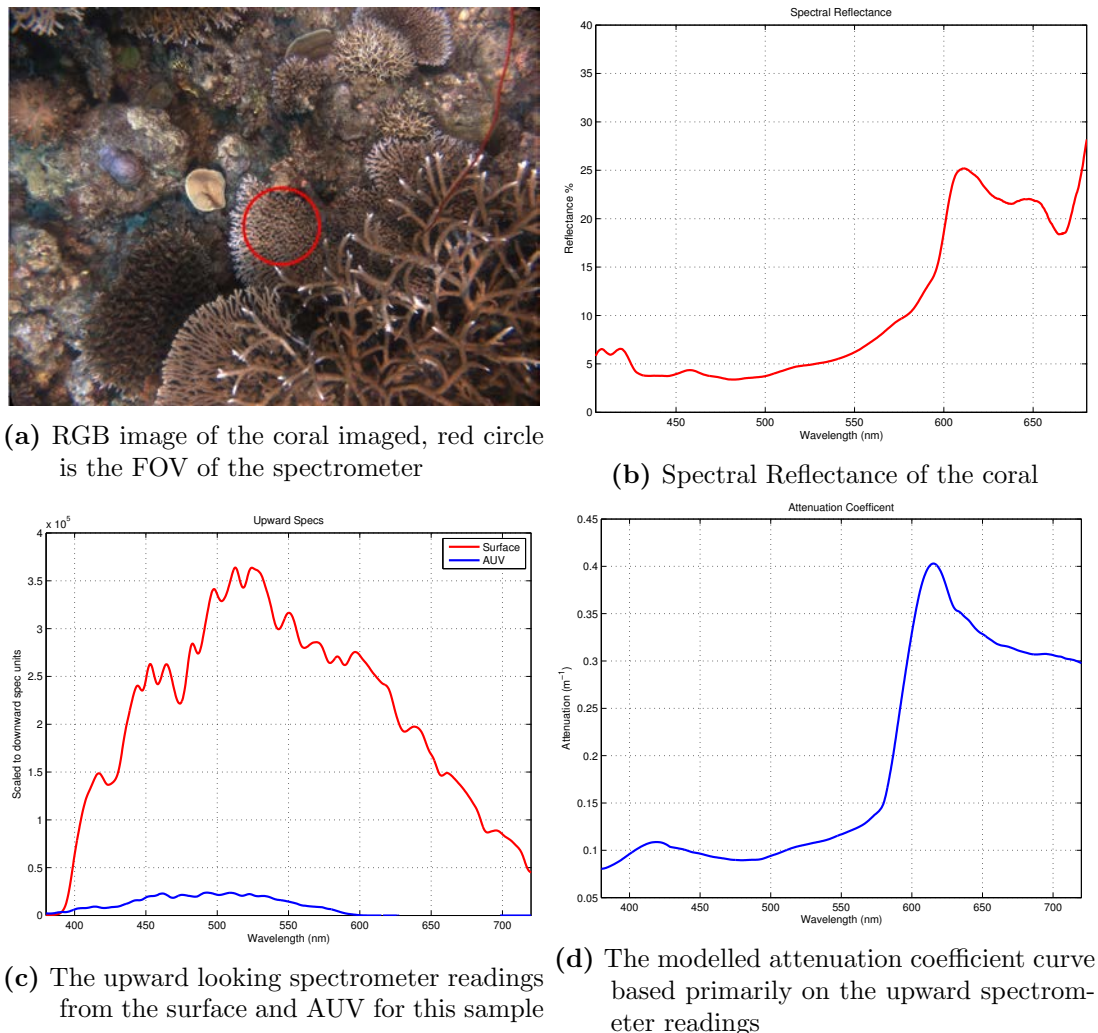


Figure 4.25 – Spectral reflectance of *Agropora Cytherea* coral

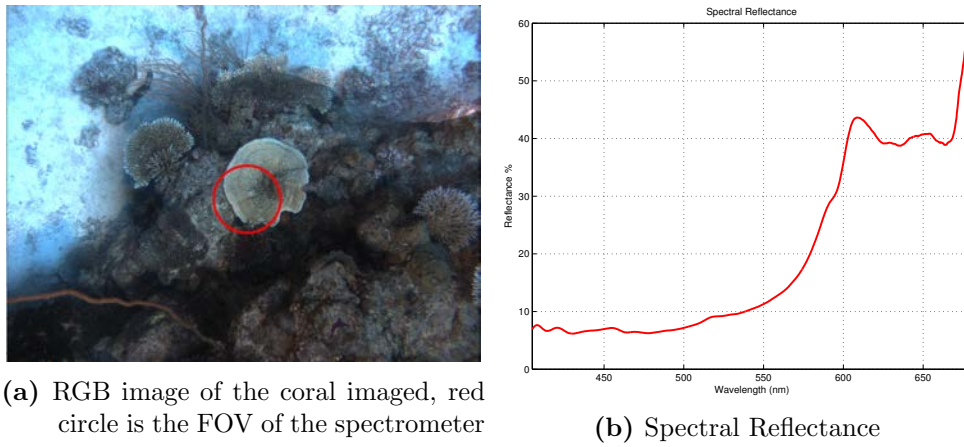


Figure 4.26 – Spectral reflectance of Montipora coral

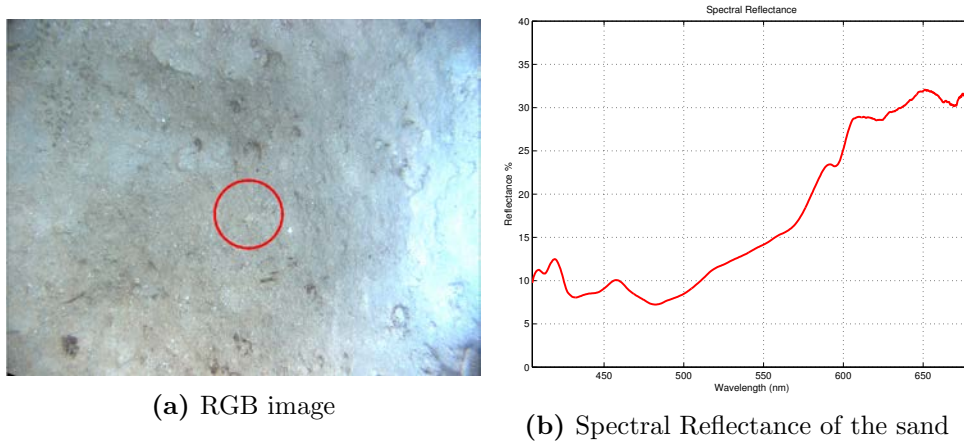


Figure 4.27 – Spectral Reflectance of the sand

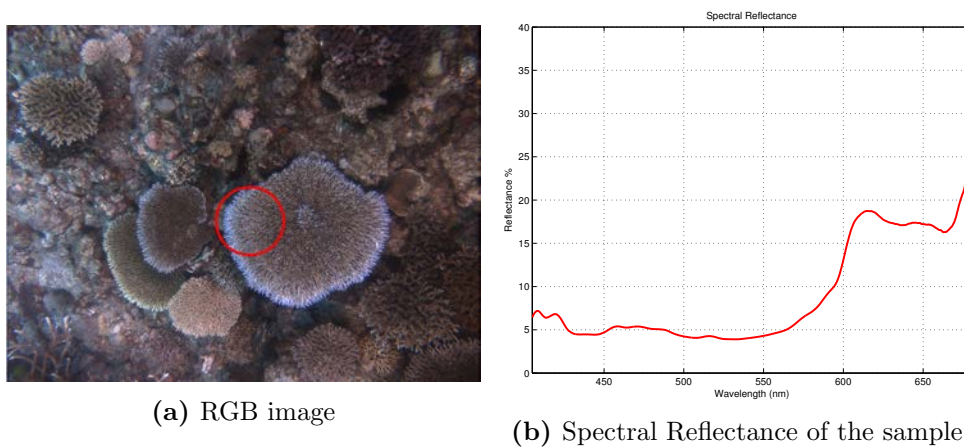


Figure 4.28 – Spectral reflectance of Acropora coral from our collected dataset

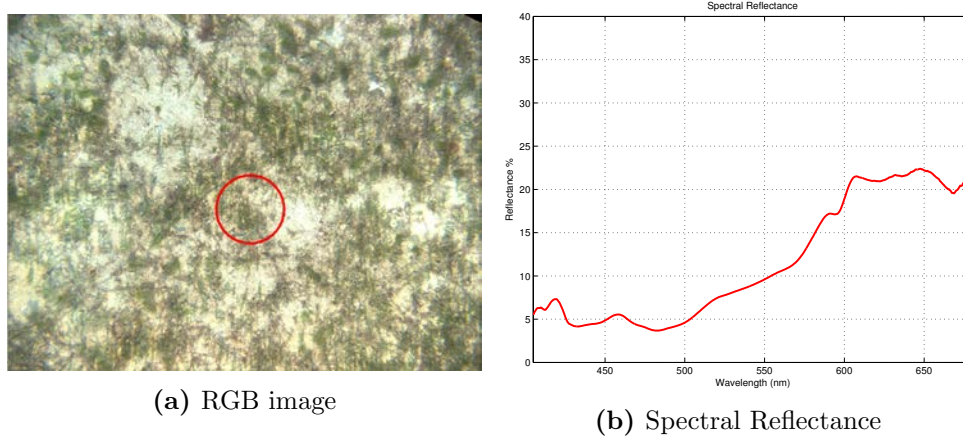


Figure 4.29 – Spectral reflectance of seagrass

Challenges in AUV spectral results validation

During the AUV survey missions the vehicle was operating at depths over 25m. This means it is dangerous and a logistically difficult task to obtain ground truth data for the areas being mapped. One method of demonstrating the validity of the reflectance results is through expert labelling with further classification to examine spectral consistency. The other is through comparison of the resultant spectra obtained through the proposed method to that published in the literature [166]. These spectra from the literature were also collected on the Great Barrier Reef near Heron Island, approximately 720km from our survey site.

A comparison is complicated due to the different methods of obtaining the spectra. In this work the AUV is measuring from a distance of 2 metres whereas the result cited in the literature involve a measurement from approximately 5cm (to be then used for classification from aerial heights). The literature methods measuring at 5cm do not take into account IOPs. The degree to which the literature measurements were altered by this small body of water is unknown and unaccounted for.

For each of the measurements in this work the degree of purity of material varies. Leiper *et al.*[124] makes the comment that spectra measured in-situ are only valid for the data set for which they were acquired because much of the light and water interactions were not measured. It has been observed that in the upper green section of the spectrum (550-600nm) the spectra from this work tend to be more attenuated than that of the literature. This was most likely due to the correction processes adjusting more heavily than should be performed. This however is not a big issue due to the whitening process before classification.

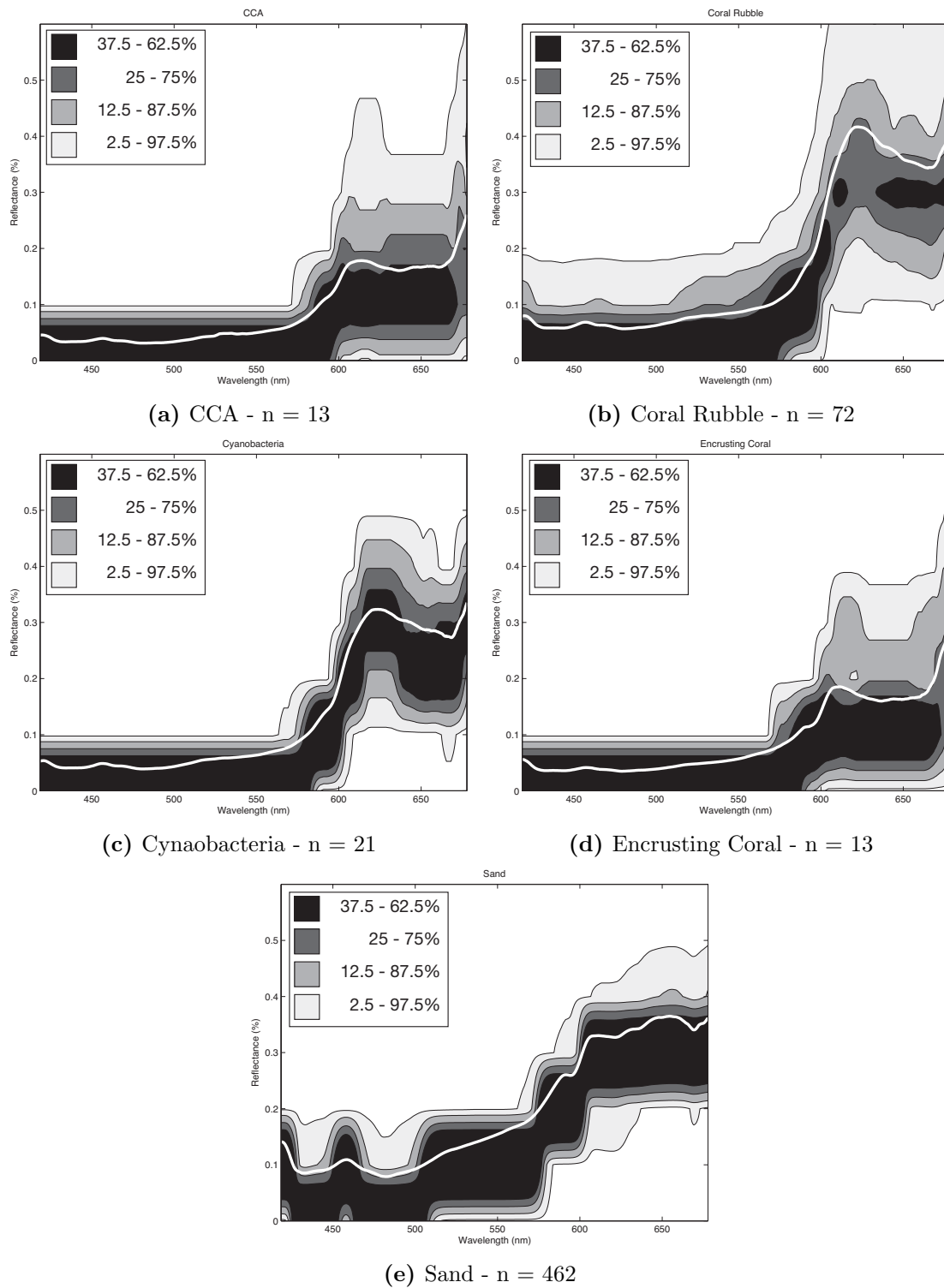


Figure 4.30 – Spectral reflectance of various benthic types, the shaded regions show the variance of the spectra in the class sets, and the white line shows the mean of the data. Light gray represents 2.5 - 97.5% of the data, medium grey: 12.5 - 87.5%, dark grey: 25 - 75% and black 37.5 - 62.5%. n denotes the number of samples of that class.

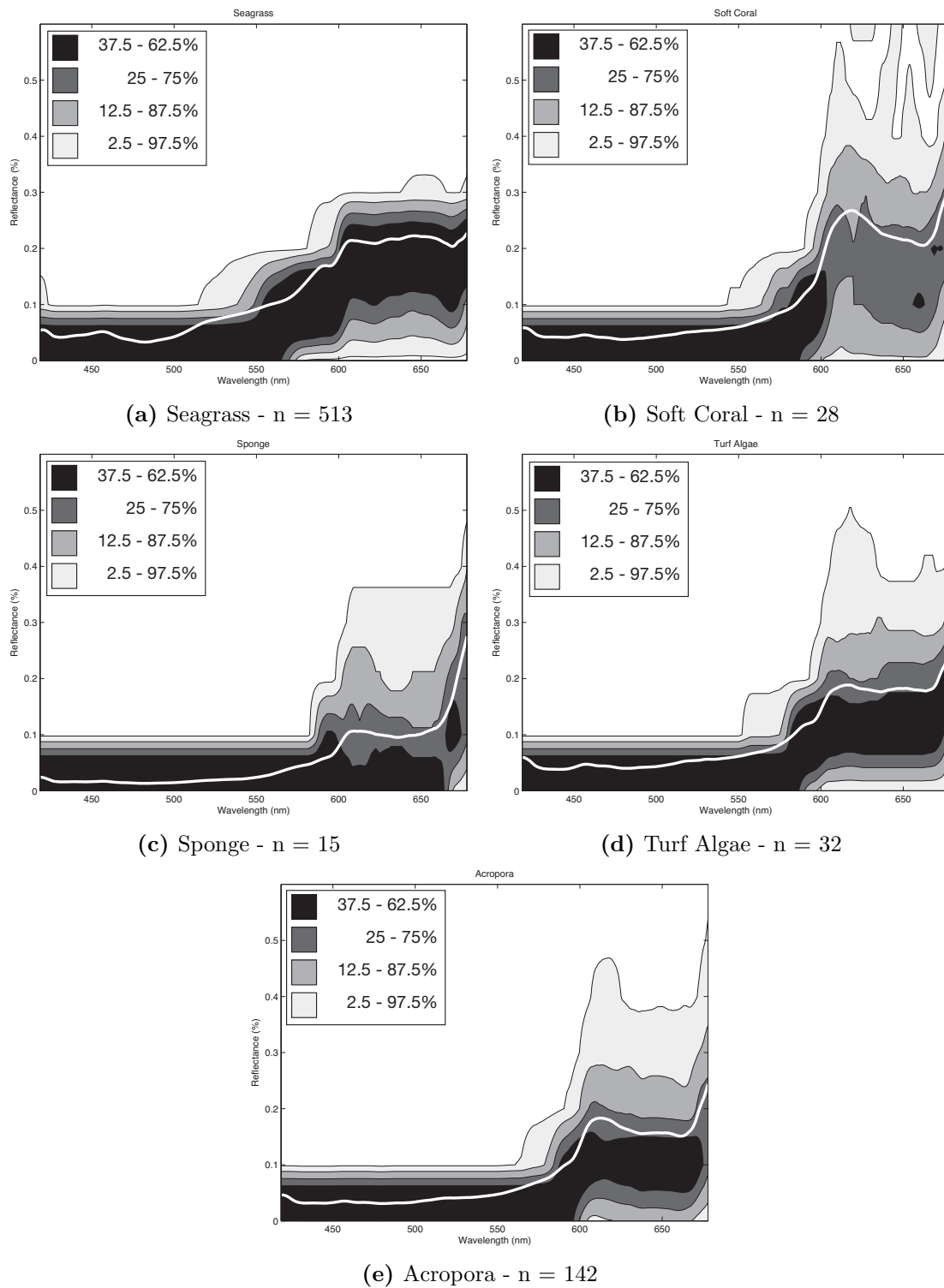


Figure 4.31 – Spectral reflectance of various benthic types, the shaded regions show the variance of the spectra in the class sets, and the white line shows the mean of the data. Light gray represents 2.5 - 97.5% of the data, medium grey: 12.5 - 87.5%, dark grey: 25 - 75% and black 37.5 - 62.5%. n denotes the number of samples of that class.

As a result feature separability is still being maintained. In the other bands 400-550nm and 600-700nm it has been found that the spectra from this work match reasonably well.

For the mentioned reasons a comparison can be challenging. The validation of the spectra has primarily been done in this work through the use of classification. A large number of spectra were hand labelled by an expert. This labelling could be done because there was corresponding colour imagery to match. From this labelling several classifiers were trained and cross validation was performed. This test revealed how separable the spectral clusters for a particular label are from other groups of spectra with different labels. This process is revealed in much more detail accompanied by results in the next Chapter in Section 5.2.

4.5 Summary

In this chapter a method for colour correction was presented. This method uses a water model parametrised by an in-situ optical system. The method was validated using three different scenarios of varying realism and control. The corrections were found to perform well for a test tank setup and in an outdoor ocean swimming spot with a single distance to the scene. The performance was evaluated by comparing the correction of the colour of a colour chart to an image of the same chart taken out of water but under the same illumination.

The method was also implemented on an AUV. The AUV had a stereo camera which delivered 3D scene information. The colour correction method was able to utilise this structure information to allow for structure invariant colour correction. The 3D structure information produced better results for complex scenes than making a single distance assumption. Results were presented which showed good performance over a range of scene structures.

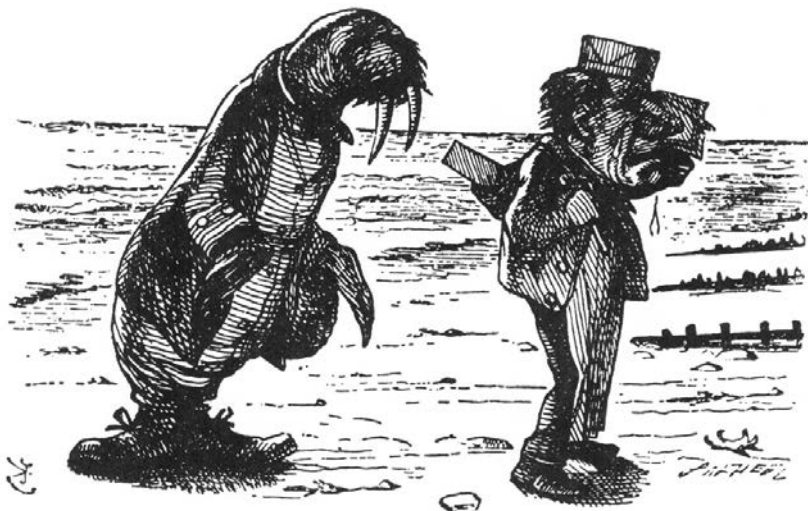
The water attenuation correction was then applied to hyperspectral data from a spectrometer mounted downward towards the seafloor on an AUV. The use of a downwards facing spectrometer allowed for good signal-to-noise while not sacrificing spatial resolution too heavily. It was also easier to implement and cheaper than a full hyperspectral camera given the restrictions on size, power for the light source, onboard storage/processing power and cost.¹² Spectral reflectance was recovered using models for the scene illumination and water. The ability to recover spectral reflectance of the seafloor was demonstrated with several examples from an AUV coral reef mapping expedition over a coral shoal on the GBR.

Above water hyperspectral imaging of the ocean benthos presents some challenges, including limited spatial resolution, air-water interface artefacts, weather reliance, time of day dependence, and depth limitation due to the attenuation of the water column. The ability to image in the hyperspectral domain in-situ largely overcomes these limitations. An AUV is an ideal platform for this application. It is able to travel to depths beyond the euphotic zone. Also its operation is not weather dependant and time of day dependence is eliminated due to self-powered on-board illumination. It also images 2m off the seabed so it achieves excellent spatial resolution and minimises the optical attenuation from the water.

¹²Comparing the Ocean Optics USB2000+ to a small hyperspectral camera available on the market (Headwall Photonics - Nano-HyperSpec <http://www.headwallphotonics.com/spectral-imaging/hyperspectral/nano-hyperspec/>). Cost: USB2000+ - \$5000 vs Nano-HyperSpec \$100k, resolution: 16-bit vs 12 bit, data per frame: USB2000+ - 4096 bytes vs 230,400 bytes, power: 1.25W vs 10W, volume: 696 cm³ vs 194 cm³, pixel bin size: 14 μ m \times 200 μ m vs 7.4 μ m \times 7.4 μ m.

Chapter 5

Spectral-based classification & mapping



5.1 Introduction

In the previous chapter a model of the water column was developed using upwards looking spectrometers. This allowed for the correction of the downwards looking spectrometer data. An illumination model could also be estimated which allowed for the recovery of the spectral reflectance of a small patch on the seabed. Using this same water model, imagery from a

conventional colour camera in the Red-Green-Blue (RGB) domain could be corrected also for the water's attenuation effects.

In this chapter the spectral reflectance curves are brought together with the colour corrected RGB imagery to create benthic habitat maps of large areas of the seafloor as surveyed by an Autonomous Underwater Vehicle (AUV). The ability to resolve subpixel (hyperspectral pixel) materials is also explored and new methods for informed spectral unmixing are presented.

5.2 Spectral and spatial classification

In the previous chapter a method was presented for recovering the spectral reflectance of measurements of the seafloor taken from an insitu platform. To demonstrate the effectiveness of this method, a spectral library was created and subsequent classification performed on the dataset. The dataset contained over 14,000 spectra and image pairs of which approximately 1,400 images were hand labelled by a coral expert, Dr. Tom Bridge (James Cook University, Queensland, Australia) [32–35]. The labels were a mixture of classes representative of the benthic stratum types present in the dataset. 10-fold cross validation [119] was used for the training of the classifier. Several of the major supervised classification techniques such as Support Vector Machines (SVM), Decision Trees, K-Nearest Neighbours (KNN), Ensemble Boosting and Bagging were implemented.

The classifiers were initially trained only on spectral reflectance data. To improve the performance of the classifier the spatial information provided by the imagery from the stereo cameras was also used as well as the first and second derivative of the spectra. To generate the spatial classifier features a Local Binary Pattern (LBP) was performed on the disc of benthos encompassed by the spectrometer's Field-of-View (FOV) (the calibration was covered in Section 3.2). LBPs are a technique of deriving a descriptor for the texture of an image [149] and have been used with good success in computer vision image classification [20, 211]. LBP's have two major adjustments parameters: the radius of the circle to be evaluated and the number of points in that circle. LBPs examine how the chosen points in the circle vary from the pixel under test (in the middle of the circle). Then the texture gradient is examined from multiple angles to ensure it is rotationally invariant. The LBP is performed for every pixel in a given image.

Two LBPs were computed on the image spot which corresponded to the FOV of the spectrometer in the FOV of the stereo camera. One LBP had a radius of 1 pixel with surrounding 8 points and the other with a radius of 3 pixels with surrounding 8 points. This combination was chosen based on its success in the literature with classifying underwater imagery from an AUV [21]. The histogram of both LBPs were added to the feature matrix for classification. Feature selection was performed while training the classifier to ensure the greatest inter-class variability in the feature matrix. Feature selection [65] is a computationally intensive process where different combinations of the features are removed with the objective function being to maximise the performance of the classifier. When testing and training, the dataset was whitened by subtracting the mean and dividing by the variance at the feature level.

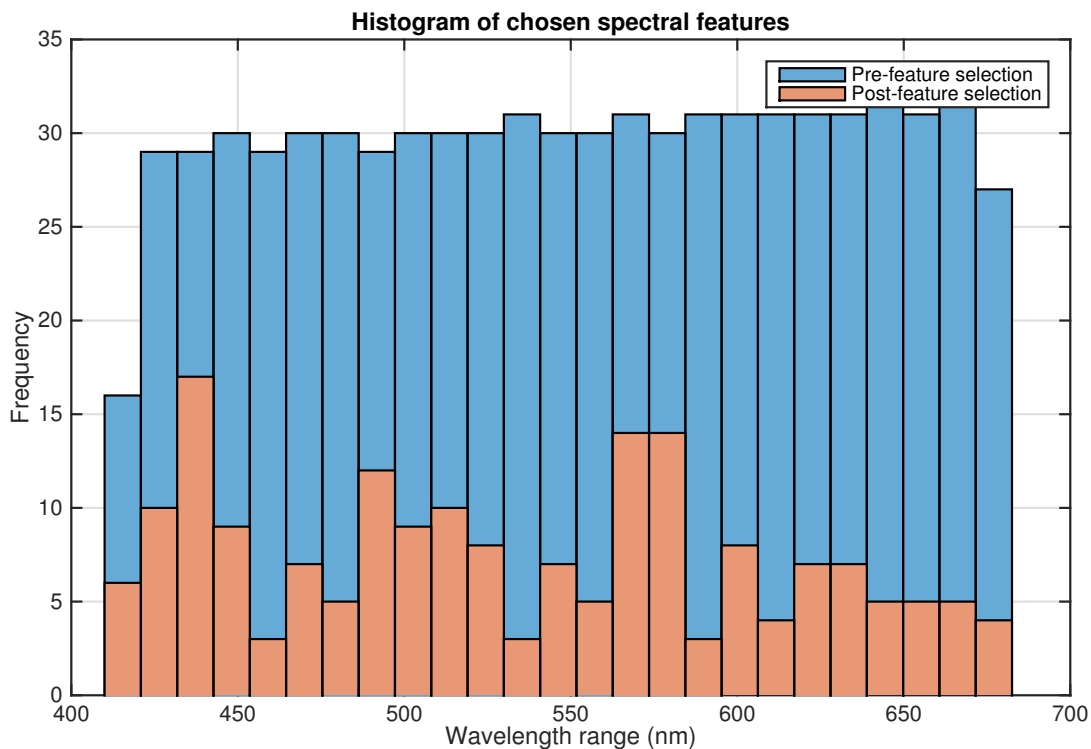


Figure 5.1 – A histogram of the spectral features chosen as a result of the feature selection process (post-feature selection). Also shown are the spectral feature prior to feature selection.

Feature selection was performed on the spectral and LBP features which encompassed 741 spectral bands from 415 - 680nm and the 2 LBPs: radius 1,8 points (1,8) and radius 3, 8 points (3,8) which made up 76 texture features. The best 200 features were chosen, of these

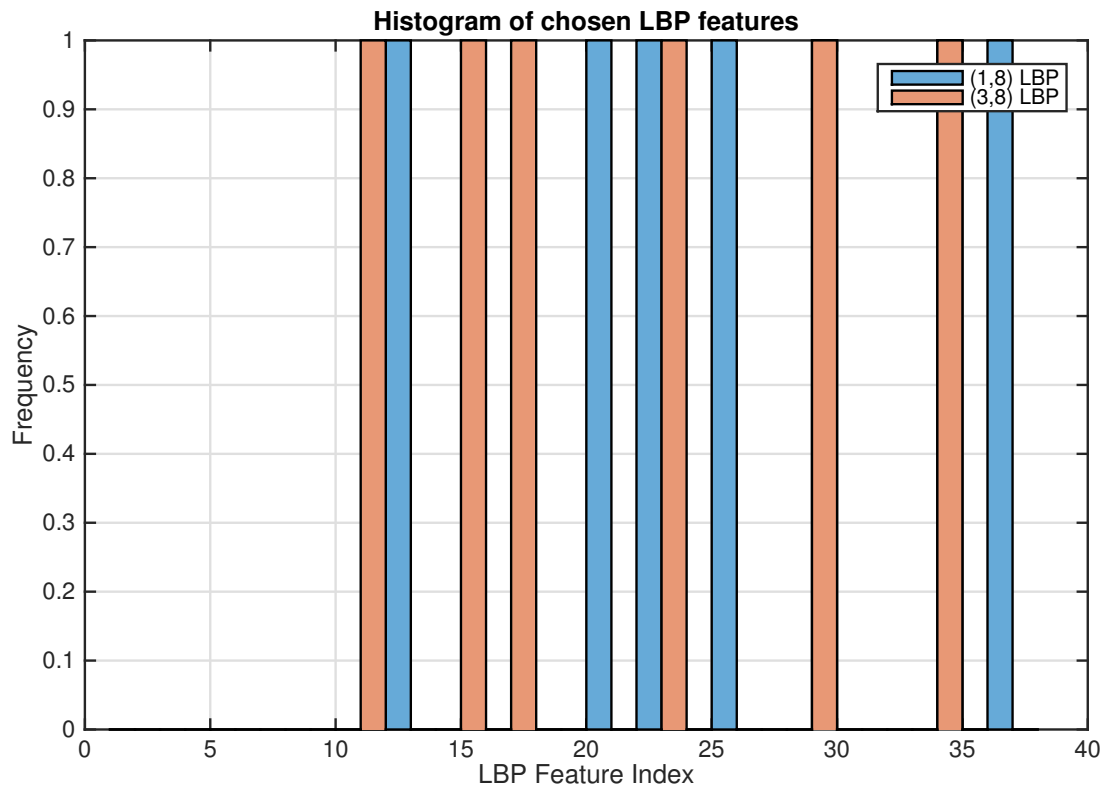


Figure 5.2 – A histogram of the LBP features chosen as a result of the feature selection process. Two LBP’s were implemented: one with a radius of 1 and 8 points, and the other a radius of 3 with 8 points. Note there are two overlapping LBP features at 29 and 34.

187 were spectral features and the remaining 13 were LBP features.

Figure 5.1 shows a histogram of which spectral features were chosen (Post-feature selection). This shows three spikes of spectral content, features around 430nm, 490nm and 570nm. This indicates that the best feature separation with this particular dataset occurs around these frequencies.

Figure 5.2 similarly shows a histogram of the LBP features. This shows which elements of the LBP histogram were chosen for the two LBPs. The first (1,8) LBP appears to be centred around index 22, whereas the (3,8) LBP appears to be centred lower, around 17. This suggests the best texture features are physically fine or small textures.

5.2.1 Classification performance

The performance of several classifiers were compared using LBP, Hyperspectral (HS) and combined LBP & HS features in training and validating the classifier used in this work. Table 5.1 shows these results. It was found that a Linear Support Vector Machine (SVM) with HS and LBP features performed the best with a classification accuracy at $91.99\% \pm 2.32$.

To provide a baseline for how colour can be used to classify substrate types, RGB was included for comparison. The RGB imagery was corrected for water attenuation and just the mean RGB values were used as features. RGB does surprisingly well given the low dimensionality of the feature set. This is a rather naive feature as it does not contain any texture information or a large degree of spatial information. RGB is not used in the HS classification. It is only included for comparison.

Just using LBP it performs quite well using the Ensemble Boosting method with a correctly classified rate of 82.38%. In comparison just using HS, it performs better (91.69%) than a LBP using a Linear SVM, Ensemble Boosting also performs well for HS only classification. When examining the combined HS + LBP the performance is not much higher than just HS alone. The error margin is slightly larger as well, this may suggest some small disagreement between the HS and LBP features. This makes sense given they are very different features, one is hyperspectral reflectance while the other is image texture. The polynomial, sigmoid kernel, and radial bases function SVMs, are all non-linear versions of the SVM algorithm, what is interesting is they perform worse than the linear counterpart. The reason for this is the high dimensionality of the HS data. With hundreds of HS features it can be linearised.

Table 5.2 shows the confusion matrix for the Linear SVM (LBP+HS) trained classifier. A confusion matrix shows the true class of a data point versus the predicted class. The confusion matrix can explain some reasons for a suboptimal classification: Coral rubble is mostly predicted accurately (84.7%), however it is also predicted to be Algae, Acropora Grandis, Other Corals and Acropora. This could be due to coral rubble being made up of broken dead corals mostly covered in algae. Seagrass was sometimes misclassified (2.1%) because images of seagrass also contain sand. Turf algae was misclassified as coral and rubble (28%) because turf algae is often present over most underwater surfaces. Soft coral was being misclassified as Acropora (39.3%) most likely because the process is picking up

Classifier	RGB	LBP	HS	HS + LBP
Linear SVM	39.13% \pm 0.51%	73.30% \pm 1.79%	91.69% \pm 1.75%	91.99% \pm 2.32%
Polynomial SVM	39.13% \pm 0.52%	39.13% \pm 0.53%	88.41% \pm 1.81%	88.48% \pm 2.99%
SVM Sigmoid Kernel	39.13% \pm 0.46%	39.13% \pm 0.41%	71.32% \pm 1.67%	71.40% \pm 1.77%
SVM Radial Basis Fn	39.13% \pm 0.48%	39.66% \pm 1.02%	39.13% \pm 0.54%	39.13% \pm 0.34%
KNN	84.59% \pm 1.47%	79.79% \pm 3.67%	86.73% \pm 1.91%	86.80% \pm 1.13%
Ensemble Boosting	82.61% \pm 2.07%	82.38% \pm 2.42%	91.00% \pm 2.28%	89.24% \pm 2.56%
Ensemble Bagging	82.68% \pm 1.13%	81.08% \pm 3.22%	90.92% \pm 1.49%	89.40% \pm 1.30%
Decision Tree	84.67% \pm 2.20%	78.72% \pm 2.20%	88.56% \pm 2.36%	88.02% \pm 2.08%

Table 5.1 – Classification performance for the 1311 data points from the hand labelled data.

The performance from several different classifiers with feature selection performed are shown. The table shows the results from using 10-Fold cross validation on the hand labelled data points. A linear SVM performed the best on a combination of hyperspectral reflectance data (HS) and LBP. We can see from this table LBP does not contribute much to the performance of the classification over just using HS. Classification results are shown with \pm the 1st standard deviation.

on a pigment common to most corals [77, 87] and the small number of samples of soft coral. There will also be confusion due to the relatively large spatial coverage of the spectrometer’s FOV. It will often cover more than one material. The spectrometer’s FOV has a diameter of approximately 30cm when imaging the seafloor from a height of 2m. This spatial attribute can also explain the poor performance in some classes. CCA, turf algae, encrusting coral, soft coral and cyanobacteria performed poorly. Most of the time they are smaller than the FOV of the spectrometer. This would result in spectral mixing. The material they are mixed with will change and thus the spectra for these materials will not be consistent leading to classification errors. To overcome this, either a finer spatial resolution is needed or closer measurements of the substrate are needed. For the larger materials such as seagrass, sand, coral rubble and Acropora they all perform well under the 10-fold cross validation due to the reduction in spectral mixing. The limited spatial resolution can be a problem for identifying these smaller materials in the scene. This leads to using spectral unmixing to assist in classifying materials at the subpixel level which is explained ahead in Section 5.4.

5.3 Spectral mapping

Through the motion of the AUV a series of spectral measurements were built up along the transect of the survey. The vehicle typically travels at 0.5m/s [204] and samples were taken at 1.5Hz of both the stereo cameras and the spectrometer, with the scene illuminated by the

		Actual class									
		CCA	Seagrass	Sand	Coral Rubble	Turf Algae	Acropora	Encrusting	Sponge	Soft Coral	Cyanobacteria
Predicted class	CCA	6	0	0	0	6	0	2	2	2	0
	Seagrass	0	502	3	1	0	1	1	0	0	0
	Sand	0	11	455	1	0	0	0	0	0	0
	Coral Rubble	0	0	4	61	4	0	1	1	4	6
	Turf Algae	4	0	0	5	15	3	3	0	0	3
	Acropora	1	0	0	0	4	130	4	2	11	0
	Encrusting	2	0	0	0	1	2	2	1	1	0
	Sponge	0	0	0	1	0	2	0	9	1	0
	Soft Coral	0	0	0	1	0	4	0	0	9	0
	Cyanobacteria	0	0	0	2	2	0	0	0	0	12
	class size (n)	13	513	462	72	32	142	13	15	28	21
	% correctly predicted	46%	98%	98%	85%	47%	92%	15%	60%	32%	57%

Table 5.2 – Confusion matrix for the classification model using a linear SVM with HSI and LBP data. The model was trained using 10 fold cross-validation on the hand-labelled dataset. CCA - Crustose Coralline Algae, Encrusting - Encrusting Corals. The major classes: Seagrass, Sand, Rubble, Turf Algae and Acropora perform very well, the other smaller classes do not, believed to be in part due to their small numbers to train the classifier. These particular classes were rare in the dataset.

strokes at either ends of the AUV. Figure 5.3 shows the proximity of subsequent spectral measurements over an area of reef. The red circles indicate the FOV of each spectrometer measurement. An AUV mission typically is run in one of three configurations [157]: first is a long single transect with a length in the order of several kilometres; secondly a broad scale sparse grid with a size 500-1000m on a side, and thirdly for comprehensive coverage the AUV conducts a ‘mow the lawn’ pattern in a dense grid pattern. The grid is typically of the order of 25m x 25m.

To visually demonstrate the classification of benthic material types, the labels obtained from the classifier have been overlaid on a subset of the mosaicked colour corrected imagery. The size and location of the circle is representative of the FOV of the spectrometer for that point on the survey. This will give the reader a better visual intuition as to the performance of the presented method. Figure 5.7a shows a section of the survey mission over a sand to seagrass transition. This section of seafloor data was new to the classifier and so was not trained on.

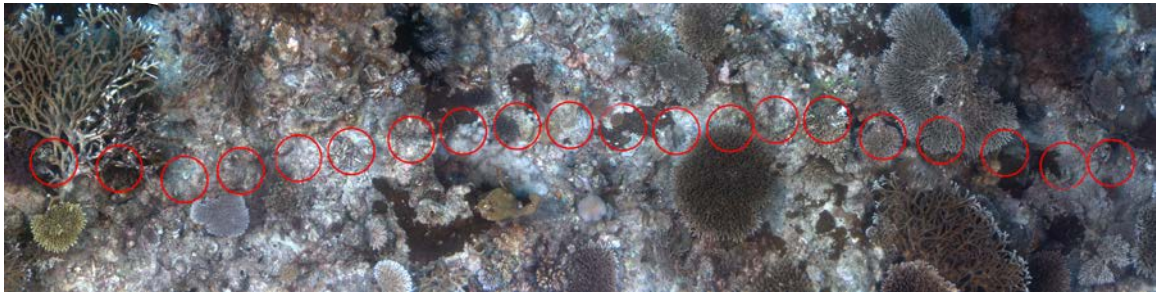


Figure 5.3 – This is a mosaic of a series of consecutive images showing the proximity of subsequent spectral measurements over an area of reef. Red circle indicates the FOV of the spectrometer measurements.

This demonstrates the typical classification performance by using the classifier trained on other sections of similar substrate. The incorrectly classified labels have been denoted on the image with a red asterisk. Some misclassification can be seen in Figure 5.7b of soft coral (just after the sandy patch but before the *Acropora*) but besides this point, the classifier manages to classify the rest of the scene quite accurately. It was found that the classifier could label the major substrates with good accuracy, but small class sizes suffered. This was also reflected in the confusion matrix, shown in Table 5.2. The reduced performance on the minor substrates was due in part to the number of training samples in the model (there were many more sand and seagrass samples than CCA). Figure 5.7c demonstrates the classification performance over a different section of coral reef.

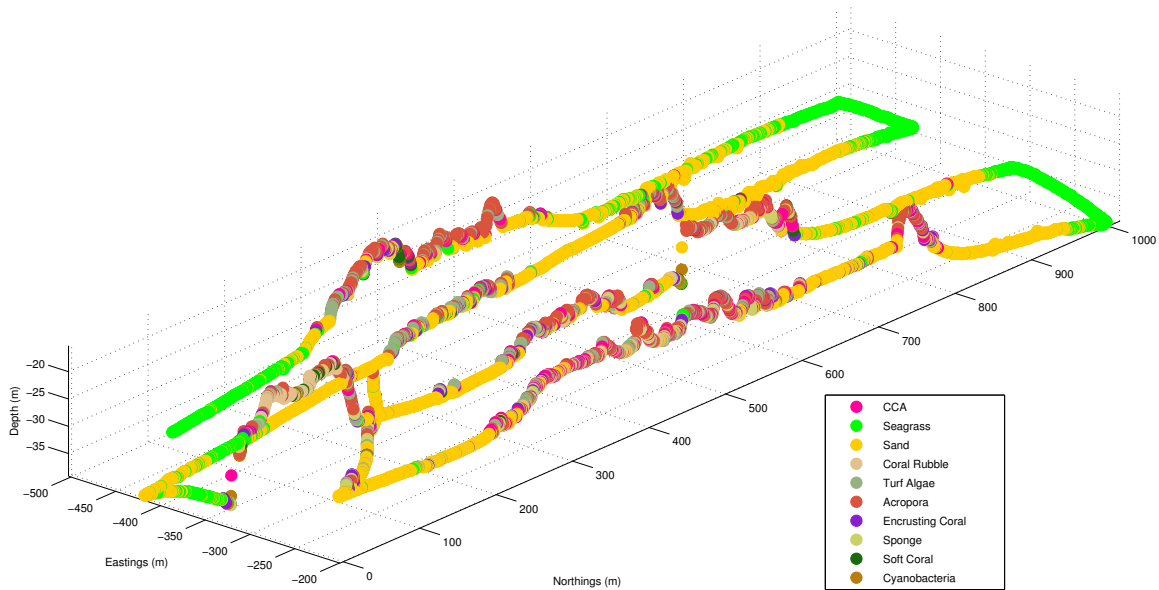


Figure 5.4 – Spectral map from an isometric angle showing the altitude distribution of the benthic types. The altitude has been amplified by a factor of 5 to demonstrate the class distribution as a function of altitude further. The key for the class labels is on the left. This dataset contains over 14,000 points, due to the size limitations of this medium, the entire detail of classification can not be fully shown in this figure. More detailed figures of subsets of the map are shown in Figure 5.7.

5.3.1 Benthic habitat map

For each spectral point measured, the position of the AUV was also recorded with position derived using a combination of data from the USBL, DVL, depth and attitude data and further corrected using the SLAM framework. [204]. Figure 5.4 shows the eastings and northings map of the survey. For each point, the spectral reflectance of the point on the seafloor was resolved.

Some biological inferences which can be drawn from this dataset are: *Acropora* tended to occur around the higher altitude areas on top of the coral outcrops, where as seagrass was growing in the lower altitude sandy patches. Coral rubble patches were more prevalent on the exposed eastern side of the reef. This makes sense given the location of this dataset. Storms in this area often come from the south-east and this was at the edge of a large flat sandy expanse. On the western side more *Acropora* is growing. It may be hypothesised that this was because it was protected by the eastern edge.

Being able to map coral reef regions at fine resolutions such as this section allows for finer

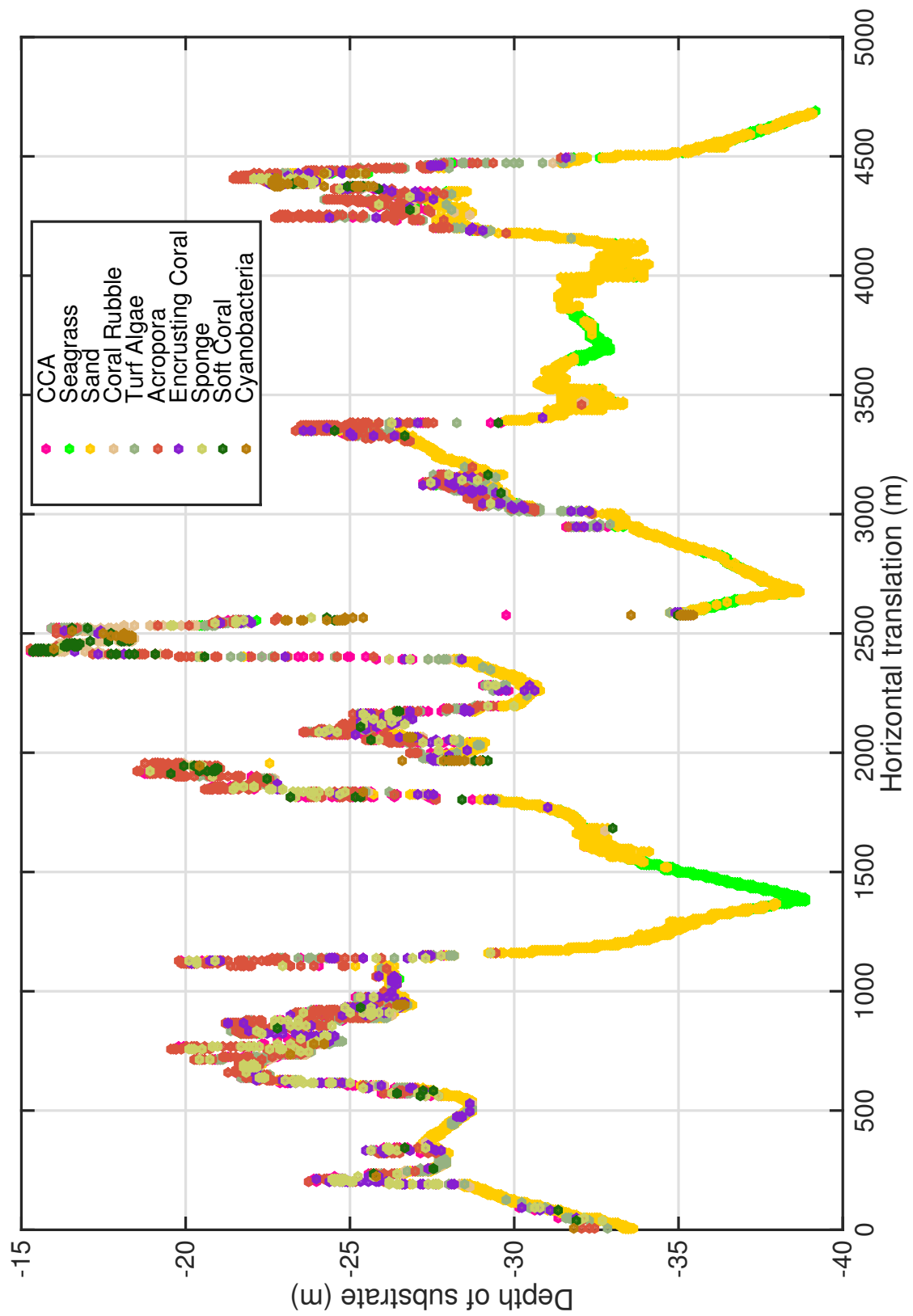


Figure 5.5 – Spectral map from a horizontal view. In this view the entire track has been stretched out horizontally. Horizontal translation represents the distance the AUV is along the track.

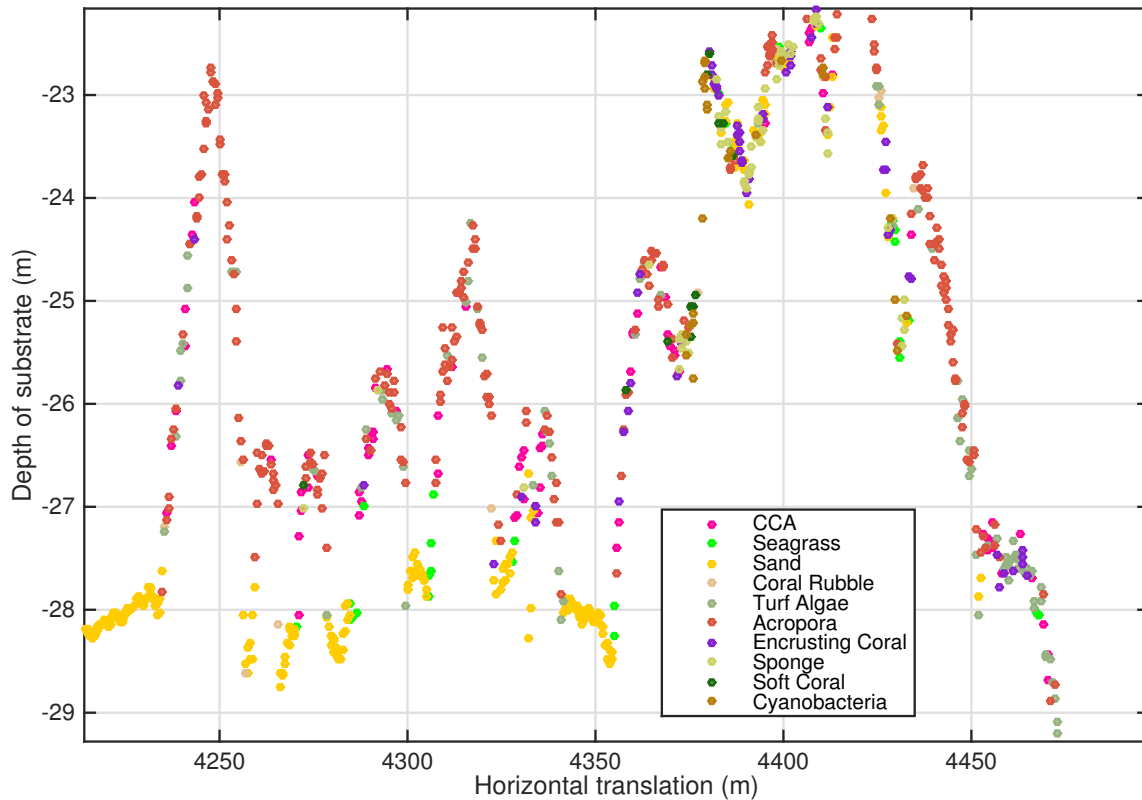


Figure 5.6 – A zoomed in section of the spectral map, better showing the spatial detail of the map. Each coloured dot represents a spectral reading.

investigations about the various indicators of the biological health or productivity of a region to be conducted. In this survey the region was about 1000m x 300m. There was over 14,000 labelled spectral points in this map.

Figure 5.5 shows the same spectral map from a horizontal view point. The track has been stretched out horizontally showing the distance travelled along the survey path. Figure 5.6 shows a zoomed in section of the spectral map. It better shows the spatial detail of the map.

5.4 Spatially assisted spectral unmixing

One of the limitations discovered in the previous section was due to multiple materials within the FOV patch of the spectrometer misleading the classifier. This results in spectral mixing. An overview of the background and current literature on spectral unmixing is provided in

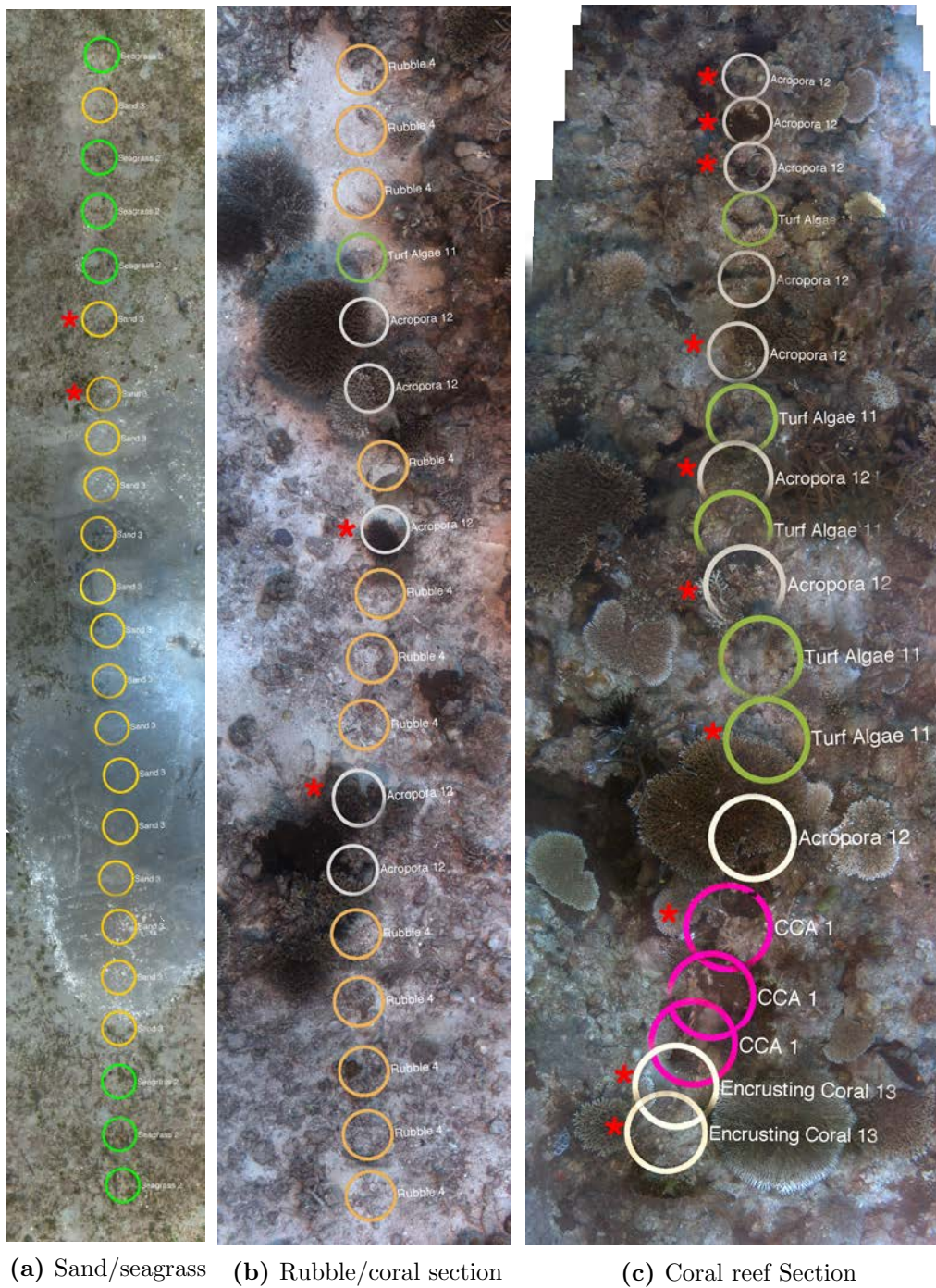


Figure 5.7 – (a) Mosaic of a small section of the classification prediction, this shows a transitional section of sand to seagrass. Yellow circles signify a label of Sand, and Green is the label for seagrass. (b) & (c) Mosaics of a small section of the classification prediction, this shows a section of coral reef. They show the transition from sandy substrate to coral and algal substratum. The Red asterisks indicate a misclassification.

Section 2.7. Many traditional methods of spectral unmixing do not rely on the large degree of information contained in the spatial component of the hyperspectral imagery, however there has been a large move in Hyperspectral Imaging (HSI) processing towards utilising this rich source of information [181]. The imaging module in the presented system differs from most HSI imaging platforms in that a very low spatial resolution spectrometer was combined with a very high spatial resolution RGB camera. Due to the relative sparsity of the HSI measurements with the spectrometer the spatially assisted unmixing methods [181] generally cannot be used. However in this work a new method was developed which utilises the high resolution RGB imagery to provide information about the components within the imagery. This in turn informs the spectral unmixing process. Usually unmixing methods do not know anything about what is within the FOV of their sensor. Results are presented which show that this unmixing method performs better than methods from the literature.

The process which informs the unmixing algorithm reveals the number of endmembers within the FOV of the spectrometer as well as their relative abundance and position within the FOV. Other methods are blind to the sub-pixel contents. They rely on a fitting process to determine the subpixel materials. The method used for informing the unmixing method developed in this work uses an existing algorithm for image and contour segmentation [10]. This information provides constraints for the unmixing process. This new method for informed spectral unmixing has been named Image Segmentation Assisted Constrained Spectral-unmixing (ISACS).

As discussed in the spectral unmixing background there are several mixture models which can be used which are dependant on the physical circumstances. A linear mixture model was chosen in this case due to several reasons. Firstly most of the literature is based around the assumption of a linear mixture model. Relating specifically to underwater spectral unmixing, it has been said that a linear mixture model is adequate for the underwater environment [124]. Secondly the computational complexity is much lower, and lastly the water and the environmental conditions under which the data were acquired are conducive to a linear mixture model.

One of the reasons the conditions are conducive to a linear mixture model is due to the underwater platform providing artificial lighting in addition to ambient illumination. This results in an even coverage of light over the scene with minimal shadows. Shadows are often a large source of non-linear mixing, this is due to light scattering off other objects illuminating

the shadow areas (second order illumination) [80]. Another reason is the imaging platform (AUV) imaged close to the seabed (2 metres) and in very clear tropical waters so scattering and absorption were minimised.

5.4.1 Resolving number of materials

The RGB imagery provides higher spatial resolution than the spectrometer. This allowed for the imagery to provide hints as to the content within the FOV of the spectrometer. Image segmentation was used to partition the patch into the different materials contained within a scene. A method which provided weighted and closed regions in the segmentation was needed. A method suitable to perform this task was the *gPB-owt-ucm* algorithm [10].

In this algorithm contour detection and image segmentation were done by deriving contours from the brightness, colour and texture gradients at different scales. The segmentation was then performed by using an oriented watershed transform [168] to join the contours to create an Ultrametric Contour Map (UCM). The UCM has the desirable characteristics of ensuring regions are always closed and each region is uniquely weighted to represent its edge contour strengths. This created a hierarchy of strong regions in an image which could then be thresholded to reveal a varying number of regions.

The contour detection algorithm [10] was used on the RGB imagery which was in the FOV of the spectrometer. The location of the spectrometers FOV within the FOV of the RGB camera was determined during the calibration routine covered in Section 3.2. Regions were picked out of the UCM by defining a minimal edge strength, a maximum number of materials and minimal size of materials. By examining several hundred images a threshold was chosen to best segment typical benthic materials. The output from the segmentation process was the number of materials in the patch, their relative abundance as a percentage of the patch area and their spatial location within the patch.

Figure 5.8 shows an example of the UCM from the *gPB-owt-ucm* algorithm on an image from the coral reef dataset. This shows the number of materials present within the scene, their abundance and location. More examples are shown later in this Chapter in Figures 5.22 - 5.24.

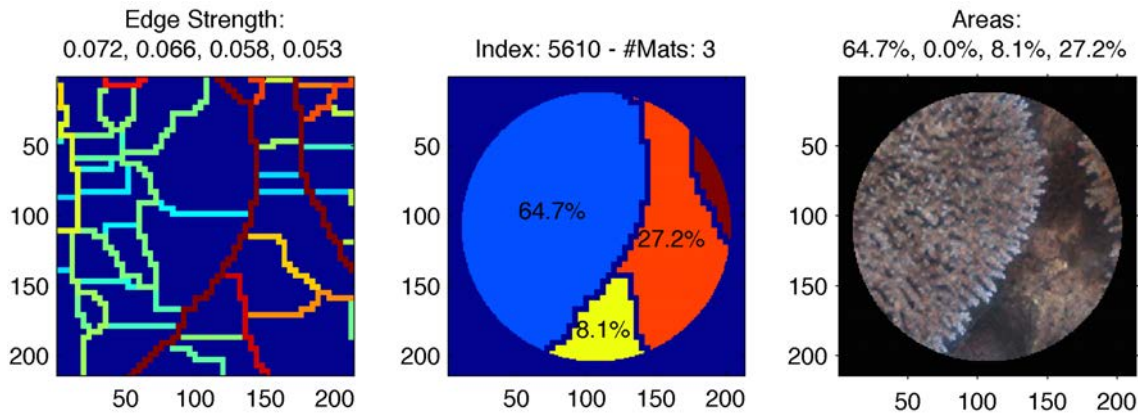


Figure 5.8 – An example of segmentation using the *gPB-owt-ucm* algorithm, the image on the left is the UCM from the output of the segmentation algorithm, the lines are in increasing edge strengths. Dark red is strongest, decreasing through yellow, green, blue to the weakest edge in dark blue. The middle image is the thresholded UCM map filled in for 3 regions which were greater than 5% of the patch area. In the right of this image is a region which does not satisfy the minimal area constraint, it has been cut out by the threshold. The right image is the colour corrected RGB image of the scene cropped to the FOV of the spectrometer.

5.4.2 Informed and constrained unmixing

The additional information gathered through the mentioned segmentation process provided constraints when finding the combination of materials present in the spectrometer patch. Traditional methods using least squares assume that all materials in a library could be present but just in very small quantities. With the extra information about the number of materials k and their abundances α , an exhaustive search can be done to find which k materials best fit to the linear mixture model. This is the underlying technique in the proposed ISACS method. The number of combinations to search for is N^k where N is the size of the spectral library and k is the number of materials present in the scene. The method to evaluate which combination is best is performed by equating the Spectral Angle Mapper (SAM) score [52] and the Euclidean distance error score [43]. Two metrics are chosen to minimise error due to noise and lighting changes.

SAM (as shown in equation 5.1) calculates the cosine angle between the measured spectra and the mixture combination obtained through the search. The advantage of using the SAM distance metric is that it is more invariant to lighting differences (constant offsets) [125]. The Euclidean distance metric is measuring the Euclidean distance between these same two spectral vectors. The choice of SAM and Euclidean metrics was also due to their

low computational cost.

$$SAM = \cos^{-1} \left(\frac{\vec{t} \cdot \vec{r}}{\|\vec{t}\| \cdot \|\vec{r}\|} \right) \quad (5.1)$$

The Euclidean metric has the advantage of being less sensitive to noise on the spectra. Noise on the spectra could result in large differences using SAM as the angle between the vectors is varying with the noise. The best unmixing combination is chosen as the one with the smallest SAM error and Euclidean error. If there exists a solution where both the SAM and Euclidean metrics are equal, the result from the whole patch SVM method is used to sway the choice of label for the classification. For example if the SAM metric labelled a sample as Sand and Euclidean labelled as Seagrass, both with equal error metrics, the decision is referred to the whole patch SVM. If the SVM labelled the sample as Sand then the final classified label is Sand. This algorithm has been called ISACS and is detailed in Algorithm 1.

Algorithm 1 ISACS algorithm

```

for each image in dataset do
  derive number of materials in patch: k
  determine % abundance of materials found: x
  for all combinations of spectra in reduced library do
    calculate SAM error
    calculate Euclidean error
  end for
  pick min error for SAM & Euclid errors
  use SVM classification on patch to assist picking unmixing solution
end for

```

5.4.3 Reducing computational complexity

The problem with the proposed algorithm for unmixing is that it is very computationally intensive for large library sizes. The number of steps required to assign the unmixed classes is $O(N^k)$ where N is the number of endmembers and k is the number of materials in a scene to be unmixed. Two methods will be presented for reducing the computational load of this process. One is a method for reducing the library size through clustering and the other is a greedy graph based search method (Section: 5.4.3.2).

5.4.3.1 Spectral library clustering

A large library was generated from the training in section 5.2. The size of the library needed to be reduced due to the combinatorial nature of the developed unmixing method. As was detailed in Section 5.4.2 the computational complexity of the ISACS algorithm can be defined as $O(N^k)$ where N is the size of the library and k is the number of materials present within the scene being unmixed. So reducing the size of the library N will greatly affect the computation time for large values of N .

One important consideration in reducing the size of the library was maintaining the variance of the interclass spectra. For example there may be 300 expert labelled examples of agropora coral but this may be reduced to 5 spectra representative of the 300. To achieve this firstly a Principle Components Analysis (PCA) of each class in the labelled training dataset was performed. The aim of this process was to best express the variance of the class, then a k-means clustering was performed on the PCA data where the number of clusters k is set to the desired number of representative spectra in the subset.

The subset is then chosen by the closest spectral data points to the centroids generated during the k-means clustering. The distance to the centroids for each of the data points was equated as the cosine between the two vectors. This is important in hyperspectral data as two spectra of identical materials with slightly differently lighting intensities will generate a constant offset between them. A conventional Euclidean based distance metric will perceive those two as different, whereas a cosine based metric will evaluate them as more similar. This is similar to the SAM algorithm for determining spectral similarity.

After the subset spectra were chosen for each label set, they were combined to form a new subset labelled library. The methodology described is illustrated in Algorithm 2.

Algorithm 2 Spectral library clustering and reduction

```

Define the size of the class subset  $j$ 
for each class type in labelled dataset do
    Take the PCA of the spectra belonging to the class
    Take k-means on the PCA subset creating  $j$  clusters
    Determine the distance of each labelled point to its corresponding cluster using the cosine metric.
    Choose the  $j$  spectral points closest to the centroids.
end for
Add chosen spectra to the new subset library.

```

5.4.3.2 Graph based search

This is the second method to reduce the computational complexity. It is based on a greedy graph search. The algorithm has been named: Image Segmentation Assisted Constrained Spectral-unmixing Greedy Ordered Graph-based Search (ISACS-GOGS). This method works by evaluating only a limited subset of unmixing combinations which appear to have a strong possibility of being the right combination. It is sub-optimal unlike the ISACS algorithm. ISACS-GOGS can be tuned to how exhaustive the search is. Greedy graph searching is the process by which a large graph is explored by choosing only the most promising nodes based on a pre-defined rule. This results in many graph paths not being explored and thus a reduced computational load.

The proposed method (illustrated in Figure 5.9) starts by ordering the abundances obtained during the segmentation method. The first graph leaves are based on all the library end-members multiplied by the largest abundance value. Then T graph leaves are chosen based on the best T scoring nodes, and all the other low scoring nodes are trimmed. T can be chosen based on the trade off between computational load and classification performance. The scoring is based on a minimal SAM and Euclidean distance error similar to the ISACS algorithm. The graph is then expanded at each chosen node, with the next highest abundance value. The new combination is tested and the graph is trimmed again. This continues until all k materials have been evaluated. This method greatly reduces the complexity from $O(N^k)$ down to $O\left(N\left(\frac{1-T^k}{1-T}\right)\right)$ where N is the size of the spectral library, k is the number of material present in the scene and T is the number of paths to expand at each branch (the tuning parameter). An advantage of this method is library reduction is not needed, so the search can be over the entire library, or a lesser reduced library can be used. The disadvantage is that it can miss materials present in the scene if it does not evaluate a particular path on the graph. The chance of a material being discovered is proportional to its abundance in the scene as it is a linear mixture assumption. The ISACS-GOGS algorithm is shown in Algorithm 3.

5.5 Unmixing results: synthetic dataset

The proposed unmixing technique was tested on two datasets to demonstrate the performance of the approach. The first dataset is synthetic and the second is on the coral reef

Algorithm 3 ISACS-GOGS algorithm

```

Sort abundances  $\alpha$  descending order
for each sorted abundance up to  $k$  do
  if at the start of the graph - initialise stack then
    else
      take previous top scoring graph paths
    end if
  for each material in library do
    Calculate reflectance with abundance and material
    Calculate SAM & Euclidean score
  end for
  pick top T SAM and Euclidean scores
  discard all but chosen scores
end for
return Top scoring graph path for SAM and Euclidean metrics

```

dataset used in Section 4.4.4. A synthetic dataset was used because it was possible to fully control the ground truth, the mixing of materials and the noise present in the set.

5.5.1 Generating a synthetic dataset

To generate a synthetic dataset spectral reflectance measurements of the squares on a Macbeth colour chart [152] were taken to form the spectral library. The number of end-members to mix k was chosen. Then k end-members were randomly picked from the library and the abundances for these end-members were determined by a Dirichlet distribution. The Dirichlet distribution generates the k abundances with the constraint that all abundances must be positive and add to one. This method for generating a synthetic dataset was based on a method popular in the literature [98]. Figure 5.10 shows the spectral reflectance curves for the patches of a macbeth colour chart which make up the end-members of the library.

$$D(s_1, \dots, s_k) = \frac{\Gamma\left(\sum_{j=1}^k \mu_j\right)}{\prod_{j=1}^k \Gamma(\mu_j)} \prod_{j=1}^k s_j^{\mu_j - 1} \quad (5.2)$$

where $\Gamma(n)$ is the Gamma function, μ is picked at random from a gamma distribution. There are k abundances generated $D(s_1, \dots, s_k)$, which sum to one and are all positive.

This was repeated for N mixtures. The result is a mixture matrix which has the dimensions $N \times B$ where B is the number of spectral bands in the library. In this case B was defined by

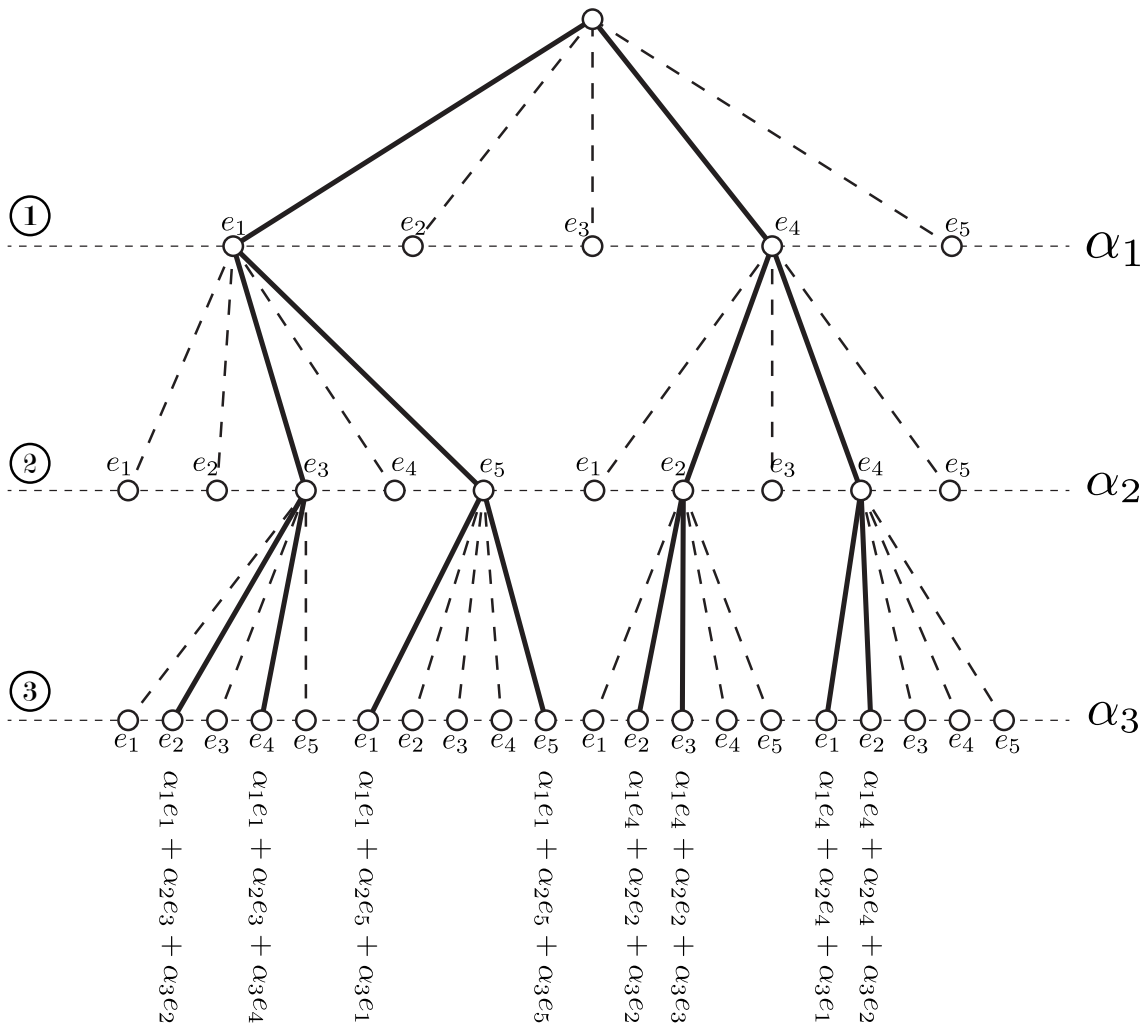


Figure 5.9 – Diagram of the ISACS-GOGS graph based search algorithm, in this graph: $T = 2$, $k = 3$, size of library = 5. e_x represents the x endmember signature. α_t represents the abundance at position t where the position is listed in descending order of size.

865 spectral bands between 409nm and 821nm. This was based on the spectral resolution of the spectrometer which was used to measure the MacBeth colour chart.

In the literature, noise on a synthetic dataset has been modelled as a proportion of the expected value of the signal, expressed as a Signal-to-Noise Ratio (SNR) Equation (5.3). Most authors implement several SNR values: 30dB, 40dB and 50dB [57, 98, 146]. This noise represents the shot noise which would result from an imaging sensor. This noise model is not entirely representative of the true noise which would exist in a true imaging system [178]. The other sources of noise include dark current noise, read/thermal noise and quantisation noise. For ease of comparison against other methods this noise model was chosen.

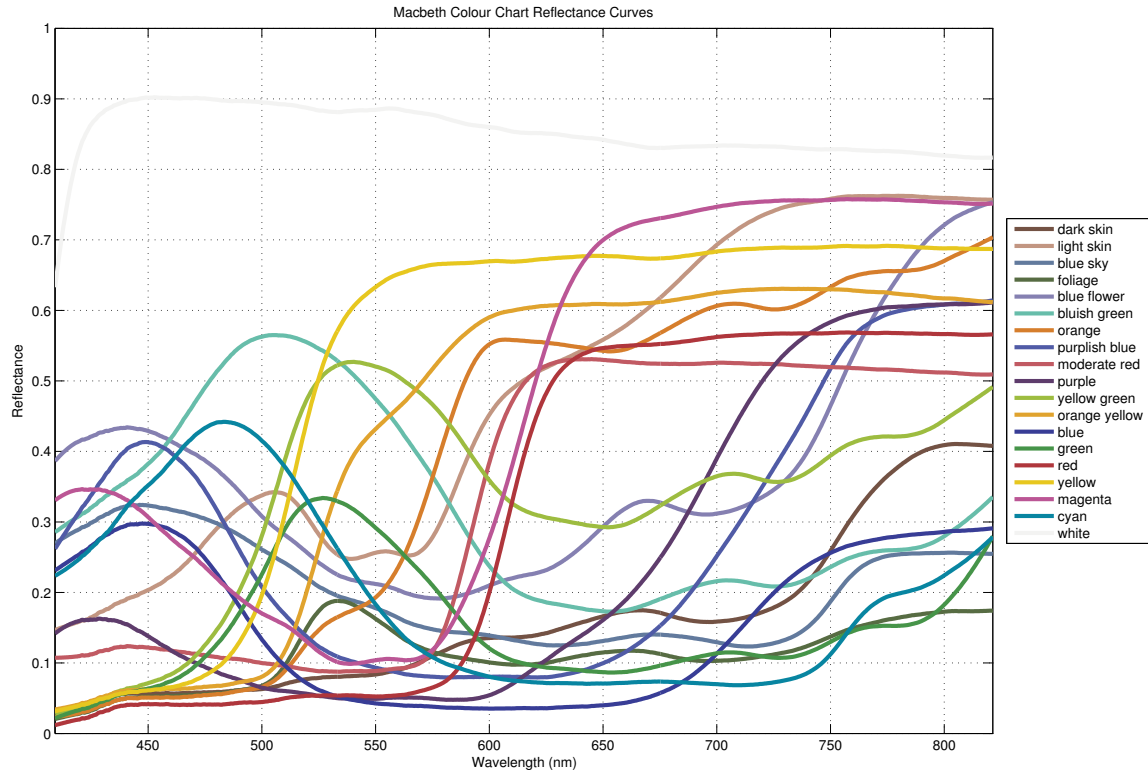


Figure 5.10 – Spectral reflectance curves for the patches of a MacBeth colour chart (taken in air), these curves were used to generate the synthetic dataset

$$SNR_{dB} = 20 \log_{10} \left(\frac{\mathbb{E}_{signal}}{\mathbb{E}_{noise}} \right) \quad (5.3)$$

where E_{noise} is the expected value for the uniformly distributed random noise. E_{signal} is the expected value of the spectra which the noise is being added to.

Figure 5.11 shows one of the synthetically generated mixed spectra. The colour curves are the 4 components which are added together to make the mixed spectra (shown in black). The component spectra are made from the fractional abundance multiplied by the randomly chosen end-member spectra. The colours of the component curves in the plot represent the RGB colour of the corresponding MacBeth colour swatch. As fractional abundances reduce and noise increases it can be challenging to resolve which materials were mixed together.

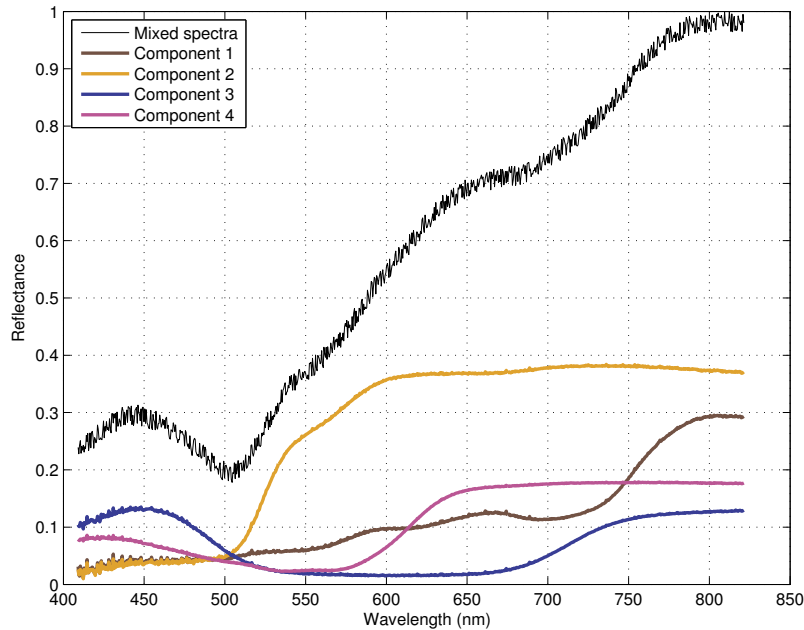


Figure 5.11 – This diagram shows the result of mixing together 4 materials/components given certain artificially generated abundances. The resultant spectra (curve shown in black) is composed by adding the four components together. In this example abundance SNR = 20dB and mixture SNR = 30dB.

5.5.2 Noise sensitivity

The synthetic dataset was used to examine the sensitivity of the algorithms ISACS and ISACS-GOGS to the presence of noise. More noise was progressively added on both the mixture matrix and the abundance matrix.

In the linear mixture model the mixture matrix is the result after combining the chosen endmembers by their respective abundance quantities (the abundance matrix). The reason for specifically adding noise to the abundance matrix in the proposed methods is to simulate noise or errors with the estimation of the fractional abundances obtained during the segmentation process. Noise was added to the mixture matrix to simulate how the methods from the literature implement a noise model as well as to evaluate the unmixing performance. The linear mixture model is denoted by:

$$Y = D(\alpha + N_a) + N_m \quad (5.4)$$

where: Y is the mixture matrix, N_m is the noise added to the mixture matrix, D is the

array of end-members in the spectral library. α is the abundance matrix, a 0 indicates the endmember at that spot was not chosen. There is also the sum-to-one constraint where $\Sigma\alpha = 1$. N_a is the noise on the abundance matrix.

5.5.3 Results

The performance under noise was evaluated using two different distance metrics, SAM and the Euclidean distance. These distances were taken between the reconstructed reflectance spectra after spectral unmixing and the ‘measured’ mixed spectra. Then the misclassification rate for the estimated unmixed endmembers to the ground truth was compared.

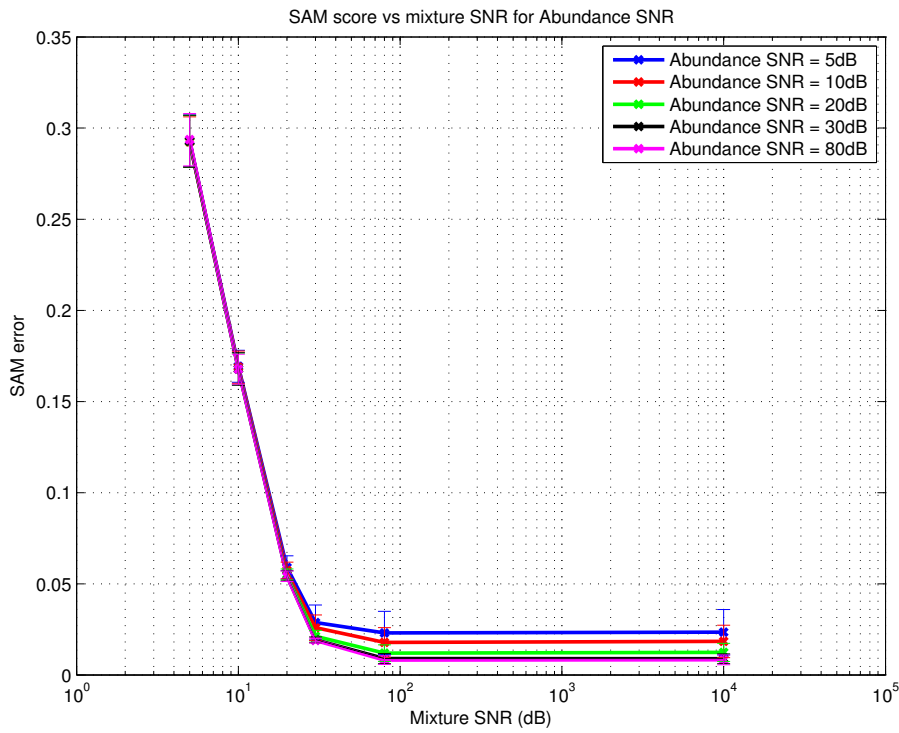
Noise analysis

The noise analysis was done for both the ISACS and the ISACS-GOGS algorithm, these results are shown in Figures 5.12 & 5.13 respectively. What can be seen is that the error (using either SAM or Euclidean distance as the error metric) drops off quite quickly with an increase in mixture SNR, levelling out after 30dB, however the error does not change significantly for increases in the abundance SNR. The same conclusion can be drawn from the ISACS-GOGS results for noise sensitivity (Figure 5.13). The noise sensitivity for ISACS is nearly identical to ISACS-GOGS.

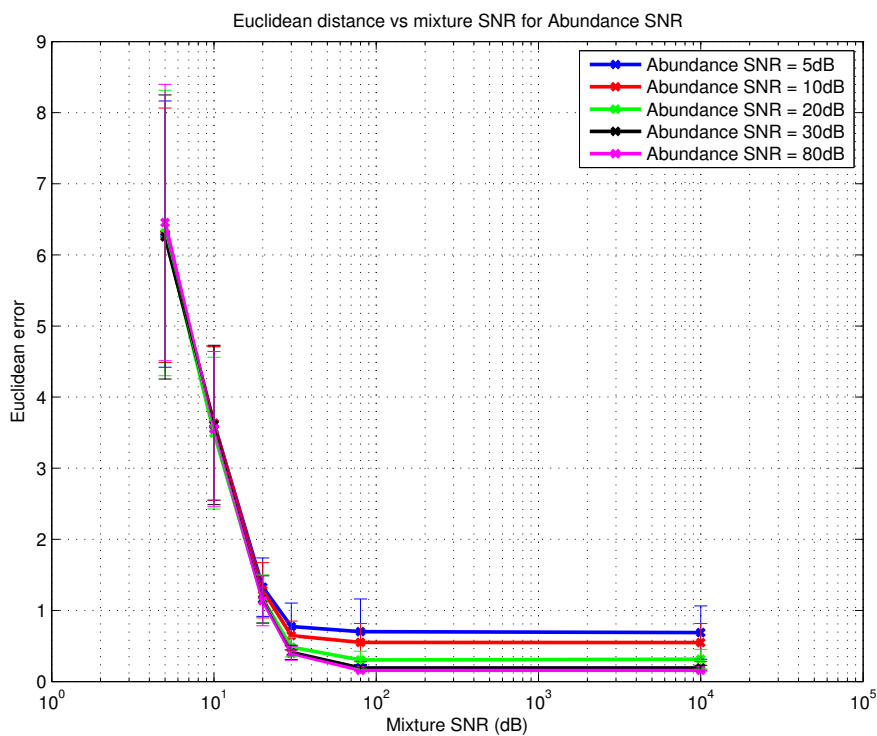
The results show that as more noise was added the performance dropped. Examining the distance metrics it was found that the error increased significantly more with noise on the mixture matrix than on the abundance matrix. This makes sense as the noise was expressed as a ratio in *dB*. The magnitude of the mixture matrix is larger than that of the abundance matrix so this would be expected.

Misclassification rate for decreasing abundances

To establish the performance of the proposed methods with the synthetic dataset, the number of misclassifications were compared. The outcome of classification is based on a binomial decision. The SAM and Euclidean scores are computed between the unmixed result and the library endmembers, then the smallest score defines the classification label. If it is incorrect for that material it counts as a 1 otherwise a correct classification is recorded

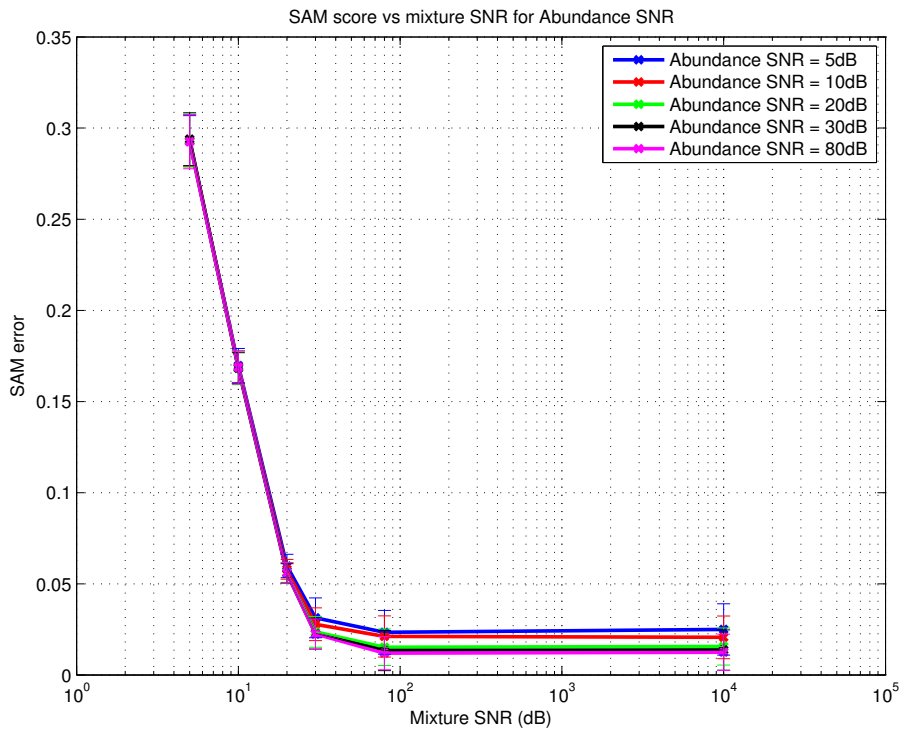


(a) SAM error score vs SNR

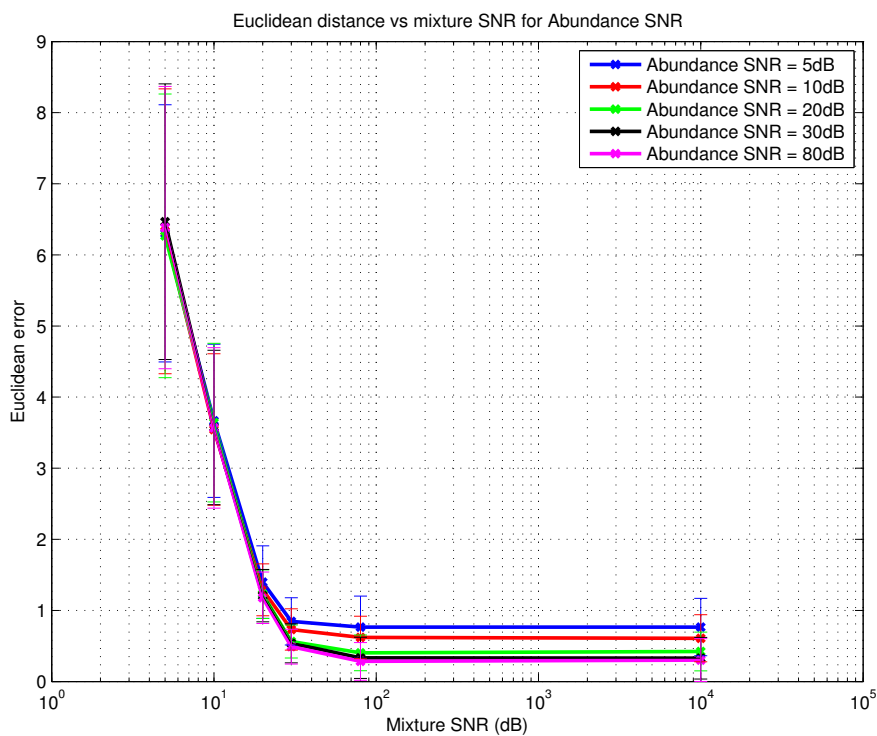


(b) Euclidean error score vs SNR

Figure 5.12 – Error of the unmixing as a function of different levels of noise on the mixture matrices and the abundance matrix. This was performed using the original ISACS algorithm. Error bars represent ± 1 standard deviation from the mean.



(a) SAM error score vs SNR



(b) Euclidean error score vs SNR

Figure 5.13 – Error of the unmixing as a function of different levels of noise on the mixture matrices and the abundance matrix. This was performed using the ISACS-GOGS algorithm, $T = 10$, $k = 4$. Error bars represent ± 1 standard deviation from the mean.

as a 0 on the misclassification score. This is evaluated for all endmembers present in the mixture.

To evaluate the unmixing performance 500 synthetic mixtures were generated with $k = 4$, (so there were 4 endmembers being mixed together). The results are presented using the ISACS and ISACS-GOGS algorithms for both the SAM and Euclidean distance metrics. For each data run (for a specific error metric and algorithm), the misclassification rate over the 500 tests is plotted against the abundance SNR and is repeated for different mixture SNR levels. For each algorithm and error metric choice results are presented for the misclassification rate for the different endmembers ranked from largest (a) to smallest (d). Results are shown in Figures 5.14 - 5.17.

Generally throughout the different combinations of error metric and algorithm choices, the smaller materials in the scene result in a higher misclassification rate, and are also more sensitive to noise on the abundance SNR. The results for ISACS-GOGS (Figures 5.16 & 5.17) demonstrate that there is a baseline misclassification rate (0.2). Even with reductions in noise on either the abundance or mixture matrices the misclassification rate remains above this baseline. In comparison the misclassification rate with the ISACS algorithm (Figure 5.14 & 5.15) drops to near zero. The performance of the ISACS-GOGS algorithm can be improved by increasing T (the number of search paths at each level of the graph search). This is covered in more detail in Section 5.5.3. It can also be seen that as the fractional abundance of a mixed material increases, the sensitivity to noise decreases with a decrease in the misclassification rate (flatter curves). This is seen for both unmixing algorithms.

Comparing between the error metrics, SAM appears to perform worse than the Euclidean distance metric. This is because this is a synthetic dataset, there is not a lot of amplitude variation. SAM is good at finding spectral similarity between spectra which are offset from each other where Euclidean is less sensitive to noise. The amplitude is nearly identical in the materials used for mixing. The Euclidean distance metric delivers the best result as SAM is being misled by the noise on the mixtures.

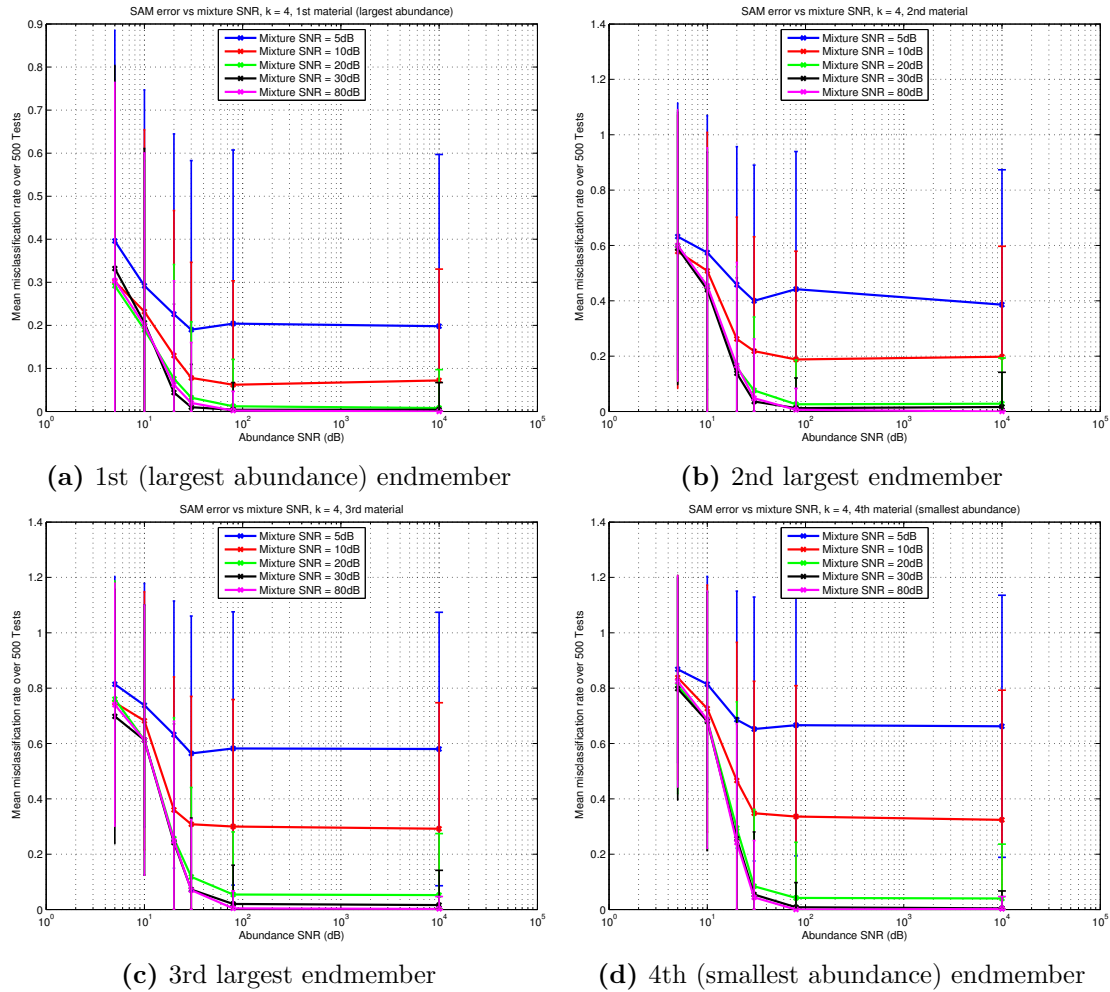


Figure 5.14 – ISACS algorithm, SAM error metric - Error on the unmixing as a function of different levels of noise on the mixture matrices and the abundance matrix. Error is calculated as the mean misclassification rate over 500 tests for unmixing one endmember of a given size from a mixture of 4 elements. Error bars represent ± 1 standard deviation from the mean.

Performance tuning

The performance of the ISACS-GOGS method increased if the number of search paths, T increased. To examine the effect of changing T had on performance for a fixed mixture SNR and a fixed abundance SNR, T was changed, taking on the values 1, 4, 8, 12, 16, with $k = 4$. Figure 5.18 shows the average number of misclassifications for 4 endmembers over 40 tests with the error bars representing 1 standard deviation.

As T was increased, the performance improved when using the ISACS-GOGS algorithm. T

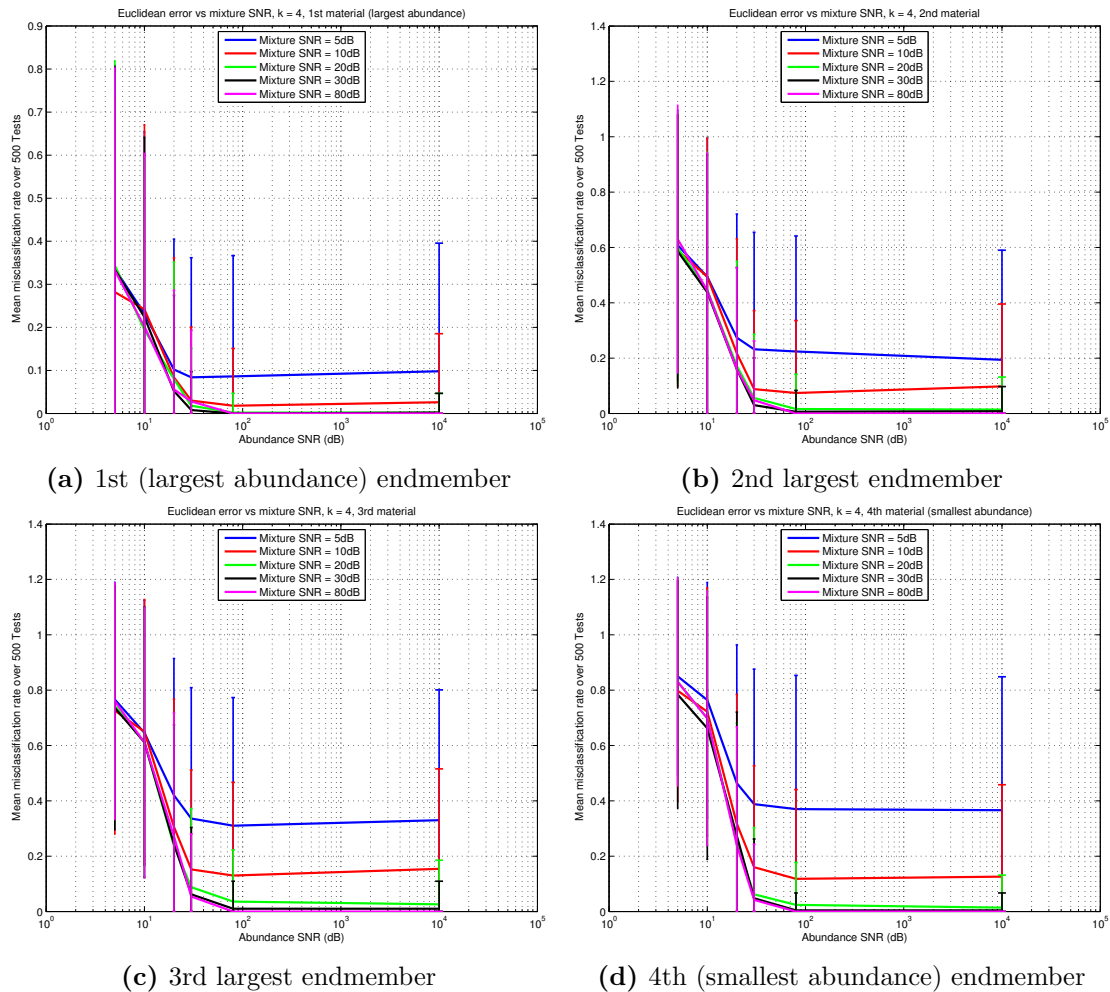


Figure 5.15 – ISACS algorithm, Euclidean error metric - Error on the unmixing as a function of different levels of noise on the mixture matrices and the abundance matrix. Error is calculated as the mean misclassification rate over 500 tests for unmixing one endmember of a given size from a mixture of 4 elements. Error bars represent ± 1 standard deviation from the mean.

can be increased until it equals the number of endmembers in the library N . Figure 5.19 illustrates this point of changing values of T and the corresponding computational load for ISACS-GOGS versus ISACS. The actual time it takes to run the algorithms are covered in Table 5.6. This table shows the unmixing algorithms running on the coral reef data (used in the next section), the full library refers to an endmember of size $N = 1311$, the reduced library only contains 7 endmembers. The algorithms ran on a machine with a dual-core intel i7 and 8GB of RAM in MATLAB. Running ISACS with a small library is quite fast, with 0.25 secs for unmixing 4 endmembers, however if ISACS is run with the full library

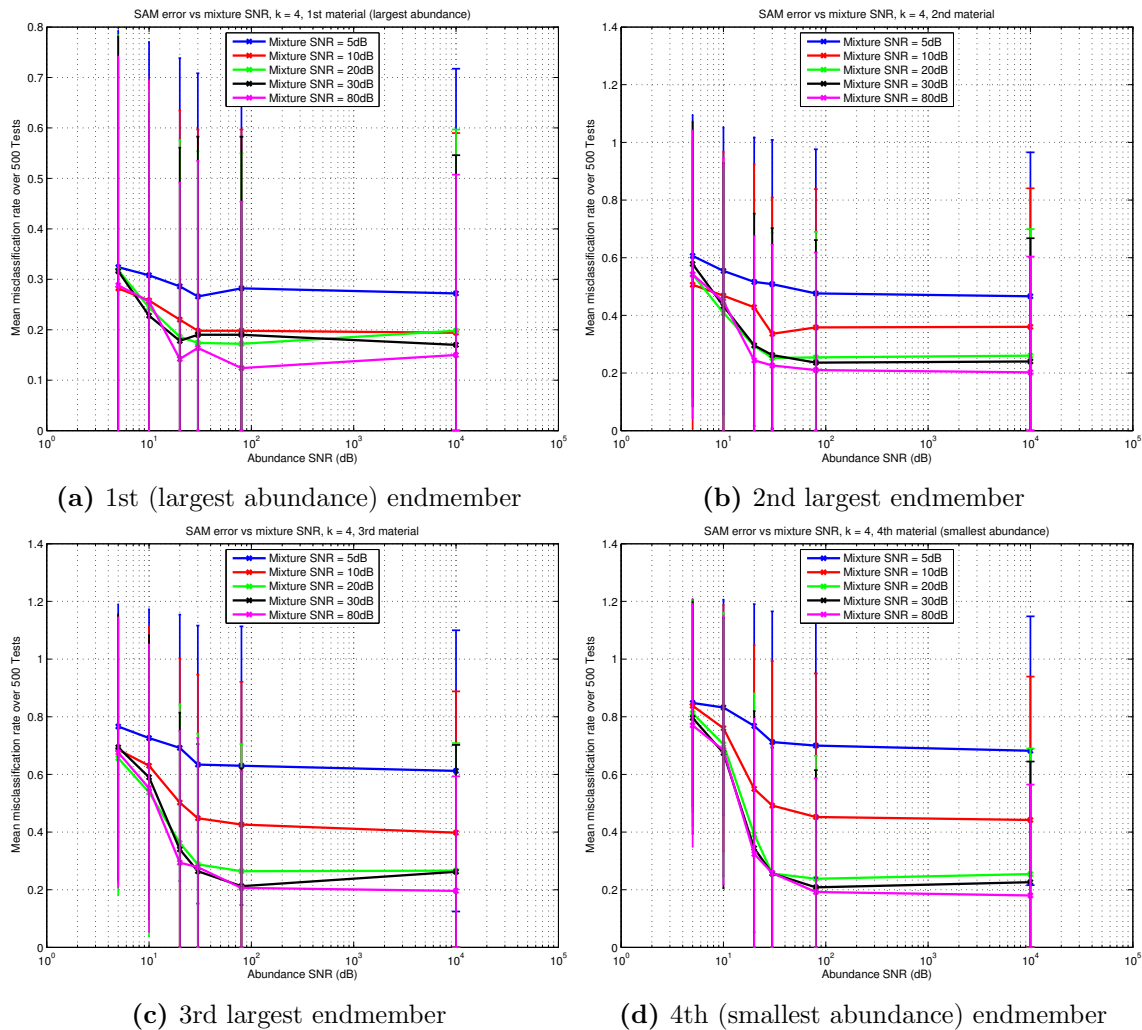


Figure 5.16 – ISACS-GOGS algorithm, SAM Error metric - Error on the unmixing as a function of different levels of noise on the mixture matrices and the abundance matrix. $T = 10$. Error is calculated as the mean misclassification rate over 500 tests for unmixing one endmember of a given size from a mixture of 4 elements. Error bars represent ± 1 standard deviation from the mean.

those same 4 endmembers take 9.6 years to unmix, making it quite intractable. Using the ISACS-GOGS algorithm it would take 59 secs to unmix 4 endmembers using the full library and $T = 10$, with the reduced library and $T = 4$ it only takes 0.07 secs. It was found for this application that a value of $T = 10$ was a good compromise between performance and computational time.

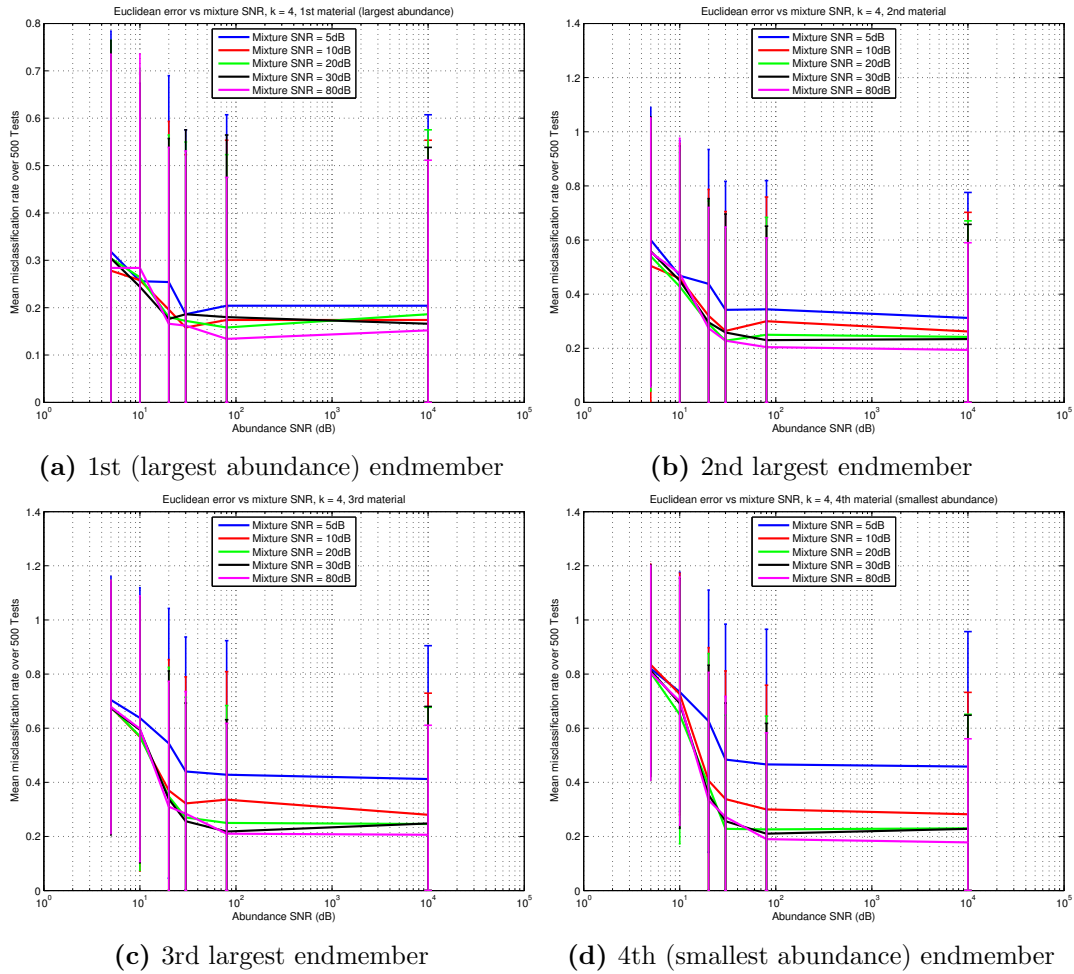


Figure 5.17 – ISACS-GOGS algorithm, Euclidean error metric - Error on the unmixing as a function of different levels of noise on the mixture matrices and the abundance matrix. $T = 10$. Error is calculated as the mean misclassification rate over 500 tests for unmixing one endmember of a given size from a mixture of 4 elements. –Error bars represent ± 1 standard deviation from the mean.

Comparative performance to conventional methods

To gauge the comparative performance of the proposed methods to literature methods, the ISACS and ISACS-GOGS algorithms were compared to three conventional unmixing algorithms. The algorithms chosen for comparison were: Fully Constrained Least Squares (FCLS), non-negative constrained least squares (NNLS) [22] and the Sparse Unmixing via variable Splitting and Augmented Lagrangian (SUNSAL) [97]. The two proposed unmixing algorithms were tested with the conventional algorithms for two abundance SNRs. The results are shown in Figure 5.20 for the abundance SNR = 20dB and 50dB for the mean

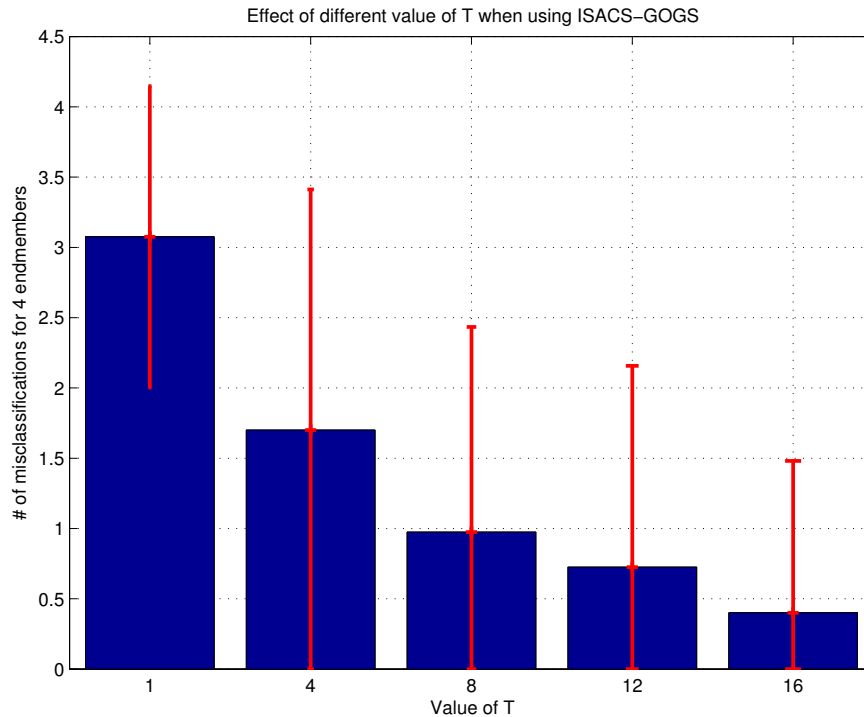


Figure 5.18 – Using the ISACS-GOGS, T can be tuned to increase performance, the graphs show the reduction in misclassifications as T is increased. This misclassification rate is calculated by unmixing 500 mixtures containing 4 mixtures, and it examines the number of misclassified elements within the mixtures.

misclassification rate of determining 4 endmembers over 500 tests. The error bars indicate the magnitude of one standard deviation.

For high noise on the abundance matrix ($\text{SNR} = 20\text{dB}$) the conventional methods perform similarly to the proposed methods. In the 50dB case however ISACS & ISACS-GOGS misclassification rate reduces to near zero and out performs conventional methods. However the difference and performance of the proposed unmixing methods is revealed when examining the unmixing of the smaller endmembers. As the proportional size of the endmember decreases the margin of improvement over conventional methods increases. Figure 5.21a shows the performance for the second largest endmember and the 4th (smallest) endmember case. The misclassification rate increased with the conventional methods whereas the proposed methods remained the same. This means that the proposed methods not only are able to determine the number and location of the materials within the scene/pixel they are able to better resolve small materials within the scene/pixel.

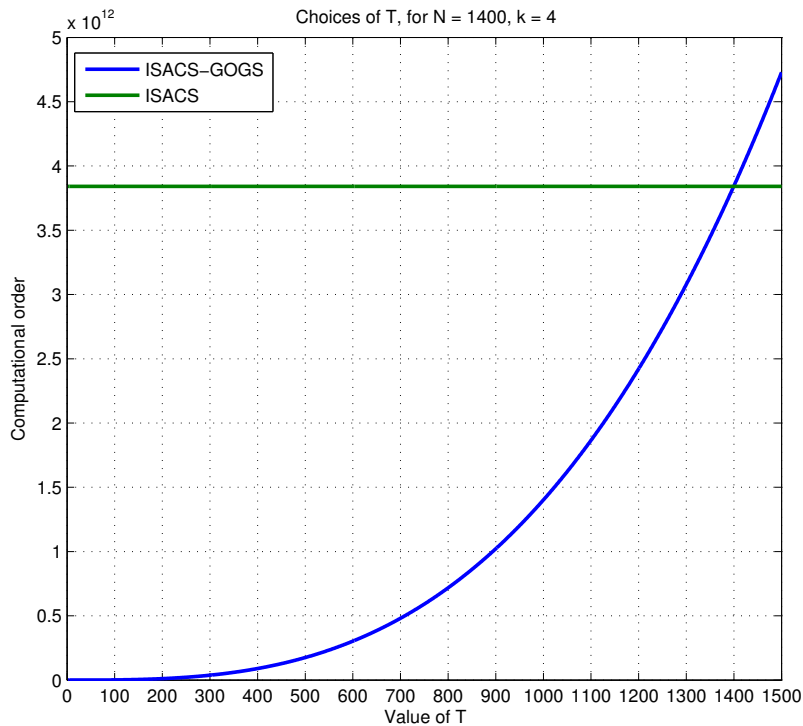


Figure 5.19 – Different values of T change the computational load for using the ISACS-GOGS versus ISACS algorithms. $N = 1400$, $k = 4$. Computational load indicates the number of cycles through the unmixing algorithm.

5.6 Spectral unmixing results: coral reef dataset

The proposed informed spectral unmixing algorithms were run on the coral reef dataset. The following figures show the unmixing results for 3 different benthic scene types. The first (Figure 5.22) is a scene in a seagrass patch. The unmixing process was able to resolve the two patches of seagrass and sand. The segmentation process split the seagrass patch, which the classifier could label both as seagrass due to its ability to allow more than one item to have the same label.

Figure 5.23 shows a scene over a coral reef section. The process was confused about the sponge and Acropora. This is most likely because the abundances were quite similar. The classifier also said there was sand in the scene. It was however a small patch of Acropora. This confusion was most likely because of the high brightness of coral compared to the other materials in the scene.

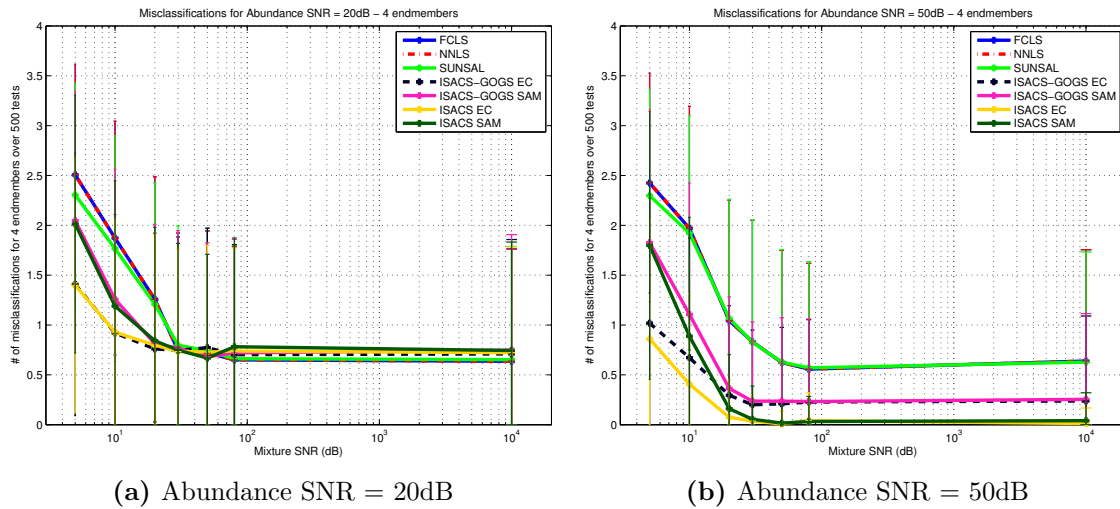


Figure 5.20 – Comparing different unmixing methods from the literature to the proposed methods ISACS and ISACS-GOGS. $k = 4$, $T = 15$

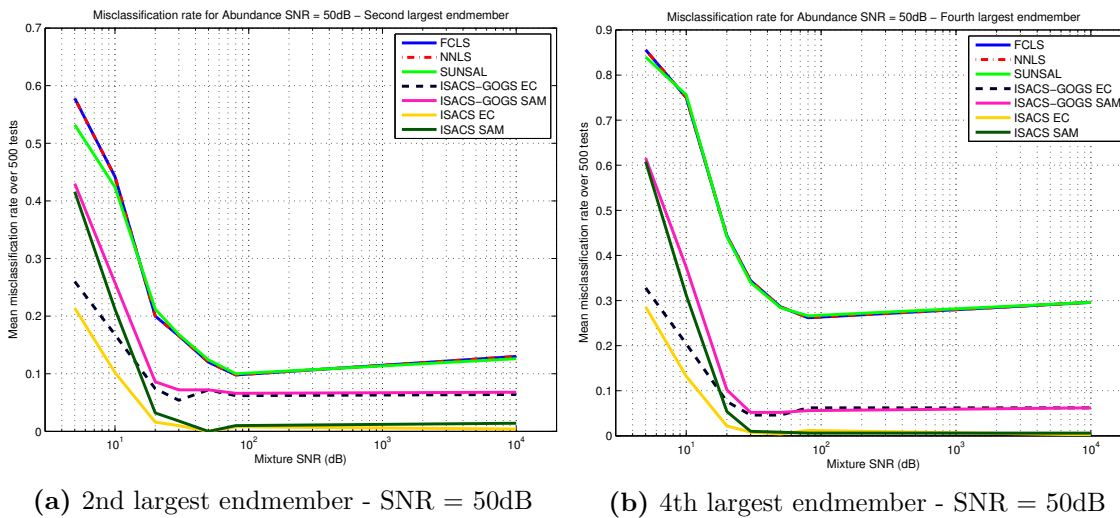


Figure 5.21 – Comparing different unmixing methods to the proposed methods for smaller endmembers. The proposed methods perform better as the abundance size drops

Figure 5.24 shows a scene over a rocky substrate, the unmixing process picked up the components in the image correctly but in the wrong locations. The large patch in the middle consists of small bits of CCA combined with turf algae. Also of note is the small piece of Acropora in the top right of the image. The segmentation process has ignored this due to it being too small. An appropriate size threshold for the segments is needed considering small patches often result in misclassification and an increased computational load.

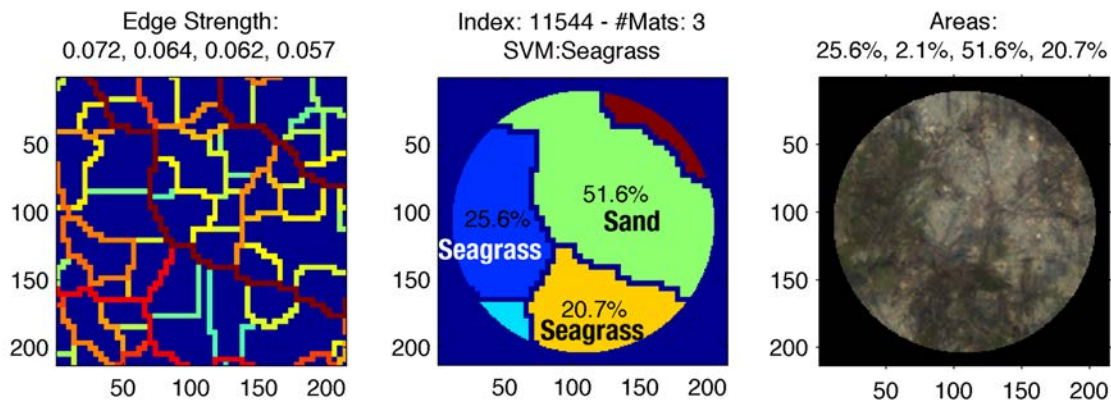


Figure 5.22 – The result for informed spectral unmixing for a seagrass scene.

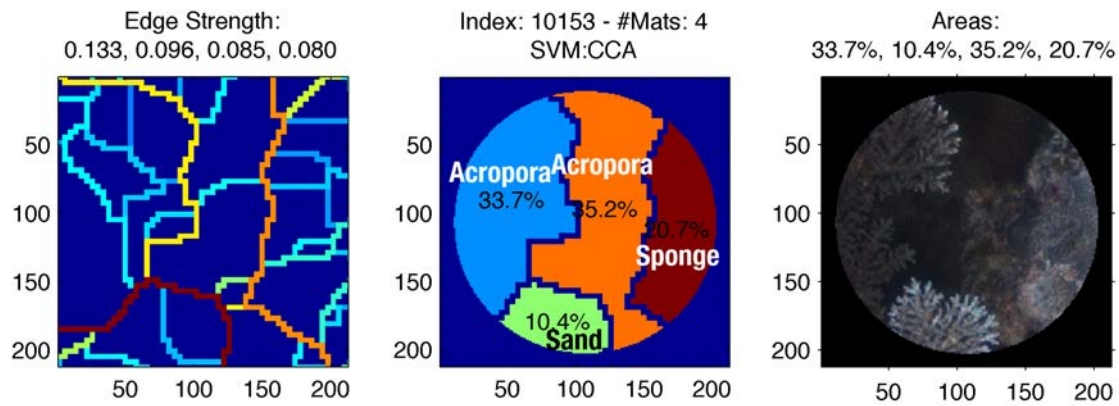


Figure 5.23 – The result for informed spectral unmixing for a coral reef scene.

To verify the performance of the ISACS and ISACS-GOGS algorithms on the coral reef dataset. The images firstly were segmented then the ISACS and ISACS-GOGS algorithm were applied. From this, 116 randomly chosen unmixed samples were examined to verify the performance and accuracy. Table 5.3 shows the number of endmembers present as a result of the segmentation algorithm in the 116 chosen samples. A majority contain just

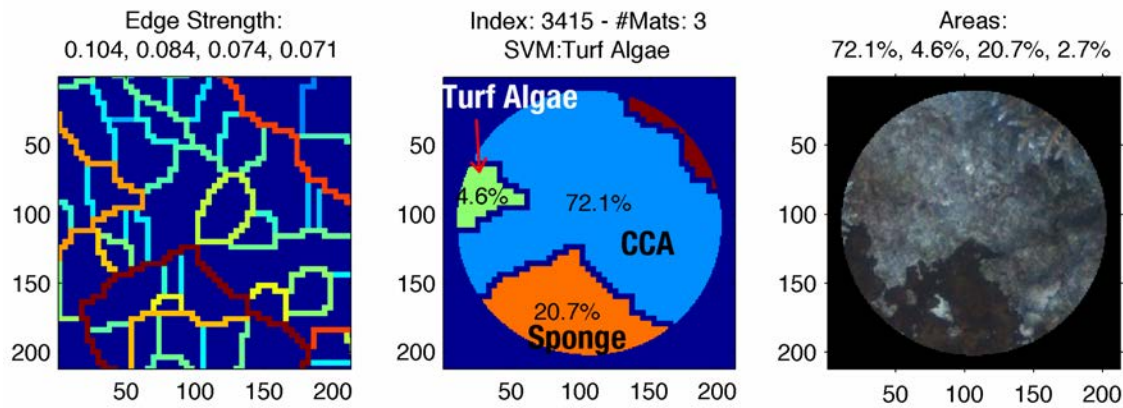


Figure 5.24 – The result for informed spectral unmixing for a rocky scene.

one endmember in the scene (58%), and very few contain 4 endmembers (5%).

	1 EM	2 EMs	3 EMs	4 EMs
Dataset size	67	30	13	6

Table 5.3 – Number of endmembers for each record in the 116 data points chosen from the coral reef dataset.

To establish the accuracy of the segmentation algorithm to resolve the number of materials in the scene, the number of materials present in the scene was evaluated by hand. This was done for the chosen samples. The accuracy rate for determining the correct number of materials present in the scene was 76%. The number of materials was determined by the *gPB-owt-ucm* algorithm [10]. Of the 24% incorrect, the mean error from the correct number of materials was ± 1.125 with a standard deviation of 0.33.

After finding the number of materials in the scene the ISACS and ISACS-GOGS algorithms were both tested. Using the ISACS-GOGS algorithm both the full hand labelled library (*Full*) and a reduced library (*Reduced*) was used. The reduced library was manually constructed from samples within the full library. Samples were chosen which appeared most pure within the FOV of the spectrometer. Materials such as CCA and turf algae were removed as they only existed on small scales and did not take up the entire FOV. Mixed pixels would cause confusion during the unmixing process. Mixed pixels as library endmembers were tested and it resulted in very poor performance (28% correctly classified for samples only containing 1 endmember).

When using the ISACS algorithm only the reduced library was used as the full library of 1131 samples took too long to compute as shown in Table 5.6. The evaluation of classi-

fied materials was done manually. The algorithms outputted the labels for the segmented sections of the coral reef imagery. Then evaluation was performed and a simple binomial, correct or not correct was applied to each label. Table 5.4 shows the correctly classified rate for each algorithm and the number of endmembers in the image. Table 5.5 shows the correct classification rate for at least one algorithm predicting the right class label. How to choose the correct solution from each of these algorithms has not been done in this work. This has been left for future work.

Method	1 EMs	2 EMs	3 EMs	4 EMs
ISACS (SAM-Reduced)	73.3%	53.1%	31.6%	50.0%
ISACS (Euclid-Reduced)	72.4%	51.0%	21.1%	66.7%
ISACS-GOGS (SAM-Full)	32.8%	22.5%	26.3%	16.7%
ISACS-GOGS (Euclid-Full)	29.3%	20.4%	26.3%	16.7%
ISACS-GOGS (SAM-Reduced)	74.1%	46.9%	26.3%	33.3%
ISACS-GOGS (Euclid-Reduced)	74.1%	40.8%	15.8%	33.3%

Table 5.4 – Results for spectral unmixing on coral reef dataset. It shows the correct classification rates for the different algorithms. EM stands for endmember and are listed in descending order of fractional abundance. Full and Reduced refer to using the full library and reduced subset library. ISACS reduced: $N = 7$, ISACS-GOGS Full: $N = 1311$, $T = 10$, ISACS-GOGS Reduced: $N = 7$, $T = 4$.

	1 EMs	2 EMs	3 EMs	4 EMs
All methods	86.2%	80.0%	63.2%	66.7%

Table 5.5 – Using all methods to find a solution

Method	1 EMs	2 EMs	3 EMs	4 EMs
ISACS Reduced Library $N = 7$	0.0029 sec	0.0085 sec	0.0559 sec	0.2457 sec
ISACS Full Library $N = 1311$ (Interpolated times)	0.5431 sec	298 sec	102 hrs	9.6 yrs
ISACS-GOGS Full Library $N = 1311$, $T = 10$	0.1043 sec	0.6932 sec	5.9250 sec	59.0237 sec
ISACS-GOGS Reduced Library $N = 7$, $T = 4$	0.0014 sec	0.0049 sec	0.0170 sec	0.0703 sec

Table 5.6 – This is the time it took to unmix the endmembers using the ISACS & ISACS-GOGS algorithms on the coral reef dataset for different library sizes and choices of T . The algorithm was running on an intel i7 2.9Ghz, 8GB RAM. The times for the ISACS full library have been interpolated from the reduced library ISACS results because the computer it was running on ran out of memory trying to run the algorithm on the full library of 1311 endmembers, and the time it would take for 4 endmembers was a little intractable.

From the unmixing results it can be seen that using a single algorithm the best performance was by using the ISACS-GOGS or ISACS algorithm with a correctly classified rate of 74.1% & 73.3% respectively. The performance decreases as the number of materials increases. This was to be expected and was reflected in the synthetic dataset. What is quite noticeable is the performance difference between using the full spectral library versus the reduced library. The performance drops to 32.8% when using the full library. This is thought to be because of the presence of mixed spectral library entries. Further analysis has not been conducted to confirm this, however it is known that mixtures exist in the spectral library. This is sometimes because the materials are smaller than the FOV of the spectrometer (as discussed in Section 5.2). As a result mixtures in the spectral library can not be avoided. The ideal practice for obtaining good spectral unmixing results is to collect a large number of samples over a survey mission then manually pick out the most pure endmembers out of the data for inclusion in the spectral library. The practicability of doing this for small materials from a moving AUV platform would be quite hard.

5.7 Summary

In this chapter several supervised classification algorithms have been used to label a real-world coral reef survey dataset. In these methods, several different features were included to increase the classification performance. In addition to the spectral measurements obtained using the methods in the previous chapter, texture features were added to utilise the co-registered imagery from the stereo camera. This imagery was of a higher spatial resolution than that of the downward facing spectrometer. It was found that a linear SVM performed the best with a classification performance of 91.99%. The trained dataset was obtained by hand-labelling over 1300 images. From the output of the classifier a large coral reef survey was labelled (over 14,000 data points), along with the location of the vehicle at the time of acquisition, the labels could be put into a 3D substrate map.

Although the spatial resolution of the spectral measurements is higher than current above water platforms, the seafloor assemblages exist at a resolution smaller than the patch covered by the downward looking spectrometer. New methods were presented in this chapter for informed spectral unmixing. This algorithm was called Image Segmentation Assisted Constrained Spectral-unmixing (ISACS). This utilised the higher resolution stereo cam-

eras to inform the number of materials and their relative abundances in the area of the spectrometer patch.

The presented unmixing algorithm was very computationally intensive, so two different methods were presented for reducing the computational load. These included a method for reducing the size of the spectral library using a clustering technique and the second was by utilising a greedy graph-based search. This algorithm was called Image Segmentation Assisted Constrained Spectral-unmixing Greedy Ordered Graph-based Search (ISACS-GOGS).

The performance of these two algorithms for spectral unmixing was demonstrated with a synthetic dataset and a real-world dataset. Noise of increasing amounts was added to the synthetic dataset to examine the sensitivity to noise. The performance of the presented unmixing algorithms was compared to the unmixing algorithms from the literature. The performance of the unmixing algorithms on the real-world datasets was found to perform well with a reduced spectral library. The library had to only contain pure materials. The informed unmixing algorithms presented show promise for improving the performance of spectral unmixing methods.

Chapter 6

Conclusions and future directions



"We're all mad here. I'm mad. You're mad"

- Lewis Carroll, Alice in Wonderland

6.1 Conclusions

Dynamic water modelling using upward facing spectrometers

In this work a new method was developed which used two upward facing spectrometers to characterise the optical properties of a water body. One spectrometer is placed above the water while the other is mounted on top of the imaging platform. Having a measurement from above the water results in a need to model the air-water interface. This can become complicated with surface platform motion, wind and time of day changes, however the presented modelling is able to take this into account.

Many methods from the literature aim to predict the optical properties of a body of water based on either above water visibility measurements or through in-situ measurements of chlorophyll and Coloured Dissolved Organic Matter (CDOM) measurements. The method presented in this work measures the optical properties of the water body through its transmission properties, this has the advantage of minimising modelling errors. Another advantage of the presented method is a new measurement is taken once a second, so a dynamic model of the optical properties can be built up. This allows for adaptability to environmental changes. This feature is particularly important for applications involving an Autonomous Underwater Vehicle (AUV). AUV survey missions can last for 8 hours, over which time the environmental conditions invariably change. In contrast, the literature methods over generalise the homogeneity of a body of water both spatially and temporally.

Design of an in-situ hyperspectral platform

In this work a new imaging modality was presented that combined a high spectral resolution spectrometer with a stereo camera system. A new calibration technique was developed to determine the spatial sensitivity of the spectrometer's Field-of-View (FOV) along with the spatial co-registration of the spectrometer's FOV with the FOV of the stereo cameras. This calibration allowed for data to be related spatially and spectrally between the two modalities. The engineering design of this combination along with data acquisition methodology was presented.

Colour correction of RGB imagery using a hyperspectral water model

The water column attenuates light in an uneven manner. This results in colour distortions in the imagery. In this work, a method was presented for correcting the colour of underwater imagery. This was performed through an inversion process by using a model of the optical properties of the water. This model was obtained using the upwards looking spectrometers. The water model exists in the hyperspectral domain. To correct for Red-Green-Blue (RGB) imagery a new method was presented for characterising spectral sensitivities of a trichromatic camera. This allowed for a new process to correct underwater RGB imagery. This method utilised not only the water model but also the 3D structure of the scene by using the stereo imagery. This resulted in imagery that is invariant to water conditions, weather, structure of the scene and lighting. Results for these methods were presented using three datasets of varying control: a test tank set, a shallow water outdoor environment and a AUV mapping mission over a coral reef.

Recovering spectral reflectance in-situ

Recovering the hyperspectral reflectance of a patch on the seabed requires knowing the incoming irradiance to a scene as well as the reflected irradiance. This method was presented in the context of recovering spectral reflectance from an AUV platform. The incoming light to a scene came from two sources: the artificial strobes onboard the AUV as well as the ambient illumination from the sun above the water. In this work a method was presented for predicting the scene illumination by modelling the strobe lighting based on the geometry of the scene to the AUV as well as the measurement of the ambient light contribution with an upwards looking spectrometer mounted on the AUV platform. The measurements for the scene illumination and the reflected light were compensated and corrected for the water's attenuation properties using the water model.

Classification of benthic types using a combined spectral and spatial classifier

In this work it was shown that spectral reflectance could be combined with the Local Binary Pattern (LBP) features from the co-registered RGB camera image data to improve

classification performance. A supervised classification approach was taken using a coral expert to label 12 different classes over 1300 data points. The trained classifier was run using 10-fold cross validation on the 1300 data points to gauge the performance of different classifiers. It was found that a linear Support Vector Machine (SVM) on the hyperspectral data combined with LBP from the RGB imagery performed the best. This combination achieved a classification rate of 91.99%. As each measurement carried a corresponding location it was possible to map out a survey which showed the locations of the various benthic types. Results were presented for a mapping mission over a coral shoal on the Great Barrier Reef (GBR).

Spectral unmixing using mixed resolution RGB imagery and hyperspectral measurements

Two new algorithms were presented for the unmixing of spectral data. These algorithms are unique in that they utilise the spatial information from imagery of a higher spatial resolution than that of the hyperspectral data to inform the unmixing process. Previous methods in the literature have sought to utilise the spatial component of a hyperspectral image further for spectral unmixing, however they were still limited by the spatial resolution underlining the hyperspectral camera. The RGB camera was used to determine the number of endmembers in a scene and their approximate fractional abundance. This was done through a hierarchical segmentation method from existing literature. The spectral data combined with the information from the segmentation presented a constrained unmixing problem which was combinatorial in nature. Two methods were developed for dealing with this computational complexity. One was a method for reducing the size of a spectral library while still maintaining the variance of that library, and the second was using a greedy graph based optimisation technique for considerable reduction in computational load. The results were presented on a synthetic and a real dataset.

6.2 Future directions

6.2.1 Water modelling onboard the AUV

In the current technique for measuring the optical properties of the water column, measurements occur in two separate locations. Onboard the AUV and onboard a support vessel on the surface. Some of the problems with this method are it can only work down to and not beyond solar penetration depth. By extension it also does not work at night time. In addition because of the separation of the measurement of these two data points, the water model can not be computed online on the AUV. It all needs to be done in post-mission processing. With the advent of online processing it would be advantageous to be able to measure the optical properties onboard the vehicle. A method for measuring the optical properties onboard could be performed with an instrument such as a *Wet Labs AC-S* in-situ spectrophotometer. This is however a particularly bulky instrument. Another method could be to fire a known broadband light source down the side of the vehicle and measure it at a fixed distance and examine the attenuation due to the water.

The current method of using two upwards looking spectrometers could further be improved by removing the need to model the air-water interface. This could be accomplished by taking the surface measurement just below the water. This could be done with a spectrometer on a buoy suspended just below the surface of the water, however it would mean that caustics and water lensing effects would come into play. The solution to these effects could be a larger receiver or temporal smoothing of the measured incoming irradiance.

6.2.2 Examining the spatial distribution of optical properties

As the AUV transits around a survey site, it is constantly collecting information about the optical properties of the water. There has been little work into examining the spatial distribution of optical properties. Most methods assume the homogeneity of a certain water model for quite large areas. Investigations into this assumption would be quite interesting. Particularly through the use of an AUV which is able to cover large areas. For example, this might be useful in the context of the modelling of the ecology living within the water column and how this may vary with location. If an area has more nutrients does this result in higher degrees of marine life?

6.2.3 Upgrading to a HSI camera

As previously mentioned, a Hyperspectral Imaging (HSI) camera was not used for taking spectral measurements due to Signal-to-Noise Ratio (SNR) concerns, and limitations on size, power and data storage onboard the imaging platform (see Section 4.5 for a comparison between a spectrometer and a miniaturised HSI camera). There was also a concern due to the modality of imaging when using a pushbroom or Acousto-Optical Tunable Filter (AOTF) HSI camera. To be able to use a HSI camera onboard an underwater platform the best option would be to use a pushbroom camera with constant illumination. Rather than illuminating the whole scene a more efficient method would be to just illuminate the small narrow strip currently being imaged. This would reduce the power burden of constant illumination and minimises backscatter. An AOTF camera could work in this environment if there was a limited subset of frequencies under investigation. The large challenge as previously mentioned would be the parallax effects of having each wavelength image from slightly different locations as the platform moves. This could be rectified if the underwater platform was able to stop during acquisition and then move to the next sample site. This would be inefficient and difficult to achieve in practice.

Utilising a HSI camera would result in much higher spatial resolutions for insitu HSI mapping. Promising work has been shown in Johnsen *et al.* [103] where they had constant illumination and a controlled camera rig on the seabed.

6.2.4 Benthic health monitoring

In the presented work LBP was used as a feature descriptor for the camera imagery, however other additional techniques could be incorporated to add more features to our classifier. The 3D data could be used for assisting in coral taxa classification. Above water hyperspectral coral classification methods have been unable to distinguish coral to the species level [83]. An additional classification feature could be the use of rugosity. This has also been shown to be an ecological indicator of bio-productivity [64].

This technique may also be used for deriving the health of the coral [90] which may have been affected by bleaching or invasive algal blooms events. An AUV is well suited for undertaking this task as an AUV is able to revisit large areas of underwater seafloor with

high accuracy. This is crucial for examining small level changes which may be occurring temporally.

6.2.5 Defence applications

There is an array of defence applications for this work particularly in Mine Counter-Measures (MCM). Current methods for finding sea mines are predominately performed using sonar based systems. In flat open seabed areas it is easier to find a mine target, however in a cluttered environment it can become quite challenging. The technique presented of measuring the optical properties of the water for correction of optical imagery could also allow for target detection. There are a series of HSI processing techniques which work by knowing the target signature. When the target is unknown anomaly detection could be applied [5, 188]. This technique involves examining the spectral data for data points which do not belong and are rare in the dataset. These rare data points could be elements such as sea-mines.

6.2.6 Spectral unmixing

Further improvements could be made in the performance of the informed spectral unmixing algorithms. Sparse regression techniques could speed up the search process. Current sparse regression unmixing is uninformed however quite fast for large library sizes.

A limitation discovered in this work for informed spectral unmixing was the need for a quality spectral library. A future avenue of this work would be to obtain a spectral library consisting of pure endmembers. This would not only improve the unmixing performance but would also be good for ground truthing the spectral measurements from the in-situ imaging platform.

Bibliography

- [1] MATLAB 2013b. Natick, Massachusetts, United States, 2013.
- [2] Julia Ahlen. *Colour correction of underwater images using spectral data*. PhD thesis, Acta Universitatis Upsaliensis, 2005.
- [3] Julia Ahlen and David Sundgren. Bottom Reflectance Influence on a Color Correction Algorithm for Underwater Images. In Josef Bigun and Tomas Gustavsson, editors, *Image Analysis*, volume 2749, pages 139–187. Springer Berlin / Heidelberg, 2003.
- [4] Julia Ahlen, D Sundgren, and E Bengtsson. Application of underwater hyperspectral data for color correction purposes. *Pattern Recognition and Image Analysis*, 17(1):170–173, 2007.
- [5] J Anderson. A Generalized Likelihood Ratio Test for Detecting Land Mines Using Multispectral Images. *Geoscience and Remote Sensing Letters, IEEE*, 5(3):547–551, 2008.
- [6] S. Andréfouët, R. Berkelmans, L. Odriozola, T. Done, J. Oliver, and F. Müller-Karger. Choosing the appropriate spatial resolution for monitoring coral bleaching events using remote sensing. *Coral Reefs*, Volume 21(Number 2):147–154, 2002.
- [7] S Andréfouët, C Payri, Eric J Hochberg, C Hu, M J Atkinson, and F E Muller-Karger. Use of in situ and airborne reflectance for scaling-up spectral discrimination of coral reef macroalgae from species to communities. *Marine ecology progress series*, 283:161–177, 2004.
- [8] Serge Andréfouët, Philip Kramer, Damaris Torres-Pulliza, Karen E Joyce, Eric J Hochberg, Rodrigo Garza-Pérez, Peter J Mumby, Bernhard Riegl, Hiroya Yamano, William H White, Mayalen Zubia, John C Brock, Stuart R Phinn, Abdulla Naseer, Bruce G Hatcher, and Frank E Muller-Karger. Multi-site evaluation of IKONOS data for classification of tropical coral reef environments. *Remote Sensing of Environment*, 88(1-2):128–143, November 2003. ISSN 00344257.
- [9] Janet Anstee, Arnold G. Dekker, Stuart R. Phinn, Paul Bissett, Vittorio E. Brando, Brandon Casey, Peter Fearn, John D. Hedley, Wojciech Klonowski, Zhong P. Lee, Merv Lynch, Mitchell Lyons, and Curtis D Mobley. Intercomparison of shallow

- water bathymetry, hydro-optics, and benthos mapping techniques in Australian and Caribbean coastal environments. *Limnology and Oceanography: Methods*, 9:396–425, 2011.
- [10] Pablo Arbeláez, Michael Maire, Charles Fowlkes, and Jitendra Malik. Contour Detection and Hierarchical Image Segmentation. *Pattern Analysis and Machine Intelligence, IEEE Transactions on*, 33(5):898–916, 2011.
- [11] Charles M. Bachmann, Marcos J. Montes, Robert a. Fusina, Christopher Parrish, Jon Sellars, Alan Weidemann, Wesley Goode, C. Reid Nichols, Patrick Woodward, Kevin McIlhany, Victoria Hill, Richard Zimmerman, Daniel Korwan, Barry Truitt, and Arthur Schwarzschild. Bathymetry Retrieval from Hyperspectral Imagery in the Very Shallow Water Limit: A Case Study from the 2007 Virginia Coast Reserve (VCR’07) Multi-Sensor Campaign. *Marine Geodesy*, 33(1):53–75, February 2010. ISSN 0149-0419.
- [12] Charles M. Bachmann, C. Reid Nichols, Marcos J. Montes, Rong-Rong Li, Patrick Woodward, Robert a. Fusina, Wei Chen, Vimal Mishra, Wonkook Kim, James Monty, Kevin Mcilhany, Ken Kessler, Daniel Korwan, W. David Miller, Ellen Bennert, Geoff Smith, David Gillis, Jon Sellars, Christopher Parrish, Arthur Schwarzschild, and Barry Truitt. Retrieval of Substrate Bearing Strength from Hyperspectral Imagery during the Virginia Coast Reserve (VCR07) Multi-Sensor Campaign. *Marine Geodesy*, 33(2-3):101–116, July 2010. ISSN 0149-0419.
- [13] CM Bachmann, CR Nichols, and MJ Montes. Airborne Remote Sensing of Trafficability in the Coastal Zone. Technical report, NAVAL RESEARCH LAB WASHINGTON DC REMOTE SENSING DIV., 2009. URL <http://oai.dtic.mil/oai/oai?verb=getRecord&metadataPrefix=html&identifier=ADA525045>.
- [14] CM Bachmann, MJ Montes, and RA Fusina. Imagery Trafficability Tool (HITT): Software and Spectral-Geotechnical Look-up Tables for Estimation and Mapping of Soil Bearing Strength from Hyperspectral Imagery. Technical report, NAVAL RESEARCH LAB WASHINGTON DC REMOTE SENSING DIV., 2012. URL <http://oai.dtic.mil/oai/oai?verb=getRecord&metadataPrefix=html&identifier=ADA569187>.
- [15] Mark E Baird, Patrick G Timko, and Luija Wu. The effect of packaging of chlorophyll within phytoplankton and light scattering in a coupled physical-biological ocean model. *Marine and Freshwater Research*, 58(2001): 966–981, 2007.
- [16] Kobus Barnard and Brian Funt. Camera characterization for color research. *Color Research & Application*, 27(3):152–163, June 2002. ISSN 0361-2317.
- [17] K Barott, J Smith, E Dinsdale, M Hatay, S Sandin, F Rohwer, and N Ahmed. Hyperspectral and Physiological Analyses of Coral-Algal Interactions. *PloS one*, 4(11):547–1742, 2009.

- [18] Jessica D. Bayliss, J. Anthony Gualtieri, and Robert F. Crompt. Analyzing hyperspectral data with independent component analysis. In *Proc. SPIE 3240, 26th AIPR Workshop: Exploiting New Image Sources and Sensors*, 1998.
- [19] S Bazeille, I Quidu, L Jaulin, and J P Malkasse. Automatic underwater image pre-processing. In *SEA TECH WEEK Caractérisation du Milieu Marin*, Brest, 2006.
- [20] M. S. Bewley, B. Douillard, Navid Nourani-Vatani, Ariell Friedman, Oscar Pizarro, and Stefan B. Williams. Automated species detection: An experimental approach to kelp detection from sea-floor AUV images. In *Australasian Conference on Robotics and Automation*, pages 3–5, 2012.
- [21] M. S. Bewley, N. Nourani-Vatani, D. Rao, B. Douillard, O. Pizarro, and S. B. Williams. Hierarchical Classification in AUV Imagery. In *Field and Service Robotics*, pages 3–16. Springer, 2015. ISBN 3319074873.
- [22] José M Bioucas-dias, Antonio Plaza, Nicolas Dobigeon, Mario Parente, Qian Du, Paul Gader, and Jocelyn Chanussot. Hyperspectral Unmixing Overview : Geometrical , Statistical , and Sparse Regression-Based Approaches. *Selected Topics in Applied Earth Observations and Remote Sensing, IEEE Journal of*, 5(2):354–379, 2012.
- [23] R B Blackman and J W Tukey. *The measurement of power spectra: from the point of view of communications engineering*, volume 1058. Dover Publications, New York, 1959.
- [24] Joseph W. Boardman. Automating spectral unmixing of AVIRIS data using convex geometry concepts. *Summaries 4th Annu. JPL Airborne Geoscience Workshop*, 1993.
- [25] Joseph W. Boardman, Fred A. Kruse, and Robert O. Green. Mapping Target Signatures Via Partial Unmixing of Aviris Data. *Proc. JPL Airborne Earth Science Workshop*, pages 3–6, 1995.
- [26] Daniel L. Bongiorno, Mitch Bryson, and Stefan B. Williams. Dynamic Spectral-Based Underwater Colour Correction. In *Proceedings of MTS/IEEE OCEANS*, Bergen, Norway, 2013.
- [27] Daniel L. Bongiorno, Adam J. Fairley, Mitch Bryson, and Stefan B. Williams. Automatic Spectrometer/RGB Camera Spatial Calibration. In *Proceedings of the IEEE International Geoscience and Remote Sensing Symposium*, Melbourne, Australia, 2013. IEEE.
- [28] Rodney Borrego-Acevedo, Chris M Roelfsema, Stuart R Phinn, and Alistair R Grinham. Predicting distribution of microphytobenthos abundance on a reef platform by combining in situ underwater spectrometry and pigment analysis. *Remote Sensing Letters*, (May):461–470, 2014.
- [29] E. J. Botha, A. G. Dekker, Y. J. Park, J. M. Anstee, N. Cherukuru, and L. Clementson. Remote sensing for habitat mapping and change detection in

- tropical Commonwealth marine protected areas phase 2. Technical Report June, CSIRO, 2010.
- [30] Vittorio E. Brando and Arnold G. Dekker. Satellite hyperspectral remote sensing for estimating estuarine and coastal water quality. *IEEE Transactions on Geoscience and Remote Sensing*, 41(6):1378–1387, June 2003. ISSN 0196-2892.
- [31] Vittorio E. Brando, Janet M. Anstee, Magnus Wettle, Arnold G. Dekker, Stuart R. Phinn, and Chris Roelfsema. A physics based retrieval and quality assessment of bathymetry from suboptimal hyperspectral data. *Remote Sensing of Environment*, 113(4):755–770, April 2009. ISSN 00344257.
- [32] T. C. L. Bridge, T. J. Done, R. J. Beaman, a. Friedman, S. B. Williams, O. Pizarro, and J. M. Webster. Topography, substratum and benthic macrofaunal relationships on a tropical mesophotic shelf margin, central Great Barrier Reef, Australia. *Coral Reefs*, 30(1):143–153, September 2010. ISSN 0722-4028.
- [33] T. C. L. Bridge, T. J. Done, A. Friedman, R. J. Beaman, S. B. Williams, O. Pizarro, and J. M. Webster. Variability in mesophotic coral reef communities along the Great Barrier Reef, Australia. *Marine Ecology Progress Series*, 428:63–75, May 2011. ISSN 0171-8630.
- [34] T. C. L. Bridge, K. E. Fabricius, P. Bongaerts, C. C. Wallace, P. R. Muir, T. J. Done, and J. M. Webster. Diversity of Scleractinia and Octocorallia in the mesophotic zone of the Great Barrier Reef, Australia. *Coral Reefs*, 31(1):179–189, October 2011. ISSN 0722-4028.
- [35] Tom Bridge, Robin Beaman, Terry Done, and Jody Webster. Predicting the location and spatial extent of submerged coral reef habitat in the Great Barrier Reef world heritage area, Australia. *PloS one*, 7(10):e48203, January 2012. ISSN 1932-6203.
- [36] X. Briottet, R. Marion, V. Carrere, S. Jacquemoud, S. Chevrel, P Prastault, M. D’Oria, P. Giloupe, S. Hosford, B. Lubac, and A. Bourgoignon. HYPXIM: A new hyperspectral sensor combining science/defence applications. In *Hyperspectral Image and Signal Processing: Evolution in Remote Sensing (WHISPERS), 2011 3rd Workshop on. IEEE,, 2011.*
- [37] P. Brusaglioni, P. Donelli, A. Ismaelli, and G. Zaccanti. Monte Carlo calculations of the modulation transfer function of an optical system operating in a turbid medium. *Applied Optics*, 32(15):2813–2824, 1993.
- [38] Mitch Bryson, M Johnson-Roberson, Oscar Pizarro, and Stefan Williams. Repeatable Robotic Surveying of Marine Benthic Habitats for Monitoring Long-term Change. In *Robotics Science and Systems*, pages 3–7, 2012.
- [39] James B. Campbell and Randolph H. Wynne. *Introduction to remote sensing*. The Guilford Press, New York, 5th editio edition, 2011. ISBN 0415282942.
- [40] T. Caras, A. Karnieli, and J. Hedley. Exploring field-of-view non-uniformities produced by a hand-held spectroradiometer. *Journal of Spectral Imaging*, 2 (January):1–11, 2011. ISSN 2040-4565.

- [41] JH Carleton and TJ Done. Quantitative video sampling of coral reef benthos: large-scale application. *Coral Reefs*, (14):35–46, 1995.
- [42] Alexey Castrodad, Zhengming Xing, and JB Greer. Learning Discriminative Sparse Representations for Modeling, Source Separation, and Mapping of Hyperspectral Imagery. *IEEE Transactions on Geoscience and Remote Sensing*, 49(11):4263–4281, 2011.
- [43] Chein-I Chang. *Hyperspectral imaging: Techniques for spectral detection and classification*. Springer, 2003. ISBN 0306474832.
- [44] Chein-I Chang and Su Wang. Constrained band selection for hyperspectral imagery. *Geoscience and Remote Sensing, IEEE Transactions on*, 44(6):1575–1585, 2006.
- [45] Chi Hau Chen and Xiaohui Zhang. Independent component analysis for remote sensing study. In *Proc. SPIE 3871, Image and Signal Processing for Remote Sensing V*, volume 3871, pages 150–158, 1999.
- [46] S. Y. Chen, Zhang Jianwei, Zhang Houxiang, Wang Wanliang, and Y. F. Li. Active Illumination for Robot Vision. In *Robotics and Automation, 2007 IEEE International Conference on*, pages 411–416, 2007. ISBN 1050-4729.
- [47] Ted R. Clem. Sensor Technologies for Hunting Buried Sea Mines. *OCEANS '02 MTS/IEEE*, pages 452–460, 2002.
- [48] Ryan Clement, Matthew Dunbabin, and Gordon Wyeth. Toward robust image detection of crown-of-thorns starfish for autonomous population monitoring. In *Australasian Conference on Robotics and Automation 2005*. Australian Robotics and Automation Association Inc, 2005. ISBN 0958758379.
- [49] Olympus Corporation. uTough 8000: Specifications.
- [50] A. Davie, K. Hartmann, G. Timms, M. de Groot, and J. McCulloch. Benthic habitat mapping with autonomous underwater vehicles. In *Oceans 2008*, pages 1–9. IEEE, 2009.
- [51] Chengbin Deng and Changshan Wu. A spatially adaptive spectral mixture analysis for mapping subpixel urban impervious surface distribution. *Remote Sensing of Environment*, 133:62–70, June 2013. ISSN 00344257.
- [52] Philip E. Dennison, Kerry Q. Halligan, and Dar a. Roberts. A comparison of error metrics and constraints for multiple endmember spectral mixture analysis and spectral angle mapper. *Remote Sensing of Environment*, 93(3):359–367, November 2004. ISSN 00344257.
- [53] T. D. Dickey, E. C. Itsweire, M. A. Moline, and M. J. Perry. Introduction to the Limnology and Oceanography Special Issue on Autonomous and Lagrangian Platforms and Sensors (ALPS). *Limnology and Oceanography*, 53:2057–2061, 2008.

- [54] M. Dunbabin and L. Marques. Robots for Environmental Monitoring: Significant Advancements and Applications. *Robotics & Automation Magazine, . . .*, (February), 2012.
- [55] M. Dunbabin, P. Corke, and G. Buskey. Low-cost vision-based AUV guidance system for reef navigation. In *International Conference on Robotics and Automation*, number April, pages 7–12, 2004. ISBN 0780382323.
- [56] Seibert Q. Duntley. Light in the Sea. *J. Opt. Soc. Am.*, 53(2):214–233, 1963.
- [57] Olivier Eches, Nicolas Dobigeon, and Jean-Yves Tournet. Enhancing hyperspectral image unmixing with spatial correlations. *Geoscience and Remote . . .*, 49(11):4239–4247, 2011.
- [58] Edmund Optics. Linear Variable Edge Filter.
<http://www.edmundoptics.com/optics/optical-filters/bandpass-filters/linear-variable-edge-filters/3367/>.
- [59] David C. English and Kendall L. Carder. Determining Bottom Reflectance and Water Optical Properties Using Unmanned Underwater Vehicles under Clear or Cloudy Skies. *Journal of Atmospheric and Oceanic Technology*, 23(2):314–324, February 2006. ISSN 0739-0572.
- [60] (EMVA) European Machine Vision Association. EMVA Standard 1288 Standard for Characterization of Image Sensors and Cameras. Technical report, 2010.
- [61] Anthony M Filippi and Rick Archibald. Support Vector Machine-Based Endmember Extraction. *Geoscience and Remote Sensing, IEEE Transactions on*, 47(3):771–791, March 2009. ISSN 0196-2892.
- [62] Graham D Finlayson, Steven Hordley, and Paul M Hubel. Recovering Device Sensitivities with Quadratic Programming. In *The Sixth Color Imaging Conference: Color Science, Systems and Applications*, pages 90–95, 1998.
- [63] Ariell Friedman, Daniel Steinberg, Oscar Pizarro, and Stefan B. Williams. Active learning using a Variational Dirichlet Process model for pre-clustering and classification of underwater stereo imagery. In *Intelligent Robots and Systems*, pages 1533–1539, 2011. ISBN 9781612844565.
- [64] Ariell Friedman, Oscar Pizarro, Stefan B Williams, and Matthew Johnson-Roberson. Multi-scale measures of rugosity, slope and aspect from benthic stereo image reconstructions. *PloS one*, 7(12):e50440, January 2012. ISSN 1932-6203.
- [65] Ariell Lee Friedman. *Automated interpretation of benthic stereo imagery*. PhD thesis, University of Sydney, 2013.
- [66] E Fuchs. Separating the fluorescence and reflectance components of coral spectra. *Applied Optics*, 40(21):3614–3621, 2001.
- [67] S. K. Fyfe. Spatial and temporal variation in spectral reflectance : Are seagrass species spectrally distinct ? *Limnology*, 48(1), 2012.

- [68] R. Garcia, T. Nicosevici, and X. Cufi. On the way to solve lighting problems in underwater imaging. In *OCEANS '02 MTS/IEEE*, volume 2, pages 1018–1024 vol.2, 2002.
- [69] Gary D Gilbert and John C Pernicka. Improvement of Underwater Visibility by Reduction of Backscatter with a Circular Polarization Technique. *Appl. Opt.*, 6(4): 741–746, 1967.
- [70] James A. Goodman and Susan L. Ustin. Classification of benthic composition in a coral reef environment using spectral unmixing. *Journal of Applied Remote Sensing*, 1(011501), 2007.
- [71] Michael D. Grossberg and Shree K. Nayar. Modeling the space of camera response functions. *IEEE transactions on pattern analysis and machine intelligence*, 26(10): 1272–82, October 2004. ISSN 0162-8828.
- [72] Mélanie a Hamel and Serge Andréfouët. Using very high resolution remote sensing for the management of coral reef fisheries: review and perspectives. *Marine pollution bulletin*, 60(9):1397–405, September 2010. ISSN 1879-3363.
- [73] Bruce Hapke. Bidirectional reflectance spectroscopy: 1. Theory. *Journal of Geophysical Research*, 86(B4):3039, 1981. ISSN 0148-0227.
- [74] Bruce W. Hapke, Robert M. Nelson, and William D. Smythe. The Opposition Effect of the Moon: The Contribution of Coherent Backscatter. *Science*, 260(5107): 509–511, April 1993.
- [75] K Hartmann, P de Souza, G Timms, A Davie, and Ieee. Measuring light attenuation with a compact Optical Emission Spectrometer and CTD mounted on a low cost AUV. In *Oceans 2009 - Europe, Vols 1 and 2*, pages 540–544. Ieee, New York, 2009. ISBN 0197-7385 978-1-4244-2522-8.
- [76] J. D. Hedley, A. R. Harborne, and P. J. Mumby. Technical note: Simple and robust removal of sun glint for mapping shallowwater benthos. *International Journal of Remote Sensing*, 26(10):2107–2112, May 2005. ISSN 0143-1161.
- [77] John D Hedley and Peter J Mumby. *Biological and remote sensing perspectives of pigmentation in coral reef organisms.*, volume 43. January 2002. ISBN 012026143X.
- [78] John D. Hedley, P. J. Mumby, K. E. Joyce, and S. R. Phinn. *Spectral unmixing of coral reef benthos under ideal conditions*. PhD thesis, April 2004.
- [79] John D. Hedley, Chris M. Roelfsema, Stuart R. Phinn, and Peter J. Mumby. Environmental and Sensor Limitations in Optical Remote Sensing of Coral Reefs: Implications for Monitoring and SensorDesign. *Remote Sensing*, 4(1):271–302, January 2012. ISSN 2072-4292.
- [80] Rob Heylen, Mario Parente, Senior Member, and Paul Gader. A Review of Nonlinear Hyperspectral Unmixing Methods. *Selected Topics in Applied Earth Observations and Remote Sensing, IEEE Journal of*, PP(99):1–25, 2014.

- [81] J Hill and C Wilkinson. Methods for ecological monitoring of coral reefs. *Australian Institute of Marine Science, . . .*, 2004.
- [82] Eric J Hochberg and M J Atkinson. Spectral discrimination of coral reef benthic communities. *Coral Reefs*, 19(2):164–171, 2000.
- [83] Eric J Hochberg and Marlin J Atkinson. Capabilities of remote sensors to classify coral, algae, and sand as pure and mixed spectra. *Remote Sensing of Environment*, 85(2):174–189, 2003.
- [84] Eric J Hochberg, Serge Andréfouët, and Misty R Tyler. Sea Surface Correction of High Spatial Resolution Ikonos Images to Improve Bottom Mapping in Near-Shore Environments. *IEEE Transactions on Geoscience and Remote Sensing*, 41(7):1724–1729, 2003.
- [85] Eric J Hochberg, Marlin J Atkinson, and Serge Andréfouët. Spectral reflectance of coral reef bottom-types worldwide and implications for coral reef remote sensing. *Remote Sensing of Environment*, 85(2):159–173, 2003.
- [86] Eric J Hochberg, Marlin J Atkinson, Amy Apprill, and Serge Andréfouët. Spectral reflectance of coral. *Coral Reefs*, 23(1):84–95, 2004.
- [87] Eric J Hochberg, Amy Apprill, Marlin Atkinson, and Robert Bidigare. Bio-optical modeling of photosynthetic pigments in corals. *Coral Reefs*, 25(1):99–109, 2006.
- [88] Heather Holden and Ellsworth LeDrew. Spectral discrimination of healthy and non-healthy corals based on cluster analysis, principal components analysis, and derivative spectroscopy. *Remote Sensing of Environment*, 65(2):217–224, 1998.
- [89] Heather Holden and Ellsworth LeDrew. Hyperspectral identification of coral reef features. *International Journal of Remote Sensing*, 20(13):2545–2564, 1999.
- [90] Heather Holden and Ellsworth LeDrew. Hyperspectral Discrimination of Healthy versus Stressed Corals Using in Situ Reflectance. *Journal of Coastal Research*, 17(4):850–858, 2001.
- [91] Heather Holden and Ellsworth LeDrew. Effects of the water column on hyperspectral reflectance of submerged coral reef features. *Bulletin of Marine Science*, 69(2):685–699, 2001.
- [92] Heather Holden and Ellsworth LeDrew. Measuring and modeling water column effects on hyperspectral reflectance in a coral reef environment. *Remote Sensing of Environment*, 81(2-3):300–308, 2002.
- [93] Heather Holden and Ellsworth LeDrew. An Examination of Variability in Vertical Radiometric Profiles in a Coral Reef Environment. *Journal of Coastal Research*, 241(241):224–231, January 2008. ISSN 0749-0208.
- [94] Weilin; Lee Hou Zhongping; Weidemann, Alan D. Why does the Secchi disk disappear? An imaging perspective. 2007.

- [95] Albert S Huang, Edwin Olson, and David C Moore. LCM : Lightweight Communications and Marshalling. In *Proc. Int. Conf. on Intelligent Robots and Systems (IROS)*, Taipei, Taiwan, 2010.
- [96] Wing-kee Huen and Yuanzhi Zhang. Spectral discrimination of coral species and habitats in Hong Kong. In *12th International Coral Reef Symposium, Cairns, Australia*, number July, pages 5–8, 2012.
- [97] Marian-Daniel Iordache, José M. Bioucas-Dias, and Antonio Plaza. Sparse unmixing of hyperspectral data. *Geoscience and Remote Sensing, IEEE Trans*, 49(6): 2014–2039, 2011.
- [98] Marian-Daniel Iordache, Antonio Plaza, Senior Member, and Ben Somers. MUSIC-CSR : Hyperspectral Unmixing via Multiple Signal Classification and Collaborative Sparse Regression. *Geoscience and Remote Sensing, IEEE Transactions on*, 52(7):4364–4382, 2014.
- [99] K. Iqbal, Michael Odetayo, Anne James, RA Salam, and AZH Talib. Enhancing the low quality images using Unsupervised Colour Correction Method. In *Systems Man and Cybernetics (SMC), 2010 IEEE International Conference on*, pages 1703–1709. IEEE. ISBN 9781424465880.
- [100] W. S. Jagger and W. R. A. Muntz. Aquatic vision and the modulation transfer properties of unlighted and diffusely lighted natural waters. *Vision Research*, 33(13): 1755–1763, 1993.
- [101] N. G. Jerlov. *Marine optics*. Elsevier Science Ltd, 1976. ISBN 0444414908.
- [102] Sen Jia and Yuntao Qian. Spectral and spatial complexity-based hyperspectral unmixing. *IEEE Transactions on Geoscience and Remote Sensing*, 45(12): 3867–3879, 2007.
- [103] G Johnsen, Z Volent, H Dierssen, R Pettersen, M Van Ardelan, F Sørreide, P Fearn, M Ludvigsen, and M Moline. Underwater hyperspectral imagery to create biogeochemical maps of seafloor properties. In *Subsea optics and imaging*, pages 508–535. Woodhead Publishing Limited, 2013. ISBN 9780857093523.
- [104] Matthew Johnson-Roberson, Suresh Kumar, and Stefan Williams. Segmentation and classification of coral for oceanographic surveys: A semi-supervised machine learning approach. In *OCEANS 2006 - Asia Pacific*, 2007. ISBN 1424401380.
- [105] Matthew Johnson-Roberson, Oscar Pizarro, Stefan B. Williams, and Ian Mahon. Generation and Visualization of Large-Scale Three-Dimensional Reconstructions from Underwater Robotic Surveys. *Journal of Field Robotics*, 27(1):21–51, 2010.
- [106] Ian Jolliffe. *Principal component analysis*. Springer Series in Statistics, Berlin: Springer, 1986.
- [107] K E Joyce and S R Phinn. Hyperspectral analysis of chlorophyll content and photosynthetic capacity of coral reef substrates. *Limnology and Oceanography*, 48(1):489–496, 2003.

- [108] Karen E. Joyce and Stuart R. Phinn. Bi-directional reflectance of corals. *International Journal of Remote Sensing*, 23(2):389–394, January 2002. ISSN 0143-1161.
- [109] P F Judy. The line spread function and modulation transfer function of a computed tomographic scanner. *Medical Physics*, 3(4):233–236, 1976.
- [110] Nir Karpel and Yoav Y Schechner. Portable polarimetric underwater imaging system with a linear response. In *SPIE Defence and Security*, volume 5432, pages 106–115. SPIE, 2004.
- [111] Douglas A Kerr. Derivation of the Cosine Fourth Law for Falloff of Illuminance Across a Camera Image. Technical Report 4, 2007.
- [112] Nirmal Keshava and John F Mustard. Spectral Unmixing. *IEEE Signal Processing Magazine*, (January), 2002.
- [113] Nirmal Keshava, John Kerekes, Dimitris Manolakis, and Gary Shaw. An algorithm taxonomy for hyperspectral unmixing. *Algorithms for Multispectral, Hyperspectral, and Ultra spectral Imagery VI*, 4049(781), 2000.
- [114] Roger King and Nicolas Younan. Pixel Unmixing via Information of Neighboring Pixels. *GIScience & Remote Sensing*, 43(4):310–322, December 2006. ISSN 1548-1603.
- [115] John T. O. Kirk. *Light and Photosynthesis in Aquatic Environments*. Cambridge University Press, 3rd edition, 2011.
- [116] Wojciech M. Klonowski. Retrieving key benthic cover types and bathymetry from hyperspectral imagery. *Journal of Applied Remote Sensing*, 1(1):011505, December 2007. ISSN 1931-3195.
- [117] Halina T. Kobryn, Kristin Wouters, Lynnath E. Beckley, and Thomas Heege. Ningaloo Reef: Shallow Marine Habitats Mapped Using a Hyperspectral Sensor. *PLoS ONE*, 8(7):e70105, July 2013. ISSN 1932-6203.
- [118] P Koepke. Effective reflectance of oceanic whitecaps. *Applied optics*, 23(11):1816, July 1984. ISSN 0003-6935.
- [119] Ron Kohavi. A Study of Cross-Validation and Bootstrap for Accuracy Estimation and Model Selection. In *International Joint Conference on Artificial Intelligence*, 1995.
- [120] Oili Kohonen, Jussi Parkkinen, and Timo Jääskeläinen. Databases for spectral color science. *Color Research & Application*, 31(5):381–390, October 2006. ISSN 0361-2317.
- [121] SB Kotsiantis. Supervised machine learning: a review of classification techniques. *Informatica (03505596)*, 31:249–268, 2007.

- [122] Z. Lee, K. L. Carder, C. D. Mobley, R. G. Steward, and J. S. Patch. Hyperspectral remote sensing for shallow waters. I. A semianalytical model. *Applied Optics*, 37(27):6329–6338, 1998.
- [123] Z. Lee, K. L. Carder, C. D. Mobley, R. G. Steward, and J. S. Patch. Hyperspectral remote sensing for shallow waters. 2. Deriving bottom depths and water properties by optimization. *Applied Optics*, 38(18):3831–3843, 1999.
- [124] Ian Leiper, Stuart Phinn, and Arnold G. Dekker. Spectral reflectance of coral reef benthos and substrate assemblages on Heron Reef, Australia. *International Journal of Remote Sensing*, 33(12):3946–3965, June 2012. ISSN 0143-1161.
- [125] Ian Leiper, Stuart Phinn, Chris Roelfsema, Karen Joyce, and Arnold Dekker. Mapping Coral Reef Benthos, Substrates, and Bathymetry, Using Compact Airborne Spectrographic Imager (CASI) Data. *Remote Sensing*, 6(7):6423–6445, July 2014. ISSN 2072-4292.
- [126] G D Lewis, D L Jordan, and P J Roberts. Backscattering target detection in a turbid medium by polarization discrimination. *Applied Optics*, 38(18):3937–3944, 1999.
- [127] Martin Ludvigsen, Geir Johnsen, Petter a. Lagstad, Asgeir J. Sorensen, and Oyvind Odegard. Scientific operations combining ROV and AUV in the Trondheim Fjord. *2013 MTS/IEEE Oceans - Bergen*, pages 1–7, June 2013.
- [128] David K. Lynch and William C. Livingston. *Color And Light In Nature*. Cambridge University Press, 2001.
- [129] Alasdair A. MacArthur, Chris MacLellan, and Tim J. Malthus. The implications of non-uniformity in fields-of-view of commonly used field spectroradiometers. *2007 IEEE International Geoscience and Remote Sensing Symposium*, pages 2890–2893, 2007.
- [130] J Maeder, S Narumalani, D C Rundquist, R L Perk, J Keck, J Schalles, and K Hutchins. Classifying and mapping general coral-reef structure using Ikonos data. *Photogrammetric Engineering and Remote Sensing*, 68(12):1297–1306, 2002.
- [131] M Marcos, M N Soriano, and C A Saloma. Classification of coral reef images from underwater video using neural networks. *OPTICS EXPRESS*, 13:8766–8771, 2005. ISSN 1094-4087.
- [132] Mikhail V Matz, N Justin Marshall, and Misha Vorobyev. Are Corals Colorful? *Photochemistry and Photobiology*, 82(2):345–350, 2006.
- [133] Christian Mauer and Dietmar Wueller. Measuring the spectral response with a set of interference filters. *Proceedings of SPIE*, 7250:72500S–72500S–10, 2009.
- [134] Anand Mehta, Eraldo Ribeiro, Jessica Gilner, and Robert van Woesik. Coral reef texture classification using support vector machines. In *VISAPP (2)*, pages 302–310, 2007.

- [135] Shaohui Mei, Mingyi He, Zhiyong Wang, and Dagan Feng. Spatial Purity Based Endmember Extraction for Spectral Mixture Analysis. *IEEE Transactions on Geoscience and Remote Sensing*, 48(9):3434–3445, September 2010. ISSN 0196-2892.
- [136] Ian Miller and R Müller. Validity and reproducibility of benthic cover estimates made during broadscale surveys of coral reefs by manta tow. *Coral Reefs*, (18): 353–356, 1999.
- [137] C. D. Mobley. *Light and water: Radiative transfer in natural waters*, volume 592. Academic Press, 1994.
- [138] C. D. Mobley. Estimation of the remote-sensing reflectance from above-surface measurements. *Applied optics*, 38(36):7442–55, December 1999. ISSN 0003-6935.
- [139] C. D. Mobley and L. K. Sundman. Hydrolight. Bellevue, WA, USA.
- [140] Mark A. Moline, Ian Robbins, Brian Zelenke, W. Scott Pegau, and Hemantha Wijesekera. Evaluation of bio-optical inversion of spectral irradiance measured from an autonomous underwater vehicle. *Journal of Geophysical Research*, 117(November 2011):C00H15, January 2012. ISSN 0148-0227.
- [141] Giorgos Mountrakis, Jungho Im, and Caesar Ogole. Support vector machines in remote sensing: A review. *ISPRS Journal of Photogrammetry and Remote Sensing*, 66(3):247–259, May 2011. ISSN 09242716.
- [142] Sushil Mujumdar and Hema Ramachandran. Imaging through turbid media using polarization modulation: dependence on scattering anisotropy. *Optics Communications*, 241(1-3):1–9, 2004.
- [143] E. Myre and R. Shaw. The turbidity tube: simple and accurate measurement of turbidity in the field. *Michigan Technology University, Michigan*, 2006.
- [144] NASA. Living Ocean. 2010.
- [145] José M. P. Nascimento and José M. Bioucas-Dias. Hyperspectral unmixing algorithm via dependent component analysis. In *International Geoscience and Remote Sensing Symposium (IGARSS)*, pages 4033–4036, 2007. ISBN 1424412129.
- [146] José M. P. Nascimento and José M. Bioucas-Dias. Hyperspectral Imagery Framework for Unmixing and Dimensionality Estimation. *Pattern Recognition - Applications and Methods*, 204:193–204, 2013.
- [147] José M. P. Nascimento and José M. Bioucas Dias. Vertex Component Analysis : A Fast Algorithm to Unmix Hyperspectral Data. *IEEE Transactions on Geoscience and Remote Sensing*, 43(4):898–910, 2005.
- [148] José M. P. Nascimento and José M. Bioucas Dias. Does independent component analysis play a role in unmixing hyperspectral data? *Geoscience and Remote . . .*, 43 (1):175–187, 2005.

- [149] Timo Ojala, Matti Pietikäinen, and Topi Mäenpää. Multiresolution Gray-Scale and Rotation Invariant Texture Classification with Local Binary Patterns. *IEEE Transactions on Pattern Analysis and Machine Intelligence*, 24(7):971–987, 2002.
- [150] B A Olshausen and D J Field. Emergence of simple-cell receptive field properties by learning a sparse code for natural images. June 1996. ISSN 0028-0836.
- [151] Mehmet Özger and Zekai en. Triple diagram method for the prediction of wave height and period. *Ocean Engineering*, 34(7):1060–1068, May 2007. ISSN 00298018.
- [152] Danny Pascale. RGB coordinates of the Macbeth ColorChecker. Technical report, 2006.
- [153] S. Phinn, M. Stanford, P. Scarth, a. T. Murray, and P. T. Shyy. Monitoring the composition of urban environments based on the vegetation-impervious surface-soil (VIS) model by subpixel analysis techniques. *International Journal of Remote Sensing*, 23(20):4131–4153, January 2002. ISSN 0143-1161.
- [154] Stuart R Phinn, Carl Menges, Greg J E Hill, and Michael Stanford. Optimizing Remotely Sensed Solutions for Monitoring, Modeling, and Managing Coastal Environments. *Remote Sensing of Environment*, 4257(00), 1997.
- [155] Thomas W. Pike. Using digital cameras to investigate animal colouration: estimating sensor sensitivity functions. *Behavioral Ecology and Sociobiology*, 65(4): 849–858, November 2010. ISSN 0340-5443.
- [156] O Pizarro, P Rigby, M Johnson-Roberson, S B Williams, and J Colquhoun. Towards image-based marine habitat classification. *Oceans 2008*, 2008.
- [157] Oscar Pizarro, Stefan B. Williams, Michael V. Jakuba, Matthew Johnson-Roberson, Ian Mahon, Mitch Bryson, Daniel Steinberg, Ariell Friedman, Donald Dansereau, Navid Nourani-Vatani, Daniel Bongiorno, Michael Bewley, Asher Bender, Nasir Ashan, and Bertrand Douillard. Benthic monitoring with robotic platforms The experience of Australia. *2013 IEEE International Underwater Technology Symposium (UT)*, pages 1–10, March 2013.
- [158] Antonio Plaza, Pablo Martinez, Rosa Perez, and Javier Plaza. Spatial/spectral endmember extraction by multidimensional morphological operations. *Geoscience and Remote . . .*, 40(9):2025–2041, 2002.
- [159] Rudolph W Preisendorfer. *Application of radiative transfer theory to light measurements in the sea*. Institut géographique national, 1961.
- [160] S. J. Purkis. A "Reef-Up" approach to classifying coral habitats from IKONOS imagery. *IEEE Transactions on Geoscience and Remote Sensing*, 43(6):1375–1390, June 2005. ISSN 0196-2892.
- [161] Autun Purser, Melanie Bergmann, Tomas Lundälv, Jörg Ontrup, and Tim W. Nattkemper. Use of machine-learning algorithms for the automated detection of cold-water coral habitats: A pilot study. *Marine Ecology Progress Series*, 397: 241–251, 2009. ISSN 01718630.

- [162] X. Quan and E. S. Fry. Empirical equation for the index of refraction of seawater. *Applied optics*, 34(18):3477–80, June 1995. ISSN 0003-6935.
- [163] R. G. Resmini, M. E. Kappus, W. S. Aldrich, J. C. Harsanyi, and M. Anderson. Mineral mapping with HYperspectral Digital Imagery Collection Experiment (HYDICE) sensor data at Cuprite, Nevada, U.S.A. *International Journal of Remote Sensing*, 18(7):1553–1570, May 1997. ISSN 0143-1161.
- [164] M. K. Ridd. Exploring a V-I-S (vegetation-impervious surface-soil) model for urban ecosystem analysis through remote sensing: comparative anatomy for cities. *International Journal of Remote Sensing*, 16(12):2165–2185, August 1995. ISSN 0143-1161.
- [165] Paul Rigby, Oscar O.R. Pizarro, and Stefan B. S.B. Stefan B Williams. Toward adaptive benthic habitat mapping using gaussian process classification. *Journal of Field Robotics*, 27:741–758, 2010. ISSN 15564959.
- [166] Chris M Roelfsema and Stuart R Phinn. Spectral reflectance library of selected biotic and abiotic coral reef features in Heron Reef. Technical report, Centre for Remote Sensing & Spatial Information Science, School of Geography, Planning & Environmental Management, University of Queensland, Brisbane, Australia, 2012. URL <http://doi.pangaea.de/10.1594/PANGAEA.804589>.
- [167] Chris M. Roelfsema, Mitchell Lyons, Eva M. Kovacs, Paul Maxwell, Megan I. Saunders, Jimena Samper-Villarreal, and Stuart R. Phinn. Multi-temporal mapping of seagrass cover, species and biomass: A semi-automated object based image analysis approach. *Remote Sensing of Environment*, 150:172–187, July 2014. ISSN 00344257.
- [168] Jos B. T. M. Roerdink and Arnold Meijster. The Watershed Transform: Definitions, Algorithms and Parallelization Strategies. *Fundamenta Informaticae*, 41:1–40, 2001.
- [169] Alex D. Rogers and Dan Laffoley. International Programme on the State of the Ocean Combined Research Papers. *Marine Pollution Bulletin*, 74(2):491–494, 2013.
- [170] Javier Romero, Antonio Garcia-Beltran, and Javier Hernández-Andrés. Linear bases for representation of natural and artificial illuminants. *JOSA A*, 14(5):1007–1014, 1997. ISSN 1520-8532.
- [171] Javier Romero, Eva Valero, Javier Hernández-Andrés, and Juan L Nieves. Color-signal filtering in the Fourier-frequency domain. *Journal of the Optical Society of America. A, Optics, image science, and vision*, 20(9):1714–24, September 2003. ISSN 1084-7529.
- [172] Vincent Roy. Sun Position - <http://www.mathworks.com.au/matlabcentral/fileexchange/4605>. 2004.
- [173] Martin Rump, Arno Zinke, and Reinhard Klein. Practical Spectral Characterization of Trichromatic Cameras. In *Proceedings of the 2011 SIGGRAPH Asia Conference*, volume 30, 2011.

- [174] Abraham Savitzky and M. J. E. Golay. Smoothing and Differentiation of Data by Simplified Least Squares Procedures. *Analytical Chemistry*, 36(8):1627–1639, 1964.
- [175] Louis L. Scharf. *Statistical signal processing*, volume 98. Addison-Wesley Reading, MA, 1991.
- [176] Y. Y. Schechner and N. Karpel. Clear underwater vision. In *Computer Vision and Pattern Recognition, 2004. CVPR 2004. Proceedings of the 2004 IEEE Computer Society Conference on*, volume 1, pages I–536–I–543 Vol.1, 2004. ISBN 1063-6919.
- [177] Y. Y. Schechner and N. Karpel. Recovery of underwater visibility and structure by polarization analysis. *Oceanic Engineering, IEEE Journal of*, 30(3):570–587, 2005.
- [178] Yoav Y. Schechner, Shree K. Nayar, and Peter N. Belhumeur. Multiplexing for optimal lighting. *IEEE transactions on pattern analysis and machine intelligence*, 29(8):1339–54, August 2007. ISSN 0162-8828.
- [179] Gary A. Shaw and Hsiao-hua K. Burke. Spectral Imaging for Remote Sensing. *Lincoln Laboratory Journal*, 14(1):3–28, 2003.
- [180] Sylvia S. Shen and Edward M. Bassett III. Information-theory-based band selection and utility evaluation for reflective spectral systems. In *Proc. SPIE 4725, Algorithms and Technologies for Multispectral, Hyperspectral, and Ultraspectral Imagery VIII*, volume 4725, pages 18–29, 2002.
- [181] Chen Shi and Le Wang. Incorporating spatial information in spectral unmixing: A review. *Remote Sensing of Environment*, 149:70–87, June 2014. ISSN 00344257.
- [182] R. B. Singer and T. B McCord. Mars: Large scale mixing of bright and dark surface materials and implications for analysis of spectral reflectance. In *Lunar and Planetary Science Conference*, pages 1835–1848, 1979.
- [183] D Smith and M Dunbabin. Automated Counting of the Northern Pacific Sea Star in the Derwent Using Shape Recognition. 2007.
- [184] Randall Smith. *Introduction to Hyperspectral Imaging*. MicroImages Inc., 2012.
- [185] Martin Solli, Mattias Andersson, Reiner Lenz, and Björn Kruse. Color Measurements with a Consumer Digital Camera. *Lecture Notes in Computer Science*, pages 105–114, 2005.
- [186] M. Soriano, S. Marcos, C. Saloma, M. Quibilan, and P. Alino. Image classification of coral reef components from underwater color video. *MTS/IEEE Oceans 2001. An Ocean Odyssey. Conference Proceedings (IEEE Cat. No.01CH37295)*, 2, 2001. ISSN 0933957289.
- [187] M C Spillane, E C Monahan, P A Bowyer, D M Doyle, and P J Stabeno. Whitecaps and Global Fluxes. In Edward C. Monahan and Gearóid Mac Niocaill, editors, *Oceanic Whitecaps SE - 19*, volume 2 of *Oceanographic Sciences Library*, pages 209–218. Springer Netherlands, 1986. ISBN 978-94-010-8575-5.

- [188] David W. J. Stein, Scott G. Beaven, Lawrence E. Hoff, Edwin M. Winter, Alan P. Schaum, and Alan D. Stocker. Anomaly detection and classification for hyperspectral imagery. *Geoscience and Remote Sensing, IEEE Transactions on*, 40(6):1314–1325, 2002.
- [189] D. M. Steinberg, S. B. Williams, O. Pizarro, and M. V. Jakuba. Towards autonomous habitat classification using Gaussian Mixture Models. *Intelligent Robots and Systems (IROS), 2010 IEEE/RSJ International Conference on*, 2010. ISSN 2153-0858.
- [190] Daniel M Steinberg, Stefan B Williams, Oscar Pizarro, and Michael V Jakuba. Towards autonomous habitat classification using Gaussian Mixture Models. *2010 IEEE/RSJ International Conference on Intelligent Robots and Systems*, pages 4424–4431, October 2010.
- [191] Daniel M. Steinberg, Ariell Friedman, Oscar Pizarro, and Stefan B. Williams. A Bayesian nonparametric approach to clustering data from underwater robotic surveys. In *International Symposium on Robotics Research, Flagstaff, Arizona, USA*, 2011.
- [192] P Stigell, K Miyata, and M Hauta-Kasari. Wiener estimation method in estimating of spectral reflectance from RGB images. *Pattern Recognition and Image Analysis*, 17(2):233–242, 2007.
- [193] G Sulzberger, J Bono, R J Manley, T Clem, L Vaizer, R Holtzapple, and Vernon Ave. Hunting Sea Mines with UUV-Based Magnetic and Electro-Optic Sensors. *OCEANS 2009, MTS/IEEE Biloxi*, pages 1–5, 2009.
- [194] Deyong Sun, Yunmei Li, Qiao Wang, Chengfeng Le, Heng Lv, Changchun Huang, and Shaoqi Gong. A novel support vector regression model to estimate the phycoyanin concentration in turbid inland waters from hyperspectral reflectance. *Hydrobiologia*, (2004), November 2011. ISSN 0018-8158.
- [195] L. Torres-Méndez and Gregory Dudek. Color correction of underwater images for aquatic robot inspection. In *Energy Minimization Methods in Computer Vision and Pattern Recognition*, pages 60–73. Springer, 2005.
- [196] T. Treibitz and Y. Y. Schechner. Instant 3Descatter. In *Computer Vision and Pattern Recognition, 2006 IEEE Computer Society Conference on*, volume 2, pages 1861–1868, 2006. ISBN 1063-6919.
- [197] T. Treibitz and Y. Y. Schechner. Active Polarization Descattering. *Pattern Analysis and Machine Intelligence, IEEE Transactions on*, 31(3):385–399, 2009.
- [198] Te-Ming Tu. Unsupervised signature extraction and separation in hyperspectral images: a noise-adjusted fast independent component analysis approach. *Optical Engineering*, 39(4):897–906, 2000. ISSN 0091-3286.
- [199] Iuliu Vasilescu and Daniela Rus. *Using light underwater: devices, algorithms and systems for maritime persistent surveillance*. PhD thesis, Massachusetts Institute of Technology, 2009.

- [200] Iuliu Vasilescu, Carrick Detweiler, and Daniela Rus. Color-accurate underwater imaging using perceptual adaptive illumination. *Autonomous Robots*, pages 285–296, August 2011. ISSN 0929-5593.
- [201] Poorvi L. Vora, Joyce E. Farrell, Jerome D. Tietz, and David H. Brainard. Digital color cameras - 2 - Spectral response. Technical report, Hewlett-Packard Laboratories, 1997. URL <http://www.hp1.hp.com/techreports/97/HPL-97-54.html>.
- [202] Poorvi L. Vora, Joyce E. Farrell, Jerome D. Tietz, and David H. Brainard. Digital color cameras - 1 - Response models. Technical report, Hewlett-Packard Laboratories, 1997. URL <http://www.hp1.hp.com/techreports/97/HPL-97-53.html>.
- [203] Clive Wilkinson. *Status of coral reefs of the world: 2008*. Global Coral Reef Monitoring Network, 2008. ISBN 1447-6185.
- [204] S. B. Williams, O. Pizarro, J. M. Webster, R. J. Beaman, I. Mahon, M. Johnson-Roberson, and T. C. L. Bridge. Autonomous Underwater Vehicle-Assisted Surveying of Drowned Reefs on the Shelf Edge of the Great Barrier Reef, Australia. *Journal of Field Robotics*, 27(5):675–697, 2010.
- [205] Michael E. Winter. N-FINDR: an algorithm for fast autonomous spectral end-member determination in hyperspectral data. In *SPIE Conference on Imaging Spectrometry V*, volume 3753, pages 266–275, 1999.
- [206] A Yamashita, M Fujii, and T Kaneko. Color Registration of Underwater Images for Underwater Sensing with Consideration of Light Attenuation. In *Robotics and Automation, 2007 IEEE International Conference on*, pages 4570–4575, 2007. ISBN 1050-4729.
- [207] Alina Zare, Paul Gader, Ouiem Bchir, and Hichem Frigui. Piecewise Convex Multiple-Model Endmember Detection and Spectral Unmixing. *IEEE Transactions on Geoscience and Remote Sensing*, 51(5):2853–2862, May 2013. ISSN 0196-2892.
- [208] David G Zawada and Jules S Jaffe. Changes in the fluorescence of the Caribbean coral *Montastraea faveolata* during heat-induced bleaching. *Limnology Oceanography*, 48(1, part 2):412–425, 2003.
- [209] David G. Zawada and Charles H. Mazel. Fluorescence-Based Classification of Caribbean Coral Reef Organisms and Substrates. *PLoS ONE*, 9(1):e84570, January 2014. ISSN 1932-6203.
- [210] P. Zege, A. P. Ivanov, and I. L. Katsev. *Image transfer through a scattering medium*. Springer Verlag, 1991. ISBN 3540519785.
- [211] Guoying Zhao and M Pietikainen. Dynamic Texture Recognition Using Local Binary Patterns with an Application to Facial Expressions. *Pattern Analysis and Machine ...*, pages 1–14, 2007.

Appendices

Appendix A

Enhanced underwater visibility through the use of polarisation

A.1 Introduction

The underwater environment present formidable barriers towards it's exploration, one of which is the limited passage of light. Optical sensing is an attractive means of underwater imaging over sonar based imaging due to it's affordability, high resolution (both spatially and chromatically) and ease of interpretation by an operator. The major inhibitor of light transmission is the presence of suspended organic matter and absorption by water molecules. This results in both absorption and scattering of the photons. Absorption lowers both the illumination of the target and the luminance returning from the target. In a medium where absorption is the only factor (no scattering), the visible range would just be a function of the light source illumination and the camera sensitivity [69]. In the blue region (480nm) of the ocean, 60% of the water's attenuation is due to scattering and 40% due to absorption, in other spectral regions absorption is the dominant attenuation factor [56].

For an actively lit scene scattering both stops or deflects light from returning from the object of interest (forward scattering) but also reflects light from the light source back into the sensor commonly called backscatter. [101, 126]

Polarisation naturally exists in the underwater environment up to depths of 200m [101]. Light can become naturally polarised through several means, firstly light from the sky can

be partially polarised and pass through into the water. Secondly scatterings of the light by the water molecules or by particles in the water column can polarise the light and finally the transmission of unpolarised sunlight through the surface of the water can result in elliptically polarised light (dependent on incident angle) [137].

One method for reducing the effect of the backscatter is through the use of polarisation filters [69]. The method is to place a filter in-front of the light source thus polarising the outbound light and another in-front of the sensor to filter the light entering the camera [176], See Figure A.1 for a visual representation of the principle behind the method. The probability of the polarisation orientation remaining intact is reduced as the number of incident reflections increases. [69] Therefore particles in the water column reflect the light back polarised whereas the object of interest, dependent on surface structure reflects the light partially or fully depolarised. [126, 177, 210].

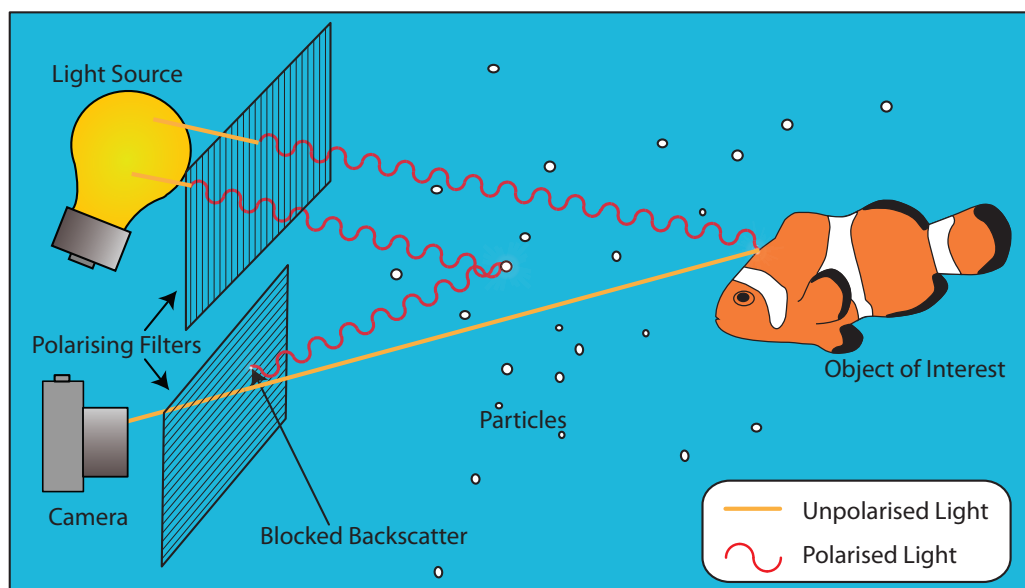


Figure A.1 – The principal Outbound light is polarised, reflections off the particles (backscatter) in the water remain polarised, reflections of objects of interest are depolarised. The depolarised light from the object of interest passes through the camera filter whereas the filter blocks the opposed polarised light from the backscatter. Thus the contrast of the objects of interest is increased.

In the case of using linear polarisation filters, if the sensor filter is at 90° to the light source filter it will have the effect of blocking the reflected light from the suspended particles which have only reflected the light very few times, hence the light will still be partially polarised. This results in reducing the amount of light reflected back into the sensor by the

suspended particles thus reducing backscatter. Several papers used circular polarisers over linear due to the angle invariance of circular polariser, the slight performance advantage and the compatibility with digital SLR auto-focusing systems [69, 110, 177].

The performance advantage of circular polarisers is alleged in [100] to be better due to circular polarised light being more easily depolarised than linearly polarised light [126]. In [126] it was also found that rougher surfaces such as rusty metal depolarise light whereas specular reflectors do not. An improvement in the performance of polarisation discrimination was found for an isotropically scattering medium as opposed to anisotropic media. Anisotropic particles are more representative of ocean particles [142]. The particles are generally of sizes larger than the wavelength of light and hence scattering is independent of wavelength [100].

This work plans to show that polarisation filters on the light source and on the receiver at perpendicular orientations reduces the magnitude of light due to backscatter. This results in an increased visibility range, higher contrast and sharper images. These improvements will be quantified through the use of the modulation transfer function and contrast ratio comparisons. Two sets of data will be examined, a tank experiment taken in a controlled environment and an outside experiment taken in a dam.

A.2 Methodology

Two experiments will be conducted to show the performance gain of using polarisation filters, first in a tank as a control and second in a dam to emulate an ocean environment to be more representative of an AUV application.

To examine the effects of using polarisation filters in a turbid media a control experiment was setup. Various objects were placed in a matte black *Pelican* case of dimensions 74x45cm, this was filled with water to a depth of 18cm, approximately 60 Litres (*Figure A.2a*). The objects selected were a standard drinking glass, a piece of hardwood, a piece of die-cast metal, a rusty bolt attached to a stick of reflective stainless steel and a piece of slightly reflective plastic (*Figure A.2b*).

To incrementally make the water more turbid small measured quantities of full cream milk were added and stirred into the water. The turbidity of the water was measured using a *OBS-3A* from *D&A Instrument Company*. The camera used was an underwater *Olympus*

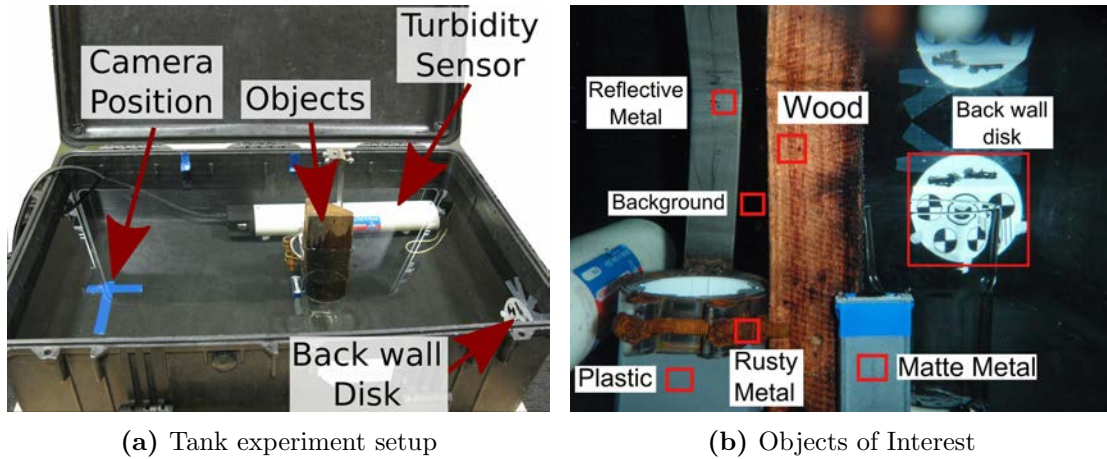


Figure A.2 – Experimental setup

μ Touch-8000 [49]. The light into the scene was provided solely by the camera’s on-board flash. The experiment was conducted in a dark room. A polarising filter was placed in front of the light source and another in front of the camera’s lens. The nomenclature regarding the filter orientation will be either 90° or 0° which refers to the relative polarising angle of the lens filter to the flash filter. At an orientation of 90° the lens filter will block reflected polarised light from the flash, and subsequently pass reflected polarised light at 0° .

Two photographs of the scene were taken at each turbidity level. The first photo was with the camera filter’s polarisation axis parallel to the flash filter’s polarisation orientation and the second with the camera filter orientation perpendicular to that of the flash. This results in the first photo passing polarised light reflected back from the scene and in the second photo polarised light is blocked.

For the realistic environment experiment, Australian Centre for Field Robotics’ (ACFR) Diver Rig was used in a freshwater dam (*Lat: -33.918007, Long: 151.230068*). The Diver Rig is a diver held stereo vision system, it contains two Prosilica GC1380 machine vision cameras, one was mono and the other Bayer arranged RGB. The images were recorded in raw. On either side of the camera housing were mounted high intensity LED strobes. Polarisation filters were placed on the strobes and in front of both camera lenses in perpendicular orientations. The target imaged was a MacBeth colour checker chart and an optical resolution chart. Three sets of experiments were conducted, first the target was imaged at different depths in a horizontal orientation to avoid non-linearities due to turbidity stratifications in the dam. The second test was establishing the visibility range for the polariser

orientations, this involved moving the target away from the cameras until they disappeared. The final test was looking down at the target on the seabed to emulate an AUV scenario.

A.2.1 Modulation Transfer Function

To quantify the effect of the turbid medium on the recorded image, the modulation transfer function is used. The Modulation Transfer Function (MTF) is the magnitude of the *optical transfer function* with the phase component ignored. It characterises the optical system's ability to reproduce frequency components within the scene being imaged. Within the imaging community it is a common metric for quantifying the optical systems ability to reproduce the scene [37, 94, 100, 109]. For this experiment, the effect the milk has upon the MTF will be examined.

The effect can be measured in two ways. The first is looking at the imaging system's ability to reproduce a 'sharp' edge [109]. Once a sharp edge is imaged at given turbidity, a scan perpendicular to the edge will show pixel values for the background transitioning into the edge material's pixel readings. As this edge becomes more blurred due to the scattering effect of the milk particles, the gradient of the transition line will decrease. By taking the first derivative of this *edge scan function* we obtain the Line Spread Function (LSF) this gives us the gradient of the edge. By taking the Fourier transform of the LSF we obtain the MTF. This is scaled from 0 to 1 on the vertical axis for fraction of contrast reproduction. The frequency response on the horizontal axis is measured in terms of *lines/mm*.

This method is quite susceptible to noise on the surfaces being sampled. To maintain the profile of the edge scan function and reduce the noise elements the Savitzky-Golay smoothing filter [174] was used. This performs a local polynomial regression for a given series of values, it is good at preserving features such as relative maxima and minima.

The more accurate second method to calculate the MTF of the system is to image a optical resolution chart. This chart has a series of vertical lines of decreasing width and increasing frequency (*lines/mm*) then from an image of this chart the MTF at a certain ω can be calculated from (A.1).

$$MTF(\omega) = \frac{max_{\omega} - min_{\omega}}{max_{\omega} + min_{\omega}} \quad (A.1)$$

Where: max_{ω} & min_{ω} correspond to the maximum and minimum intensity pixel values respectively for the corresponding frequency ω .

A.2.2 Contrast Comparison

The second method to measure the polarising filters improvement to the image is to compare the contrast of the image [176]. Turbidity has the effect of clouding or washing out the image, a higher contrast enables the discernment of greater detail in the picture. To measure contrast it is a ratio of the pixel intensities for neighbouring parts of an object within a scene. In this experiment we shall compare a piece of an object with a piece of the background.

To determine the contrast of the scene for a user selected ($j \times k$) crop of the image, the average pixel value is calculated according to (A.2):

$$avg_{colourband} = \frac{\sum_{a=1}^j \sum_{b=1}^k p_{ab}}{jk} \quad (A.2)$$

where p_{ab} is the pixel value for the colour band at pixel position (a, b) . This is repeated for the other colour bands *Red*, *Green*, *Blue* then the overall pixel average is computed according to (A.3):

$$avg_{object} = \frac{avg_{red} + avg_{green} + avg_{blue}}{3} \quad (A.3)$$

The average pixel value is repeated for a user chosen section of the background within the image, from this the contrast is computed

$$contrast = \frac{avg_{obj} - avg_{bk}}{avg_{bk}} \quad (A.4)$$

where avg_{obj} and avg_{bk} are the average pixel values over red, green and blue for the user chosen area for the object of interest and the background. This is repeated for all the turbidity records and the other materials.

A.2.3 Visibility Enhancement

The use of polarisation filters also has the benefit of increasing the visibility distance. In a homogeneous water medium with low backscattering the light intensity will attenuate according to Beers-Lambert Law.

$$I = I_0 \exp^{-ad} \quad (\text{A.5})$$

$$a = \textit{scatter} + \textit{absorb} \quad (\text{A.6})$$

Where I is the intensity of light at distance d from the source, I_0 is the intensity of the light source and a is the attenuation coefficient. Where a is made up of the scattering coefficient (*scatter*) and the absorption coefficient (*absorb*).

The method to measure the improvement to visibility with the tank experiment is quite rough. This is done by observing when an object disappears from view for both filter orientations. In the case of the tank experiment an easy object to track which disappears quickly is the disk on the back wall of the tank (Figure A.2a). This object is 63.5cm from the camera. The visibility distance for a certain turbidity can be calculated from [143]:

$$\textit{distance} = 244.13(\textit{turbidity})^{-0.662} \quad (\text{A.7})$$

Where: *distance* is the visibility distance in cm and *turbidity* is measured in Nephelometric Turbidity Units (NTU).

For the dam experiment the visibility distance was obtained by moving the target away from the camera and observing when it is no longer visible on both the 90° and 0° orientations. Then to compute the visibility enhancement a ratio of d_{90°/d_{0° are calculated. Where d_{90° & d_{0° are the visibility drop off distances at 90° and 0° orientations respectively.

A.3 Results

Using the polarisations filtered produced some quite obvious visibility improvements. The tank results produced slightly better results, this was expected given the controlled nature

of the test environment. Images from the tank experiments for a turbidity of 3.2 NTU and 13 NTU can be seen in figures A.4 & A.3. Some noticeable observations of the tank results are the 90° orientation appears a lot less washed out and the colours appear more vivid. In figure A.4 for the 0° orientation the backscatter is very obvious on the right of the image, which completely masks the view of the objects on the right of the scene. The filters also have the effect of removing reflections from the reflective metal and plastic objects. This allows us to view greater detail on the surface of the metal object and removes the halo around the reflection point.

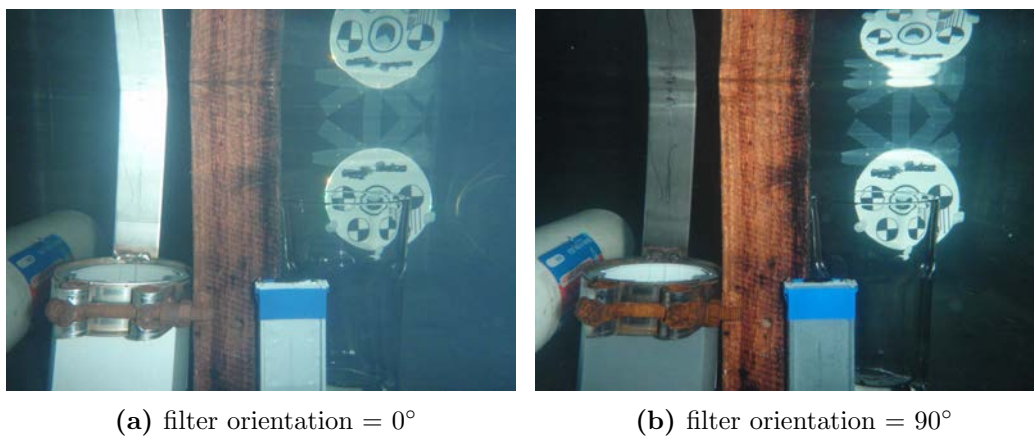


Figure A.3 – Turbidity = 3.2 NTU

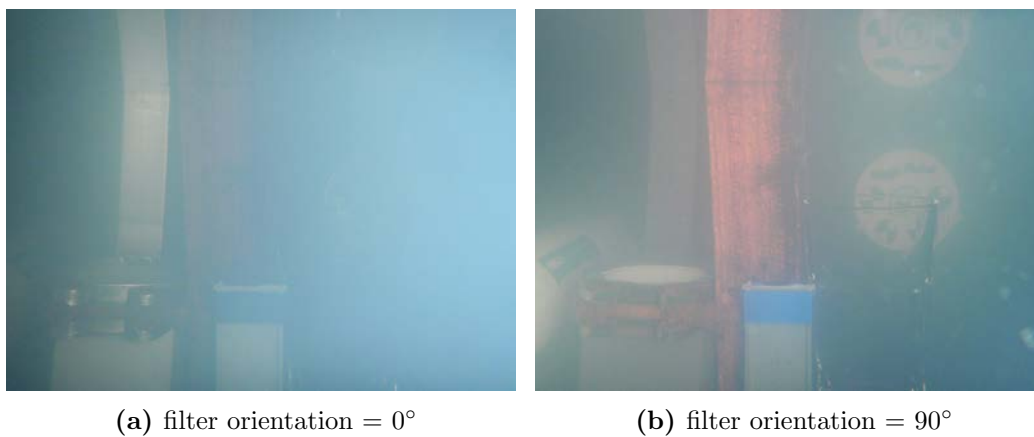


Figure A.4 – Turbidity = 13.0 NTU

A.3.1 Improvement to the Modulation Transfer Function

To test the comparison of sharpness between 90° and 0° degree orientations we chose a turbidity of 7.3 NTU to represent an set of images which are undoubtedly clouded by the milk. Then by applying the MTF analysis technique described earlier figure A.5 was obtained. Both responses were scaled by the same amount to make the 90° set become scaled from 0 to 1. The results show that the 90° orientation was more able to reproduce higher frequency components so we would subsequently expect this image to be sharper than the 0° image.

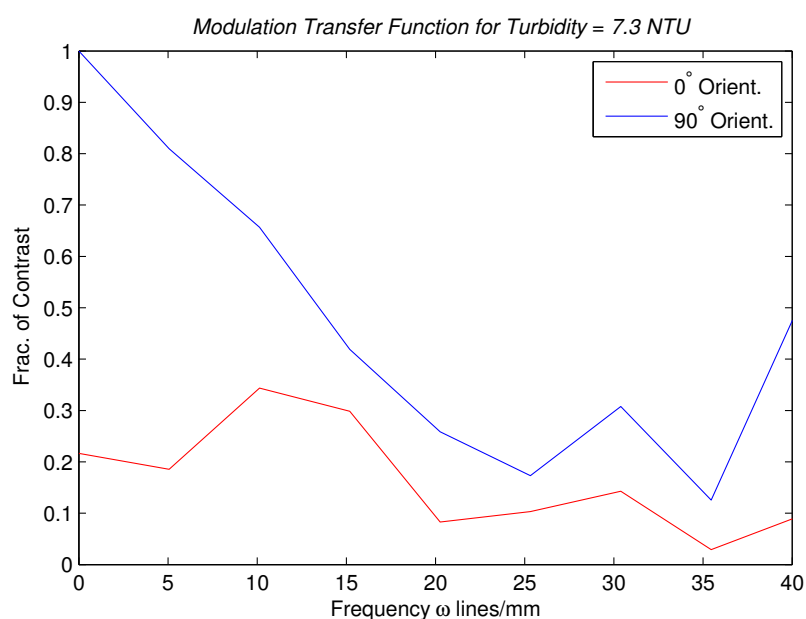


Figure A.5 – A comparison of the MTF for different polarisation filter orientations for turbidity = 7.3NTU

A.3.2 Contrast Improvements

Polarisation made a difference to the contrast ratio as show in Figure A.6. It is consistently higher for the 90° orientation than for the 0° up until a turbidity of 21 NTU. This point corresponds to the limit of visibility for the 90° set. This is a noticeable contrast increase for the wood, but it this performance gain varied for the different materials present in the scene. Figure A.7 shows the difference between the contrast ratios of 90° minus the 0° orientation. For the reflective plastic there was actually a reduction in contrast, this

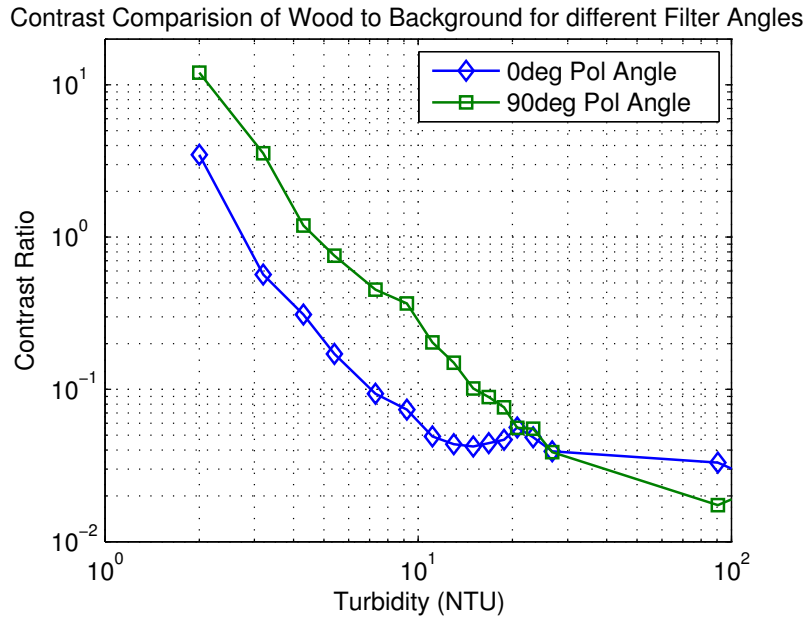


Figure A.6 – Comparing the contrast with the wood to the background for filter angles parallel and perpendicular to the orientation of the light source filters

fits with our expectations. We would expect the return intensities of the more reflective materials to be reduced by the cross polarisation of the filters.

A.3.3 Increased Visibility

For the tank experiment the back wall disk is observed to disappear at the image for 18.8 NTU for 90° orientation and between 9.2 and 13 NTU for 0°. So using Equation (A.7) 18.8 NTU should correspond to a vis distance of 35cm so for a distance of 63.5cm that is an improvement of 1.81 half way between 9.2 and 13 NTU results in a visibility distance of 49 cm for 63.5cm the corresponding turbidity is 7.64 NTU.

A.4 Discussion

The calculation of the MTF for the tank experiments is not very reliable for high frequencies because of noise on the sensors as mentioned. A more accurate measure of the MTF is to image the optical resolution chart. The segment that was used to create the MTF was a section of the background onto the edge of the wood. High frequency components on the

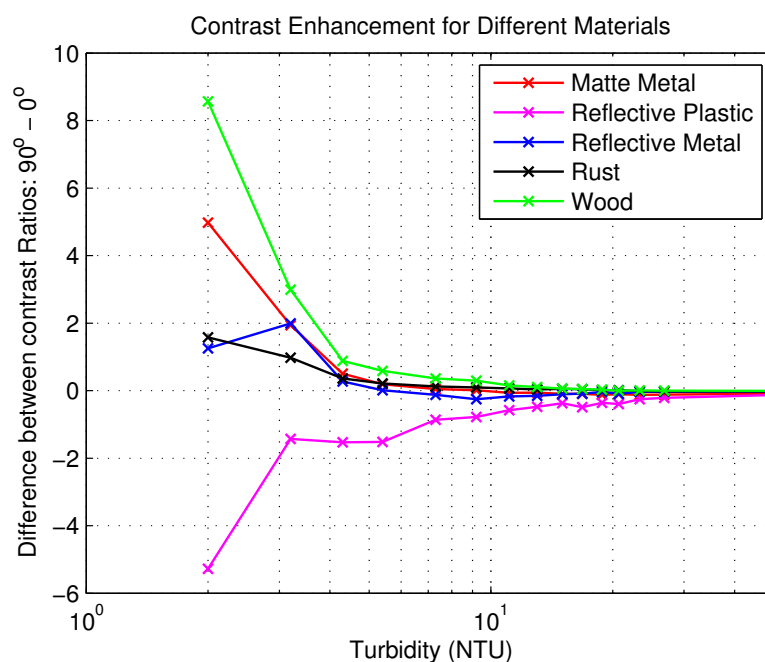


Figure A.7 – Shows the contrast improvement with the use of polarisation filters

edge scan function were being created in the MTF by the noise in the black background and the texture of the wood surface. Hence the result for the tank experiment using the edge scan function should only be used for comparison with the two measured filter angles. (Figure A.5)

The tank experiment suffered from some minor issues which might influence the results, these include uneven lighting of the scene, camera movement and the nature of milk as a turbidity medium. The camera flash was on the right of the device so the scene tended to be illuminated more on the right side, this may result in the contrast ratios for the objects in the left of the scene being lower. Milk is an isotropic scattering medium as opposed to an anisotropic medium which is more representative of an ocean environment. So the performance gain on the tank experiment may be inflated in comparison to a more representative medium.

One of the big issues to using polarisation filters is the reduction of light intensity, typical transmission is approximately 30% with 95% polarisation efficiency. Higher transmission filters are available but at the cost of polarisation efficiency. So combining the loss from two filters on both the light source and sensor, the resultant transmission is only in the order of

9% of the original light intensity. So either one must put a greater intensity of light into the water or be able to manage a reduction in the signal to noise ratio. Increased light comes at the cost of electric energy which is limited in the application of AUVs.

Besides the obvious improvement to visibility there is also an application for discriminating objects of different specular reflectance, this could be useful in detecting man-made objects on the seabed. This could be done by taking two images simultaneously similar to the dam setup with differing filter orientations and looking at the differences.

A.5 Conclusion

Polarisation filters placed on the light source and on the camera sensor at a perpendicular orientation were found to improve underwater visibility in a turbid environment. The improvement was shown through the increased contrast ratio between an object in the scene and the background. The image was sharper using the filters as proven using the modulation transfer function and the point at which visibility dropped off was extended by a factor approximately equal to two. The negative factor to using polarisation filters is a significant drop in light intensity being transmitted and received from the scene, requiring a higher powered light source or a reduction in the signal to noise ratio of the resultant image.